A Thesis Submitted for the Degree of PhD at the University of Warwick

Permanent WRAP URL:

http://wrap.warwick.ac.uk/106551

warwick.ac.uk/lib-publications

Enhanced absorption of infrared radiation in semiconductor photodetectors using micro-antenna arrays

Robert Espley-Jones

Thesis submitted for the degree of Doctor of Philosophy at the University of Warwick

Contents

List of figures

List of tables

Acknowledgements

I would like to express my sincerest gratitude to my supervisor, Prof. Tim Ashley for his support, patience and enthusiasm when helping throughout this process. His wealth of knowledge has been tremendously helpful to my improved understanding of these studies.

I would like to thank the rest of Quantum Devices Group at Warwick University: Dr. Richard Jefferies, Corinne Maltby, Dr. Mark Ashwin, Dr. Yasaman Alimi and Dr. Mark Crouch. They have provided considerable help and expertise during device fabrication and analysis.

Finally, I would like thank my family: My parents; Margret Espley-Jones and Gordon Espley-Jones and my siblings; Richard Espley-Jones and Caroline Espley-Jones. Their support coming up to submission deadlines was paramount and deeply appreciated.

Declaration

I declare that the thesis has been written by myself and that the work has not be submitted for any other degree or professional qualification. I confirm that the work submitted is my own, except where specifically noted. Some of the work has been submitted for publication as a jointly-authored paper. My contribution to this work was the simulation of the antennas; fabrication of devices; measurement and analysis of dielectric properties of $Al_{0.05}In_{0.95}Sb$; assessment of the components and analysis of results.

R. J. Espley-Jones, R. Jefferies, Y. Alimi, M. J. Ashwin and T. Ashley, "Enhanced absorption of infrared radiation in thin semiconductor photodetectors". Submitted to Optics Letters. (2018)

Glossary

Note: Some letters or symbols are used differently for multiple equations. The section they

are used in is specified in the definition to avoid confusion.

Symbol	Value	Units	Definition
A_{Frame}	-	m^2	Surface area of the frame
A_{Metal}	-	m^2	Surface area of the metal
B	-	Vs	Magnetic flux
B_W	2898	mK	Wien's displacement law constant
C	-	F	Capacitance
d	-	-	Edge cell path length
D	-	Cm^{-2}	Electric flux (section 3.4)
D	-	-	The far field directivity (section 3.8)
$D*$	-	-	The semiconductor detectivity
E	-	Vm^{-1}	Electric flux
E_G	-	eV	The semiconductor energy band gap
F	-	$\Omega\, m^2$	The resistance times the surface area of the mesa
G	-	Ω^{-1}	Conductance
h	6.62×10^{-34}	$m^2\, kg\, s^{-1}$	Planck's constant
H	-	Am^{-1}	Magnetic field strength
I	-	A	Current (section 3.1)
I	-	Wm^{-2}	Intensity received at the detector (section 5.1)
j	-	-	Mesh terminal
J	-	Am^{-2}	Current density
k	-	-	Mesh terminal
k_B	1.38×10^{-23}	$m^2\, kg\, s^{-2}\, K^{-1}$	Boltzmann's constant
k_E	-	-	Extinction coefficient
L	-	m	Arbitrary measurements regarding metal contact
L	-	H	Inductance (section 3.7)
L	-	m	Cubic length of the blackbody (section 7.1)

m	-	-	Component integer
M	-	$\Omega\,m^2$	The resistance times the surface area of the contact metal (section 5.4)
m_e	0.0178 m_0	kg	The effective electron mass in InSb
m_e	0.0116 m_0	kg	The effective electron mass in $Al_{0.05}In_{0.95}Sb$
m_0	9.1 x 10^{-31}	kg	The rest mass of an electron
n	-	-	Refractive index
$n_{k,j}$	-	-	Unit edge normal vector
p	-	-	Edge cell path length
P_{av}	-	Wm^{-2}	Time averaged Poynting vector
P_{in}	-	W	Input power
P_{rad}	-	W	The radiated power
P_L	-	W	Power that is lost (absorbed in the antennas or reflected)
q	1.60×10^{-19}	C	Charge of an electron
Q	-	-	Quality factor
r	-	Ω	Normalised resistance
R	-	Ω	Resistance
R	-	m	Radius of the sphere containing the far-field
$\vec{R}$	-	m	The magnetic field trajectory vector
R_0	-	Ω	Zero bias resistance
R_{Frame}	-	Ω	The resistance of the mesa frame
R_{Metal}	-	Ω	The resistance of the contact metal
R_s	-	Ω	Minimum reverse bias resistance
S	-	Wm^{-2}	Intensity of the monochromatic source
t	-	s	Time
$t_{k,j}$	-	-	Field propagation vectors
T	-	s	Time period (section 3.6)
T	-	K	Temperature (section 3.1)
U	-	W	The power radiated for a specified trajectory

V	-	m^3	Volume (section 3.1, equation 3.1.7)
V	-	V	Voltage (section 3.1, equation 3.1.8)
V_{eff}	-	m^3	Effective volume
w_A	-	m	The dipole aperture width
w_H	-	m	Hexagonal width
W_0	-	J	Time averaged stored energy
x	-	Ω	Normalised reactance (section 3.7)
x	-	m	Square length of the mesa surface (section 4.1)
x	-	m	Distance (section 4.2)
Y	-	Ω^{-1}	Admittance
Z	-	Ω	Impedance
α	-	-	Propagation attenuation coefficient
β	-	-	Propagation phase constant
γ	-	-	Propagation constant
Γ	-	-	Emission rate of the antennas
Γ_0	-	-	Emission rate of the bulk system
γ_M	-	-	Incident EM wave's mode of oscillation
Γ_R	-	-	Reflection coefficient
Δl	-	m	Length of the transmission line
ε	-	-	Dielectric permittivity
ε'	-	-	Real part of the dielectric permittivity
ε''	-	-	Imaginary part of the dielectric permittivity
η	-	-	Complex propagation mode
η'	-	-	Real part of η
η''	-	-	Imaginary part of η
λ	-	m	Wavelength
λ_{res}		m	Resonant wavelength
μ	-	NA^{-2}	Magnetic permeability
μ_0	1.25663706	m kg s^{-2} A^{-2}	Permeability of free space
ρ	-	Cm^{-3}	Charge density

σ	-	$kg^{-1}m^{-3}s^3A^2$	Electrical conductivity
υ	-	s^{-1}	Frequency
ϕ_R	-	-	Reflection phase
ω	-	s^{-1}	Periodic frequency

Abbreviation	Definition
AEI	Active element impedance
AR	Anti-reflection
CEM	Computational electromagnetics
CMT	Cadmium mercury telluride
CMT	Coupled mode theory
CST	Computer Simulation Technology
EBL	Electron beam lithography
EM	Electromagnetic
F	Field number
FD	Frequency domain
FDFD	Finite-difference frequency-domain
FDTD	Finite-difference time-domain
HF	Hydrofluoric
LED	Light Emitting Diode
LNH	Lactic acid, nitric acid and hydrofluoric acid mixture
LP	Log periodic
LPE	Liquid phase epitaxy
LSPR	Local surface plasmon resonance
M	Mesa set number
MBE	Molecular beam epitaxy
MIR	Mid Infra-red
MOS	Metal oxide semiconductors
NEP	Noise equivalent power

NMP	N-Methyl-2-pyrrolidone
NTA	Nanoantenna test array
P/A	Perimeter to area
P7	Paliney 7
PBS	PolyButene-1-Sulfone
PCB	Printed circuit board
PGMA	Polyglycidal methacrylate
PL	Photolithography
PMMA	Poly(methyl methacrylate)
QCL	Quantum cascade lasers
QWIP	Quantum well infrared photodetectors
S/N	Signal-to-noise
SEM	Scanning electron microscope
SRH	Shockley-reed-hall
TD	Time domain
TIA	Trans impedance amplifier
TPL	Two-photon excited luminescence
VSWR	Voltage standing wave ratio
W	Wafer

Abstract

This thesis is focused on signal-to-noise (S/N) enhancement of III - V semiconductor

photodetectors for use in gas sensing applications within a specific frequency band of interest

in the mid infrared (MIR) range. The semiconductor photodetectors can be grown as

homostructures, but experiments have shown a clear benefit to using heterostructures and the

quantum barriers they incorporate to reduce diode leakage. The proposed method of

enhancement is the use of waveguide coupling with different resonating materials of different

shapes, known as micro-antennas. The antennas were designed to be responsive to an

incoherent light source, such as LEDs. State of the art examples were considered to optimise

all aspects of the antenna design (i.e. the length, thickness, pitch and the dielectric constant)

to reduce surface scattering and enhance coupling. The experimental demonstration requires

consideration of maximisation of energy coupling into the intrinsic regions of $Al_{0.05}In_{0.95}Sb$

(Aluminium Indium Antimonide) semiconductor diodes. The theoretical results were

generated as a hybrid model to ensure full calibration and accuracy. Measurements of the

semiconductor attenuation coefficient were taken externally and applied to sophisticated

Electromagnetic (EM) simulation software. The EM simulations were done using Computer

Simulation Technology (CST^{TM}). It was used to verify the expected results for different

antenna sizes and to provide confidence for the outcomes of more elaborate design

enhancements, including large scale selective removal of the semiconductor. Selective

removal capitalises on energy coupling towards a specific position and depth close to the

surface. Further work into investigating far field manipulation effects of antenna design

applied to isotropically stimulated LEDs was included. Theoretical and experimental studies

are reported that show that the antennas needed to be of an appropriate size to resonate at the

appropriate wavelength. The variation with the antenna's dielectric properties as well as the

polarisation angle and trajectory angle of the stimulating source are reported. There are

numerous shapes to be considered for various intended applications. The antenna design that has suited our specific purpose has an efficient packaging density, is responsive to a non-collimated stimulation source, is made out of low cost conductive materials, is fabricated in a commercially viable way and provides consistent and stable results.

1) Chapter 1: Introduction

Antennas have been extensively used across numerous frequencies as an effective means of light manipulation. They give us a practical means to increase the path length of EM waves after coupling[1,2,3]. Antennas are made uniformly of a single conducting material that will experience resonance effects at specific frequencies depending on their geometry and dielectric properties.

The application these antennas are intended for is the signal enhancement of aluminium indium antimonide (AlInSb) semiconductor LEDs and photodetectors used in non-dispersive gas sensors in the mid-infrared (MIR) spectral range (see figure 3.0 (b)). The limitations of these semiconductors are the amount of light reflected at their boundaries. The amount of reflected light has been recorded to vary with frequency and trajectory angle but AlInSb photodetectors reflect about a third of the incoming radiation within this spectral range and < 95% of the AlInSb LED's stimulated light are reflected internally. Antennas are implemented in this research to reduce the reflections at the semiconductor boundaries, produce a wavelength filter and (for photodetectors) reduce the optical path length of the coupled radiation. It is estimated these improvements to the semiconductor gas sensor will increase the efficiency by several factors and is therefore a worthy investigation to conduct.

An electromagnetic field incident on the antenna conducting material will stimulate the clouds of electrons within the antennas into collective oscillation, called plasmons. These plasmons can be resonantly driven when they are stimulated with a specific wavelength. The conditions can conventionally be assessed by the dipole rule[4], where the plasmonic path length must be approximately equal to one quarter of the stimulating wavelength to tune the antennas to 1st order harmonic resonance. It is emphasised that this is an approximation because of the complexities regarding the antenna's dielectric properties and skin depth, δ.

The path length will reduce as a result of this effect so it is likely that a fully iterated antenna design needs to have a smaller conducting target wavelength. Furthermore, is has been noted that in pursuit of minimising the antenna size for compatibility with devices of very small dimensions, conventional (wavelength scale) antenna physics can no longer be applied when the materials are purposely made lossy to meet the requirements for plasmonic resonance[5].

$$\varepsilon_{metal} = -2\varepsilon_{dielectric} \qquad\qquad\qquad\qquad (1.0.1)$$

Plasmonic resonance is energy propagation through oscillating clouds of electrons and not simply conduction at the metal's surface. At optical frequencies this causes physical alterations to how the antennas are expected to resonate. The conducting material acts as a quasi-static antenna if the antenna size is significantly smaller than the stimulating wavelength, i.e. when it is small enough to be uniformly stimulated by the incident electric field at all moments of periodic incidence[5]. The solution in this scenario is known as the quasi-static approximation[6] which can be solved by calculating the electrostatic potential of the structure for a given geometry and dielectric constant embedded within a uniform electric field. This requires correct tailoring of the antenna size and dielectric properties. This difference is what makes quasi-static antennas fundamentally different from wavelength scale antennas. Due to their competitive coupling capabilities and relative ease of fabrication, wavelength scale antennas account for the higher proportion of work that is described in this thesis, but plasmonic antennas will also be considered (see section 6.4).

When considering antennas for waveguide coupling, it is important to correctly determine specific antenna parameters since the resonance peak is extremely sensitive to antenna geometry. A large focus of this thesis is therefore dedicated towards accurate simulation of the antenna resonance. There will also be consideration regarding its effect on the

interconnected circuitry, when the devices are tested by means of probing. To do this, simulations were performed using a 3D finite difference frequency domain (FDFD) electromagnetic simulator (CST Microwave Suite®). The mathematics that govern these simulations are derived from Maxwell's curl equations which will be explored further in chapter 3. Another factor considered is the scattering parameter calculated from impedance mismatch theory between two mediums[8].

$$\Gamma = \frac{R_L + iX_L - Z_0}{R_L + iX_L + Z_0} \tag{1.0.2}$$

Where R_L is the load resistance, X_L is the load reactance, Z_0 is the impedance and Γ is the boundary reflectivity. The parameters given in equation 1.0.2 are all part of the transmission line connection between two conductors. This analysis is necessary as it takes into account the boundary conditions for a given segment of the device. The segment is the coupling between air to antennas to semiconductor and the other way round in the case of light emitting diodes (LEDs).

Higher order wavelength scale antennas are as small or as large as they need to be if they are to be tuned to the fundamental harmonic oscillations, in accordance to the dipole rule. The alternative would be that they are tuned to resonance integers of higher order magnitudes which would be optimum provided the antenna conducting length is large enough for multiple half wavelength current oscillations to be a factor[7]. Antennas with effective design parameters are derived from determining the standing wave reflection phase at the path length terminals, ϕ_R. If the phase of the propagating standing wave, however long, is at a quarter integer at the transition terminals, then the optimum amount of energy will be re-emitted after being subject to reduced boundary impedances. The condition that dictates

whether an antenna with a conducting length L will resonate when stimulated by a wavelength (λ) at any resonance harmonic integer is given in equation 1.0.3 and 1.0.4[8,9].

$$\lambda = \lambda_{eff} \cdot \eta' \tag{1.0.3}$$

$$L = \frac{\lambda_{eff}}{2\pi}\left(m \cdot \pi - \phi_R\right) \tag{1.0.4}$$

Where m is the harmonic integer and η' is the real part of the standing wave propagation mode which varies with the antenna conducting length and dielectric properties. Equation 1.0.3 references the Fabry-Perot model which describes the eigenmodes of a resonant system of a finite conducting length. There are other factors that need to be considered and tuned to get the maximum S/N ratio for the intended application of this thesis – gas sensing. These parameters are listed in figure 3.6.1. The aim of this research is to understand the parameters engineers in this field can control and what impact changing the parameters will have on the photodiode response and relate it back to what semiconductor enhancements are possible compared to standard semiconductor or semiconductor with antireflection coatings of the surface[10].

1.1) Research aims and objectives

The aim of this research is to enhance the signal output from conventional gas sensors in the mid-infrared spectral range as much as possible using enhanced surface coupling and focusing techniques provided by surface antenna designs for both the semiconductor photodiode and the LED emitter. This research and modifications to the fabrication procedures are documented in this thesis as evolutionary improvements to gas sensors in the mid-infrared spectral range. Each modification need to provide justifiable and relevant

contributions to a factor of 8 speculated signal-to-noise (S/N) improvement. This factor of 8 improvement is believed to be possible by means of:

1) Photodiode surface antireflection.

2) Thinning down the photodiode epitaxial layers.

3) Localised signal focusing in the detector.

4) Selective removal of the semiconductor volume.

5) Focusing the far-field emission of the LED emitter.

The factor improvement of the photodiode is targeted at 4 and the factor improvement for the LED is targeted at 2, making the combined enhancements capable of providing a factor of 8 improvement. The majority of these modifications concern photodetector alterations and therefore will make up the larger proportion of research and alterations. The antenna designs considered for both the emitter and the detector are numerous and varied. All considered designs are used in hybrid based models to gain a better understanding of how they function and whether they are of the appropriate design to achieve and optimum semiconductor enhancement.

1.2) Gas sensor technologies and applications

The applications for gas sensors in today's market are broad. A gas sensor becomes a necessary investment in situations where one's business or wellbeing is dependent on the amount of specific gases in the atmosphere. They are bought for insurance purposes to detect the leakage of volatile hydrocarbons in refineries or oil rigs. They are used as smoke detectors or can be used in ventilation systems to maintain an adequate level of carbon dioxide in the room. They can also provide ideal atmospheric conditions for plant growth.

The aim of the thesis is to develop a non-dispersive infrared (NDIR) gas sensor with the optimum S/N ratio for a given application. The choice of gas sensor must therefore have competitive benefits so as to avoid needlessly improving the device when there is another technology available that can already compete with these improvements. However, with such a variety of uses it is justifiable to argue that different gas sensing technologies are more suitable then others depending on the application. To resolve these disputes, existing gas detection technologies are compared with each other in various aspects with relevance to the specific application given in a QFD (Quality Function Deployment) chart. Figure 1.2 provides one example for methane detection in oil refineries. The application will dictate the weighted importance in various figures of merits. In the example given, oil refinery engineers are likely to pay more for a gas detector as long are it can detect volatile gases with a prompt response time and also function for a long time before maintaining or replacing the device becomes necessary. It is also likely that there are no strict requirements on detector size. Therefore, the weighted importance of cost, longevity, power consumption, response time, safety considerations, sensitivity, size and specificity in this example will respectively be, 2, 3, 1, 2, 2, 2, 1, 3.

Application:
Oil rig CH$_4$ detection

Key:

Competitive = Θ = 9
Average = O = 3
Poor = Δ = 1

	Weighted importance	Metal oxide semiconductors	Catalytic sensors	Electrochemical sensors	Resistive Thermal Detectors	Golay cells	Pyroelectric detectors	Thermopile detectors	Semiconductor photodiodes
Cost	2	Θ	O	Θ	O	Δ	O	O	O
Longevity	3	O	O	O	Θ	Θ	Θ	Θ	Θ
Power consumption	1	Θ	O	O	O	Θ	Θ	O	Θ
Response time	2	Δ	O	Δ	O	O	Θ	Θ	Θ
Safety considerations	3	O	O	Θ	O	Θ	O	Θ	Θ
Sensitivity	2	Θ	O	Θ	O	Θ	Θ	O	Θ
Size	1	Θ	Δ	Θ	Θ	Δ	Θ	O	Θ
Specificity	3	Θ	Θ	Δ	Θ	Θ	Θ	Θ	Θ
Score		110	65	86	93	121	123	117	141

Figure 1.2: QFD chart summary of the gas sensing devices compared to one another. The score is given by adding the symbol value provided in the key for each category.

Devices are compared to one other in the following respects:

Cost: There are many factors here that are not simply down the device volume and price per kg of needed materials. There is also design complexity, fabrication techniques, rate of production, where it is made, delivery costs and mark-up prices if the device is modified and sold on. For these reasons it is difficult to get a pricing comparison that is consistently valid. Therefore, the costs figure of merit will address more obvious differences in required material costs, manufacturing technology, maintenance, design complexity and ease of fabrication.

Longevity: This will compare the average life time of devices before maintenance or replacements are needed to address problematic drifting in measurement accuracy.

Power consumption: This will address the cost of operation.

Response time: The time before a reading can be given.

Safety considerations: The more dangerous the device is to use, the lower the score it will receive. This addresses operating temperatures as well as hazardous chemicals and reactions. These considerations only address safety when using the final product and not any hazards during device manufacturing.

Sensitivity: Also given as detectivity for some devices. This assesses the response signal of the device while accounting for any noise sources.

Size: If the intended application requires integration into small or compact environments this will assess whether it is possible as well as any proximity difficulties to adjacent components.

Specificity: There are different ways different gas sensing technologies can detect gases. Specificity does not dispute the sensitivity or efficiency of the detection method, but simply whether it can detect specific molecules that are relevant to the application and whether there are any relative difficulties in doing so.

This QFD chart features allocated scores based on advantages and weaknesses detectors have compared to what is available, where the symbol:

Θ: means this detection method has a clear advantage over most alternatives in the depicted category. It is considered one of the devices competitive selling points that is relevant to the intended application.

O: means this detection method is good in its own right in the depicted category, but not particularly special.

Δ: means this detection method has a relatively poor performance in this category. The engineer should be aware of these short comings when considering the detector if these symbols are featured.

To calculate a score for the technology, the numeric value of the allocated symbol is multiplied by the weighted importance. The rows are then added up and total at the bottom of the chart.

As shown in the example QFD chart in figure 1.2, photodiodes are a competitive product for methane detection on oil rig applications because of its competitive advantage in categories that are considered particularly important. Whether that score is maintained depends on the application, but generally the photodetector can continue to remain competitive as long as the gas specificity remains in its spectral bandwidth. It is not suitable for the detection of molecules with a non-asymmetric structure.

1.2.1) The metal oxide semiconductor (MOS) sensor

The MOS sensor is a relatively low cost semiconductor that detects gas types when they are chemisorbed on to a heated surface at around $200 - 400^{o}$C. The surface is catalytically oxidised, which leads to changes in resistance of the material. These sensors can give a quick response, but the precision is relatively low, the lifetime is limited and not very selective and the device needs to be frequently cleaned[11,12].

Cost: Production costs are kept low due to the simplicity of the metal oxide structure.

Longevity: Typically more than 5 years.

Power consumption: ~250 mW.

Response time: Varies with grain size and humidity, but it takes of the order of minutes.

Safety considerations: High temperatures required for operation.

Sensitivity: The sensitivity changes depending on factors that influence the surface reactions[13]. However these devices are generally considered to have a high sensitivity. Tin oxide with an indium oxide composite it recorded to give the best results.

Size: These devices are microstructures and can be used for compact applications.

Specificity: The gas must be able to chemisorb the oxygen molecules of the SnO_2 surface if it is going to work. Identifying and ratioing multiple combustible gases in the chamber is difficult.

1.2.2) The catalytic sensor

Catalytic sensors are used to detect combustible gases when they are oxidised. The sensor is in the form of a spiral coil made of platinum and coated with layers of Alumina and Thorium oxide with a palladium or rhodium catalyst[11]. As the spiral coil heats up as a result of the reacting gas, its resistance will change. This change of resistance is measured and can give an indication of the gas density.

Cost: The catalytic sensor has been in use for over 50 years and has served as a relatively cost effective device. However, in recent years alternative gas sensors are becoming cheaper and more competitive, particular where the catalytic spare parts costs are concerned[14].

Longevity: Exposure to heat and gas pressures are known to cause sensor deterioration and shifts in the zero of up the 10% per year of use. The lifetime of the product can vary but typically lasts 3 years before a replacement is needed.

Power consumption: ~100 mW

Response time: 10 – 15 seconds.

Safety: Requires high room temperature to meet gas ignition conditions. This temperature varies based on what gas needs to be ignited and which catalyst is being used, but operating temperatures can be as high as 60°C. CH_4 experiments are intrinsically unsafe and cannot be held in flammable environments. Fortunately, most catalytic sensors provide ATEX housing that much the detection of CH_4 safe.

Sensitivity: The sensitivity of this device has been documented to vary depending on which gas is being used[15]. The sensor outputs is proportional to the rate of oxidation for which there is an optimum voltage that can be applied. The problem with this sensor is that the gas must be able to oxidise. CO_2 is not a gas that is able to do so.

Size: The coil requires a large surface area to be effective during oxidation. The detector must necessarily take up a large amount of space.

Specificity: Unable to detect gases that do not combust.

1.2.3) Electrochemical sensors

Electrochemical sensors function by using the principle of the Galvanic cell – where two electrodes are connected via a salt bridge. Most are amperometric. Once activated, the toxic gas diffuses through the membrane and oxidises on the target electrode. This causes a measurable potential difference between the electrodes to indicate the gas density[11].

Cost: Competitive.

Longevity: Typically 2-3 years.

Power consumption: None

Response time: Varies depending on the material of the electrodes used, but response times are of the order of 10s – 30s[16].

Safety: Non-hazardous set-up.

Sensitivity: Competitive[17].

Size: Competitive.

Specificity: Recommended for the detection of most hazardous gases, but there is no electrochemical sensor for CH_4.

1.2.4) Bolometers

Bolometers are components of a non-dispersive gas sensing system that detect the presence of infrared radiation by the change in power absorbed.

- They have a long lifetime.

- They require less maintenance.

- Their spectral bandwidth is considerably wide and although that makes them poor frequency filters they can be used to detect a vast variety of molecules. Their vast specificity makes them a competitive choice for a wide range of applications.

- Some designs require high temperature for operation, but they have no potentially dangerous reactions when they are used.

- They have a vast specificity restricted only by whether the molecule vibrates at a characteristic frequency

They come in five different categories:

1.2.4.1) Resistive thermal detectors

Resistive thermal detectors are constructed from semiconductor materials having very small thermal capacity and large thermal coefficient so that the absorbed incident radiation produces a large change in resistance. They are made up of an absorptive element connected to a heat sink. The increase in temperature causes a change in thermal conductivity of this

device. Thus, by measuring the resulting current or voltage changes, information regarding the frequency of the radiation can be deduced prior to proper bolometer calibration[18,19,20].

These devices are very versatile as they are responsive to all frequencies where the power absorbed is linear and in proportion to the frequency of the radiation it is exposed to. Equally, if there is a specific frequency range of interest bolometers make very poor filters to undesirable frequencies. Induced power is proportional to the frequency as well as the intensity of the incoming light and the device can be imprecise at distinguishing whether it is one or the other. Their response time is also subject to the rate of thermal dissipation, making the delay of this device considerable compared to alternatives. There is also an environmental factor to consider. These devices will heat up. This can either introduce heated conditions that are straining to users or it can introduce additional maintenance costs of keeping the devices cool in an effort to suppress thermal or photon noise and to avoid enhancing the noise equivalent power (NEP).

Cost: Competitive, although manufacturing costs may be a factor due to complex fabrication techniques and reduced device sizes.

Power consumption: Uses a current of the order of hundreds of milliWatts but has document benefits to a reduced NEP if higher currents are used.

Response time: 1.5s thermal time constant.

Sensitivity: W-B song et al. provides a summary of the microbolometer NEP, where it is proportional to the fluctuating noise voltage, target frequency, the amount of surface reflection the microbolometer conductance. It is inversely proportional the resistance, bias current and temperature coefficient of resistance. The NEP can therefore be low if tailored correctly, but high degrees of noise are unavoidable at high frequencies (such as MIR).

Size: Documented parameters can be as small as microns (see figure 1.2.4.1).
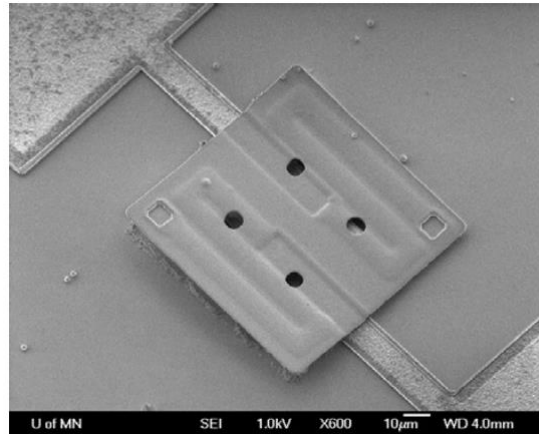
Figure 1.2.4.1: SEM image of an individual 100µm by 100µm microbolometer device[18].

1.2.4.2) The Golay cell

The Golay cell is another MIR detector that functions by means of absorbing THz (Terahertz radiation) and generating heat. It works at ambient temperatures and has broad spectral response. The basic elements that make up a Golay Cell are the transparent IR window, a small gas chamber that includes a thin, partially absorbing metallic film and the IR absorber (also known as an optical microphone)[21]. When the optical microphone absorbs IR radiation it will heat up and by extension heat the gas adjacent to it. The pressure in the gas chamber will increase which will distort a flexible and fragile glass and a silver based mirror. An optical readout system will monitor the distortion of the mirror and consequently the irradiance onto the photodetector.
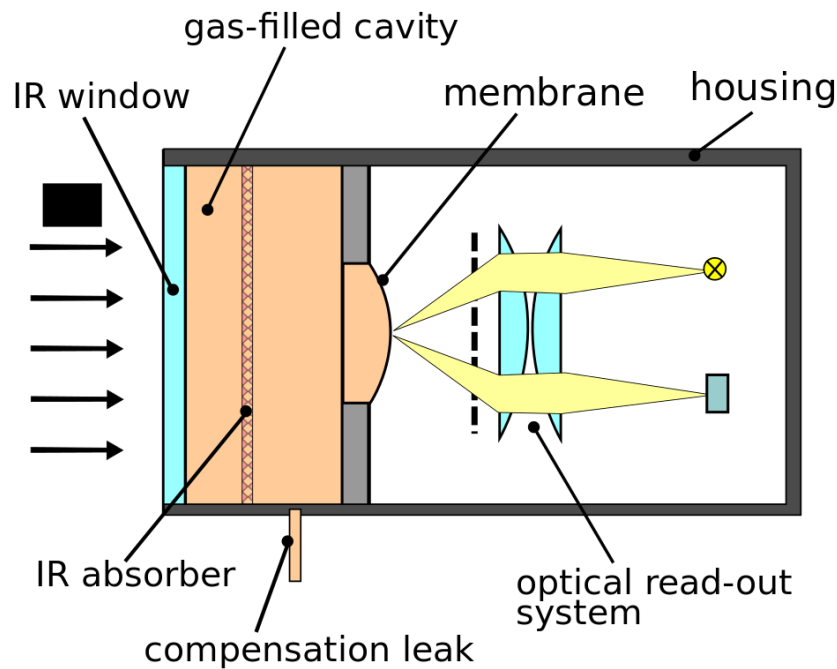
Figure 1.2.4.2: A diagram of the Golay cell[22].

While the device is large as a necessity, the design does feature an IR window which can be used to incorporate optical filters making the response tailorable to more desirable frequencies. The compensation leak acts as heat sink to cool the device and as such it can function at room temperature where no cooling is needed. Due to thermal dissipation in to the gas chamber before the flexible mirror distorts, the response is slow[23].

Cost: Several components are needed with the filter and housing making up the bulk of the cost. Relatively expensive.

Power consumption: ~ 10 μW

Response time: ~ 25ms. Relatively slow.

Sensitivity: High sensitivity, which an accuracy of sub nW.

Size: Large. Unable to function in small compact spaces.

1.2.4.3) Pyroelectric detectors

Pyroelectric detectors function on the basis of converting thermal energy to electrical energy in a very thin pyroelectric plate. This plate has top and bottom electrodes which form the radiation sensitive detector element. Changing the temperature by incident radiation on the pyroelectric plate will influence charges in the electrodes. The resulting short circuit current is proportional to the rate temperature change. The pyroelectric source is a high impedance device and therefore needs to be converted by a pre-amplifier that is also tolerant of an impedance source. Similar to the thermopile detector, these devices are distinguished by the advantages of a wide wavelength response, no requirement for cooling, high-temperature stability and low cost[24]. However, the single quality of both the pyroelectric detectors and the thermopile detectors degrades with frequency. They are only reliable at low frequencies which make them unsuitable for our intended application.

Cost: Relatively inexpensive.

Power consumption: 50 mWcm^{-2}

Response time: ~100 μs.

Sensitivity: Competitive, although vibration sensitive. Poor at high frequencies.

Size: Small, compact housing.

1.2.4.4) Thermopile detectors

Thermopile detectors consist of many thermocouples connected in series. The thermocouples are made of two dissimilar yet conductive metals (such as antimony (Sb) and bismuth (Bi)) to influence a potential difference when the electrons in each metal shift to difference energy levels. They generate an output voltage that is proportional to the temperature difference across the two metals (or between the hot and cold junctions). The hot junction is the active

metal that is exposed to the radiation and the cold junction is the metal that is connected to the detector package. The thermopile detectors exhibit an inherently stable response to DC radiation. They have been recorded to have a lower detectivity than pyroelectric devices, but have better noise suppression.

Cost: Relatively inexpensive.

Power consumption: ~ 100 μW[25]

Response time: 5-10 μs

Sensitivity: Relatively low. Worse at high frequencies

Size: Realistic parameters can be as small as 2 mm.

1.2.4.5) Photodiode detectors

Semiconductor photodiodes are structured as a p-n junction, with an intrinsic or low doped region between the highly doped n-type and p-type regions. Their advantage over thermal sources is a response time of a microsecond, which is roughly x1000 faster compared to delays from thermal dissipation. The advantage semiconductor LEDs have over QCLs is that they are spectrally broader and thus can be used to sample all parts of a given spectral width. LEDs are smaller and cheaper to fabricate and maintain. They have long term stability, commercial viability and resistance to poisoning. They have been used a number of applications, such as communications, healthcare, missile countermeasures and gas sensing[26].

Cost: Relatively inexpensive.

Longevity: Expected to exceed 3 years.

Power consumption: 44 μW – 560 μW.

Response time: ~ 1μm

Sensitivity: Peaks have been recorded at 0.065 AW^{-1}.

Size: Can be grown as thin as nanometers.

Specificity: Dependant on the bandwidth of the semiconductor material. Has been recorded to be responsive between 2.5 µm and 4.5 µm.

1.3) Thesis outline

Chapter 2: Antenna literature review

Chapter 2 provides a literature review that will cover the range of antenna designs intended for semiconductor photodiode enhancements. This review will compare the results of each documented result so designs suitable for our application can be identified and considered for localised enhancements.

Chapter 3: Theory

Chapter 3 covers the theory of how these devices work. The semiconductor physics will address their spectral response as a function of the tailored band gap, how a photocurrent response related to the Shockley-Reed-Hall effect and the necessity of having doped epitaxial layers. The antennas function according to Maxwell's equations and transition line measurements. This theory provides the basis of how computational electromagnetics are used in simulation, which will be applied in later chapters.

Chapter 4: Fabrication methodology

Chapter 4 will outline how all state-of-the-art semiconductor gas sensors in this thesis are fabricated and will focus on how enhancements are implemented. This overview is utilised in future chapters concerning semiconductor gas sensor evolutionary development.

Chapter 5: Results analysis

Chapter 5 provides results of the enhanced photodiode experiment and compares it is the CEM and theory described in chapter 3. Studies of the antenna's response to the semiconductor attenuation coefficient and the use of quantum barriers are assessed as well as the measurement techniques employed and the consequences of excessive use. Original designs include a prototype for initial proof of concept and a more elaborate design to expand on it. Analysis includes how the samples are tested, how the semiconductors function in relation to control samples, how the signal response varies with temperature and any details during the fabrication and analysis steps that have proven detrimental to the device performance or longevity.

Chapter 6: Micro-antenna progression and alternative designs

Chapter 6 consists of theoretical additions when more complex designs are modelled and considered for fabrication despite the difficulty in precision. These alternative designs include very precise selective, large scale volume reduction, forwarding the signal to a single feed point and tuning to first order plasmonic resonances to assess the difference between plasmonic and higher order wavelength scale resonance. The same modelling procedures described in chapter 3 and 5 are used to support the theoretical modelling outcome.

Chapter 7: LED emission antennas

Chapter 7 focuses on the simulated benefits of using antennas as waveguide manipulators and assess the enhancements in terms of gain, beamwidth and bandwidth for different potential designs. The application is applied to 5%AlInSb LEDs and focuses on far field manipulation and bulk enhancements to analyse the change in power emitted.

Chapter 8: Conclusions and recommendations for future work

This is the main conclusion that provides a summary to what this research has accomplished over all chapters and how it has contributed to gas sensor enhancements. Original contributions to this field of research are clearly stated will references to previous chapters for further information. Future work discusses objectives not yet achieved in this research, how to achieve them and the benefits of doing so. Comments that are based of the experimental and simulated work of this thesis will be made on what is achievable in theory and what can realistically be done in practice.

1.4) Chapter 1 conclusion

Chapter 1 introduces the topic of gas sensing applications and provides an insight to different, modern, state of the art methods of detecting MIR light and converting it into a meaningful signal. The advantages and disadvantages of each gas detection methods are covered so that the decision to specifically use semiconductor photodiodes for our enhancements is justified for further study and development.

In regards to the gas sensor application, this chapter has considered various means of detection carbon dioxide and methane gas while collectively assessing and comparing each detection methods. The methods of detection are judged based on cost, longevity, power consumption, response time, safety considerations, sensitivity, size and specificity.

The scoring depicted in section 1.2 shows that semiconductor photodetectors are a justifiable choice based on their competitive features in 8 categories as well as not having any major weaknesses. It is for these reasons that semiconductor photodiodes are used for further development.

This chapter has outlines the aims and objectives that will be pursued in an effort to enhance both the photodiode devices and the LEDs. These improvements are addressed both theoretically and experimentally in later chapters. They will address the characteristic flaws of a photodiode and the modifications that can be made to improve these flaws. Control devices (standard LEDs photodiodes) are featured for comparison and so that numerical enhancement values can be obtained and how close these enhancements come to the predicted factor of 8 improvement.

2) Chapter 2: Antenna literature review

This literature review assesses advances in the field of localised enhancements in semiconductor devices in the mid infrared range and how the documented achievements can be related to the signal-to-noise (S/N) ratio enhancements in the semiconductors considered in this thesis. Note: all images and diagrams in this chapter are taken and referenced from literature sources unless specified in the image description.

When comparing results, it is worth mentioning the different terminologies used in antenna applications. For example, Adato et al.[27] has described successful resonance of gold dipole antennas in terms the amount of light that is reflected at the antenna terminals. Other publications regard reflected light as light that is lost and can be counter intuitive to claim that maximised reflectance is desirable.

In Adato's work, the light is then coupled into a protein monolayer of varying thickness that absorbs wavelengths characteristic of its own size and can therefore by used as an in-built filter. This provides insight on how the entire system can potentially be used as collective wavelength filters. However, semiconductor epitaxial layers (see section 3.1) have a marginal impedance difference and cannot capitalise on internal resonance unless a more intrusive method is used, such as grown wavelength filters in between the layers.

The wavelength range is 2.5 μm – 20 μm which is an adequate wavelength range for the gas detector application and therefore antenna dimensions that are directly applicable. It is unfortunate that this work has only considered linearly polarised light, which not a commercially viable way is simulating the intended target. With a dipole conducting length of 1.6 μm the antennas meet the dipole rule requirements, but interestingly there are other publications that claim this is not a strict requirement.

Law et al.[5] have documented antenna scattering to describe antenna influence in the redirection of light and features plasmonic antennas. The plasmonic antennas provide interesting insight towards how resonance can be achieved in a much smaller volume of antenna. They have used differently doped InAs for the antenna material and the substrate it is grown on. InAs is not a good conductor compared with conventional conducting metals, but is used to meet the requirements for plasmonic resonance. That requirement is that the magnitude of the antenna dielectric constant (ε_m) is twice that of the semiconductor underneath (ε_s) – see equation 1.0.1.

Their work features antennas with a radius of 0.435 that resonant at 9.8 μm. These antennas are therefore small enough to make the dipole rule non-applicable making this research worth investigating further if smaller antennas become a necessity for smaller devices. Section 6.4 features simulated plasmonic coupling results that are inspired by this work. These investigations are conducted for the purpose of identifying a material that meets the plasmonic resonance requirement but also to identify the intricacies of the plasmonic coupling propagation path.

Olmon et al.[7] have displayed results in terms of impedance matching at the antenna terminals to describe coupling into the material underneath (silicon). The antenna length in relation to the simulating wavelength changes the impedance between different materials. They have targeted a resonant wavelength of 10.6 μm and features dipoles lengths of 2.6 μm so their antennas operate on wavelength scale harmonics. The Olmon example is more closely related to S/N ratio enhancement via amplified absorption in the material but silicon is not a diode and therefore cannot directly provide any enhanced photocurrent information. This work does emphasise a beneficial degree of coupling that is dependent on the antenna dimensions

relative to the target wavelength, but further investigation is warranted to verify if this is applicable to all conducting materials (see section 5.5.3).

A common message the literature contains is that antenna resonance in its most fundamental terms is light manipulation in an alternate direction that is influenced by the size and shape of a conducting material on the surface. This has influences on a number of measurable differences in device performance. It is therefore not expected for all meaningful graphs and measurements in the literature to have consistent units. That would either be beside the point of the results or would not be possible based on how the device structure is used. There are also aspects of antenna resonance that are not addressed, such as light propagation as a function of difference harmonic resonances after coupling. This information likely not featured because it is already well established[4], but this is still very relevant information when the thesis is concerned with localised focusing – which is dependent on the propagation pattern.

That said, there are many examples that can infer an enhanced S/N ratio, but few can give a measured example that can compare directly to enhanced semiconductor absorption prior to taking into account circuitry impedance. To address this, the computational electromagnetics (CEM) will be used later to test the designs featured in this literature review to establish a more direct comparison to the (S/N) ratio. This method can also address other factors such as the standing wave harmonics, the attenuation coefficient and the refractive index that is specific to the material that is being used.

The aim of this literature review is:

1) To determine which kind of antenna is most suitable for localised focusing that can enhance light absorption with in the i-type epitaxial layer of the 5% AlInSb semiconductor.

2) To determine the benefits of these antenna designs for transmission purposes when applied to semiconductor LEDs.

All antenna designs that have been read and documented for the purposes of background research fall into one of the following designs displayed in figure 2.0.
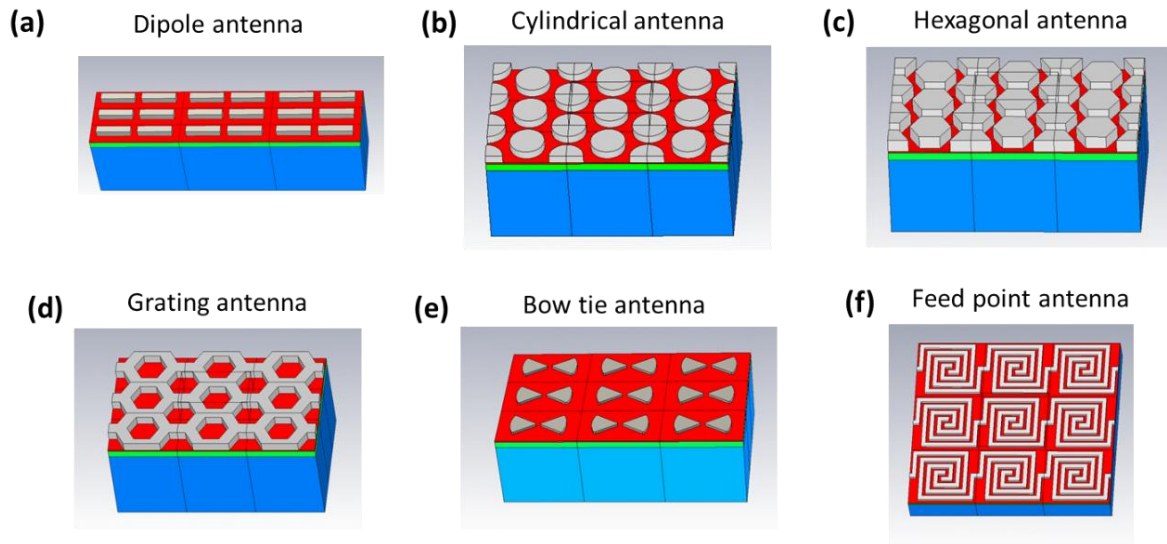
Figure 2.0: 3D CAD based diagrams of different antenna designs. (a) Dipole antenna array (b) Cylindrical antenna array (c) Hexagonal antenna array (d) Grating antenna array (e) Bow-tie antenna array (f) Feed point antenna array (spiral). These images were made by author.

There are additional designs such as patch antennas, spiral antennas and helix antennas, but these are the most prevalent examples accompanying recorded work as well as being the most realistic designs to fabricate.

With reference to the dipole rule of the first resonating order, the wavelength (λ) of a dipole antenna is expected to be responsive to a ¼ λ conducting length integer assuming the incident polarisation is parallel to this length. More accurately, it is the conducting path length that the incident EM wave will resonant in after induction. The resonant wavelength is expected to change in the antenna material once the wavelength has been shortened in accord to the dielectric properties, which are considered to be lossier at MIR or visible wavelengths compared to MHz or GHz frequency range used for telecomunications[8,28]. Therefore, in the

spectrum of interest the dipole rule is no longer accurate and there are many cases where the

conducting length is approximately 20% shorter than the dipole rule would have predicted.

Regardless of how the effective wavelength changes and which harmonic order the antenna is

tuned to, the current will still propagate in the same nature as described in equation 2.0.

$$E_\theta = \frac{i\eta I_0 e^{-ik_E r}}{2\pi r} \left[\frac{\cos\left(\frac{k_E L}{2}\cos\theta\right) - \cos\left(\frac{k_E L}{2}\right)}{\sin\theta} \right]$$ (2.0)

Where E_θ is the electric field strength of the propagation angle into the semiconductor (θ), η

is the refractive index, L is the length of the conductive material, k_E is the extinction

coefficient, r is the propagation factor and I_0 is the current amplitude[29]. Equation 2.0 describe

the distribution of the electric field as it flows alone the conducting length where the electric

field will be at its most potent at $L = \lambda/2$ integers.

There are other cases where antennas are made larger than the first order dipole rule so that

they are tuned to a higher order resonant peak. This is done to achieve lower angular widths

of the coupled radiation with in the aperture and is necessary if near field focusing is desired.

This is in accordance with equation for far field radiative patterns[4]. This is described

mathematically in equation 2.1 where S is the time averaged power density radiated in a

certain direction, θ.

$$S(\theta) = \frac{|E_\theta|^2}{2\eta} = \frac{\eta I_0^2}{4\pi r^2} \left[\frac{\cos\left(\frac{k_E L}{2}\cos\theta\right) - \cos\left(\frac{k_E L}{2}\right)}{\sin\theta} \right]^2$$ (2.1)

Equation 2.1 can be used to derive a coupling pattern into the substrate where the first order

harmonics (when $L = \frac{1}{4}\lambda$) provides a distributed coupling pattern. The next order harmonics

(when $L = \lambda/2$) has a similar radiation pattern but half the beamwidth and the $L = \frac{3}{4}\lambda$

harmonic exhibits multiple lobes at wide trajectory angles. This is the oscillation mode that is most beneficial for antenna tuning as it exhibits the largest degree of localised coupling.

Due to their size, micro-antennas have higher resistive impedances than nanoantennas and rely more heavily on efficient propagation of electromagnetic energy if they are going to remain competitive. Thus, it is often beneficial to use highly conducting materials to achieve a minimum amount of losses, where Au, Ag, Al, and Cu are common examples of antenna materials. However, there have been efforts to make antenna material out of photonic crystals or doped metallic compounds so as to reduce the surface reflection during electromagnetic induction into the antennas, since energy transmission form one medium to another is dependent on the impedance mismatches. Law et al. have these photonic crystals featured in their work[5] to provide emission enhancements to the radiative bandwidth and the far field patterns. They have demonstrated radiative cross sections that are over 3 times more intense at a wavelength of 6 μm than those emitted by wavelength scale antennas at 0.5 μm. It is therefore worth investigating whether plasmonic antenna emission is possible for semiconductor LEDs as well as whether InAs demonstrates an advantage for LED applications (see section 7.3).

This chapter will reference the examples of successful antenna design and highlight the documented advantages when these designs are compared to one another.

2.1) Dipole antenna design

Adato, Yi, Novotny and Neubrech[8,27,30,31] are a few examples of where dipole designs have been necessary for experimental work. Dipole antennas are two monopoles brought in close to each other for the benefit of enhanced light coupling in close proximity to standing wave eigenmodes (i.e. the energy state of oscillating wave vectors) of opposing phases known as Two-Photon excited Luminescence (TPL). These eigenmodes act like oscillating point

charges that can enhance coupling between two wires over a narrow gap and can create highly localised and strongly enhanced optical near fields inside the gap size which later will be referred to as hotspots[9]. It is this effect which makes such an arrangement highly efficient. Applications for dipole antennas are very common in the MIR and visible spectrum. The bandwidth of dipole antennas can be adjusted by varying the antenna aperture width (and by extension the antenna pitch)[32,33].

However, these designs are polarisation sensitive and require a coherent source to obtain an optimum output. When incoherent light is used, there are expected to be significant losses since the dipole antenna can only accept a small range of polarisation angles and still work efficiently. Using a coherent light source (such as a QCL) is expensive and may be impractical for use in low cost, point gas detection.
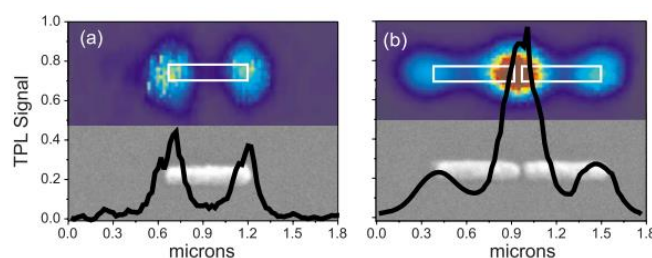
Figure 2.1: The amplified effect of the TPL signal when monopoles are in close proximity to each other[34]. (a) Monopole antenna (b) Dipole antenna.

Alternatively, largely polarised light could be produced from an LED if the dipole designs are also applied to the LED surface. However, the dipole antennas are equally as dependant on polarisation angle of the LEDs. The internal generation is isotropic which results in very poor coupling and impedance issues.

To summarise, the dipole design is only applicable to linear polarised applications if it is to remain a competitive design option.

2.2) Cylindrical antenna design

For non-collimated applications, cylindrical designs are one of the suitable alternatives. This antenna array has the advantage of having a uniform length for each incoming polarisation angle. It is a common occurrence that these devices have rounding (side wall angle) defects when used at the wavelength that are intended for MIR and optical applications (see figure 2.2 (c)). While monitoring absorption in thin solar cells, Langhammer et al. [35] have documented that rounding has blue shifting effects as well as a reduction in intensity as a result a reduction in path length and reduction in the antenna quality factor, Q. The Q factor is a measurement of the antenna's ability to store energy[36]. It is important to consider these observations should any defects occur in the devices fabricated in this thesis (see section 5.3).
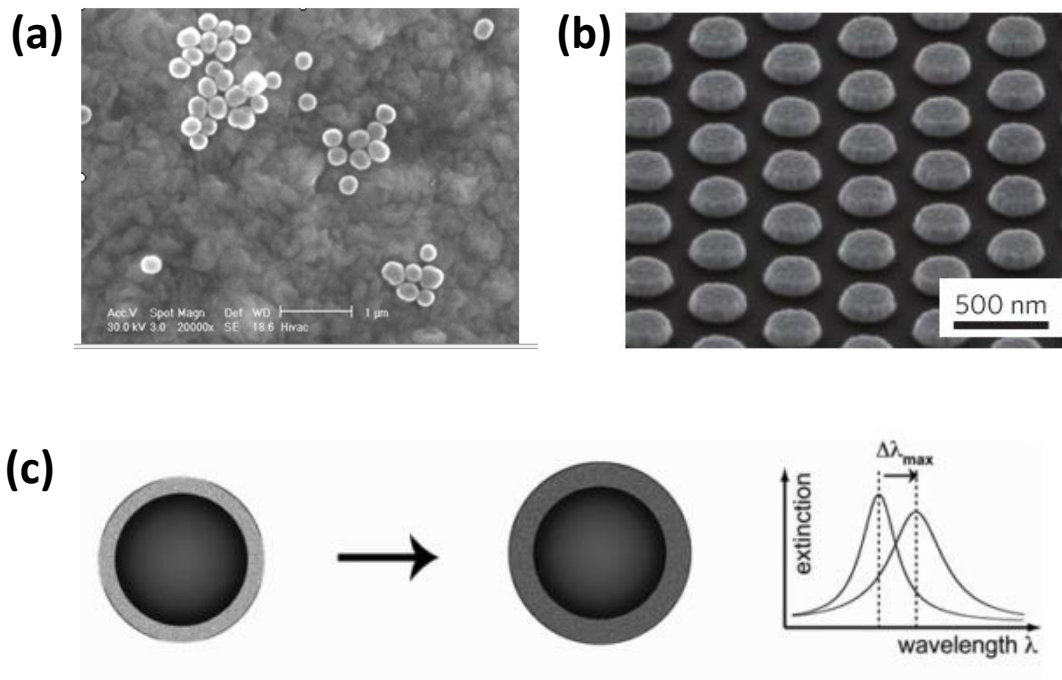
Figure 2.2: Examples of cylindrical antenna applications. a) Gold cylindrical antenna used for photo acoustics bio imaging[37]. b) Silver hexagonal nanoparticles evaporated through a porous alumina template, annealed at 200 °C for the purposes of enhanced photovoltaic absorption in thinned solar cells[38]. (c) The effect of side wall defects upon interaction with a substrate[35].

Despite that these devices have also been successfully used in clusters, it is beneficial to have devices arranged with a consistent pitch to stabilise the intensity and bandwidth. Circular and hexagonal antennas have a high tolerance to incoherent light will function in similar ways but it is noted that hexagonal antennas have a slightly better package density and consistent aperture size[39,40].

When applied to emission applications, the antennas can produce a much more centralised bulk magnitude emission and can potentially concentrate the emitted radiation in a reduced beamwidth increasing the power density. This is what has been observed in section 7.3.

2.3) Grating antenna design

Grating antennas (also known as cavity or hole antennas) are a favourable design for "bull's eye coupling" (i.e. when the near field coupling has a focal point on the cavity central aperture). The disadvantage of these designs is that they are interconnected and suppresses coupling in the apertures when the antennas act as a conducting wire[41]. These devices still produce a clear bandwidth for incident radiation but these antennas are the most reflective and absorbing design per unit cell. The shape of the cavities can be dipole or circular depending on what is more compatible with the stimulation source.
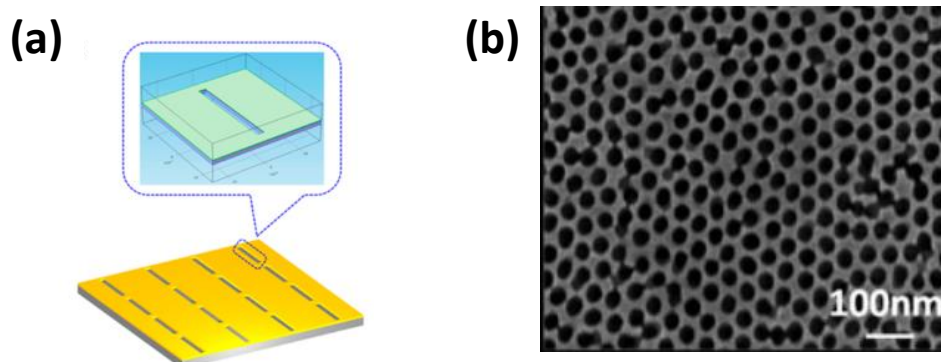
Figure 2.3.1: Different types of antenna cavity designs (a) Dipole cavity design[31] (b) Circular cavity design[42].

The advantage is that the antennas can be used for high angle re-emission. An example of this

is their use in Quantum Well Infrared Photodetectors (QWIPs). QWIPs are semiconductor

photodetectors that are only responsive to propagating waves with an E_z component (i.e. the

electric field propagation in the direction of material growth)[43]. The semiconductor epitaxial

layers are grown on top of the GaAs layer and the antenna structure is grown on top of the

semiconductor. The incident radiation will go through the GaAs layer at a normal angle of

incidence. They will then propagate through the semiconductor layers and become incident

on the antenna arrays as shown in figure 2.3.1. The cavity antenna structures will provide a

complementary advantage to these devices when they absorb and remit EM waves at high

angles of incidence so total internal reflection can occur.
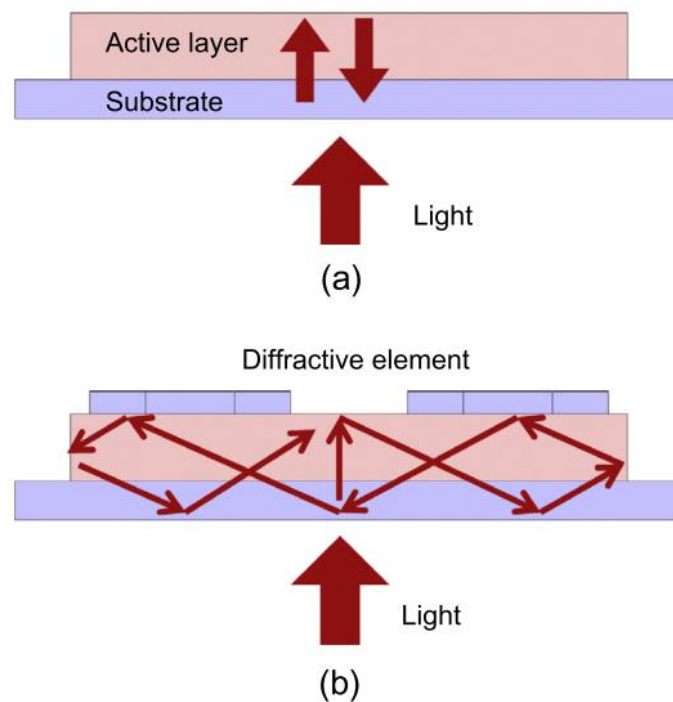
Figure 2.3.2: Diagrams of how QWIPs capitalise on total internal reflection with the aid of grating antennas (a) The light passing through the substrate underneath at normal incidence. (b) The light passing through the substrate and active layer but is now under the influence of a different element, i.e. the antennas[43].

The antenna grating structure may have suppressive reflections compared to other designs,

but that comes as an inherent advantage for emission applications. Grating antennas have

been recorded to produce clear spectral bandwidths and good control over the radiation

pattern. Any frequency that mismatches resonant parameters is reflected internally as shown

in figure 2.3.2.

With regards to emission application, the interconnected conducting metal greatly affects the

emission angle. There is a dependence of the degree of coupling but the far field emission is

very dispersed for the circular and hexagonal grating designs. The same dispersive tendency

applies to the dipole grating, although it still has influences of its emission dipole counterpart.

The bow tie grating antennas are considered by Guo et al[44] for far field emission. His work

details an emission dependency on antenna material. The design is much more tolerant of

polarisation angles compared to the dipole grating and can potentially reduce the beamwidth.
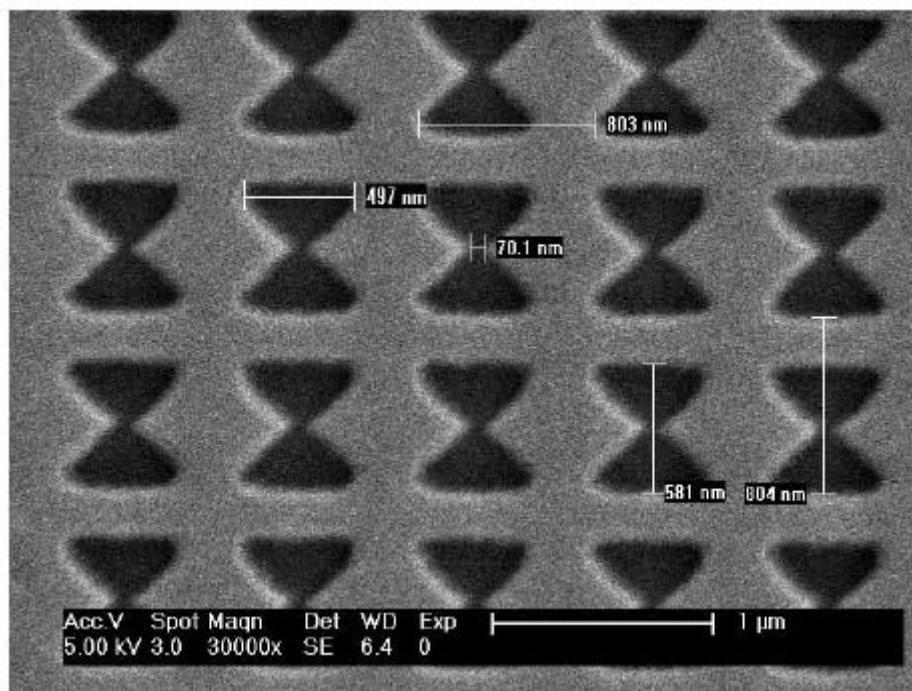
Figure 2.3.3: The bowtie grating array used to focus transmission beams from LEDs[44].

2.4) Bow-tie antenna design

The bow-tie antenna design (also known as cone or butterfly antennas) functions as smaller versions of feed point antennas. Both the bow tie antenna design and the bow tie grating design have an advantage of being more tolerant of non-collimated incident radiation and they can collect a larger sum of electromagnetic states and focus it onto a single point. Because of the designs relatively inefficient packing density, it is reliant on the central point being of particular importance. An example is given by Fang et al.[45] where light is collected and forwarded to a nanowire. The relative simplicity of this design is appealing, but this design does not have a bandwidth that is as undesirably broad due to the more expansive shape. A proposed way the solve this is to introduce log periodic (LP) antennas.
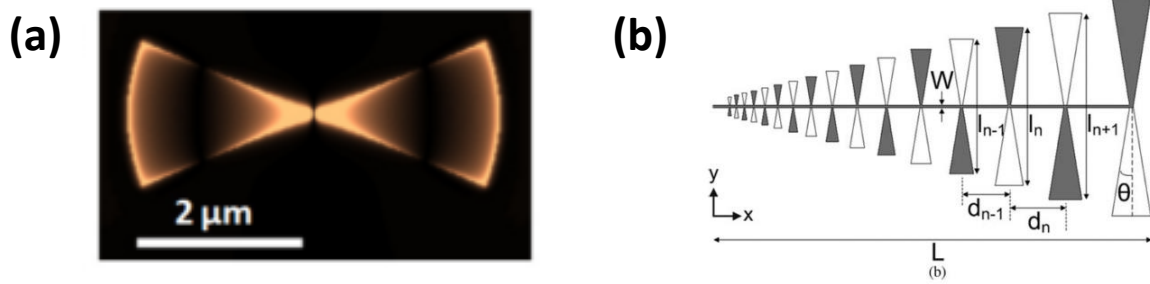
Figure 2.4: (a) A colour coded representation of the electric field distribution as the bow tie antennas resonate[46]. (b) A sketch of a log periodic antenna design to enhance the bandwidth responsivity[47].

LP antennas are a variation of the bow tie design with exponentially increasing conducting lengths separated by a spacing multiplication factor denoted by the expansion coefficient, τ. The expansion coefficient is a factor increase value applied subsequent lengths, l_{n+x} of the LP array.

$$l_{n+1} = \tau \cdot l_n = \tau^2 \cdot l_{n-1} \tag{2.4}$$

This expansion rule applies to the spacing between the different conducting lengths. The spacing is representative of the wavelength the conducting lengths are resonating with so that

when all signals are collectively forwarded to the feed point the front-to-back ratio (i.e. the ratio of signal transmitted to the feed point compared to the reflected signal) the gain is optimised. Leo et al.[47] have recorded a far field gain enhancement of 5.5 dBi - 7.3 dBi in the 1 GHz to 6 GHz frequency range using 16 different sized bow-tie antennas. This is a design alternative that is available for bow tie design, but it still produces a compromised packing density and it is questionable whether the centralised focusing or the bandwidth tailoring can compensate for this.

2.5) Feed point antenna design

Feed point antennas are resonating conducting volumes that can focus on small targets compared to the antenna size. They are expansive designs and often produce larger bandwidths on account of their volume and the numerous wavelengths they can resonant with depending on the position and orientation of the incoming wave in a similar respect to LP bow tie antenna designs. This is undesirable for precision in resonant wavelengths but is very beneficial with regards to gaining as much power as possible at a wide spectral array, which is normally the goal when applying feed point antennas to bolometers or silicon based photo voltaic cells in solar panels to increase the efficiency[48]. Given the application, it is likely that they are intended to collectively be rectennas (RECtifying antennas).
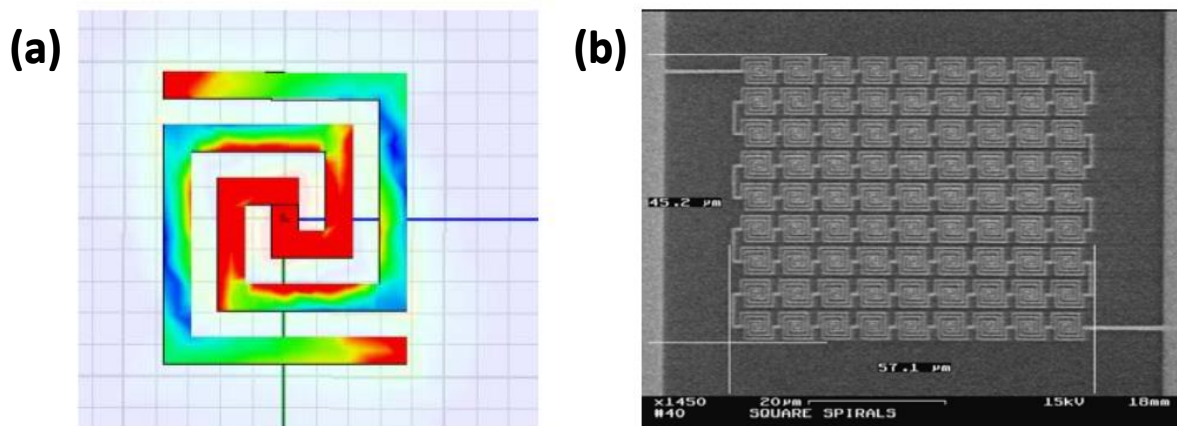
Figure 2.5.1: A square feed point antenna for solar cell applications[49] (a) A colour coded representation of the electric field strength as the feed point antenna resonates with THz radiation where red is the most intense. (b) An array of nantennas (rectifying nanoantennas), printed in gold and imaged with a scanning electron microscope.

Rectennas are antennas based devices that rectify the input EM waves into a DC current and are a combination of a receiving antennas and a rectifier. Converting to a DC signal is desirable in power generation applications to conserve energy when transmitting over long distances.
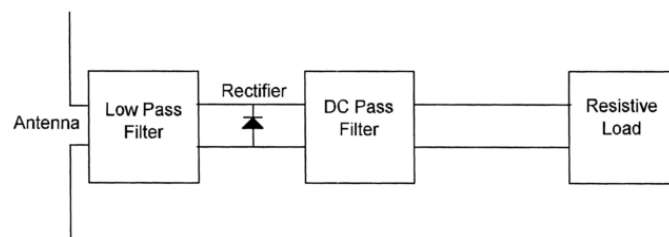
Figure 2.5.2: A block diagram of the rectenna attachment prior to antenna coupling[50].

A variation to the feed point antenna design shown in figure 2.5.1 is the spiral feed point antenna. The spiral antennas are responsive to circularly polarised light which is useful for signal encryption since a dipole antenna is less responsive to circular polarised light However, by extension spiral antennas are less responsive to linearly polarised light and they will only receive half the signal. If it illuminated with circularly polarised light in the opposing direction (i.e. clockwise rotation when the antenna is an anti-clockwise spiral) then no signal is received.

They have a higher bandwidth compared to dipole antennas as a result of how expansive the design is. Spiral antennas typically have a LP design to minimise the return loss. The spiral antenna width w will exponentially increase as the spiral arms get longer in accordance to the spiral flare constant, a[51].

$$w = w_0 e^{a\phi} \tag{2.5}$$

Where w_0 is the initial spiral antenna width and ϕ is the angle. The width increases at the

same rate as the antenna radius in order to maintain a constant spacing, low return losses and

larger bandwidth response.

The alternative is to keep the arm widths the same size. This is a variation known as an

Archimedean spiral antenna which behaves more like a dipole in the sense that a narrower

bandwidth is expected provided the incident polarisation is compatible to the spiral antenna

consistent shape.

Feed point antenna and bow tie antenna have potential for single point focusing to the

detriment of coupling into most of the volume and so it is likely that these designs will not be

recommended unless the semiconductor i-type layer is selectively removed, the narrow

bandwidth response is necessary or whether circular polarised light needs to be featured in

the application.

2.6) Chapter 2 conclusion

There is a wide variety of antenna options to consider. They all provide documented

enhancements at frequencies characteristic of their size. The applications can vary between

light focusing, light scattering, light trapping and responsivity to polarisation type.

Bandwidths can vary depending on the size variety introduced into the design. The results

show that the antennas are responsive but cannot provide a like-for-like comparison to

epitaxial layer absorption – due to the antenna designs being used for different applications.

One can argue the benefits by logical extension, but to determine specifically how much

enhancement one can expect to get it is necessary to simulate the designs.

Of the many antenna designs that are available, it is desirable have documented features that are beneficial for the intended gas sensing application. A beneficial antenna design will include:

- A narrow bandwidth. The antenna design can provide better precision if it features a narrow bandwidth where the peak matches the specificity.

- A good response to a non-collimated light source (i.e. random polarisation angles, random trajectory and random phases with time). For the photodetector, this ensures good compatibility with more economically viable light sources. It also ensures that the antennas are more responsive to the internal isotropic emission of the semiconductor LEDs.

- An efficient packing density to ensure all parts of the semiconductor surface are influenced by the antenna array.

- A good responsivity to MIR frequencies.

In order to better understand how these antennas will benefit photodiode and LED enhancements it is necessary to understand the theory of how these enhancements are obtained and how computational electromagnetics (CEM) will provide this information. Numerical values can be associated with different designs so that they can be compared and provide context to the advantages and disadvantages specified in the antenna literature review.

3) Chapter 3: Theory

Now that the semiconductor gas sensing technology has been decided on and the background of how antennas will influence the semiconductor has been established, context is provided to the theoretical simulations that are to be used for results comparison as well as preparation for practical experiments.
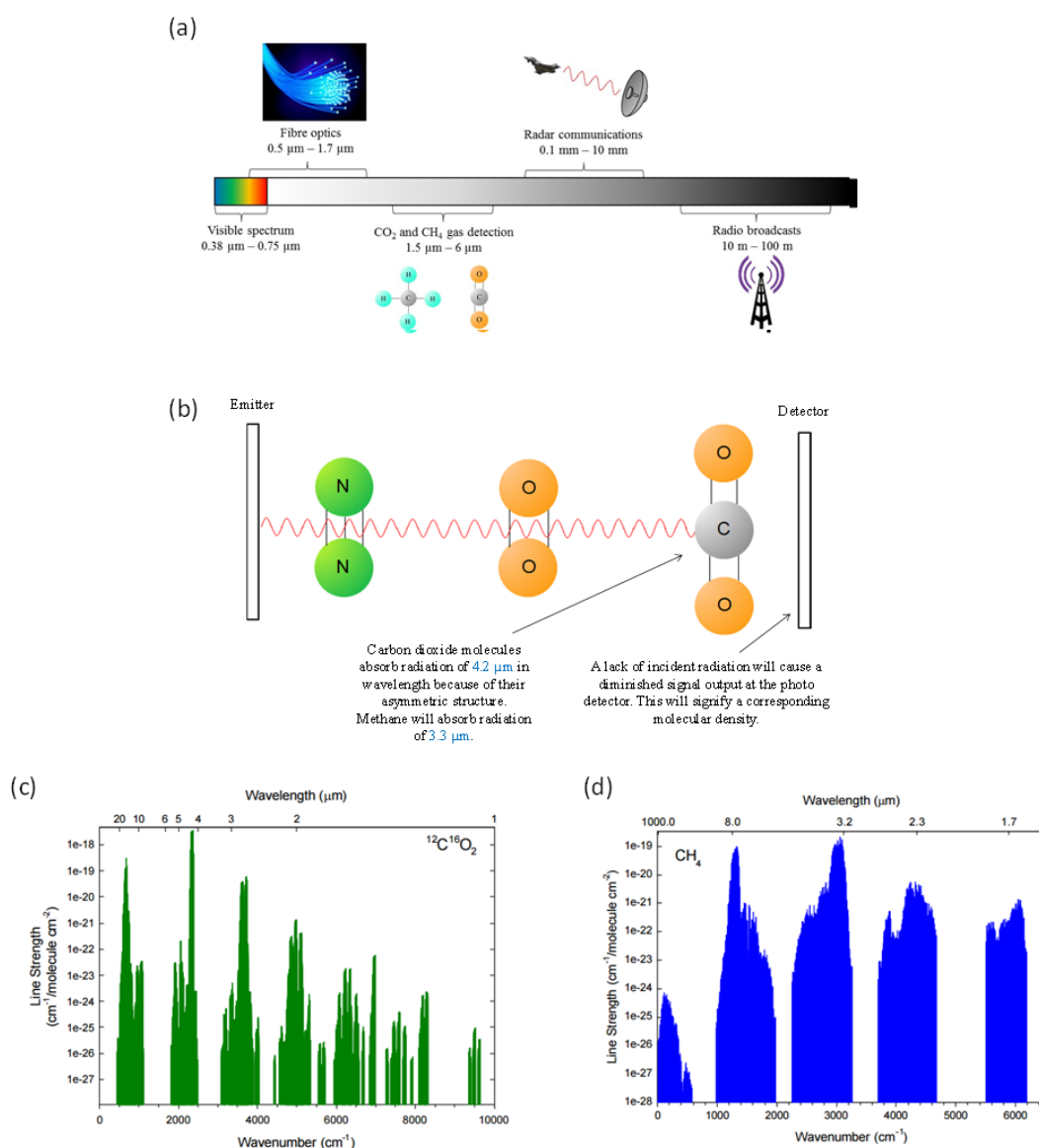
Figure 3.0: Summary of gas sensor application. (a) The spectral region of interest for several antenna applications[52,53]. The detection of hazardous gas molecules is between 1.5 μm and 6 μm. (b) Diagram depicting how a gas detector works. Graphs of the absorbance/transmission ratio vs. the wavelength of the incident radiation for: (c) CO_2 molecules[54] and (d) CH_4 molecules[55].

As depicted in Figure 3.0, the frequency of interest is between 1.5 μm - 6 μm (50 THz – 200 THz). This wavelength range will be able to detect the target hazardous gas molecules; carbon dioxide (CO_2) and methane (CH_4). These molecules will resonantly absorb a number of wavelengths, but a wavelength of 4.2μm (71.3 THz) will be absorbed most significantly for CO_2 and a wavelength of 3.3 μm (90.8 THz) will be absorbed most significantly for CH_4[56]. The photodiode therefore needs to be tailored to absorb these wavelengths and to minimise response for others. Once the semiconductor has covered this bandwidth, the varying attenuation coefficient needs to be determined across this spectrum.

As discussed in chapter 2, the signal-to-noise ratio for the photodetector can be enhanced by antenna arrays by reducing surface reflectivity and redirecting incoming energy to a certain depth in the photodetector. The surface reflectivity and impedance mismatch at the antenna terminals therefore need to be determined as well as the loss in the antenna material and the reduction of reflectivity compared to anti-reflection coatings[10].

For LED emission applications, the impedance mismatches need to be taken into account for isotropic emission within the LED, the change in far field beamwidth needs to be established and the intensity variation need to be derived to assess signal enhancement by introducing a more intense signal.

Even after this has been determined there is still the matter of understanding the signal loss in the circuitry used to produce experimental data as well as minority carrier influenced diode leakage on the semiconductor surface.

This provides context to the complexity of obtaining reliable theoretical data for this research. This chapter will go through the theoretical physics of how semiconductors and antenna designs work in theory and how it is applicable in computational electromagnetics (CEMs).

However, since the system is too convoluted for CEM modelling to solve in its entirety, individual measurements featured in chapter 5 will be taken and integrated with the model, resulting in a more accurate hybrid model.

3.1) The semiconductor LED/photodiode epitaxial homostructure

The semiconductor homostructure shown in figure 3.1.1 provides the basic structure for the semiconductor LEDs and photodiodes. The aluminium is implemented as 5% of the overall composition so that the energy-gap is increased to be better matched to higher EM frequency compared to plain InSb.

$p^+ Al_x In_{1-x} Sb$: Be	0.1 μm
u.d. $Al_x In_{1-x} Sb$	0.5 μm
$n^+ Al_x In_{1-x} Sb$: Te	5 μm
$Al_x In_{1-x} Sb$	Buffer layer
GaAs	Substrate
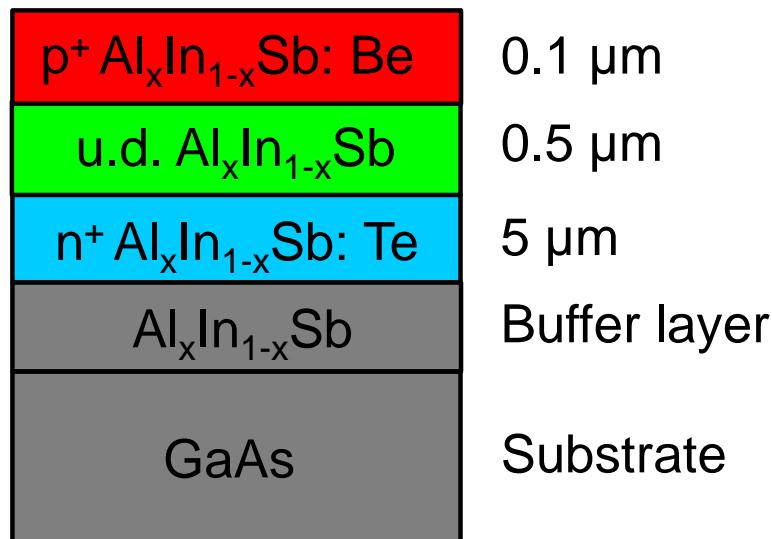
Figure 3.1.1: AlInSb photodiode epitaxial layer homostructure, where x = 0.05. n^+ is the n-type semiconductor layer, p^+ is the p-type semiconductor layer and u.d. (undoped) is the intrinsic or undoped layer. $x \cong 0.05$[57,58]. Note: Because these semiconductor epitaxial layers are a homostructures, they are susceptible to reverse bias current flow. Conductive materials placed on the surface will stimulate the flow of reverse bias minority carriers; therefore changes to the structures will be made to account for this.

The GaAs substrate is a mechanical layer for everything that is deposited on top by means of molecular beam epitaxy (MBE). There is a difference in lattice parameters between the AlInSb and the GaAs substrate. As such, the AlInSb lattice will be strained, which can result in dislocations. These dislocations will produce a drop in overall performance as a result of

defects that will increase the carrier recombination rate. The buffer layer exists to provide a standard transition from the substrate material to the epitaxial active layers.

The n-type (n^+) and p-type (p^+) semiconductor layers are the doped layers. They have electron excess and electron deficiencies (holes) respectively. Degrees of doping are what generation and recombination (G – R) effects depend upon. The intrinsic layer of the semiconductor is the undoped region, so unlike the p^+ and n^+ type layers, charge density depends solely on the volume and background doping properties of the material and not on the degree of intended doping. A thickness of 0.5 μm to 3 μm are typical examples of an intrinsic layer for LEDs and photodetectors respectively. The i-type layers in semiconductor LEDs are grown thin via molecular beam epitaxial (see section 4.1) so the reabsorption of light is minimised. The i-type region of the photodetector is grown thicker because there has to be sufficient absorption, although there is an advantage in growing the i-type as thin as 0.5 μm when near field focusing and precision selective removal is involved. The n-type and p-type layers may also be inverted if it better suits waveguide coupling into the i-type region.

When these semiconductors are used as photodiodes for gas sensing applications, the detector's figure of merit is the detectivity (D^*). It quantifies the S/N ratio that is expected from the semiconductor[59,60,61,62].

$$D^* = \frac{\sqrt{A_d}}{NEP} \sqrt{\Delta f} \qquad\qquad (3.1.1)$$

Where NEP is the noise-equivalent-power, A_d is the detector area and Δf is the electrical bandwidth. There are a number of different noise sources in this device, but at room temperature - which is the condition that these devices are intended to function in - the noise as a function of carrier generation and recombination is by far the most dominant.

$$D* = \frac{R_I \sqrt{A_d}}{I_n} \sqrt{\Delta f} \tag{3.1.2}$$

Where I_n is the induced current and R_I is the current responsivity. The noise current due to generation and recombination (g-r) is given as:

$$I_n = q\Gamma \sqrt{2(G_{g-r} + R_{g-r})\Delta f} \tag{3.1.3}$$

Where G_{g-r} is the generation rate in the semiconductor volume and R_{g-r} is the recombination rate, q is the electron charge and Γ is the photoelectric gain. In LEDs, the dominant contributor to the noise is the non-radiative Auger process, which gains precedence over other factors such as Shockley-Read mechanisms because of the high carrier density featured in narrow band gap applications, whereas at low or zero bias SRH recombination is more important.

The quantum efficiency is given as:

$$\eta = \frac{hc}{q} \frac{R_I}{\lambda} \tag{3.1.4}$$

When incorporated into equation (3.1.2), the detectivity becomes:

$$D* = \frac{\eta\lambda}{hc\sqrt{2(G_{g-r} + R_{g-r})}} \frac{\sqrt{A_d}}{\sqrt{d}} \tag{3.1.5}$$

Where d is the optical path length derived as the root proportionality factor to the photoelectric gain (Γ). d can be optimised by means of localised focusing or light trapping design (such as QWIPs). The semiconductor total generation and recombination rate has a direct proportionality to the semiconductor volume, V.

$$(G_{g-r} + R_{g-r}) \propto V \tag{3.1.6}$$

Thus, the semiconductor figure of merit has an inverse proportionality with the root volume.

$$D* \propto \frac{1}{\sqrt{V}} \qquad\qquad\qquad (3.1.7)$$

Equation 3.1.6 and 3.1.7 addresses what is fundamentally crucial in a photodetector design where the noise is reduced as much as possible, i.e. a much larger S/N ratio is obtainable when the incident signal supersedes the noise induced volume assuming the temperature remains constant. If the incident radiation can be absorbed in a smaller volume, for example by the use of antennas, then the $D*$ will increase. It is the objective of this research to determine the extent to which this can occur.

The photocurrent that is generated from these semiconductor devices becomes the predominant diffusion current – which is generated from thermal diffusion of minority carriers from the quasi-neutral n^+ and p^+ regions. The dark current – the amount of reverse bias current will degrade the diode performance and is considered to be leakage[63]. At zero bias, the current is ideally meant to be zero. This is likely not to be the case if the diode is subject to background light. It is therefore important to take into account whether the photodiode is being measured in dark conditions, despite the relative intensity of the stimulating source compared to the background light.
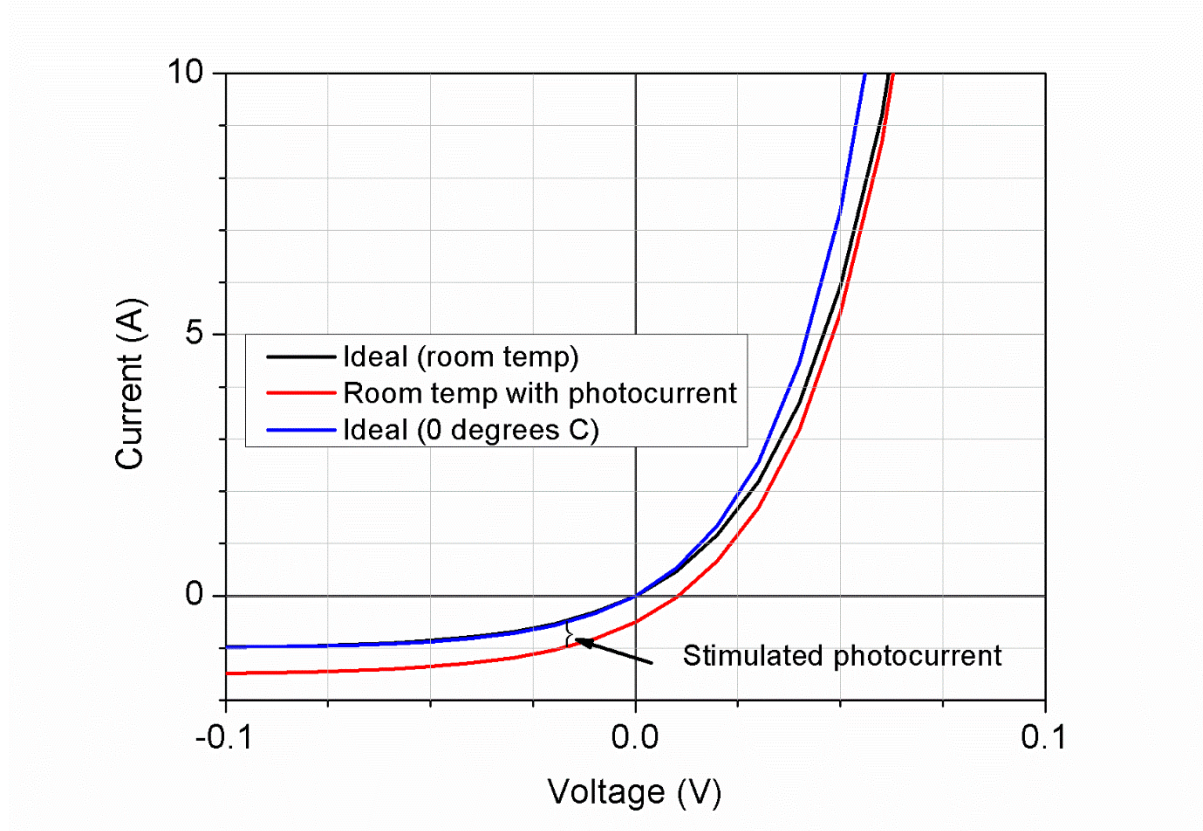
Figure 3.1.2: Diagram comparing the ideal photodiode at room (22°C) temperature (black line), the ideal photodiode at 0°C (blue line) and the room temperature (22°C) photodiode with a stimulated photocurrent that degrades the diode quality. Figure was created by author.

The semiconductor device is strongly dependant on the background temperature. Lower temperatures will lower the reverse leakage and increase the amount of forward biased current. When the intended enhancement is the amplified waveguide coupling, it is important to record and maintain a constant laboratory temperature so that the improvements are entirely to do with antenna enhancements and not the semiconductor's thermal dependency. The ideal diode equation is given in equation 3.1.8:

$$I = I_0(e^{\frac{qV}{kT}} - 1) \tag{3.1.8}$$

Where I is the net current flowing through the diode, I_0 is the dark saturation current. q is the charge of an electron, k is Boltzmann's constant, V is the voltage applied to the photodiode and T(K) is the temperature.

It is important to understand this when considering the detrimental effects to the diode quality that temperature, external light or minority carrier generation will cause. Minority carrier generation happens when conducting materials in close proximities to the semiconductor epitaxial layer (such as antennas or contact pads) cause a net flow of changes that oppose the flow of charge for the Shockley Read Hall (SRH) effect (i.e. the device will be leaky). If the assessment of the benefits of antennas is going to be fair then the test samples must be kept at a constant temperature, must be tested in a dark environment and must either have protection from the antenna minority carrier generation or the testing must provide a means to take them into account. These conditions were strict and consistent with all measurements shown in this thesis to avoid diffusion based resistances.

3.2) Semiconductor lattice alterations

If the Indium atoms in InSb were to be replaced by Aluminium (Al) atoms which have fewer full electron shells, then the energy band gap will increase. It does so because outer electrons in Al occupy a shell with a lower energy level than that of In. This causes an increase in the electron energy required to rise up to the conduction band.

The Al atoms are not impurities. They are replacing the In atoms which makes them part of an altered lattice constant. The growth and contraction of the material lattice constants can occur as a result of material composition alterations can cause a change in the energy gap as illustrated in figure 3.2 between the AlSb point and the InSb point.
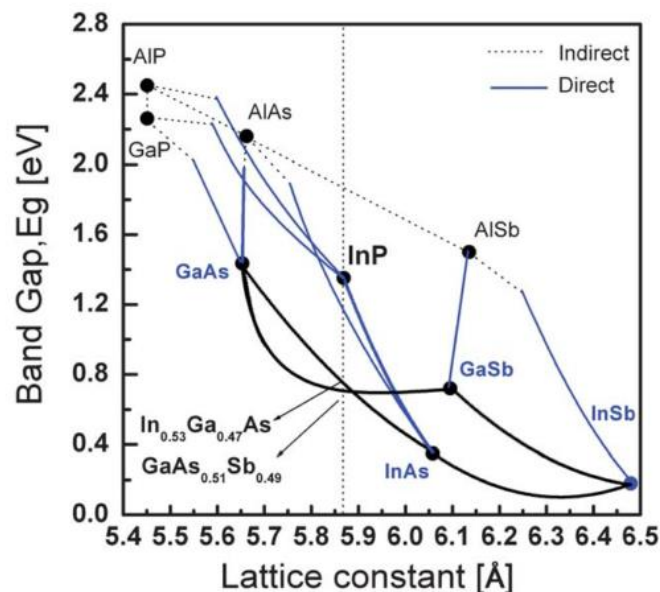
Figure 3.2: A range of energy gaps sizes for group IV, III-V and II-VI semiconductors. The figure illustrates that InSb has a suitably close energy gap before the addition of materials with different periods in the periodic table[64]. Note: an indirect semiconductor band gap (dashed line) means that the conduction and valence band are misaligned on the reciprocal lattice vector.

In accordance to figure 3.2, there are a few LED contenders with good suitability in the mid-infrared region. There is a whole family of group III-V materials which can have their material and lattice parameters appropriately altered to be suitable for emitting/detecting radiation of wavelength 3.3 μm. InSb is one of them, but there are variations such as InAs or GaAs based material. There are also additional semiconductor groups, such as HgTe which is a group II-VI material and there are group IV-VI materials which are Pb based, such as PbSe[65].

Impurities and native lattice defects will cause an increase in non-radiative Shockley-Read-Hall recombinations, and which will decrease the semiconductor efficiency[66]. Therefore, these impurities and defects must be kept to a minimum. InSb, which has a starting energy band gap of 0.17eV, has the closest energy band gap to that of the 0.38 eV energy band requirement for the 3.3 μm wavelength. This would mean that after the addition of 5% Aluminium ($Al_{0.05}In_{0.95}Sb$), InSb has better performance data then that of other semiconductors for CH_4 detection.

HgTe also has a suitable starting band gap. It can match the InSb band gap in figure 3.2 with enough Cd to take up 25% - 30% of the lattice constant. HgCdTe does have a detectivity that can surpass that of InSb-based structure. The technological disadvantages of this material come from the bulk, surface and interface instabilities as a result of its weak Hg-Te bond[67]. Hg is also highly toxic, which brings a risk that can be avoided with InSb.

3.3) Semiconductor heterostructures

AlInSb based semiconductors have great potential for CO_2 and CH_4 gas detection. However, the homostructures are susceptible to minority carrier generation. This effect is well known in InSb[68], but was solved by introducing a thin higher Al composition region between the p+ and i region to control minority carrier leakage from the p+ contact[68]. This is known as the heterostructure[69,70]demonstrated in figure 3.3:
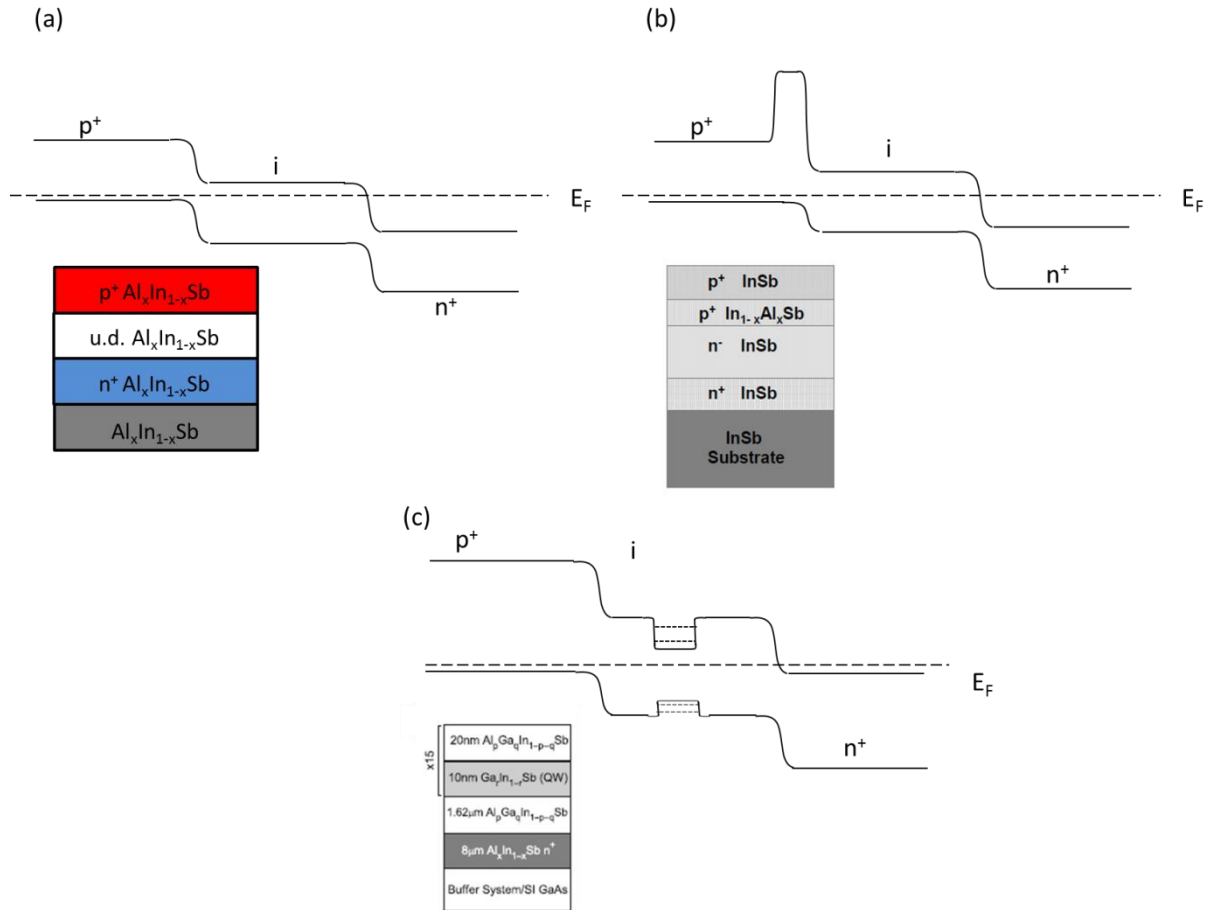
Figure 3.3: Band gap diagrams of difference semiconductor epitaxial structures. (a) An InSb based homostructure[57]. (b) An InSb based heterostructure with different semiconductors of a higher band gap added in[71]. (c) An InSb based heterostructure with different semiconductors of a lower band gap featured[67,72]. The x15 is the quantum well (QW) repetition factor.

As shown in figure 3.3 (a), the homostructure consists of like semiconductor materials and a high intrinsic band gap to hold electron carriers. By adding semiconductors of different materials into the band structure, either a quantum barrier will form if the different material has a larger band gap (see figure 3.3 (b)) or a series of quantum well confinements will be created for electrons to occupy if the different material has a smaller band gap (see figure 3.3 (c)).

The quantum well can reduce lasing threshold in the semiconductor and potentially increase efficiency by widening the wavelength response of the semiconductor.

The advantage of the quantum barrier is that it restricts the flow of carriers from the p-type towards the n-type i.e. minority carrier leakage. This will reduce the diode leakage and increase the diode R_0. Conventionally in a double heterostructure device a larger barrier throughout the entire p-type would be introduced, but the strain will be too high which will cause relaxation. So a quantum barrier of 20 nm thickness taking up roughly a fifth of the p-type thickness will be implemented so that the critical thickness for strain relaxation is not exceeded.

Investigations towards the impact of minority carrier generation and how heterostructure epitaxial layers can improve results are detailed in section 5.4 and 5.5. These adjustments to the epitaxial layers of the photodiode are necessary sine it is expected that the antenna influenced localised focusing is most impactful in the first few nanometres of semiconductor depth. The models demonstrating how this is derived will now be addressed.

3.4) Maxwell's equations and EM simulation

This section will provide analytical insight on how antennas respond to an electric field with a wavelength range between 1.5 μm and 6 μm. Much of the analytical analysis is devoted to finite-difference time-domain (FDTD) and finite-difference frequency-domain (FDFD) modelling using Computer Simulated Technology (CST^{TM}). A comprehensive understanding of the laws of electromagnetics and how they are applied to our proposed antenna design is essential. Its application to the simulation meshing density is addressed as well as the absorption in certain CEM was first introduced by Yee K. S. et al[73] in 1966. Generating meshing grids in a conducting volume that will become active element impedance (AEI) grids when solved has been an evolutionary process which is now done more thoroughly and easily using computers. These AEI grids provide data at certain parts of the system so that design efficiency can be better understood and appropriate modifications can be identified. The efficiency of the antennas is dependent on the complex dielectric constant (ε), the antenna geometry and the antenna response to the type of incoming signal (trajectory angle, polarisation, frequency, etc.). In order for this analysis to be complete and the chosen design fully justified, a variety of shapes and conducting materials will be considered through simulations to identify which ones to recommend for practical experiments. This chapter focuses on the physics and figures of merit that are relevant to an antenna design when being used as a photodetector.
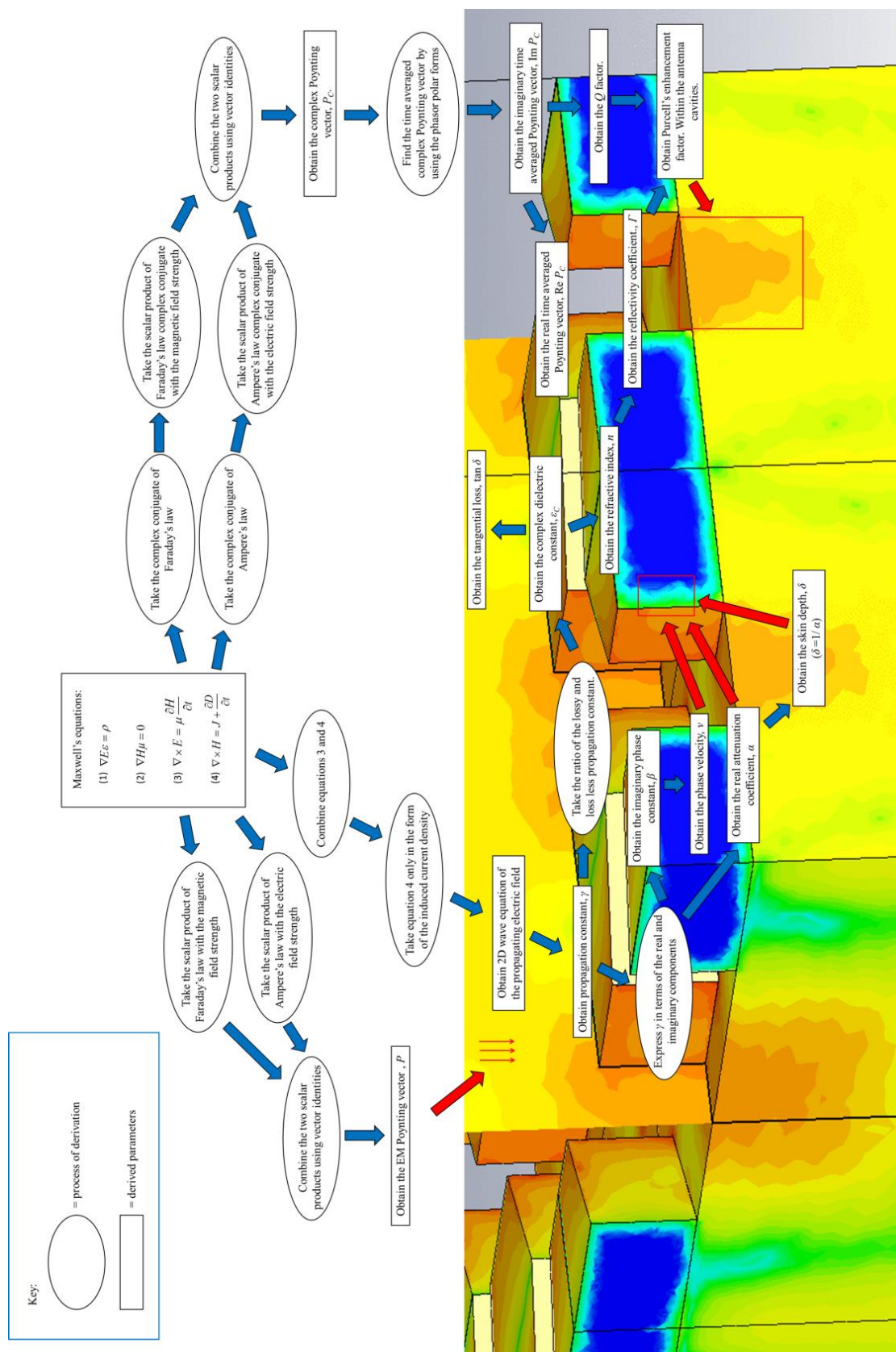
Figure 3.4: A sketch of how Maxwell's curl equations can be used to derive essential parameters and figures of merit in an antenna system applied to a semiconductor photodiode.

Figure 3.4 provides details of how light interacts with an array of hexagonal structures and light coupled in the semiconductor at hot-spot regions. It serves as an example of how the antenna designs discussed in chapter 2 will be compared to one another in simulation. The outcome is dependent on the component volumes and dielectric constants. It is Maxwell's equations that are used to derive the figures of merit in an antenna system; i.e. the antenna losses, the propagation constant, the scattering coefficient, the amount of energy coupled into the semiconductor and ultimately how much more energy is absorbed in the intrinsic layer with and without the antenna array.

Maxwell's equations are as follows:

$$\nabla \cdot D = \nabla \cdot E\varepsilon = \rho \,[\text{Gauss's law}] \qquad (3.4.1)$$

$$\nabla \cdot B = \nabla \cdot H\mu = 0 \,[\text{Gauss's law of magnetism}] \qquad (3.4.2)$$

$$\nabla \times E = \mu \frac{\partial H}{\partial t} \,[\text{Faraday's law of induction}] \qquad (3.4.3)$$

$$\nabla \times H = J + \frac{\partial E\varepsilon}{\partial t} \,[\text{Ampere's circuital law}] \qquad (3.4.4)$$

Where E is the electric field strength, ε is the permittivity or dielectric constant, ρ is the charge density, H is the magnetic field strength, D is the electric flux, B is the magnetic flux, μ is the magnetic permeability and J is the current density. These equations and the derivation described in figure 3.2 are what the simulation software package (CST[TM]) uses to generate an appropriate meshing grid and produce an answer prior to fabrication. The accuracy of the simulations depends on the following simulation settings:

- The meshing density.

- The incorporation of the incident electric field Ergodic effect (necessary if the stimulation is not collimated).

- Human error regarding complex input parameters.

These are typically the factors to reconsider if the results are not as accurate as expected. A higher meshing density will eliminate electromagnetic dispersion error. The incorporation of the Ergodic effect is an analysis when a wide array of input trajectory and polarisation angles are used. These are important to take into account if two incoherent stimulation sources are used. The dielectric constants of the system materials and, by extension, the model accuracy are ultimately determined by the user. The complex dielectric function will change the systematic outcome in accordance to figure 3.7.2. To understand this better, the mathematical derivations will be addressed.

3.5) Simulated computational electromagnetics (CEM) as a derivative of Maxwell's curl equations

Time domain computational methods work by solving the partial differential equations of Maxwell's curl equations via incorporation of both Faraday's and Ampere's law given in equation 3.4.1 and 3.4.2 respectively for each element the system is divided into, i.e. its mesh. This is known as the time domain computational method and it is one of the mathematical systems used to solve problems involving electromagnetic compatibility, wave manipulation, impedance differences and energy attenuation in the different mediums the EM waves are incident on. It has become an essential part of modern radar cross-section calculations, integrated circuit designs, microwave interaction assessments and antenna synthesis, the latter of which is the focus for this thesis.

A fundamental time domain (TD) solution method is given by calculating the change of electric field strength within a given volume for each of the partial differential equations

arranged in a hexahedral array. The x, y and z components are applied to the centre boundaries of each individual mesh. This solving method is often the recommended simulation method for macro systems thanks to relatively simple mesh generation and solving method[74].

$$\varepsilon \frac{\partial E}{\partial t} = -\nabla \times H \Rightarrow \begin{cases} \varepsilon \dfrac{\partial E_x}{\partial t} = \dfrac{\partial H_z}{\partial y} - \dfrac{\partial E_y}{\partial z} - \sigma_E E_x \\[2mm] \varepsilon \dfrac{\partial E_y}{\partial t} = \dfrac{\partial E_x}{\partial z} - \dfrac{\partial E_z}{\partial x} - \sigma_E E_y \\[2mm] \varepsilon \dfrac{\partial E_z}{\partial t} = \dfrac{\partial E_x}{\partial x} - \dfrac{\partial E_y}{\partial y} - \sigma_E E_z \end{cases} \tag{3.5.1}$$

$$\mu \frac{\partial H}{\partial t} = -\nabla \times E - \sigma E \Rightarrow \begin{cases} \mu \dfrac{\partial H_x}{\partial t} = \dfrac{\partial E_y}{\partial z} - \dfrac{\partial E_z}{\partial y} - \sigma_H H_x \\[2mm] \mu \dfrac{\partial H_y}{\partial t} = \dfrac{\partial E_z}{\partial x} - \dfrac{\partial E_x}{\partial z} - \sigma_H H_y \\[2mm] \mu \dfrac{\partial H_z}{\partial t} = \dfrac{\partial E_x}{\partial y} - \dfrac{\partial E_y}{\partial x} - \sigma_H H_z \end{cases} \tag{3.5.2}$$
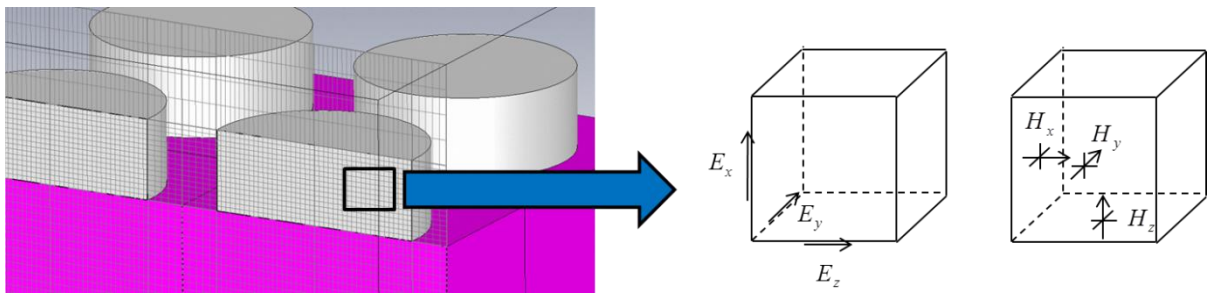
Figure 3.5.1: The visual discretization of how Maxwell's curl equations are converted into a cubic meshing grid for a time domain semi-infinite unit cell.

This however is an unsuitable solving technique for variations in stimulating frequencies due to frequency dispersion inaccuracies in the generated mesh. Additionally, the boundary

conditions can cause difficulties when trying to incorporate a uniform incident wave, making this method unsuitable for a semi-infinite unit cell application.

The antenna analysis must include absorption responses to different incident frequencies within a repeating unit cell, which is why the frequency domain (FD) solver is used. The advantages this solver has over its TD counterpart are as follows:

-   The FD solver operates as a unit cell where the cell is duplicated an unlimited number of times in each direction. The solver can incorporate a uniform incident wave due to this feature. This is known as a Floquet port.

-   The FD solver can resolve dispersion inaccuracies by generating a tetrahedral meshing grid, which has its own spatial discretization which solves equations 3.5.1 and 3.5.2 by utilising unit edge normal vectors, n as well as electric and magnetic field propagation vectors, t for the dual edges k where d and p are edge cell path lengths.

This mesh generation method functions as response to the arithmetic mean of the electric fields in the centre of two mesh cells. In that sense the magnetic component of the mesh will always update in accordance to equation 3.5.3:

$$\frac{\partial H \cdot n_{j,k}^{d}}{\partial t} = \frac{E_z\big|_q - E_z\big|_i}{\Delta_{j,k}^{d}\, \widetilde{\mu}_{j.k}^{d}} \tag{3.5.3}$$

where $\widetilde{\mu}_{j.k}^{d}$ is the average permeability between two cells. The projected magnetic field along a given edge vector is given by:

$$H \cdot t_{i,m}^{p} = H \cdot n_{j,k}^{d}\left(n_{j,k}^{d} \cdot t_{i,m}^{p}\right) + \frac{1}{2}\Big[\left(H_j + H_r\right) - \left(\left(H_j + H_r\right)\cdot n_{j,k}^{d}\right)\Big]\cdot t_{i,m}^{p} \tag{3.5.4}$$
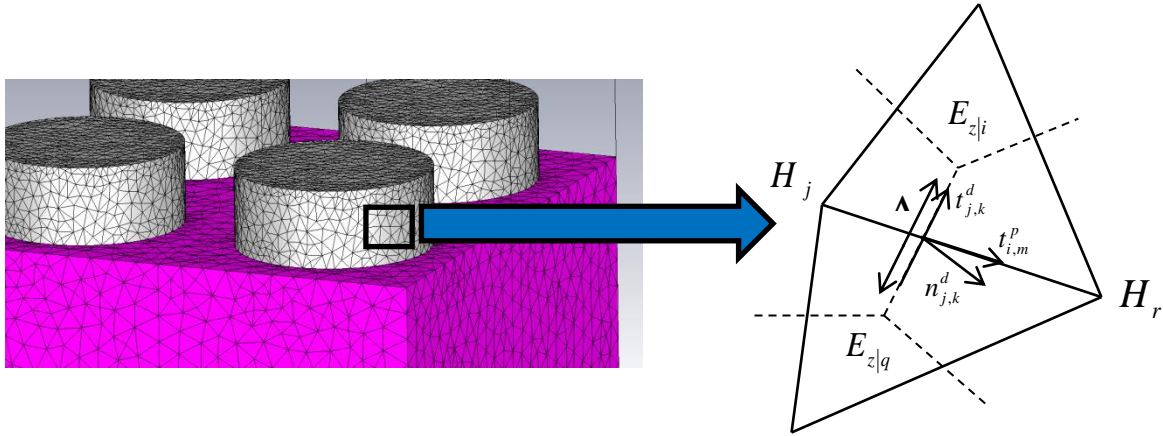
Figure 3.5.2: A visual discretization of how Maxwell's curl equations is converted into a tetrahedral meshing grid for a frequency domain semi-infinite unit cell.

This is the basic principle of how the frequency domain solver is used and how CST will distribute different degrees of power loss in the system as a function of surface impedance and material attenuation, both of which are governed by the material dielectric properties.

3.6) Antenna resonant theory and tuning

In CEM theory and simulation, the complex dielectric constant, ε, provides to how reflective the materials are, their ability to store this incident electromagnetic radiation and how much is lost as a result of their conductivity, σ. The dialectic constant can provide information to derive the resistance, capacitance, inductance and conductance which is essential for deriving an impedance Smith chart and power acceptance data (see figure 3.7.2)[75,76].

$$\varepsilon_c = \varepsilon' + i\varepsilon'' \tag{3.6.1}$$

$$\varepsilon' = n^2 - k_E{}^2 \tag{3.6.2}$$

$$\varepsilon'' = 2nk_E \tag{3.6.3}$$

$$k_E = \frac{\alpha\lambda}{4\pi} \tag{3.6.4}$$

Where ε' is the real part of the dielectric constant, ε'' is the imaginary part of the dielectric

constant, n is the refractive index, k_E is the extinction coefficient, α is the attenuation

coefficient and λ is the wavelength.

The parameters depicted in figure 3.6.1 are derived from Maxwell's equations and coupled

mode theory (CMT) [4,8,9,36,78,79,77].

Input parameters:
w_H = antenna hexagonal width (μm)
 t = antenna thickness (μm)
w_A = antenna aperture width (μm)
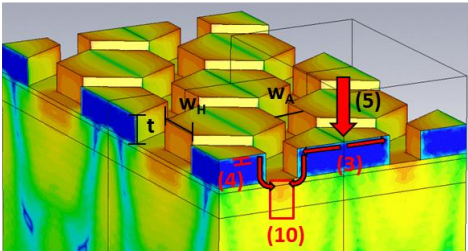
No.	Equation	Description	No.	Equation	Description
1	$\lambda_{res} = \dfrac{\sqrt{3}w_H \cdot 2\pi \cdot \eta'}{m\pi - \phi_R}$	Conditions for antenna resonance	8	$W_0 = \dfrac{(\varepsilon E \cdot E^* - \mu H \cdot H^*)}{4}$	Time-averaged stored energy
2	$\dfrac{\gamma}{k_0} = -\eta' + i\eta''$	Propagation mode index	9	$Q = 2\pi \dfrac{W_0}{P_L T}$	Quality factor
3	$\gamma = (1+i)\sqrt{\dfrac{i\sigma\mu\omega}{\sqrt{2}}} = \alpha + i\beta$	Propagation constant	10	$\dfrac{\Gamma}{\Gamma_0} \propto \dfrac{Q\gamma_M \lambda_{res}^3}{V_{eff}}$	Purcell's enhancement factor
4	$\delta = \dfrac{1}{\alpha} = \dfrac{1}{\sqrt{\pi v \sigma \mu}}$	Skin depth	11	$V_{eff} = \dfrac{\iint \varepsilon|E|^2 dxdy}{\max\left[\varepsilon|E|^2\right]} \cdot w_A$	Effective volume
5	$P_{av} = \dfrac{1}{T}\displaystyle\int_0^T E(t) \times H(t)$	Poynting vector			
6	$\mathrm{Re}\left\{\displaystyle\oint_S P_C \cdot ds\right\} = \int_V \dfrac{\sigma E \cdot E^*}{4}dV$	Real part of the complex conjugate solution for (5)			
7	$\mathrm{Im}\left\{\displaystyle\oint_S P_C \cdot ds\right\} = \omega\int_V \dfrac{(\varepsilon E \cdot E^* - \mu H \cdot H^*)}{4}dV$	Imaginary part of the complex conjugate solution for (5)			

Figure 3.6.1: The different aspects of antenna resonance and how the resonance conditions, antenna loss and coupling into the semiconductor underneath depend on them.

Each equation relates to the parameters that are relevant to how much light gets reflected off

the surface, how much energy gets absorbed in the antenna and how much gets coupled into

the antenna apertures.

Equation 1 describes the resonance conditions with reference to the Fabry-Perot resonance model. Where λ_{res} is the resonance wavelength, w_H is the antenna hexagonal width, w_A is the aperture width, t is the antenna thickness, η' is the real part of the standing wave propagation mode[77].

Equation 2 and 3 in figure 3.6.1 is the propagation mode index and the propagation mode (γ) respectively. It is derived from solving Helmholtz function for a 2D metal stripe when applying it to Maxwell's third equation to account for induction and Maxwell's fourth equation to account for the flow of current[36]. The propagation constant provides information of the metal attenuation coefficient, (α) the phase constant (β) and the skin depth (δ).

Equation 5 in figure 3.6.1 describes the time averaged power flux density of the EM wave or Poynting vector. It is this vector that is applied to Maxwell's third equation to calculate the power flux density of the EM wave after induction into the metallic surface area and through integration, the antenna surface volume.

Equation 6 in figure 3.6.1 is the real part of the complex conjugate solution. It is simply the power flowing through the surface of the conducting material that encompasses the volume. Equation 7 in figure 3.6.1 is the imaginary part of the complex conjugate solution. It is the reactive power density, which describes the power density that flows along the surface of the substrate. From this, an expression for the amount of energy contained in the conducting volume as the antenna responds to an incident energy flux density can be found. This term is given as W_0, which is given in equation 8[36].

Equation 9 in figure 3.6.1 is the quality factor, Q. Q is defined as the ratio of the time-averaged stored energy in the conducting material to the power loss P_L, in one periodic cycle,

T. Accounting for how much power is containing and how much is lost during energy transfer to the antenna terminals is what is need to be applied to Purcell's enhancement factor given in equation 9[78],[79].

Figure 3.6.1 provides a summary of factors an engineer would have control over and how they would change the result of the surface reflectivity and absorption in various materials.

Purcell's enhancement factor is one example of this. It is important to clarify the optimum cavity size, w_A for a given resonance wavelength, λ_{res}. Finding the optimum aperture size is an iterative procedure as it is very dependent on the directionality on the recently derived Q factor and V_{eff}, which in turn is dependent on the antenna cavity size. This is illustrated in Figure 3.6.2.
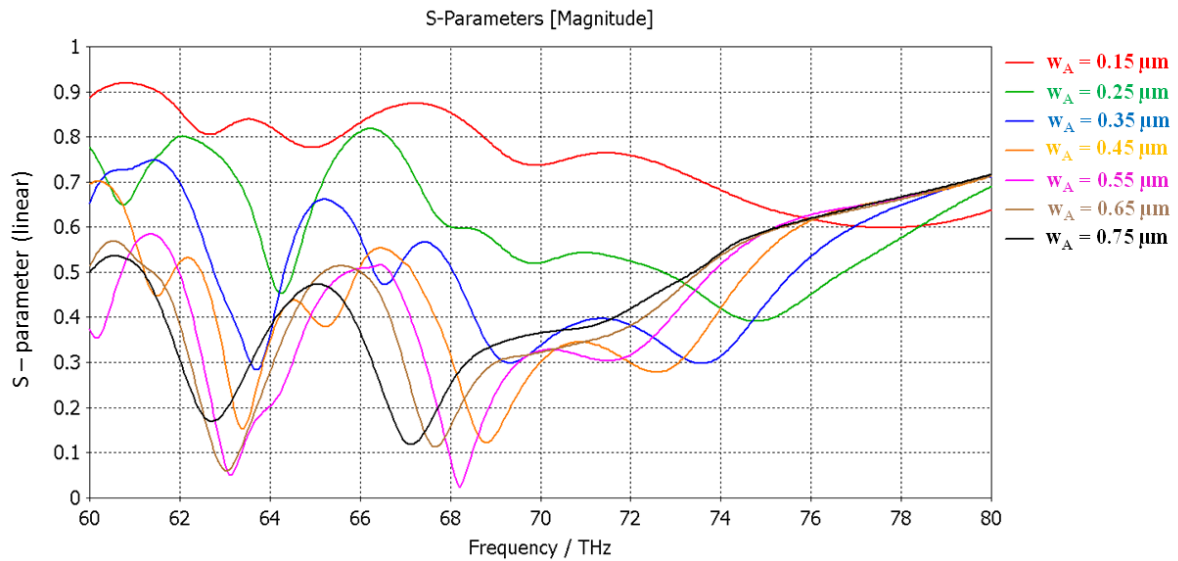
Figure 3.6.2: CEM generated S-parameter measurements vs. the input frequency for a varying aperture width, w_A within a hexagonal micro-antenna array 1.5 µm in length 0.92 µm in thickness.

The scattering parameter or S-parameter used in Figure 3.6.2 is a measurement of the proportion of incoming electromagnetic energy which is reflected as a function of the aforementioned Purcell factor. The optimum aperture varies with the materials dielectric

constant and the absorption in the antenna which has a direct relation to the antenna path length. A low reflectivity is dependent on the aperture with being small but not so small the eigenvalues do not have any space to couple into the semiconductor, whereas if the antenna were too far apart the effect of the antenna would deteriorate.

An important part when tuning the antenna is to determine how each parameter the user controls is impacting on the resonance wavelength and the absorption in the i-type layer. Figure 3.6.3 provides a rule of thumb of the change in wavelength and absorption as one parameter changes relative to the other of the same amount.
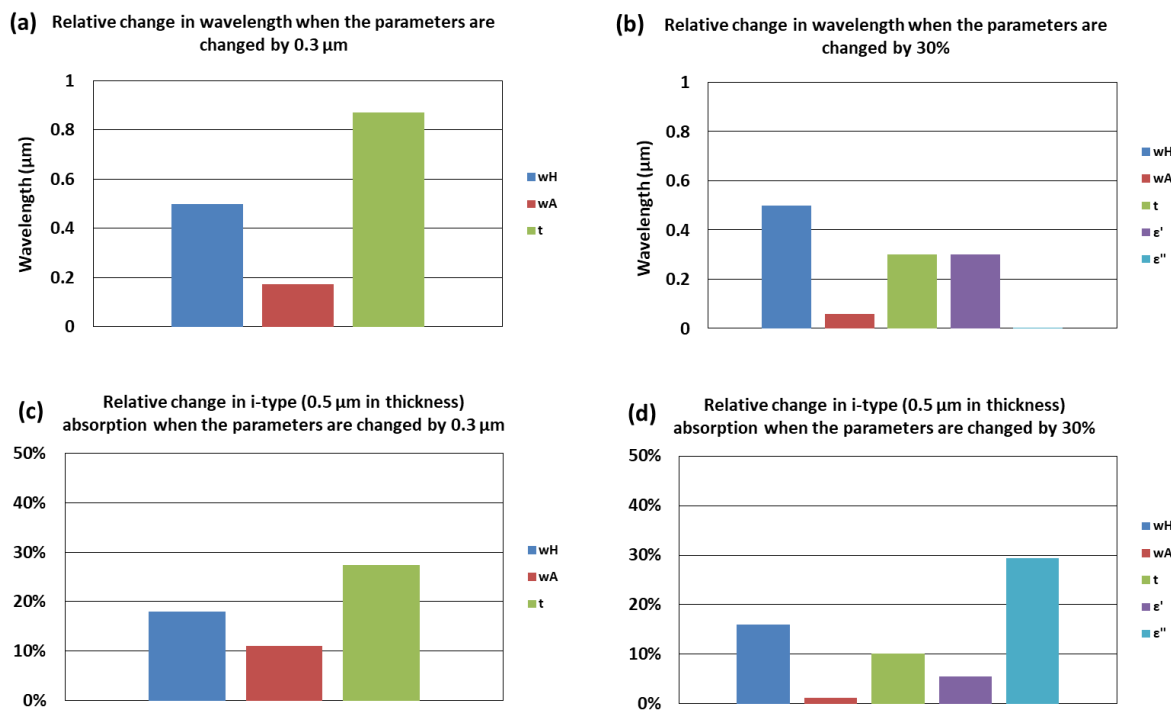
Figure 3.6.3: The relative change in wavelength and i-type absorption vs. the hexagonal width, w_H (blue), the aperture width, w_A (red) and antenna thickness, t (green) when each parameter is shifted from the optimum settings by 0.3 μm in graphs (a) and (c) and when each parameter is changed by 30% from the optimum in graphs (b) and (d). The optimum parameters are $w_H = 1.20$ μm, $w_A = 0.70$ μm, t = 0.60 μm. This data was obtained though CEM modelling.

From this data it can be concluded that all three physical parameters in the hexagonal structure have a noticeable impact. All of them will be tuned to as close to optimum as possible but if there are any compromises in the parameter specifications these charts can give an idea of the impact it will have of the peak wavelength and the signal enhancement. Note: the alterations detailed in figure 3.6.3 are only intended to be used as a rule of thumb for minor alterations from the optimum antenna parameters.

3.7) Antenna impedance

In the field of electromagnetic engineering, the antenna interaction with an incoming wavelength is conventionally summarised in a Smith chart[80], where information on the degree to which the incident electromagnetic waves are being accepted into the conducting shape is given in accordance to the complex impedance.

In order to determine the complex impedance, the antenna equivalent circuit needs to be considered. The antennas will allow the incorporation transmitted of wavelengths within a certain bandwidth. This is the circuitry equivalent of an LCR (Inductance, capacitance, resistance) circuit as shown in Figure 3.7.1. The conductance, G is also included in to derivation.
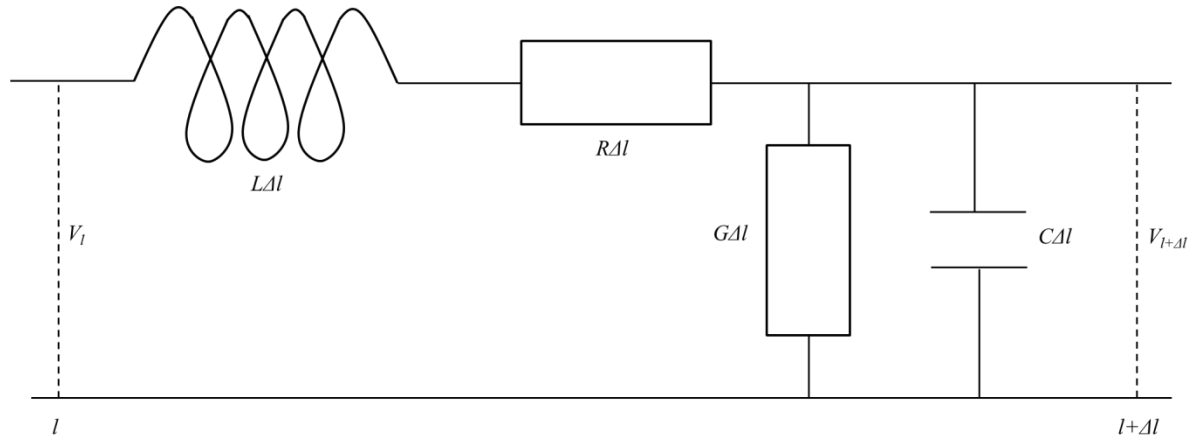
Figure 3.7.1: The circuitry equivalent of an antenna array when Δl represents one of many segments that make up the array.

The circuitry impedance for a segment of the antenna array is given in terms of the resistance and inductance, the latter of which is frequency dependent:

$$Z = R\Delta l + i\omega L\Delta l \; [\Omega] \tag{3.7.1}$$

The admittance into the circuit is given in terms of the conductance and the capacitance. As with the inductance, the capacitance is frequency dependent.

$$Y = G\Delta l + i\omega C\Delta l \left[\frac{1}{\Omega}\right] \tag{3.7.2}$$

At this point the equivalent potential across one segment can be deduced as:

$$V(l + \Delta l) - V(l) = -I(l)\left[R\Delta l + i\omega L\Delta l\right] \tag{3.7.3}$$

$$\frac{V(l + \Delta l) - V(l)}{\Delta l} = -I(l)\left[R + i\omega L\right] \tag{3.7.4}$$

If Δl is assumed to tend to zero, the left hand side of equation is equivalent to the voltage derivative. This assumption is justifiable if Δl is so arbitrarily small that the Taylor expansion becomes $V(l+\Delta l) \approx V(l)$.

$$\frac{dV(l)}{dl} = -I(l)[R + i\omega L]$$
(3.7.5)

Similarly the current derivative can be written as:

$$I(l+\Delta l) - I(l) = -V(l)[G\Delta l + i\omega C\Delta l]$$
(3.7.6)

$$\frac{I(l+\Delta l) - I(l)}{\Delta l} = -V(l)[G + i\omega C]$$
(3.7.7)

$$\frac{dI}{dl} = -V(l)[G + i\omega C]$$
(3.7.8)

From here the wave propagation constant, γ can be determined in terms of the antenna equivalent LCR circuit. To do that, the second order derivative must be calculated.

$$\frac{dV^2(l)}{dl^2} = \frac{I(l)}{dl}[R + i\omega L] = V(l)[G + i\omega C][R + i\omega L]$$
(3.7.9)

$$\frac{dV^2(l)}{dl^2} - [G + i\omega C][R + i\omega L]V(l) = 0 \Rightarrow \gamma^2 = [G + i\omega C][R + i\omega L]$$
(3.7.10)

$$\gamma = \sqrt{[G + i\omega C][R + i\omega L]}$$
(3.7.11)

The characteristic impedance (i.e. independent of a load source) is defined as the ratio of the forward propagation voltage divided by the forward propagating current. Now that the propagating constant has been determined in a way that incorporates the antenna LCR circuit properties, the impedance can be expressed thus:

$$Z_0 = \frac{\vec{V}e^{-\gamma l} + \tilde{V}e^{\gamma l}}{\vec{I}e^{-\gamma l} + \tilde{I}e^{\gamma l}} \quad [\Omega]$$

(3.7.12)

When only forward propagation is assumed and when inclusion of the propagation constant into equation 3.7.5, it becomes:

$$\frac{d(\vec{V}e^{-\gamma l})}{dl} = -\vec{I}e^{-\gamma l}[R + i\omega L]$$

(3.7.13)

After taking the derivative:

$$-\gamma \vec{V}e^{-\gamma l} = -\vec{I}e^{-\gamma l}[R + i\omega L]$$

(3.7.14)

Similarly:

$$-\gamma \vec{I}e^{-\gamma l} = -\vec{V}e^{-\gamma l}[R + i\omega L]$$

(3.7.15)

Substituting equation (3.7.14) and equation (3.7.15) into equation (3.7.12) provides an expression for the impedance in terms of the propagation constant:

$$Z_0 = \frac{1}{\gamma}[R + i\omega L] = \gamma \frac{1}{[G + i\omega C]} \quad [\Omega]$$

(3.7.16)

$$Z_0 = \sqrt{\frac{R + i\omega L}{G + i\omega C}} \quad [\Omega]$$

(3.7.17)

The impedance will change under the influence of an external load. The load impedance is calculated in much the same way as the characteristic impedance:

$$Z_L = \frac{V_L}{I_L} = \frac{\vec{V}_L + \tilde{V}_L}{\vec{I}_L + \tilde{I}_L} = \frac{\vec{V}_L + \tilde{V}_L}{\dfrac{\vec{V}_L}{Z_0} - \dfrac{\tilde{V}_L}{Z_0}} = Z_0 \frac{\vec{V}_L + \tilde{V}_L}{\vec{V}_L - \tilde{V}_L} \quad [\Omega]$$

(3.7.18)

Equation (3.7.18) can be taken in terms of forward propagation only, but this would mean that the load impedance is equal to the characteristic impedance. When this occurs, there are no internal reflections in the system, which ultimately is what is being investigated. When there is an impedance mismatch the reflected propagating voltage comes in the form of a fraction of the forward propagation wave. This fraction is determined by the aforementioned impedance mismatches:

$$\tilde{V} = \vec{V} \frac{Z_L - Z_0}{Z_L + Z_0} \tag{3.7.19}$$

From this, an internal reflection coefficient, Γ can be derived:

$$\Gamma = \frac{\vec{V}}{\tilde{V}} = \frac{Z_L - Z_0}{Z_L + Z_0} \tag{3.7.20}$$

The load impedance is a complex number which describes the material resistance, R_L and reactance, X_L to an incoming load (or source):

$$Z_L = R_L + iX_L \tag{3.7.21}$$

The reflectivity is then written as:

$$\Gamma = \frac{R_L + iX_L - Z_0}{R_L + iX_L + Z_0} = \Gamma_r + \Gamma_i \tag{3.7.22}$$

$$\Gamma_r + \Gamma_i = \frac{\dfrac{R_L}{Z_0} + i\dfrac{X_L}{Z_0} - 1}{\dfrac{R_L}{Z_0} + i\dfrac{X_L}{Z_0} + 1} = \frac{r + ix - 1}{r + ix + 1} \tag{3.7.23}$$

Where r is the normalised resistance and x is the normalised reactance. At this point the reflectivity information can be applied to a Smith chart.

Where r is the normalised resistance and x is the normalised reactance. At this point the reflectivity information can be applied to a Smith chart.
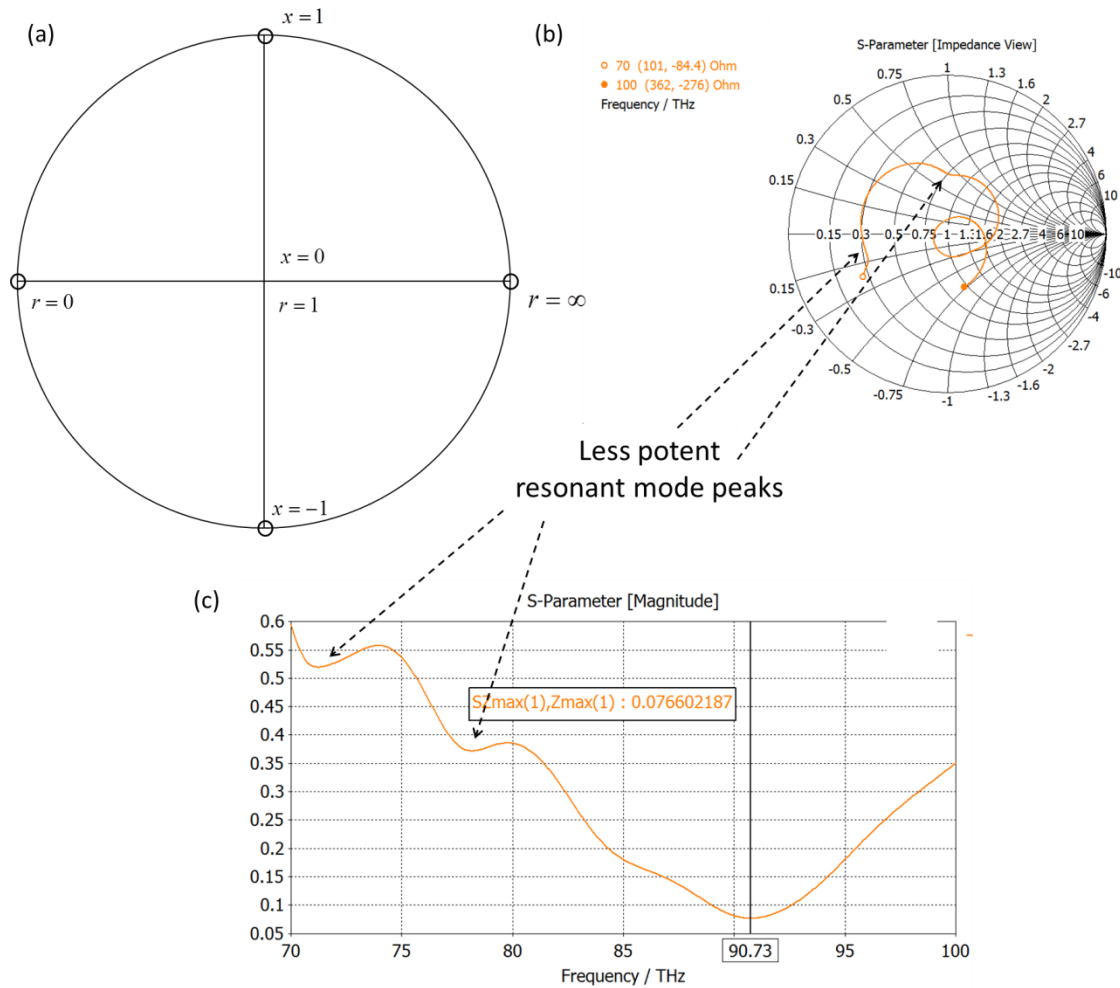
Figure 3.7.2: Impedance diagrams (a) An impedance Smith chart with perfect impedance matches indicated in the centre. (b) An example Scattering (S) Parameter resonance curve applied to an impedance Smith chart. (c) The equivalent S parameter plot.

The impedance information displayed in figure 3.7.2 can be reinterpreted as the amount of power accepted in the system. The maximum amount of power the system can accept is based on the normalised 0.5 W power incident on each unit cell. This is show in figure 3.7.3:
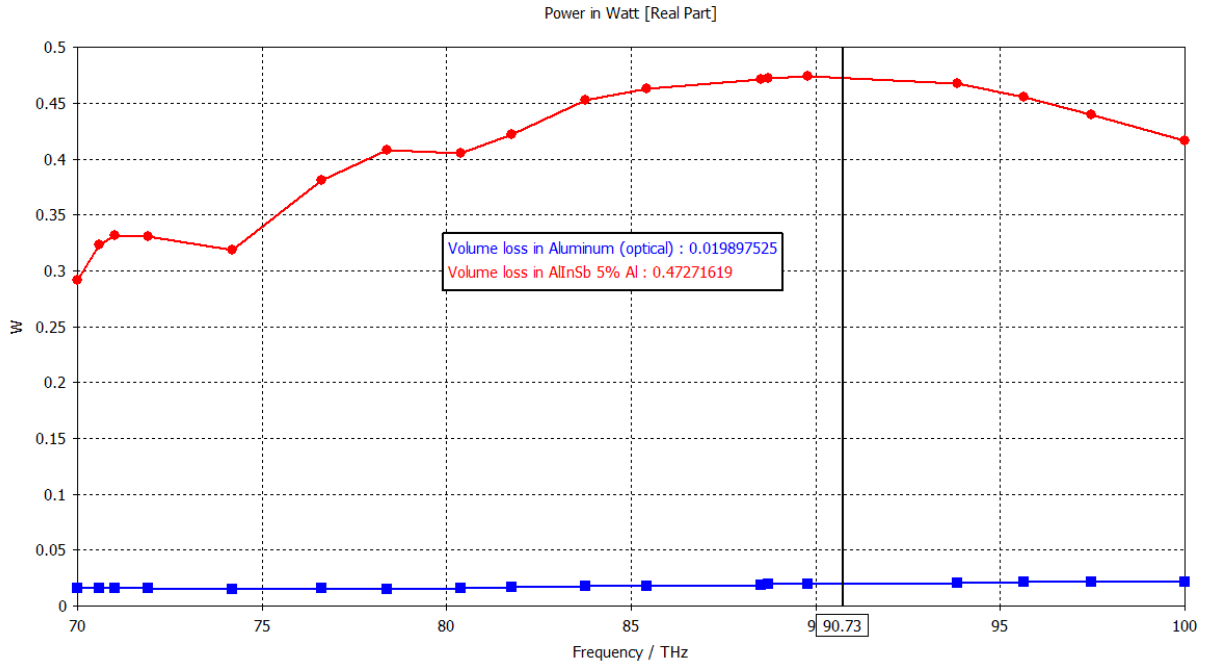
Figure 3.7.3: The power accepted as a fraction of a normalised 0.5 W incident on a semiconductor with hexagonal antenna array on the surface. The red line is the amount of absorbed in the semiconductor and blue line is the amount of power absorbed in the Aluminium antenna.

Any amount of power that is absent is considered a loss factor that is the result of a sub optimal Q factor. As a condition for achieving the largest degree of Q factor, the array must resonate at the target wavelength which, in turn, produces standing waves within the conducting material. When considering the parameters that can be controlled (i.e. w_H, w_A and t) this is an achievable pursuit. However, when considering the sensitivity that these parameters have on the peak wavelength and the semiconductor absorption, it is necessary the used CEM simulation software to predict the response.

3.8) LED theory

The same impedance matching problem detailed in section 3.6 and 3.7 applies to semiconductor LED far field enhancement measurements. From this the far field results can be derived. This section will briefly detail how the electromagnetic projection and the figures of merit that correspond to an enhanced signal-to-noise ratio at the photodetector.

The far field results can describe the wave trajectory when radiated away from the device. The bulk magnitude of the emitted field is given in equation (3.8.1)[81].

$$P_{rad} = I_0^2 \frac{n\pi}{3} \left(\frac{w_A}{\lambda} \right)^2 \tag{3.8.1}$$

Where I_0 is the current within the 2D dipole scenario for a given polarisation angle, w_A is the aperture width, n is the conducting material refractive index and λ is the wavelength. When considering the device occupying a sphere of an arbitrary radius, R (see figure 3.8.1 (b)), the bulk magnitude describes the total power that is radiating out of it.
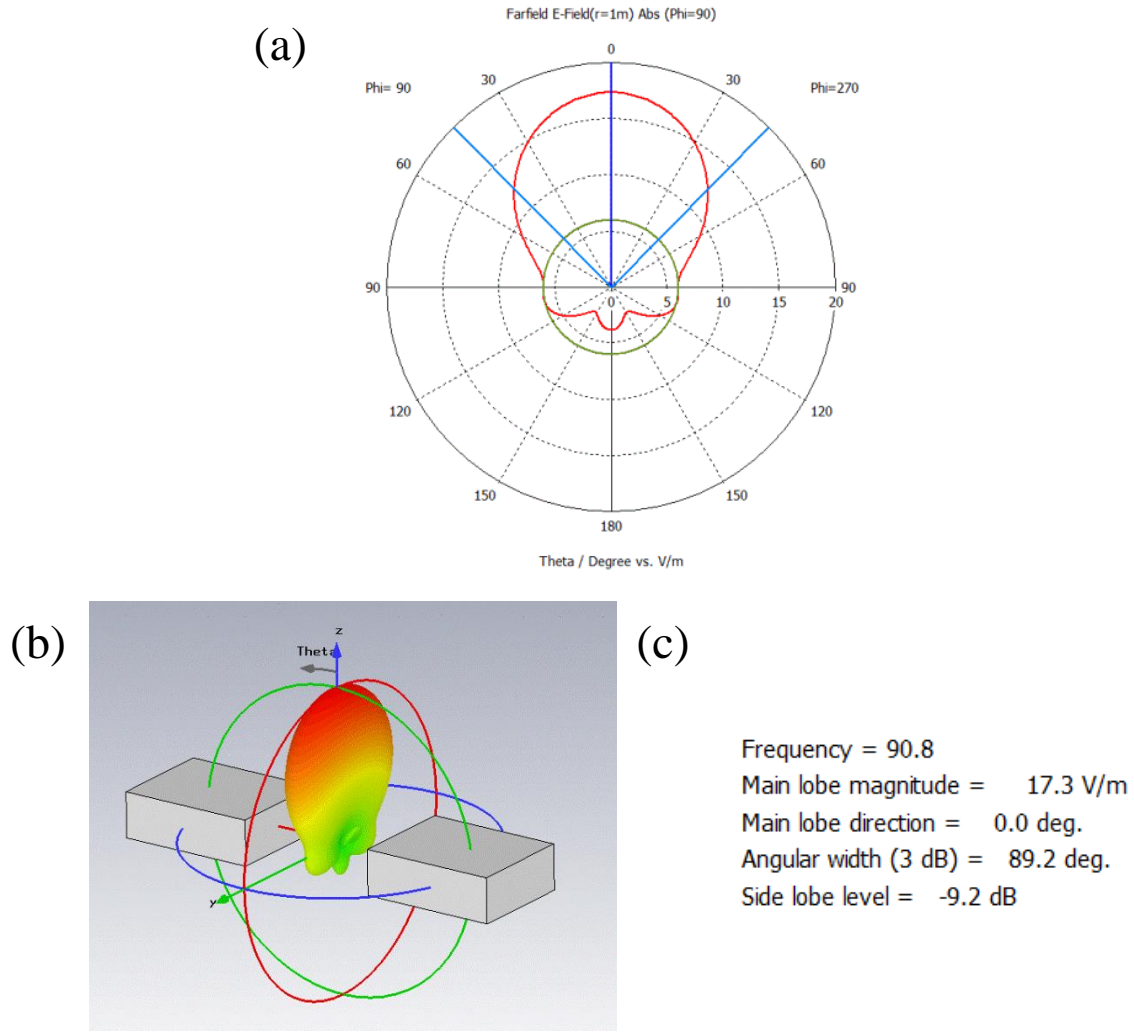
Figure 3.8.1: LED far field examples. (a) The far field antenna radiation pattern at 90.8 THz for a two aluminium strip application. (b) The 3D radiation pattern. (c) The details of the electric field main lobe magnitude and the direction of re emission.

The far field emission of the source is described by the radiated power directivity, *D*.

$$D(\theta,\phi) = \frac{4\pi \cdot U(\theta,\phi)}{P_{rad}}$$

(3.8.2)

In order to consider the radiated intensity, P_{rad} at the edge of the sphere radius, R, the time averaged power density needs to be integrated over the solid angle, κ, depicted in figure 3.8.2.
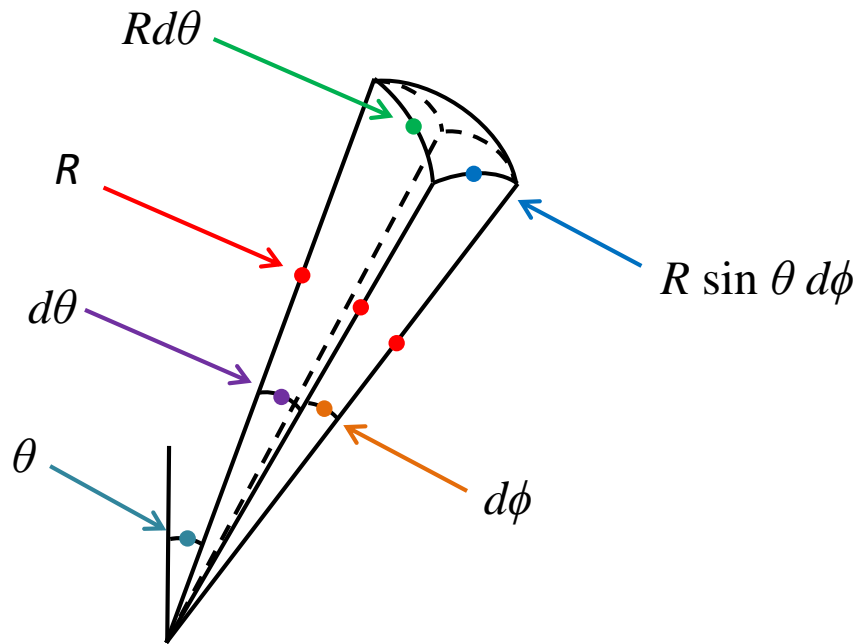
Figure 3.8.2: A diagram showing the solid angle derivation at a distance R away from the source. This is representative of the change in intensity as θ is varied between 0 and π degrees while ϕ is varied between 0 and 2π over the surface area for the given solid angle, κ at a distance, R away from the source. The element of surface area, dS area is thereby derived as:

$$dS = R^2 \sin\theta d\theta d\phi \qquad\qquad (3.8.3)$$

The total radiative power is calculated as the average power integral over a given surface area defined in equation 3.8.3:

$$P_{rad} = \int_S P_{avg} dS = \int P_{avg} R^2 \sin\theta d\theta d\phi = \int_S P_{avg} R^2 d\kappa \tag{3.8.4}$$

Where $P_{avg} R^2$ is the radiative intensity, $U(\theta,\phi)$ and $\beta = 2\pi/\lambda$.

$$P_{rad} = \int_{\phi=0}^{\phi=2\pi} \int_{\theta=0}^{\theta=\pi} \vec{R} \frac{\eta I_0^2 \Delta w_A^2 \beta^2}{32\pi^2 R^2} e^{-i\beta R} \sin^2\theta d\theta d\phi \tag{3.8.5}$$

$$P_{rad} = \frac{\eta I_0^2 \Delta w_A^2 \beta^2}{32\pi^2} \frac{8\pi}{3} = \frac{I_0^2 \eta\pi \Delta w_A^2 \pi}{3\lambda^2} = I_0^2 \frac{\eta\pi}{3} \left(\frac{w_A}{\lambda}\right)^2 \tag{3.8.6}$$

Where P_{rad} is the radiated power for the propagating wave.

The gain, G is the first figure of merit in the emission antenna theoretical assessment, where P_{in} is the input power.

$$G(\theta,\phi) = \frac{4\pi \cdot U(\theta,\phi)}{P_{in}} \tag{3.8.7}$$

A parameter to consider by extension is the antenna's radiative efficiency, which describes the ratio of the output power to the input power:

$$eff = \frac{P_{rad}}{P_{in}} = \frac{P_{rad}}{P_{rad} + P_d} \tag{3.8.8}$$

Where P_d is the amount of power lost in the antennas or reflected off the antenna surface. With this data, the efficiency of the antenna material can be taken into account. This is useful

information when assessing the how much radiation the antenna array is going to block as a result of impedance mismatches.

The second figure of merit is the beamwidth. This is an important figure of merit regarding the directivity. In a gas sensing system the detector cannot be assumed to be a point target, it will instead be roughly the same size as the source and therefore, despite the gain's dependency on the angular width, the beamwidth does not have to be small if the antenna array is going to work. It is nevertheless important when considering the trajectory angle and therefore the amount of surface reflectivity. This effect can be negated however, if an antenna design that is responsive to wide trajectory angle is used.

The third figure of merit is bandwidth. Emission antenna arrays should block out light of all frequencies, except those frequencies that match the resonance harmonics.

The far field plots are featured in this thesis as a means to describe the antenna directional qualities as opposed to the near field results. There are two reasons for this: The first is because in the near field results the signal has not stabilised and the readings taken from the simulation are characteristically random and noisy. The second reason is because the target wavelength (3.3 µm) is very small, and when the far field pre-requisite distance is several wavelengths away before the signal stabilises, the detector will be receiving the far field wherever it is placed (from a macroscopic perspective). The quality of the antenna main lobe magnitude is the antenna realised gain. It is given as the power per unit surface area divided by a perfectly isotropic radiation pattern. The units can very between decibels (dB); decibels in relation to an isotropic field pattern (dBi); decibel volts per meter (dBVm^{-1}); or just a linear

gain, which has no units at all. An example is the far field pattern linear form and is often used to emphasise the main lobe magnitude and suppress the side lobes as displayed in figure 3.8.3.

The alternative non-linear polar plot is given in decibels, which is a logarithmic unit. A main lobe magnitude of 10 dB would mean the propagated power in a single direction is 10 times what it would be at 0 dB. Whereas 3 dB is approximately double. Any decibels with a negative number is a fraction of 1 where -3dB is half.
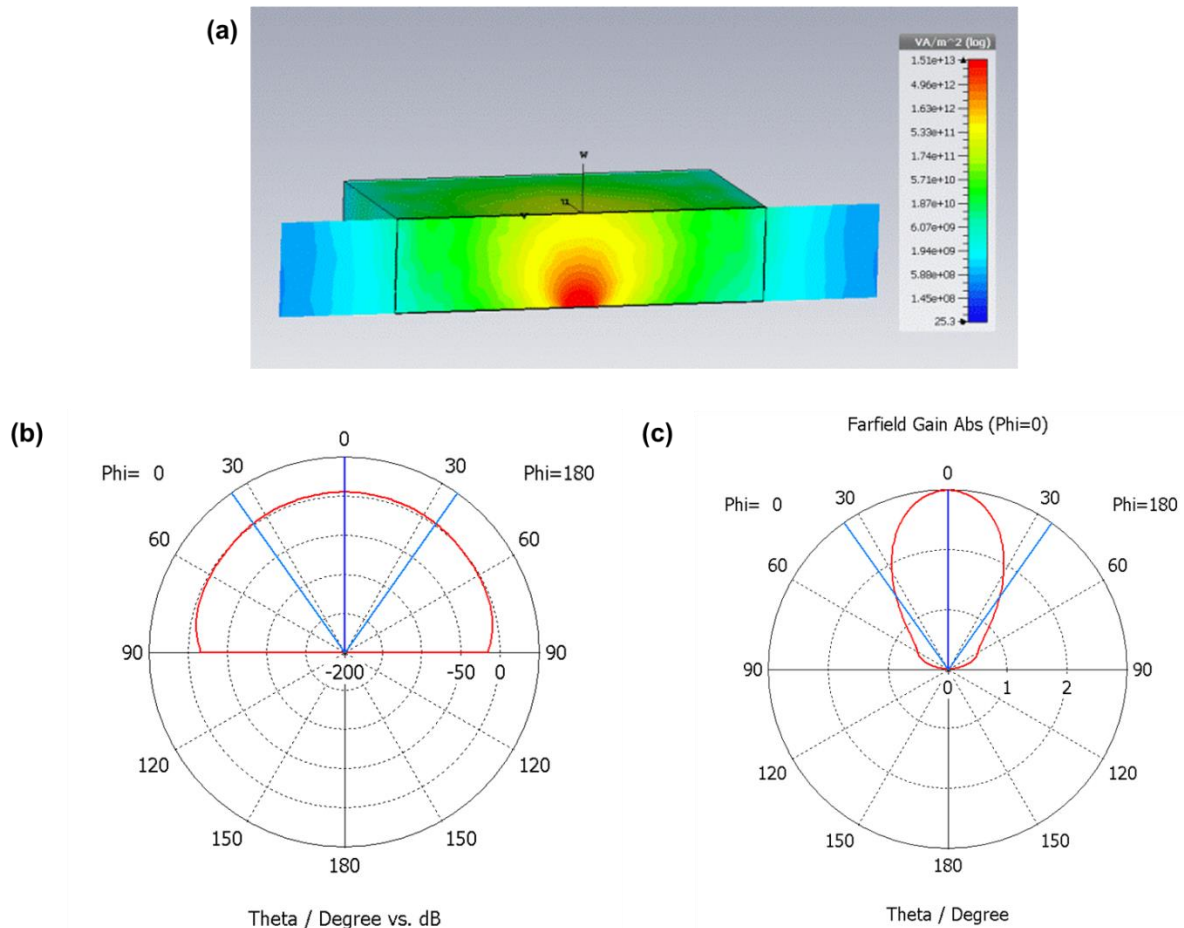
Figure 3.8.3: An illustration depicting the difference between linear and non-linear polar diagrams. The material is i-type $Al_{0.05}In_{0.95}Sb$ with a length and width of 2 µm and a thickness of 0.5 µm. (a) The propagation from a square waveguide port at the bottom of the substrate with a normal mode of oscillation. (b) The far field polar diagram shown in decibels. (c) The linear far field polar diagram.

When applied to CEMs, the input port cannot be the same as the uniform incident wave used in the photodetector setup shown in figure 3.4. Internal emission is isotropic and after taking into account total internal emission on the surface the emission is Lambertian (i.e. the linear far field emission is circular. There are software limitations that make producing a Lambertain emission difficult to in CST^{TM}. The emission can be tailored with port modes but the closest replica that has been produced is a semi-circle. This means that beamwidth analysis is not entirely representative of practical conditions. However, there is still a benefit in emission filtering on LEDs that will be explored further in chapter 7.

3.9) Antenna designs and conductive materials

As discussed in chapter 2, there have been numerous papers emphasising the importance of specifically tailoring dimensions in order to achieve resonance at specific frequencies. The modelling objective is to design a micro-antenna array with frequency enhancements strictly within a frequency bandwidth the semiconductor is responsive to for eventual comparison to practical results.

Theoretically, the antenna array itself can be made of any material as long as it conducts. Several conducting materials were considered for modelling bearing in mind the consequences of different degrees of volume loss in the antenna and the change in response frequency, both as a function of the material's dielectric constant and the antenna volume relative to polarisation plane.

Gold, silver, aluminium and copper are considered as antenna materials for theoretical simulations for the photodiode and LED responses[82,83]. Gold is a popular choice because of its higher conductivity and minimal energy losses when forming standing waves. At the

frequencies of interest, the ratio of losses between gold and aluminium is given in TABLE 3.9. It also lists the price of materials for large scale fabrication. In pursuit of obtaining the optimum S/N ratio it would be the best material to use. However, gold is unable to rest on a surface without an adhesive layer of titanium or chromium. The thickness of the adhesive layer can realistically be as thin as 10nm compared to a 750nm - 1000nm thick gold structure resting on top of it. This makes the advantage of using gold very marginal for a more expensive production material. So much so that silver, aluminium and copper all surpass it. Silver and aluminium both oxidise but no considerable detrimental effects are evident in these studies. Similar to gold, silver also requires a thin adhesion layer, making less conductive materials more competitive as long as they are reasonably conductive themselves. Titanium was considered as an intentionally lossy material to prove the relevance of having good conducting materials for antenna arrays.

TABLE 3.9: The real and imaginary dielectric constants of aluminium, gold, chromium and silver copper and titanium at 90.8 THz (3.3 μm) and the simulated percentage of incident power absorbed within the antenna for hexagonal design where $w_{H(base)} = 1.28$ μm, $w_{A(base)} = 0.56$ μm and $\theta = 73°$ [84].

| Element | Antenna thickness (μm) | At the 90.8 THz target | | | |
		-Re(ε)	Im(ε)	Antenna absorption (%)	Cost (£/kg)
Al	0.65	1010	315	5.82	1.52
Au (+ Cr)	0.60 (+ 0.01)	437 (94.2)	74.9 (66.7)	5.40 (+ 2.41)	3,122.00 (1.82)
Ag (+ Cr)	0.61	461 (94.2)	64.3 (66.7)	4.62 (+ 2.41)	416.14 (1.82)
Cu	0.64	469.42	73.063	5.20	4.27
Ti	0.55	20.6	57.311	48.5	2.77

The information shown in Table 3.9 are obtained from CEM simulations discussed earlier in the chapter and provides meaningful data on how a conducting material will perform at a peak wavelength of 3.3μm based on the real and imaginary dielectric constants. θ is the experimentally observed side wall gradient of the antenna design (see section 5.4). $w_{H(base)}$ and $w_{A(base)}$ are the base hexagonal width and base aperture width after affected by the side wall gradient. As described in sections 2.7, the dielectric constant will govern how the system will react to an incoming plane wave and the current induced into the system.

CST^{TM} has been used to perform the Finite Difference Time Domain (FDFD) modelling in which Maxwell's time-dependent curl equations are solved over a periodic 3D grid. Several original simulations were conducted to see if the software could mimic resonances and produce local field enhancements while demonstrating the relationship between antenna dimensions and the frequency it is most responsive to. This data has experimental data of the dielectric properties of $Al_{0.05}In_{0.95}Sb$ include for enhanced accuracy (see section 5.2).

There are a number of literature inspired antenna designs for devices on the micro-metre scale. Producing the best possible design is a matter of identifying which array will maintain the greatest Q factor. The design must be as geometrically efficient as possible whilst also being suitable for an incoherent light application, i.e. light with inconsistent incident polarisation angles, trajectory angles and phases. To best take this into account there are several potential designs that have been recorded to be successful at the MIR to optical wavelengths and all arrays were tested. These arrays are summarised in figure 2.0 (replicated here as figure 3.9.1 for the convenience of the reader). The conducting length, thickness and

aperture widths are optimised as fully as possible to make a fair assessment between the different designs.
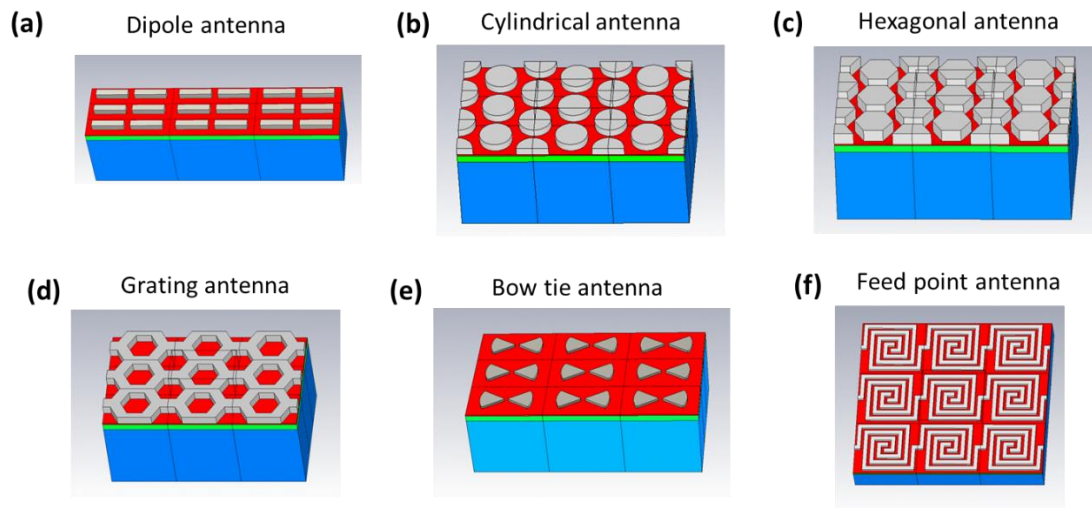
Figure 3.9.1: 3D CAD based diagrams of different antenna designs. (a) Dipole antenna array (b) Cylindrical antenna array (c) Hexagonal antenna array (d) Grating antenna array (e) Bow-tie antenna array (f) Feed point antenna array (spiral).

All simulations in this section are designed with thin semiconductor epitaxial layers where the p-type thickness = 0.1μm, the i-type thickness = 0.5 μm and the n-type thickness = 5 μm. The power absorbed in the i-type region is the figure of merit to determine the benefits of using these antenna designs. It is given as a fraction of the incident radiation which is 0.5W of normalised incident radiation. Each antenna design has had their parameters (thickness, aperture width and conducting length) optimised for maximum i-type absorption at 90.8 THz (3.3 μm).

The dipole antenna (shown in figure 3.9.2) is the most efficient design when dealing with a coherent light source or light that has been polarised prior to its interaction on the substrate. However, using a coherent light source (such as a QCL) is expensive and impractical for its

use in gas detection. Additionally when incoherent light is used, there are expected to be significant losses since the dipole antenna can only accept a small range of polarisation angles and still work efficiently.

Dipole antenna. L = 2.4 µm, w = 0.5 µm, w_A = 0.5 µm, t = 0.5

(a)

(b)

Dipole antenna polarisation sweep; 0,10,20,….,90

P-polarised

S-polarised
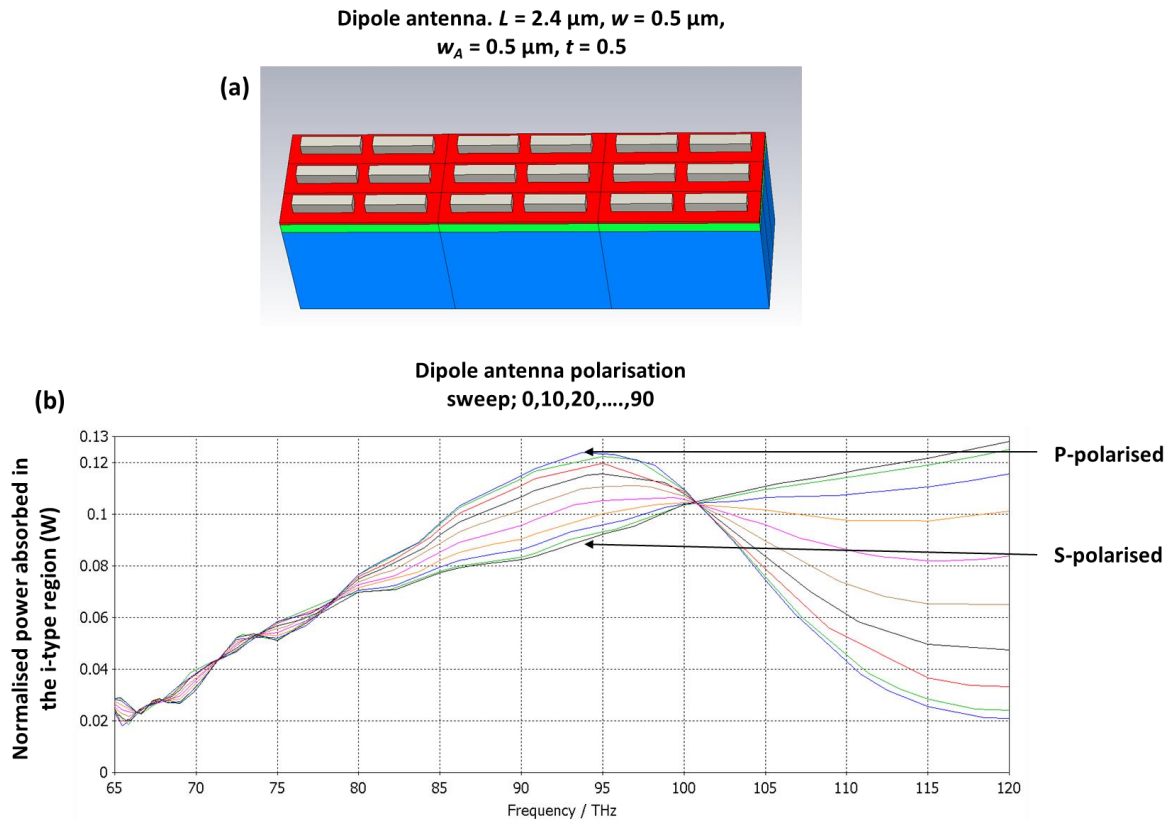
Figure 3.9.2: Dipole antenna simulation for a normalised 0.5 W of incident power. (a) CAD based diagram of a dipole antenna array simulated in a Floquet port where L is the antenna length and w is the antenna width, w_A is the aperture width and t is the antenna thickness. (b) The normalised power absorbed in the i-type region at different polarisation angles. The bandwidth is 1.06 µm when the incident radiation is p-polarised.

Feed point and bow tie antenna are designed to redirected energy towards a target area. They have larger bandwidth responses and can maintain good coupling at different polarisation angles. These designs lack precision and have a bandwidth that is dependent on the polarisation angle. They are applicable to bolometers or photovoltaic cells. The bow tie

antennas have difference peak frequencies as a result of different apparent conducting length with different incident polarisation angles.
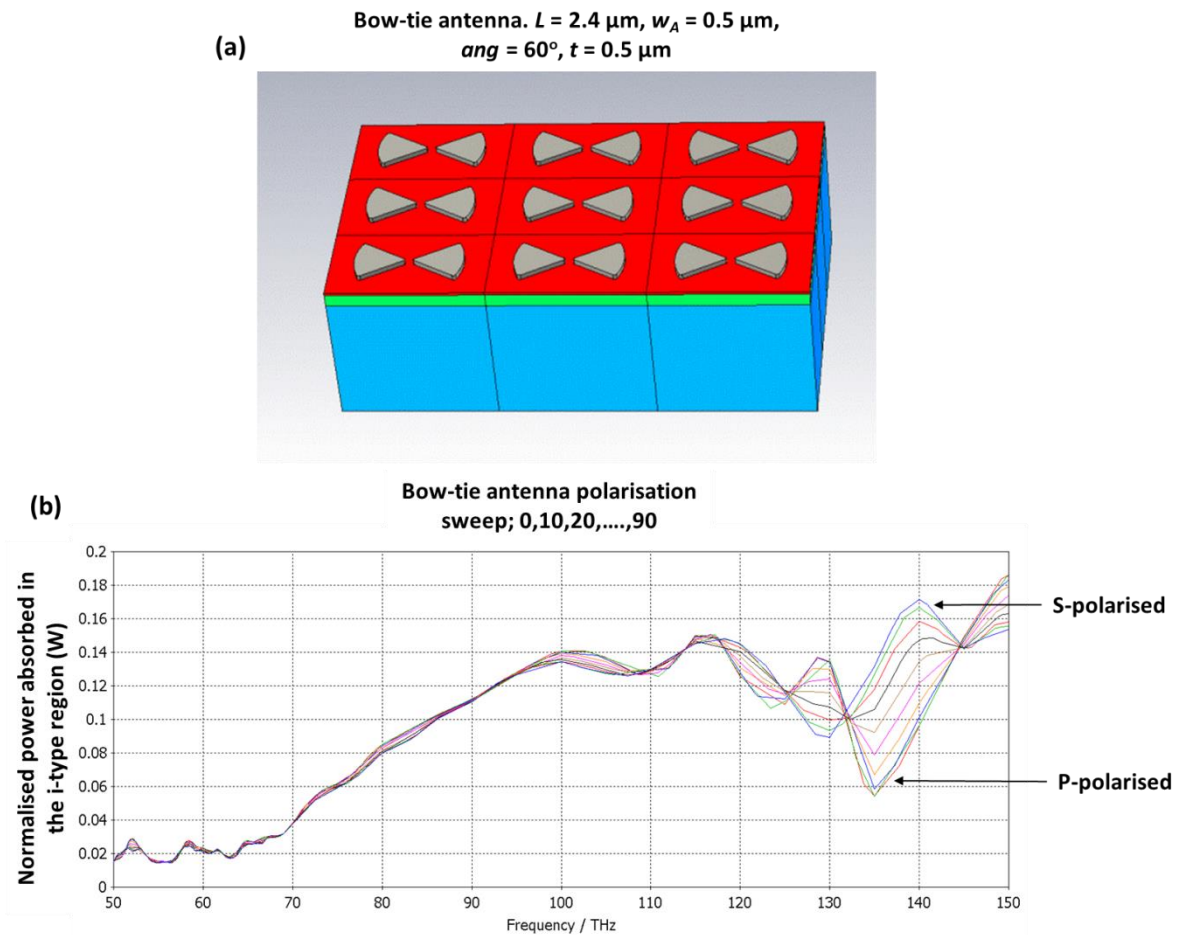
Figure 3.9.3: Bow-tie antenna simulation for a normalised 0.5 W of incident power. (a) CAD based diagram of a bow tie antenna array simulated in a Floquet port where *ang* is the angular girth of the bow tie, *L* is the bow-tie length, w_A is the aperture width and *t* is the antenna thickness. (b) Graph demonstrating the bow tie tolerance to polarisation sweeps.

Spiral antennas function in a similar way to the bow tie antenna where the peak responses are characteristic of the apparent conducting lengths. Compared to the bow tie antenna, the peaks have a reduced bandwidth and a reduced coupling due to an interlinked structure.
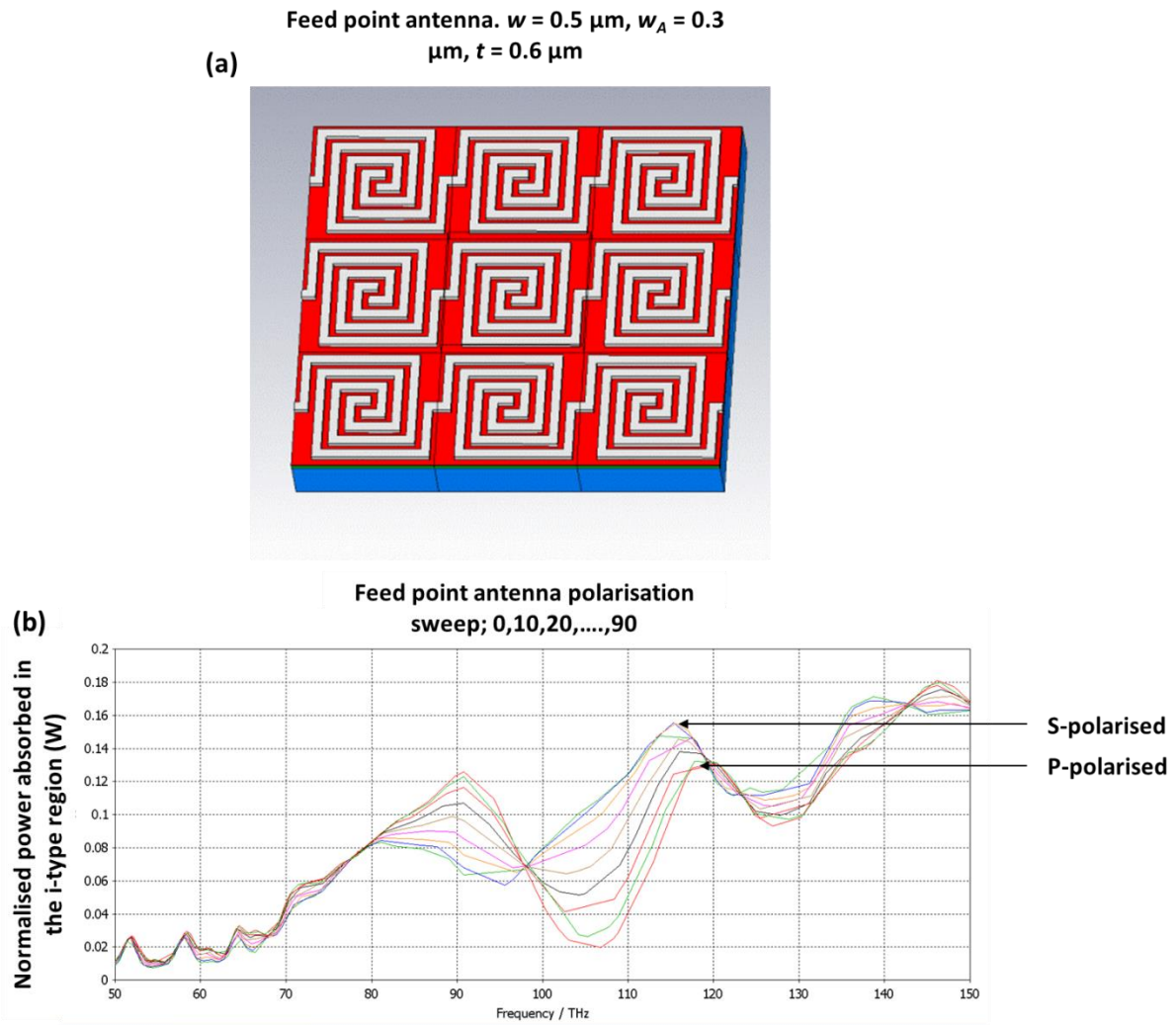
Figure 3.9.4: Feed point antenna simulation for a normalised 0.5 W of incident power. (a) CAD based diagram of a feed point antenna array simulated in a Floquet port, where w is the antenna width, w_A is the aperture width and t is the antenna thickness. (b) Graph demonstrating the feed point antenna tolerance to polarisation sweeps. The bandwidth is not consistent and has been recorded to be 1.60 μm or larger depending on whether it is p-polarised or s-polarised.

A grating antenna array has the advantage of having a concentration point that is equidistant from all the antenna edges, making this array a good focusing tool. It benefits from a relatively small bandwidth and consistent data at all polarisation angles. However, a lower

proportion of EM waves will be re-emitted in the grating cavities as a result of the grating

antennas acting like a wire as a result of being linked together.

Grating antenna. w_A = 1.1 µm, w_H = 1.8 µm,
t = 0.8 µm

(a)

(b)

Grating antenna polarisation
sweep; 0,10,20,….,90
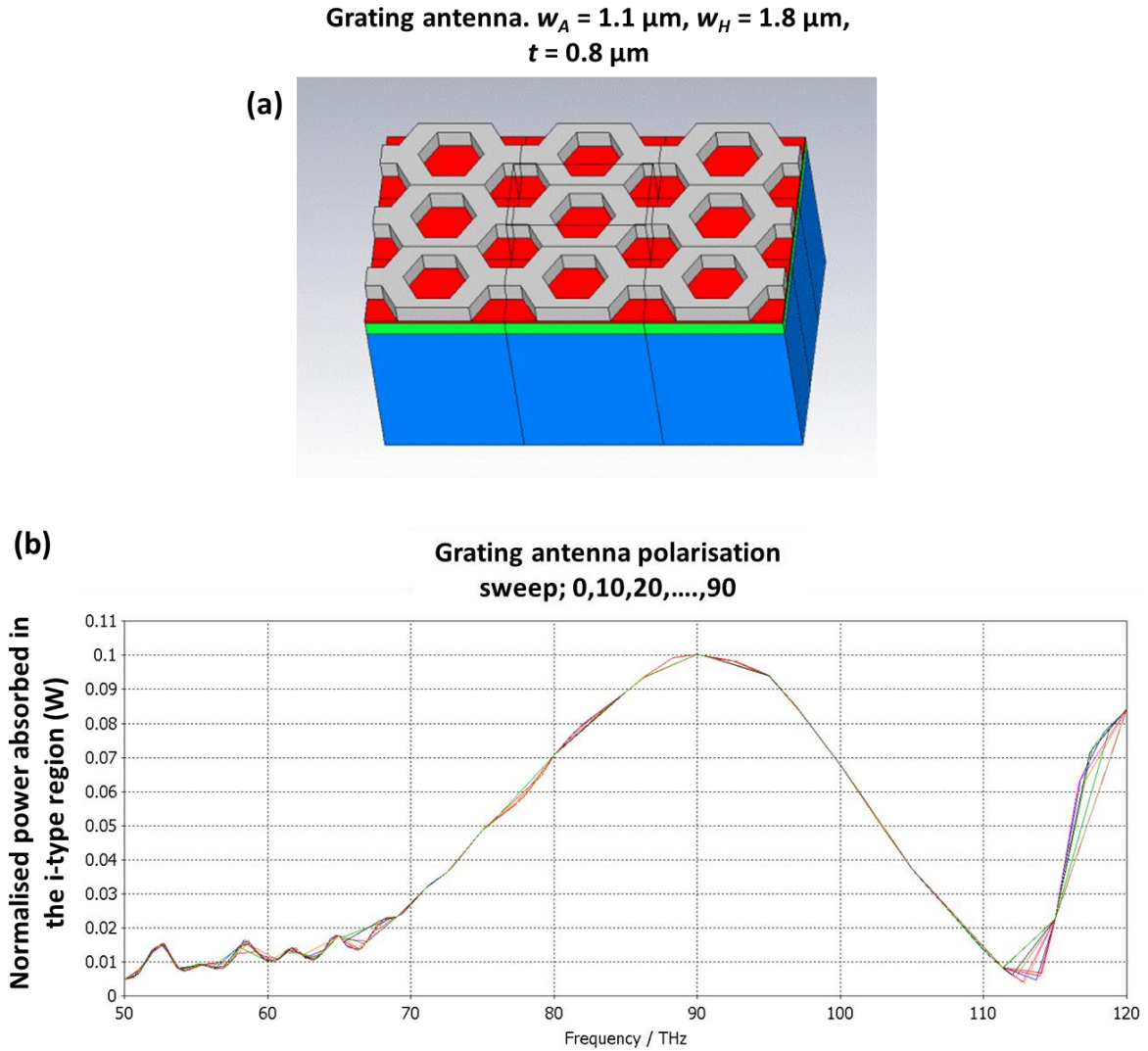
Figure 3.9.5: Grating antenna simulation for a normalised 0.5 W of incident power. (a) CAD based diagram of a grating antenna array simulated in a Floquet port, where w_A is the grating width, w_H is the cavity hexagonal width and t is the antenna thickness. (b) Graph demonstrating the reduced i-type absorption of a grating antenna and the tolerance to polarisation angle. The bandwidth has been recorded to be approximately 1.06 µm.

A cylindrical antenna array has the advantage of having a uniform length for each incoming

polarisation angle. However, the aperture width is inconsistent which will have an impact on

coupling efficiency. There is an optimum aperture the micro-antenna array can have. Deviating from the optimum will increase the proportion of light scattered off the surface. A hexagonal antenna array has the advantage of an efficient packing density and consistent spacing so that coupling is consistently optimised. Both designs will work, but the efficient packing density of the hexagonal structure produces better enhancement results due to the amount of unused space being reduced to a minimum on a macro scale. This is illustrated in figure 4.3.6.
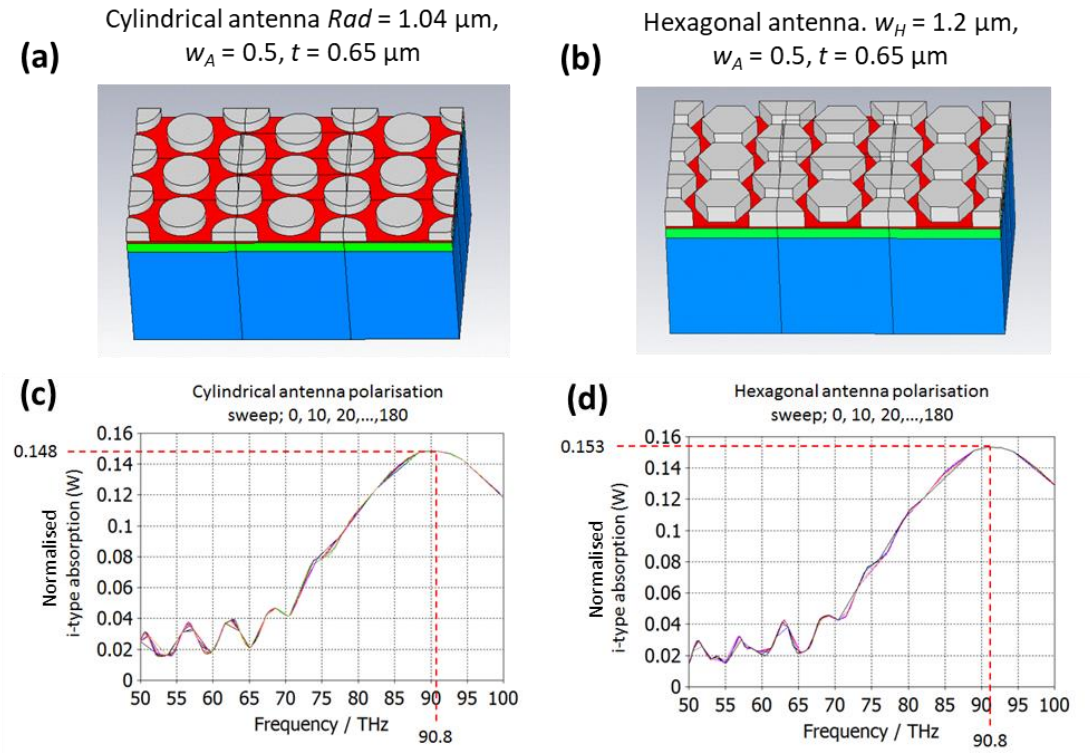
Figure 3.9.6: Cylindrical and hexagonal antenna array comparison for a normalised 0.5 W of incident power. (a) CAD based diagram of a cylindrical antenna array simulated in a Floquet port, where *Rad* is the cylindrical radius, w_A is the aperture width and t is the antenna thickness. (b) CAD based diagram of a hexagonal antenna array simulated in a Floquet port, where w_H is the hexagonal width. (c) and (d) demonstrate the marginal improvement in absorption enhancements in the i-type region of the hexagonal antenna array over the circular antenna array. Both designs have been optimised to respond to a frequency of 130 THz (or 3.3μm). The data given is a proportion of the normalised 0.5W of power incident of the array. So about 30% is absorbed in the i-type region depicted in light green in the array sketches. The bandwidth has been recorded to be approximately 1.40 μm.

3.10) Chapter 3 conclusion

Fabricating an enhanced semiconductor device is relatively time consuming and expensive compared to simulating it. This is why it is important to have a thorough understanding of the theoretical physics of both the semiconductor and the antennas before experimental fabrication.

The physics of LEDs have been outlined in the chapter as well as their detectivity and how it relates to the material composition and epitaxial layers. This theory has already been well established and is featured in this thesis for evolutionary device designs, (i.e. to consider what is currently possible and how to improve on it). Minority carrier generation is a foreseeable problem when doing this. The precise impact of which is unknown at a theoretical basis, but steps will be taken to add context to this problem (see section 5.4). The solution is to implement heterostructure barriers to mitigate minority carrier flow and assess the benefits.

The physics of how micro-antennas function are also well established. This chapter considers Maxwell's equations, the micro-antenna equivalent circuit and how applicable the impedance based derivations and calculations are to a meshing grid in a detector and emitter antenna simulation. Important material parameters, such as the attenuation coefficient, skin depth, refractive index and the antenna quality factor (Q) are all theoretically derived so as to provide an insight on how these simulations are generated and to emphasise the importance of including accurate complex dielectric constant data, not only for the antenna conducting material, but also for the $Al_{0.05} In_{0.95}Sb$ semiconductor. This data is important for accurate impedance difference measurements between the two materials.

Another point that this chapter considers is the antenna size, shape and loses due the volume and various polarisation angles. The size of the antenna will change the antenna frequency response in accordance with the effective volume (see figure 3.6.1 equations 10 and 11). The application to simulation software involves conventional antenna mathematics in finite difference frequency domain (FDFD) electromagnetic simulations.

The antenna itself can be made of any material as long as it conducts. However, most published work has featured antennas made of gold and silver because of their particularly good conductivity[82,83]. After considering the dielectric properties of these materials, it was realised that the adhesive layer necessary to keep the gold and silver on the surface was detrimental enough for both aluminium and copper to surpass them.

The benefits of antenna influenced localised focusing in the i-type layer will need to make up for the minimum simulated antenna losses being between 5% - 6% of the total incident power.

4) Chapter 4: Fabrication methodology

The fabrication methodology chapter discusses the technology and process flows required to make the semiconductor device as well as all the antenna enhancements. Molecular beam epitaxy (MBE) has been used for semiconductor fabrication and because of its financial viability; photolithography has been used to fabricate the semiconductor enhancements. Intricacies of the designs such as mask aligners, perimeter to area test structure and contact probes are discussed to insure successful development.

Difficulties in the development process and the changes to the design are documented in this chapter to address device reproducibility. Any compromises to the overall aim of obtaining an optimised S/N ratio are accounted for.

4.1) Semiconductor growth

The semiconductor fabrication procedure and its precision for a given fabrication time is important when the change in signal-to-noise (S/N) ratio is dependent on the size of the epitaxial thicknesses. There are several different types of each with their associated advantages and disadvantages.

Molecular beam epitaxial was the method used for semiconductor epitaxial growth[85].

Images of the MBE growth chamber are given in Figure 4.1. The tool consists of a buffer chamber, a trolley, a growth chamber, a transfer arm, a liquid nitrogen pump, shutters, a manipulator and a load lock. The semiconductor is grown by means of evaporation. It was the semiconductor method that was chosen for its precision in growing thin epitaxial layers that

micro-antenna influenced localised focusing could benefit from.
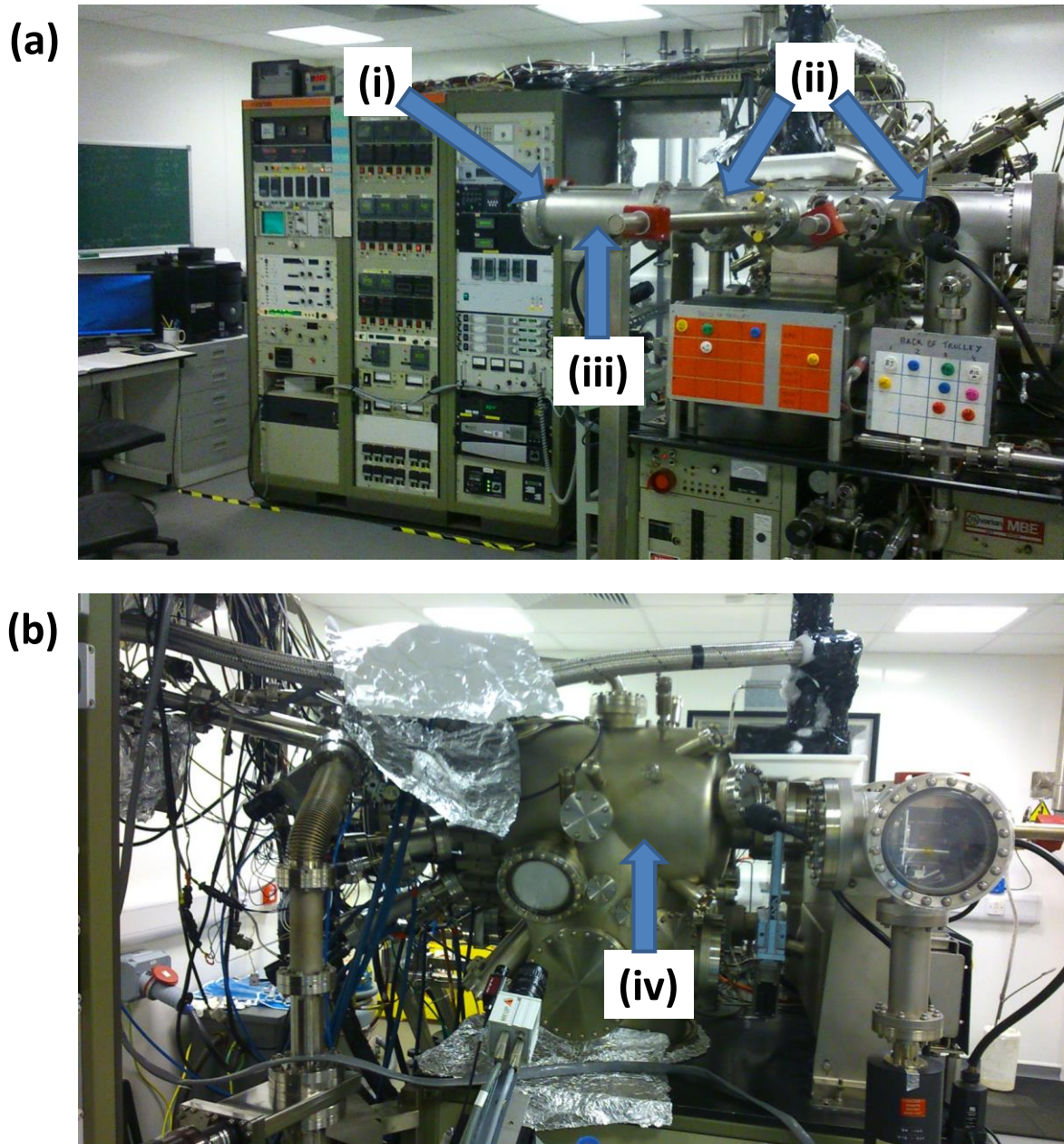
Figure 4.1: The molecular beam epitaxy laboratory. (a) The growth chamber as seen from the front. (b) The growth chamber as seen from the side. (i) The Buffer chamber. (ii) Windows to check the wafer condition when entering and leaving the growth chamber. (iii) A trolley to transport the wafer. (iv) The growth chamber. Photos were taken by author.

The semiconductor is grown on a Gallium arsenide (GaAs) wafer approximately 600 micrometres thick. The Wafer is placed in the Buffer chamber and the vacuum chamber is evacuated to a pressure of 10^{-8} Torr (1.33 x 10^{-6} Pa).

A trolley then transports the wafer to a transfer arm. The pressure is now decreased to 10^{-9} Torr to remove any surface water or carbon monoxide. Windows are there to check the wafer condition before a transfer arm pulls it into the growth chamber.

Inside the growth chamber, the wafer is placed on a manipulator to adjust the direction it is facing and to ensure uniform deposition across the substrate. The K cells at the side of the chamber are where the source materials are contained. Shutters control whether the material is to be deposited and temperature controls the rate of flow. Liquid nitrogen is pumped into the growth chamber cryo-shield to prevent de-sorption of any background materials. The wafer is cooled prior to removal from the growth chamber. A trolley then transports it to the load lock from where it is removed.

4.2) Semiconductor device process flow

The semiconductor must be given structure in order to probe the device and apply a forward or reverse bias current to the LED or photodiode.

This involves definition of structures down to ~ 0.5 μm in thickness. This can be achieved by means of electron beam lithography (EBL)[86] or photolithography (PL). EBL uses a finely focused electron beam to draw fine patterns into a master quartz stamp. This stamp can be used as a nano imprinting tool to filter out the resist in certain areas. PL is a faster and more financially viable alternative. It works by using chromium masks and either positive or negative resists. The resists change their molecular bonding properties when exposed to light.

The chromium masks (examples given in chapter 4.1) filter out the development pattern where the molecular bonding is intended to remain the same. As light goes through the chromium mask, it will diffract more prevalently around small gaps. As such the disadvantage of PL is that it lacks precision if the intended structure in development is of a few hundred nanometres in scale or less. The antenna size must follow the dipole rule and have a path length to the antenna aperture that approximately matches $\lambda 3/2$, where λ is the target wavelength. The target wavelength is 3.3µm and 4.2µm. This means that the antennas that need to be considered are of the micro scale and not the nano scale. Micro-antennas of this size are large enough so that the fabrication using photolithography should give an acceptable yield.

A positive resist (e.g. PMMA poly(methyl methacrylate) or PBS (PolyButene-1-Sulfone)) has a chemical composition that is broken down by light interaction. Should enough polymer chains break in this fashion, then the resist can be dissolved off using a photoresist developer.

In a negative resist (e.g. PGMA (polyglycidal methacrylate)), light interaction causes positive cross linking. This is where adjacent chains cross-connect to form a complex three dimensional structure. This increases the average molecular weight and decreases the solubility to photoresist developer[87]. The negative photoresist used for precision photolithography is the AZ 5124 resist[88]. This was used on antenna structures where the required aperture parameters need to be as small as 0.7µm.

Negative resists have very good dry etching characteristics. They are also better suited for precision photolithography where the necessary cavity can be as small as 0.7 µm.

The choice of either a positive or negative resist depends on the method used to develop the semiconductor. For example, positive resists have high resolution and have poor dry etching characteristics. So a wet etching method must be used to remove the resist and develop the semiconductor underneath.

Wet etching is the process whereby the semiconductor is immersed in a bath of agitated chemicals, such as Hydrofluoric acid (HF). This will etch the semiconductor, not entirely anisotropically associated with the zinc blende crystal form.

Dry etching is used to produce a vertical mesa, which is important for the device. This is where the semiconductor is bombarded with ions so that semiconductor molecules react with the ions to form a gas. This dry etching process can be performed using argon ions for semiconductor milling, or it can be done using reactive ion etching which uses boron trichloride or methane.

In the initial stages, the semiconductor mesas were fabricated at a relatively large scale, i.e. 200 μm in length or more. Hence a wet etching process using positive resist was used.
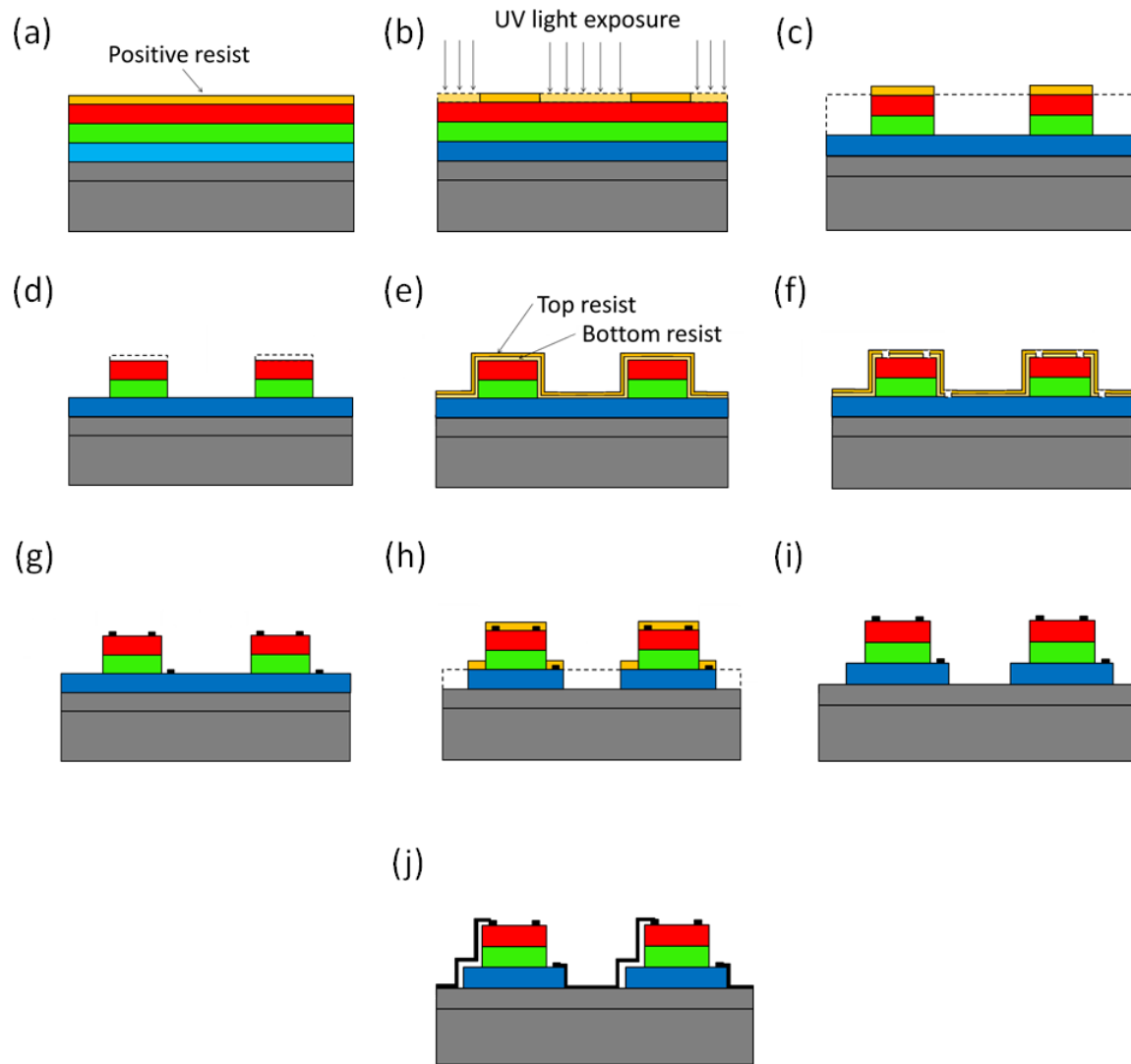
Figure 4.2.1: Schematic diagram illustrating the 250µm x 250µm interlinked semiconductor mesa fabrication process. (a) Before etching, a layer of PMMA is spun on (b) The molecular bonds are weakened when exposed to UV light. The shadow mask uses filters for UV exposure so that parts of the semiconductor will remain protected. (c) Using a lactic acid, nitric acid and hydrofluoric acid mixture (LNH) the semiconductor is etched down to the n-type layer. (d) The resist is rinsed off with acetone so a new patterning can begin. (e) So as to ensure a successful lift-off, two resists are used in this step, S1818 on the bottom and S2020 on the top. (g) Metal contacts are deposited within the cavities and the metal in the remaining areas is rinsed off with the resist. Figures (i) and (h) show the bottom mesa being developed using the same wet etching process which was used in steps (a) to (d). (j) The final sample when the metal contacts have been linked together.

Once the sides of the mesa are etched away, the remaining photoresist can be removed by use

of a solvent (e.g. Acetone or TMAH tetramethylammonium hydroxide). This removal is

known as the lift off. The lift off process can be done more easily if there is an undercut underneath the photoresist. For this reason it is good practice to spin on two different photoresists of different solubilities - where the more soluble resist is spun on first - when attempting to lift-off the annular contacts as shown in the (f) to (g) transition in figure 4.2.1.

The metal contacts are needed in order to apply a forward or reverse bias voltage within the semiconductor. The contacts need to be a material of very high conductivity (e.g. Au)[89]. After the contacts have been deposited they can be interconnected for the final semiconductor product as shown in figure 4.2.1 (j). Interconnecting the mesas provides an advantage when probing the device as the signal will stack. For experimental propositions it was decided not to do this so as to assess the signal enhancements on the antennas own merits and to minimise the influence of external sources. The white area between the semiconductor and the contact is an insulator needed to prevent a short circuit between the semiconductor p-type and n-type. This can be in the form of an insulting layer, but this has been observed to cause a detrimental effect to the semiconductor zero bias resistance. In order to improve semiconductor quality, an air bridge can be used instead. Air bridges are implemented by using a soluble photoresist instead of a more permanent resist such as polyimide.

A profilometer is used to measure the height of the mesa and contact pad, but cannot eventually be used to measure the antenna height as they are too small and compact. For that, a scanning electron microscope is used (see section 5.3).

Figure 4.2.2 shows the fabrication procedure described in figure 4.2.1 in 3D formatting while figure 4.2.3 shows the final product using an alternative air bridge.
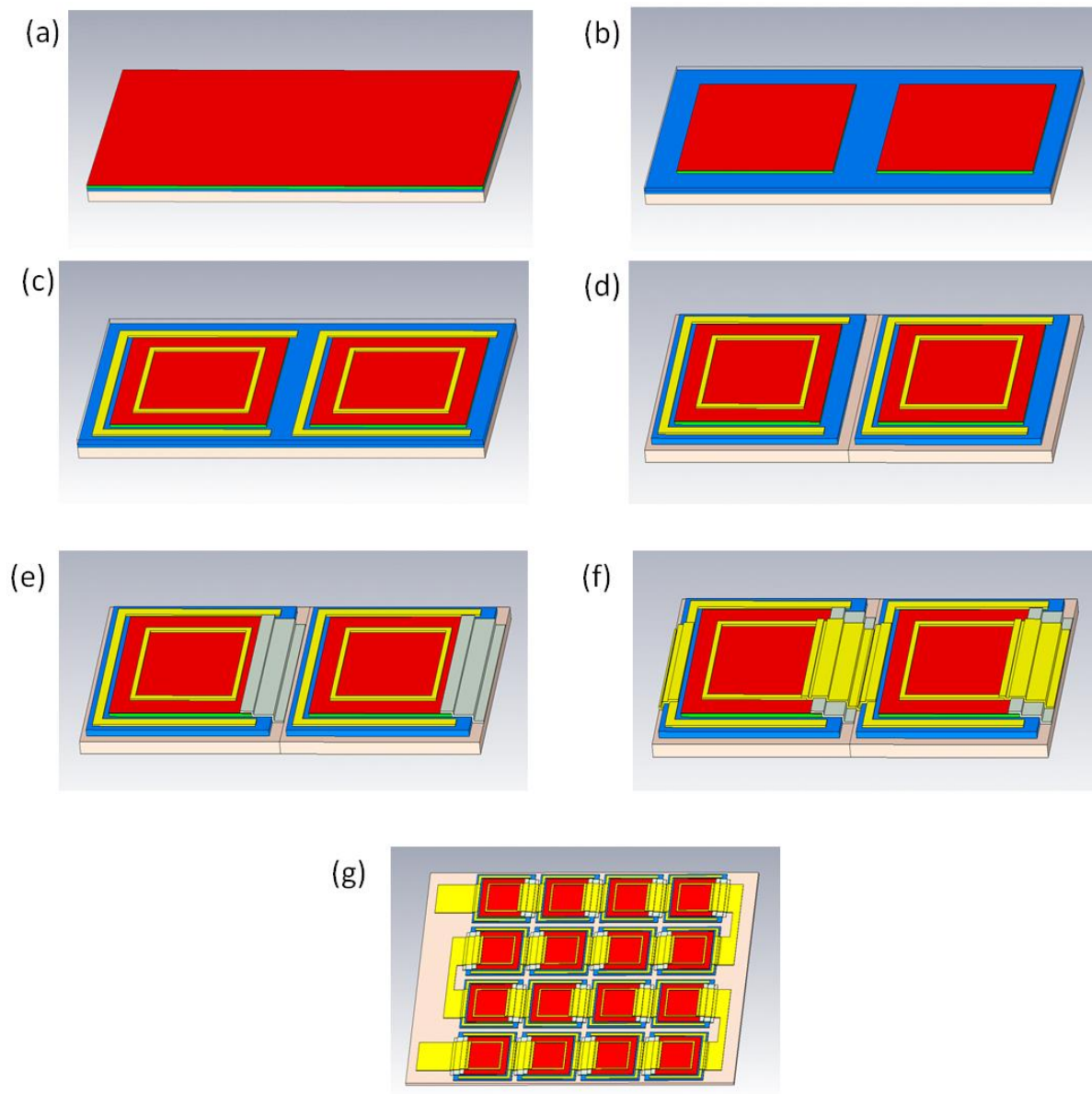
Figure 4.2.2: The 250µm x 250µm interlinked semiconductor mesa fabrication process in 3D form. (a) The plain AlInSb substrate (b) The 250 x 250 µm mesas developed after wet etching. (c) The gold annular contacts patterned on after positive photoresist produced the necessary cavities (d) The wet etching technique used a second time to etch out the bottom mesa. (e) A polyimide resist is patterned on at the side of the mesas. (e) The metal annuluses are linked to an adjacent mesa. (g) The final product. A 4x4 array of linked together mesas.
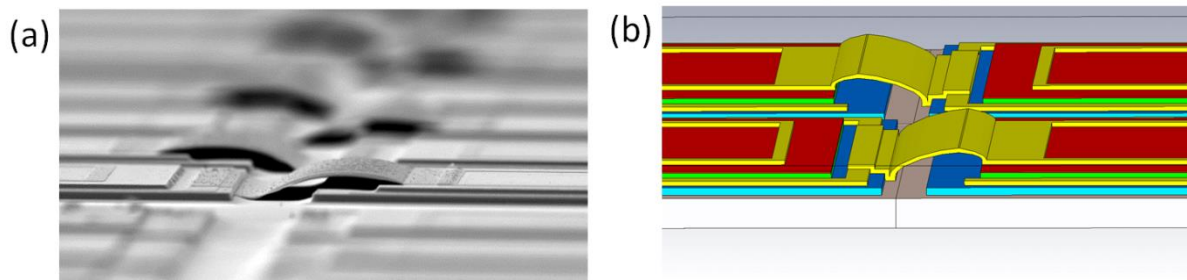
Figure 4.2.3: A visual demonstration of a contact air bridge being used as an alternative to a dielectric insulation; (a) as shown under the scanning electron microscope (SEM). (b) As shown in CAD based modelling software.

Figure 4.2.2 (g) is a finished semiconductor gas sensor device that can be used as a photodetector or LED[26,68,71]. This is the basic design will be modified with waveguide manipulators so as to improve the S/N ratio.

In an effort to reduce the diode leakage to a minimum, it is recommended that air bridges are used if mesas are to be interconnected. These air bridges are, however not featured in the antenna array fabrication method. The reason for this is not to undermine the importance of these features, but rather to minimise the design complexity so that any improvements can be entirely to the merit of the newly implemented micro-antennas.

4.3) Micro-antenna fabrication procedure

A target wavelength of 3.3 μm or 4.2 μm range makes the ideal antenna size tiny compared to standard antenna used in radio or radar communications and detection. To put this in context, the conducting length needs to be considerably shorter than the width of a human hair. An additional difficulty is that they also need to be sufficiently closely packed for meaningful interaction between opposing eigenmodes [90,91]. This poses a challenging fabrication problem. Electron beam lithography or focused ion beam milling has shown to be potential fabrication techniques for micro-antenna arrays of this size, but commercial viability is also something to consider if these micro-antenna arrays are to be used in large scale production. It is for this reason that it is a worthwhile investigation to consider conventional photolithography techniques with the inherent fabrication limitation of this technique being 700nm. It has been decided that is an acceptable fabrication method since the research is primarily interested in the MIR (mid infrared) spectral range.

4.3.1) NTA 1: The prototype mask design

NTA 1 (Nanoantenna test array 1) is designed to demonstrate quickly and cheaply the antenna resonance effect. Analysis of this design will provide initial evidence that a resonance effect is possible for MIR range wavelength and that appropriately small devices can be made.

The term "nanoantenna test array" (abbreviated as NTA) was the name given to the new mask designs for intended nanoantenna fabrication. It wasn't realised until further investigation that it is more beneficial in terms of localised focusing to tune the antennas to ($L = ¾ \lambda$) resonance harmonics, rather than first order. This meant that the antenna parameters

that gave the most promising outcomes were large enough to be classified as micro-antennas. The name remains as a reference to the original thought process with reference to the fundamental order dipole rule.

In accordance to equation 2.0 and section 3.6, the antenna conducting path lengths needs to be approximately equal to the wavelength if it is going to resonate at the seconded order integer and couple into the semiconductor photodetector more effectively. Larger antenna designs were considered to verify if resonance at higher harmonic integers warranted further pursuit. NTA 1 therefore includes a larger antenna structure to verify this possibility.

The figure of merit is the amount of light transmitted into the surface of a single undoped layer of 5% AlInSb with and without semiconductor enhancements. The $Al_{0.05}In_{0.95}Sb$ in shown as a thin purple layer in figure 4.3.1.
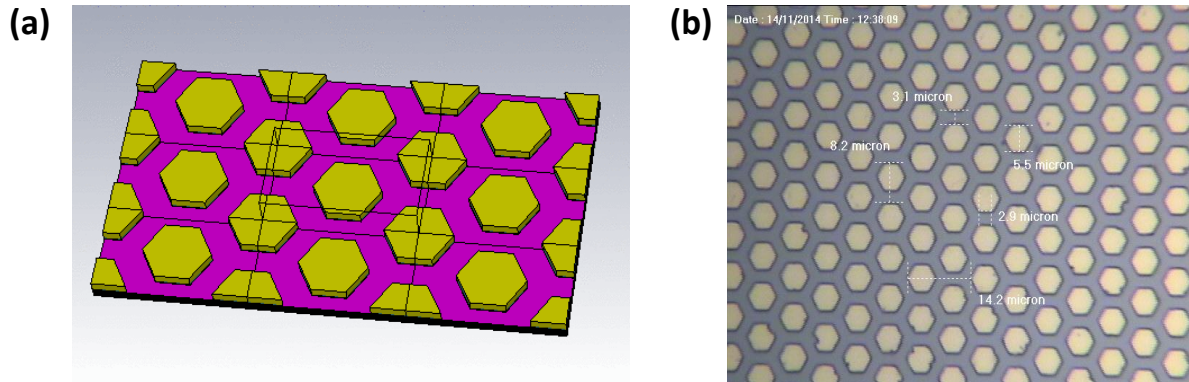
Figure 4.3.1.1: An example of successful development of the largest size gold hexagonal antenna development. This example is of feature size 10. (a) The modelled unit cell. (b) The fabricated arrays as viewed under a microscope.

The fabrication procedure uses a AZ 5124 E negative resist for its precision down to 0.7 µm as opposed to the positive S1818 and S2020 positive resists which are conventionally used

for much larger structures, such as the mesa structure which will eventually be featured (Refer to section 4.2). The prototype was designed in L-edit, which is a commercial software used to build schematics form printed circuit boards (PCBs). The prototype mask schematics and developed images are given in figure 4.3.1.2 (a).
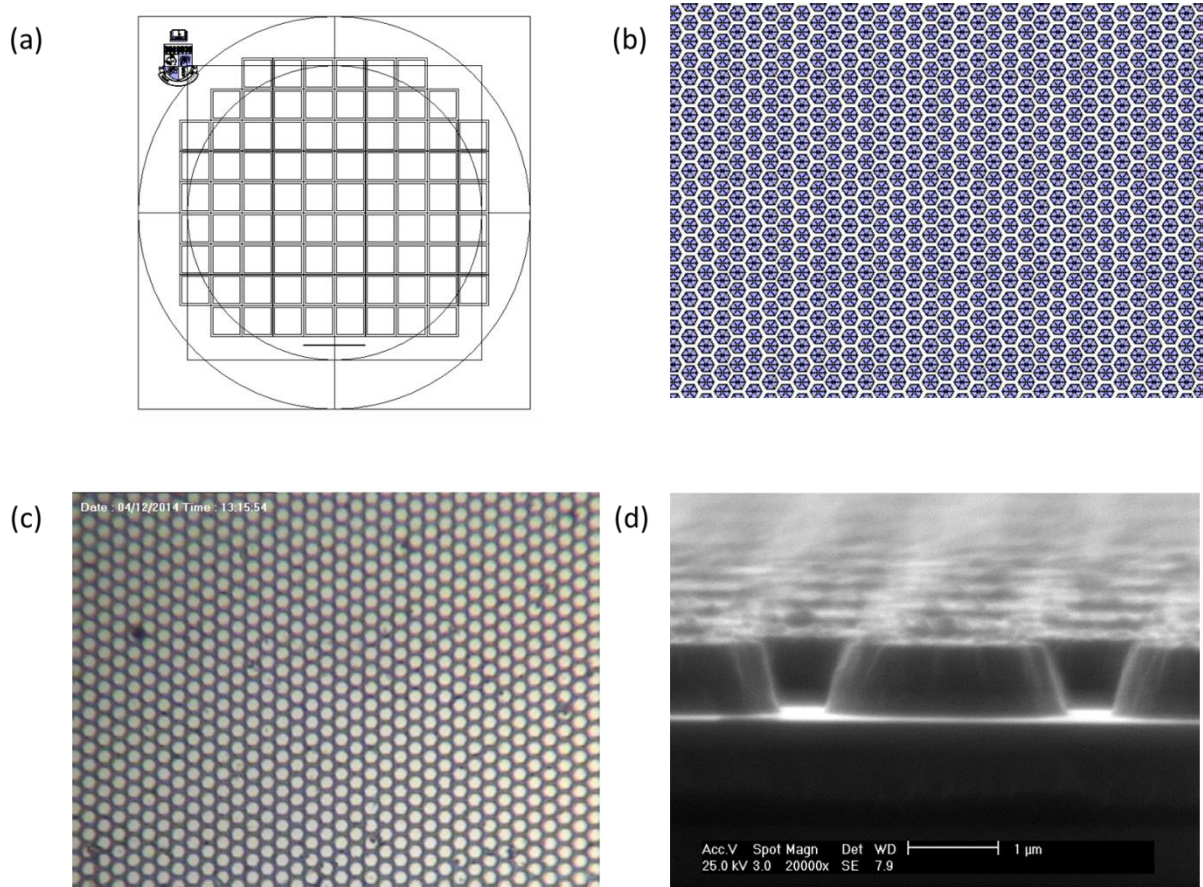
Figure 4.3.1.2: NTA 1 schematics and development. (a) The complete prototype mask 4 inches in length with 82 fields allocated to different micro-antenna widths and spacings (b) A close up of one of the fields with an antenna width of 1.5 and a spacing of 0.75. (c) A microscopic image of successful antenna development in a region with the same width and spacing parameters. (d) A scanning electron microscope (SEM) image of the antenna array developed in (c).

When the wafer is grown, its thickness is slightly non-uniform and the thicker and higher quality epitaxial layer is situated near the centre, whereas the thinner material at the edge accounts for a 5% reduction in thickness. The structures have therefore been distributed in pseudo random positions with some degree of artificial rearrangement so that at least one of each type of antenna array is positioned at the side of the wafer and at least one nearer the centre as shown in figure 4.3.1.3. This is done that so no particular feature is necessarily better than the others for reasons beyond the antenna parameters or quality factor. The variations in antenna parameters consist of hexagonal widths (w_H) of 1.0 µm, 1.5 µm and 3.0 µm, where each of those widths have aperture widths (w_A) of 0.75 µm, 1.5 µm and 3.0 µm in different fields.

Figure 4.3.1.2 (d) shows that the antenna sides are not completely vertical as a consequence of photoresist undercut during development. This is not considered to be a major development flaw but it will still have a noticeable influence on the results (see section 5.4). It is therefore worth considering a more refined process development to eliminate these side wall defects.

(a)

(b)

No.	Shape	l (µm)	w_H (µm)	w_A (µm)	x-axis pitch (µm)	y-axis pitch (µm)
1	Control (no antenna)	n/a	n/a	n/a	n/a	n/a
2	Hex	2.6	1.50	0.75	5.80	3.35
3	Hex	1.73	1.00	0.75	4.30	2.48
4	Hex	5.20	3.00	0.75	10.30	5.95
5	Hex	2.60	1.50	1.50	7.10	4.10
6	Hex	1.73	1.00	1.50	5.60	3.23
7	Hex	5.20	3.00	1.50	11.60	6.70
8	Hex	2.60	1.50	3.00	9.70	5.60
9	Hex	1.73	1.00	3.00	8.20	4.73
10	Hex	5.20	3.00	3.00	14.20	8.20
11	Squ	2.50	n/a	1.50	4.00	4.00

Figure 4.3.1.3: NTA 1 shape, size and positioning. (a) L-edit wafer map. (b) The conducting length (l), the hexagonal width (w) and aperture width (w_A) information for the individual antenna array. The numbers given in green co-respond to the antenna shapes, size and spacing given in Table 4.3.1.4 (b). The numbers given in red are the location indices located in the top left hand corner of each field. The location indices are arranged so that the y-axis number is first and the x-axis number is second.

The wafer was not cleaved into quarters for the NTA 1 antenna design. Once the antennas have been fully developed the full wafer was cleaved into the many 5mm square pieces which make up the wafer. The antennas on the NTA 1 mask array were made out of gold with a layer of chromium underneath for better adhesion.

4.3.2) NTA 1 process flow

1) Antenna photolithography

Use ¼ of a AlInSb wafer (3 inches in diameter).

Solvent clean using acetone and propanol.

Dry on hotplate 115°C 3 min.

Primer – 1 min exposure to vapour under a petri dish.

Spin AZ 5214 photoresist for 300 rpm 5s then 3000 rpm 30s. This gives ~ 1.5 μm resist.

Bake at 115°C for 1 min.

Using rubylith to remove the edge bead by exposing to 250mJ/cm² then develop in MF 319 .for 30s, DI rinse and dry with nitrogen gas.

Using the Nanoantenna design 1 mask, expose to 60mJ/cm² in vacuum contact.

Allow the nitrogen generated in the resist to evolve for 10 min.

Reverse bake 120°C 2 min.

Flood expose to 250mJ/cm².

Develop in MF 319 for 30s

Rinse with de-ionised water.

Dry with nitrogen gas.

Measure the resist height – should be ~ 1.5 μm.

2) Antenna metal deposition

Evaporate metal onto sample using evaporator.

Lift-off in a beaker of N-Methyl-2-pyrrolidone (NMP) immersed in the water bath set at 70°C to give a solution temp of 60°C. Use the wafer holder to support the wafer upside down. After 10 min place the beaker in the ultrasonic bath set at power 3 and run until all the metal has lifted off. Rinse in a beaker of DI water. Dip in propanol for 20s then dry with nitrogen gas.

4.3.3) NTA 2: Semiconductor mesas with antenna enhancements

Nanoantenna test array (NTA) 2 is a development of NTA 1, whose purpose was to verify a reduction in surface reflectivity. While a reduction in light reflection at certain tailorable frequencies has been proven from the NTA 1 results (see section 5.2), NTA 2 is designed to take the semiconductor testing a step further. The mesas developed from the newly developed mask set will verify whether the radiation is being directed in the desired region of the semiconductor. The main objective is to measure the amount of localised light concentration within the semiconductor i-type layer that can stimulate an enhanced response. This means that it will need to be compatible with an autoprober unit so that the semiconductor output can be assessed. The schematics were generated in the L-edit software and consist of a 3 part mask set.

This section will discuss the NTA 2 mask design; different antenna parameters; how the practical spectral results were obtained; and how the experimental results compare with the theoretical ones.

NTA 2 is designed to enable fabrication of a close-packed array of antennas of the size of 1.0 µm – 2.0 µm on top of relatively large mesas of size 200 µm – 400 µm. The design includes contact pads for probe analysis and annular contacts for photocurrent uniformity. The mask set has 32 fields that can be patterned on a full 3 inch wafer. Each field has 100 mesa sets. Each mesa set has 4 different mesa sizes. This makes 12800 different test structures that can be tested upon completion. A full hierarchical diagram of NTA 2 is provided in figure 4.3.3.1:
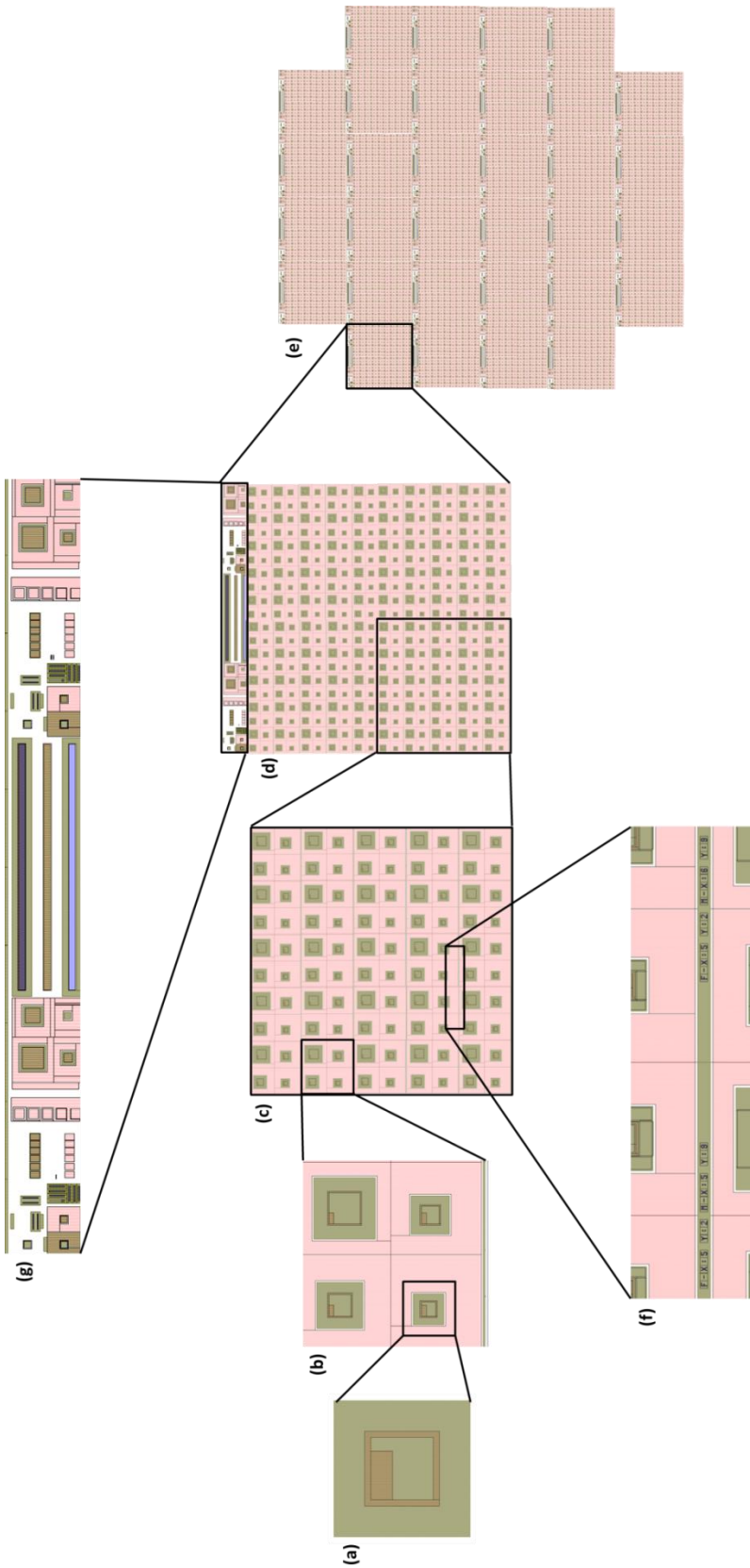
Figure 4.3.3.1: Hierarchical diagram of the fully developed wafer. (a) Individual mesas. (b) 4 mesas of different square lengths. (c) A field quarter with the antenna size variations. (d) A 2 by 2 array of the quarter field. (e) 32 across the entire mask. (f) Field and Mesa set identity numbers. (g) Field alignment markers.

The semiconductor fabrication process for NTA 2 is done in three steps for three mask designs as shown in figure 4.3.3.2.

Mask 1: patterns out the photoresist cavities that are used to evaporate antenna arrays and mesa set labels of the semiconductor surface. A negative resist will pattern the surface, meaning the photoresist will cross link when exposed to UV light making it more difficult to dissolve. It is shown here as a light field schematic, meaning the coloured areas are blocked in the mask design.

Mask 2: is used to protect the antennas on the surface during the wet etching process to shape the mesas. A positive resist will pattern the surface, meaning the photoresist will become more soluble when exposed to UV. It is a light field schematic.

Mask 3: patterns out the photoresist cavities that are used to evaporate conducting annuluses and contact pads. It uses a positive photoresist. It is shown here as a dark field schematic, meaning the coloured areas are transparent in the mask design.
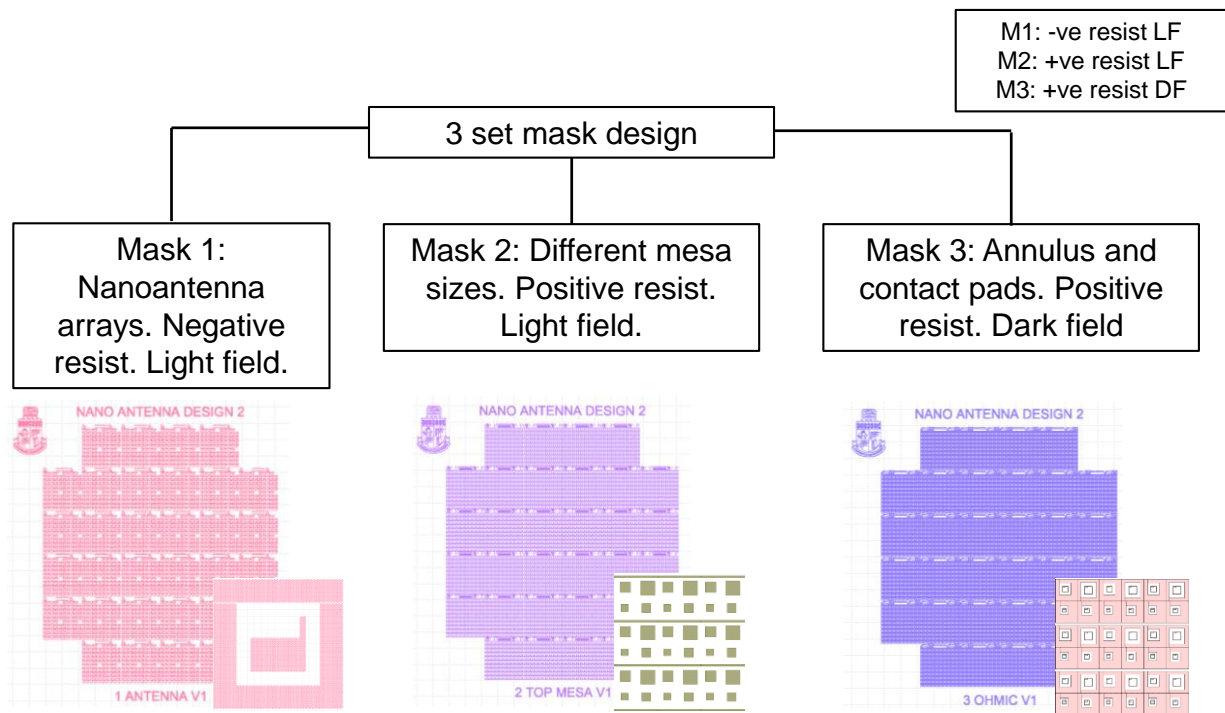
Figure 4.3.3.2: The schematic design of the three mask sets for the fabrication of antenna arrays on semiconductor epitaxial layers. Each design has a complete macroscopic picture together with a close up of the most relevant parts adjacent to them. Mask 1 is the ANTENNA mask. It will use a negative (-ve) resist to pattern out cavities used for the lift-off process. Mask 2 is the TOP MESA mask. It will use a positive (+ve) resist to cover the mesas that are to be protected during Lactic acid/Nitric acid/Hydrofluoric acid (LNH) etching. Mask three is the OHMIC mask. It will use a +ve resist to pattern out the mesa annuluses and contact pads.

Mask 1: requires the highest degree of precision available in this photolithography process flow in order to get successful lift-off of an array with less than 2.0 µm in pitch. The AZ 5214 resist is therefore chosen for antenna patterning in the initial stages because it can be used for small photoresist cavities[92]. Figure 4.3.3.3 shows an example of the antenna development compared to the schematic.
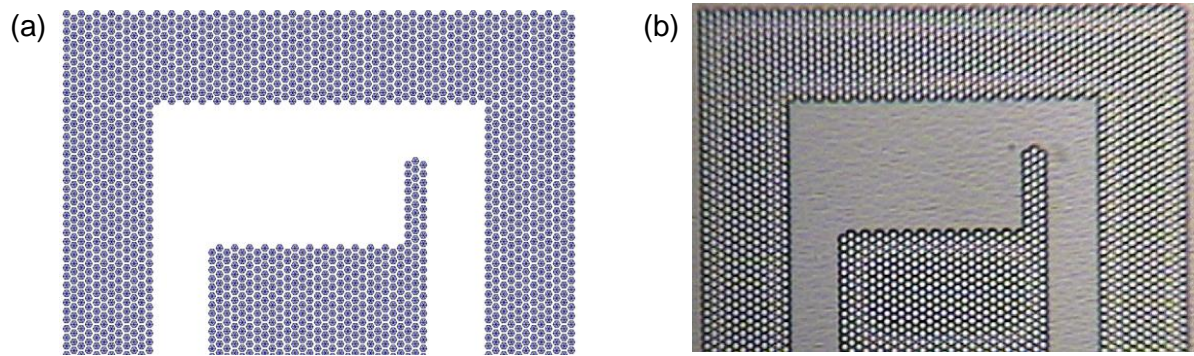
Figure 4.3.3.3: An example of an antenna array to be fabricated using NTA 2 Mask 1. The antennas in this example are labelled F: X-1 Y-2 M: X-7 Y-3 (w_H = 1.4 µm, w_A = 0.8 µm) and have a square length of 200µm. (a) The L-edit schematic. (b) The fabricated antennas as viewed under a microscope.

The mesa sets have 24 different antenna size and spacing variations patterned on them and one control. They are then expanded into a 2 by 2 array. Their allocated labels are at the bottom of each and depict the field (F) x and y numbers and the mesa set (M) x and y numbers. The mesa set coordinates are important for identifying the antenna parameters. As shown in figure 4.6.4 the hexagonal width (w_H) of the antennas range from 1.0 µm to 1.5 µm in increments of 0.1 µm. The antenna aperture width (w_A) ranges from 0.7 µm to 1.0 µm with the same increments as w_H.

No.	w_H (µm)	w_A (µm)	M X	M Y
1	1.0	0.7	0	0
2	1.0	0.8	1	0
3	1.0	0.9	2	0
4	1.0	1.0	3	0
5	1.1	0.7	4	0
6	1.1	0.8	0	1
7	1.1	0.9	1	1
8	1.1	1.0	2	1
9	1.2	0.7	3	1
10	1.2	0.8	4	1
11	1.2	0.9	0	2
12	1.2	1.0	1	2

No.	w_H (µm)	w_A (µm)	M X	M Y
13	1.3	0.7	2	2
14	1.3	0.8	3	2
15	1.3	0.9	4	2
16	1.3	1.0	0	3
17	1.4	0.7	1	3
18	1.4	0.8	2	3
19	1.4	0.9	3	3
20	1.4	1.0	4	3
21	1.5	0.7	0	4
22	1.5	0.8	1	4
23	1.5	0.9	2	4
24	1.5	1.0	3	4

21	22	23	24	C
16	17	18	19	20
11	12	13	14	15
6	7	8	9	10
1	2	3	4	5

Figure 4.3.3.4: The antenna parameter memoir. The centre numbers in the square array show the relative position of the antenna array grown on the allocated mesa set. They are the equivalent of figure 4.6.1 (c). The width and spacing column specify the antenna parameters that are to be deposited there. The M X and M Y values are the Mesa set coordinates are included in the mesa set labels.

The mesa set numbers in the memoir do not go up to 5 as they are considering 25 mesa sets (¼ of the total number of mesa sets in a field). So when arranged in a square, the x and y mesa set coordinates range between 0 and 4. However, when the square is replicated into a 2 by 2 array in the field, each of the 25 mesa sets are identical. This means that in order to determine the parameters of a mesa set in an adjacent array, one would need to reference how much the mesa set has been displaced from the original, i.e., subtract 5 from the axis number. This would make mesa set number X-7 Y-3, shown in figure 4.6.3 equivalent to X-2 Y-3, which means that the antenna parameters; $w_H = 1.4$ µm and $w_A = 0.8$ µm.

The transition from one mask to another will require alignment markers. The alignment markers are positioned at the top of each field (see figure 4.6.1 (g)), occupy a surface area that allows clear and simple transition from one field to another, and contains extra features

such as structures for perimeter-over-area (P/A) and transmission line measurement assessment.

The P/A structures in the alignment structure bars are included to enable demonstration of the relative contribution of the perimeter to surface area to leakage current. For more information on contact degradation see section 4.1.
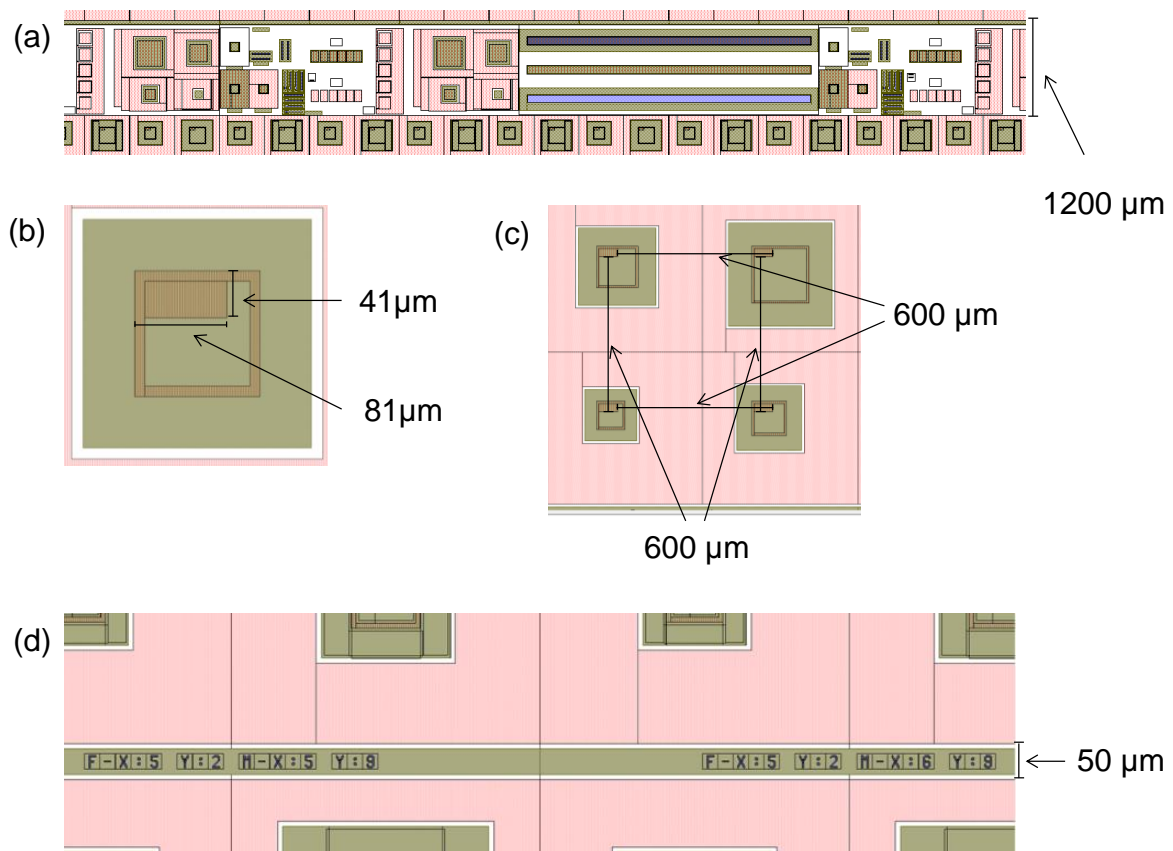
Figure 4.3.3.5: Measurements of mesa spacing in each field. (a) The alignment markers, perimeter to area (P/A), and transition line measurement structures. These features are all positioned in a strip above every field. (b) The size of the mesa contact pads used for probing. The contact is a rectangle 72 µm wide and 32µm high and adjacent to a 9µm wide annulus. The annulus width and size of the contact pads are consistent for all mesa sizes. (c) The mesa contact pad positioning for each mesa size in the 2 x 2 array. (d) The mesa set labels displaying the x and y coordinates of the field and the mesa set within the field. The label width is 40 µm will a 5 µm gap on either side.

Mask 2: will pattern out the mesa sets shown in brown in figure 4.6.1 (b) using the AZ 2690 positive resist. Each mesa set has 4 different mesa sizes of 200 μm by 200 μm, 250 μm by 250 μm, 300 μm by 300 μm, and 400 μm by 400 μm. The mesa will then form once the surrendering regions have been etched down using a Lactic acid/Nitric acid/Hydrofluoric acid (LNH) solution.

Mask 3: will pattern out the cavities in the photoresist for the metal contact shown in red on the mesa surfaces. It utilises the bilayer resist development procedure described in section 3.2. Annuluses and mesa contact pads are needed for probing and are patterned out on the mesa structures. They are carefully designed to be as small as possible so as to minimise the minority carrier generation from the gold contact pads whilst also being large enough to allow for probe overdrive i.e. the lateral displacement of the probe tip. After extensive manual probing analysis, a width of 41 μm and a length of 81μm were chosen. The pink area around the mesas indicates the position of the n-type contact pad.

4.3.4) NTA 2 process flow

After some iteration with photoresist chemicals, development time and lift-off times the instructions on how to use the mask set are as follows:

1) Antenna photolithography

Use ¼ of a AlInSb wafer (3 inches in diameter).

Solvent clean using acetone and propanol.

Dry on hotplate 115°C 3 min.

Primer – 1 min exposure to vapour under a petri dish.

Spin AZ 5214 Program 8 (300 rpm 5s, 3000 rpm 30s) gives ~ 1.5 μm resist.

Bake at 115°C for 1 min.

Using rubylith remove the edge bead by exposing to 250mJ/cm² then develop in MF 319 for 30s, DI rinse and dry with nitrogen gas.

Using the Nanoantenna design 2 no. 1 ANTENNA V1 mask expose to 60mJ/cm² in vacuum contact.

Allow the nitrogen generated in the resist to evolve for 10 min.

Reverse bake 120°C 2 min.

Flood expose to 250mJ/cm².

Develop in MF 319 for 30s.

Rinse with de-ionised water.

Dry with nitrogen gas.

Measure the resist height – should be ~ 1.5 μm.

2) Antenna metal deposition

Evaporate metal into sample using evaporator.

Lift-off in a beaker of N-Methyl-2-pyrrolidone (NMP) immersed in the water bath set at 70°C to give a solution temp of 60°C. Use the wafer holder to support the wafer upside down. After 10 min place the beaker in the ultrasonic bath set at power 3 and run until all the metal has lifted off. Rinse in a beaker of DI water. Dip in propanol for 20s then dry with nitrogen gas.

3) Mesa etching photolithography

Spin AZ 9260 resist using Program 19 (300 rpm 5s, 2000 rpm 60s) gives ~ 9 μm resist.

Using a tray bake at 110°C for 2 min 45s.

Rehydrate 10 min.

Using rubylith remove the edge bead by exposing to 1500mJ/cm² (recipe

GS_AZ9260_FLOOD_V1) then develop in AZ 726 for 5 min.

Rinse with de-ionised water.

Dry with nitrogen gas.

Align Nanoantenna design 2 no. 2 TOP MESA V1 mask and expose to 1500mJ/cm² hard

contact, recipe GS_Top_Mesa V1.

Develop in AZ 726 for 4 min 30s.

Rinse with de ionised water.

Dry with nitrogen gas.

Measure the resist height – should be ~ 9 μm.

4) Etching

Etch in LNH with the ratio (100:16:4) for 1 min.

Remove resist in acetone (x2) then dip in propanol for 20s and dry with nitrogen gas.

Should get an etch depth of ~ 1.4 μm.

5) Ohmic contact photolithography

Ensure the wafer is dry - hotplate 115°C 3 min.

Spin AZ 9260 resist using Program 19 (300 rpm 5s, 2000 rpm 60s) gives ~ 9 μm resist.

Using a tray bake at 110°C for 2 min 45s.

Rehydrate 10 min.

Using rubylith remove the edge bead by exposing to 1500mJ/cm² (recipe GS_AZ9260_FLOOD_V1) then develop in AZ 726 for 5 min, DI rinse and N_2 dry.

Align Nanoantenna design 2 no. 3 OHMIC V1 mask and expose to 1500mJ/cm² hard contact, recipe GS_Top_Mesa V1.

Develop in AZ 726 for 4 min 30s.

Rinse with de-ionised water.

Dry with nitrogen gas.

The resist height should be ~9 μm.

6) Metal deposition

Evaporate using recipe IBM TiAu (500-3000A).

Lift-off in acetone for approximately 10 min then ultrasonic power 1. Gently spray with acetone and transfer to propanol. Hold for 20s then dry the nitrogen gas.

Rinse with de-ionised water.

Dry with nitrogen gas.

4.3.5) NTA 2: Experimental set-up

In accordance with the NTA 2 mask design, contact pads have been included so that electrical contact can be made with the p-type and n-type semiconductor layers in order for the stimulated photocurrent to be forwarded to an amplifier in a photodiode set-up.

For the initial stages of the device analysis, the zero bias resistance (R_0) of the diodes was assessed. The R_0 resistance is a measurement of the diode quality and serves as a means to quickly assess the expected magnitude of the resistance when applying a reverse bias (i.e. the larger the R_0 magnitude is the larger the reverse bias resistance is going to be and less leakage will occur as a result). Figure 4.3.5.1 (a) shows an example of the how the contact probes are places on the semiconductor p-type contact (on the mesa surface) and the n-type contact pad (any of the surrounding area). This will connect the diode to a power supply that can assess the diode resistance as a forward and reverse bias voltage is applied. Figure 4.3.5.2 shows an example graph of the R_0 bias that is generated as a result to quantify the quality of the device. The semiconductor was measured using the Agilent B1500 semiconductor device.
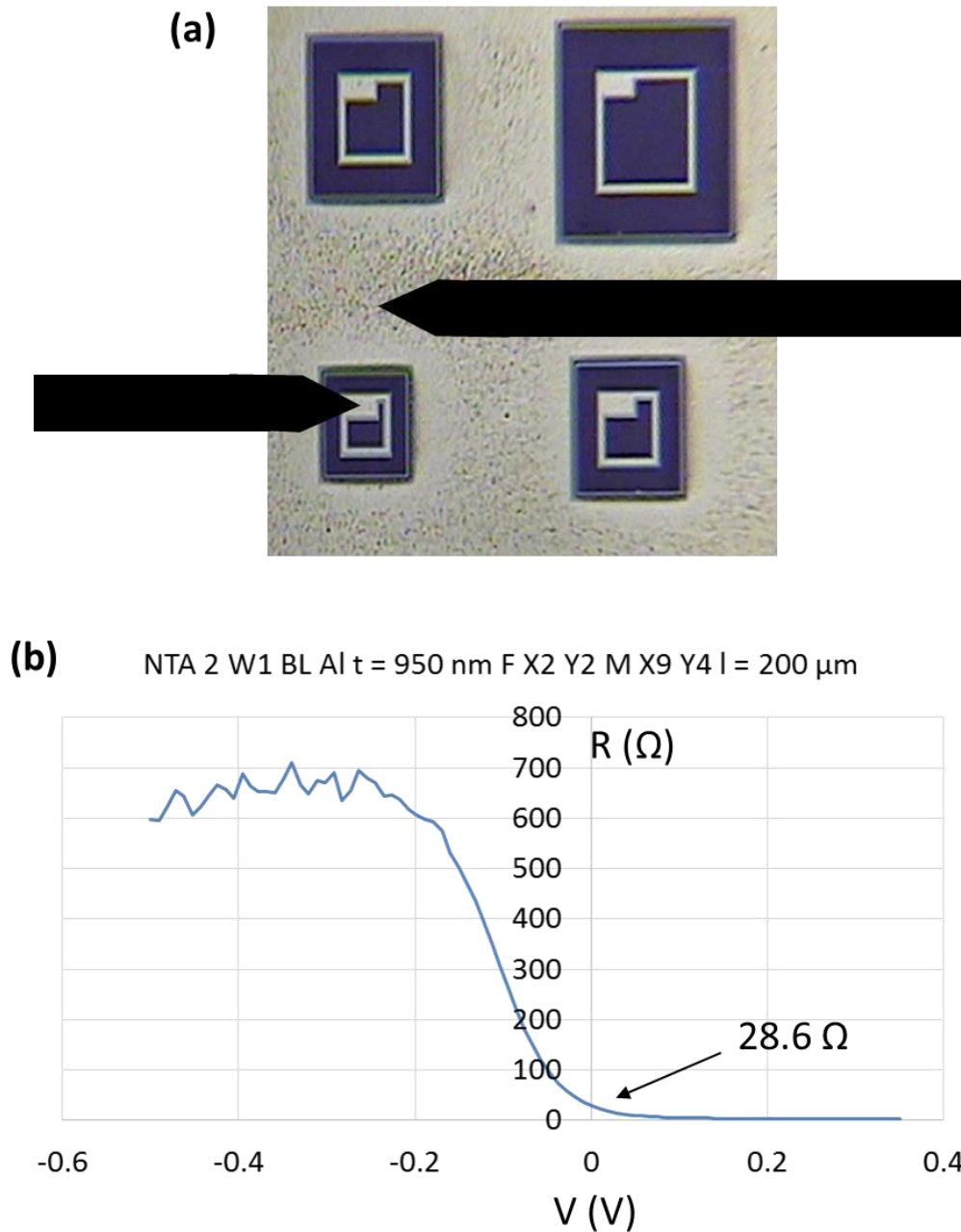
Figure 4.3.5.1: Probing the NTA 2 device. (a) A 200 μm by 200 μm with antenna arrays on the surface being probed. The top contact connects to the p-type layer and the surrounding area connects to the n-type layer. (b) A probe resistance measurement of the sample 200μm by 200μm mesa when a forward and reverse voltage is applied. The R_0 is this case is 28.6 Ω.

The equipment detector set up is given in figure 4.3.5.2. Similar to the FTIR BRUKER set-up

for the NTA 1 experimental procedure (see section 5.2), the FTIR unit used for the probed

measurements uses adjustable mirrors to project a range of monochromatic radiation onto the

photodetector. This monochromatic range will span between 1.5 μm and 9 μm.
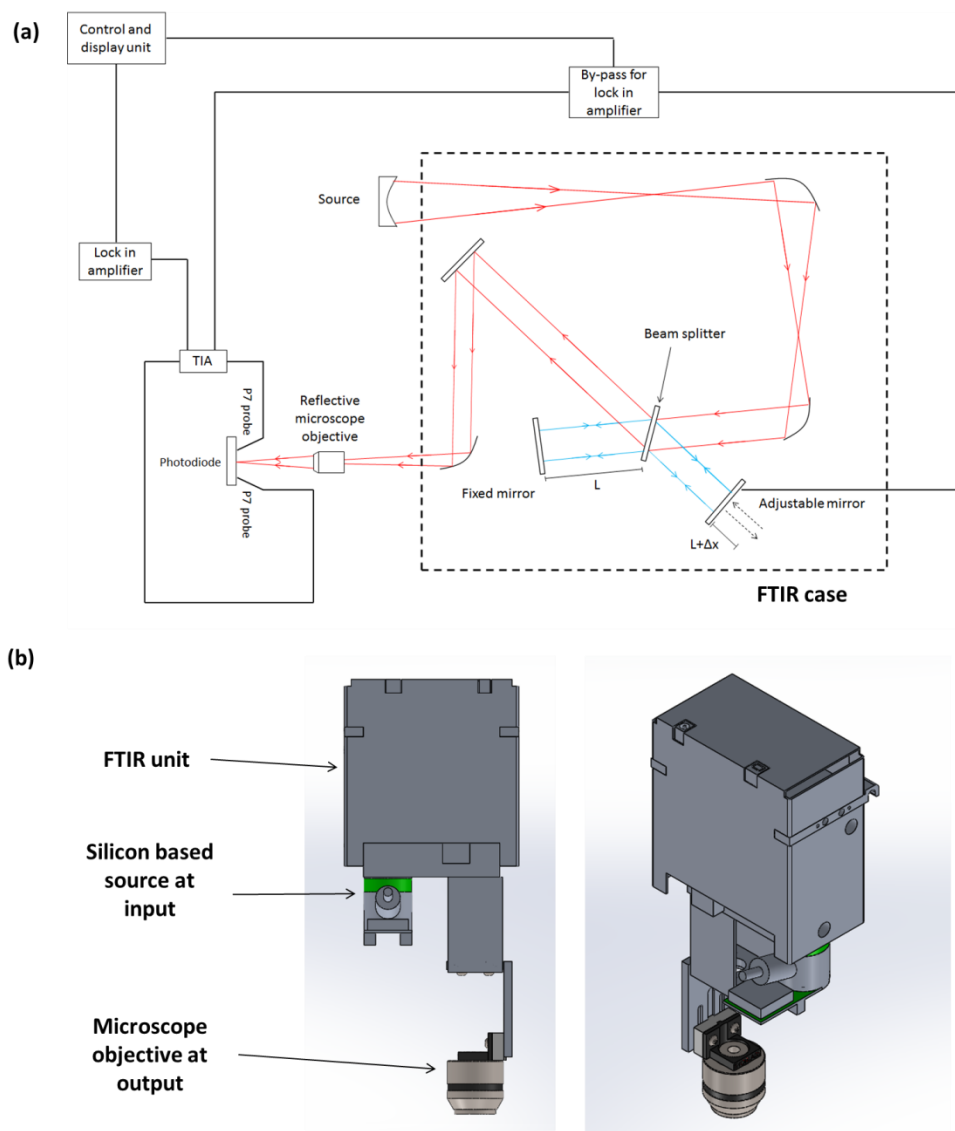
Figure 4.3.5.2: The FTIR spectrometer applied to NTA 2 device analysis. (a) Schematic diagram of the spectral response measurement set-up. (b) CAD based schematics showing details of the FTIR unit.

The probes themselves need to be soft and have suitable high conductivity so as to make the

equivalent circuit as efficient as possible. Thus, either gold or Paliney 7 (P7) probes are to be

used[93]. The photocurrent will be forwarded to the TIA using P7 contact probes. P7 probes are

made of a palladium alloy suitable for contact with gold contact pads. They retain a high degree of conductivity and ductility and minimise scratches on the contact pads.

The lock-in amplifier will specify the amplification to be applied to the signal and what the internal TIA resistance will be as function of this. If the resistance is to remain at the minimum, i.e. 50 ohms, then the signal amplification can only go up the 1000x. The spectral response is recorded as a function of mirror position and therefore the wavelength of the stimulating light.

4.4) Antenna materials

A variety of metals were considered for the antennas. Aluminium is brittle and lifts off very well at this stage and because its dielectrics are only marginally poor than gold, it has been used. Gold is much softer and requires a much more vigorous ultra-sonic vibrational lift-off. Gold has also demonstrated a tendency to sink into the antenna cavities if not immediately removed. There have been occasions where gold has been entirely and successfully removed, but that requires either growing the antennas very thin making the antenna pitch very large or using a lift-off vibration frequency that risks damaging or even shattering the substrate. This poses a problem when trying to find a process flow that can reliably and consistently make reproducible micro-antenna arrays. It is noted that aluminium is not the most conductive metal that can be used for this application. However, it is cheap, brittle and only accounts for a 1.2% increase in antenna absorption (see TABLE 3.9). It was for these reasons that aluminium antenna analysis for the NTA 2 mask was chosen. The annuluses and contact pads

were large enough to float off easily and therefore remained as Au with a thin layer of Ti for adhesion. Figures 4.41 and 4.4.2 show the lift of examples of gold and aluminium respectfully as well as the relative ease of using aluminium as the antenna material.
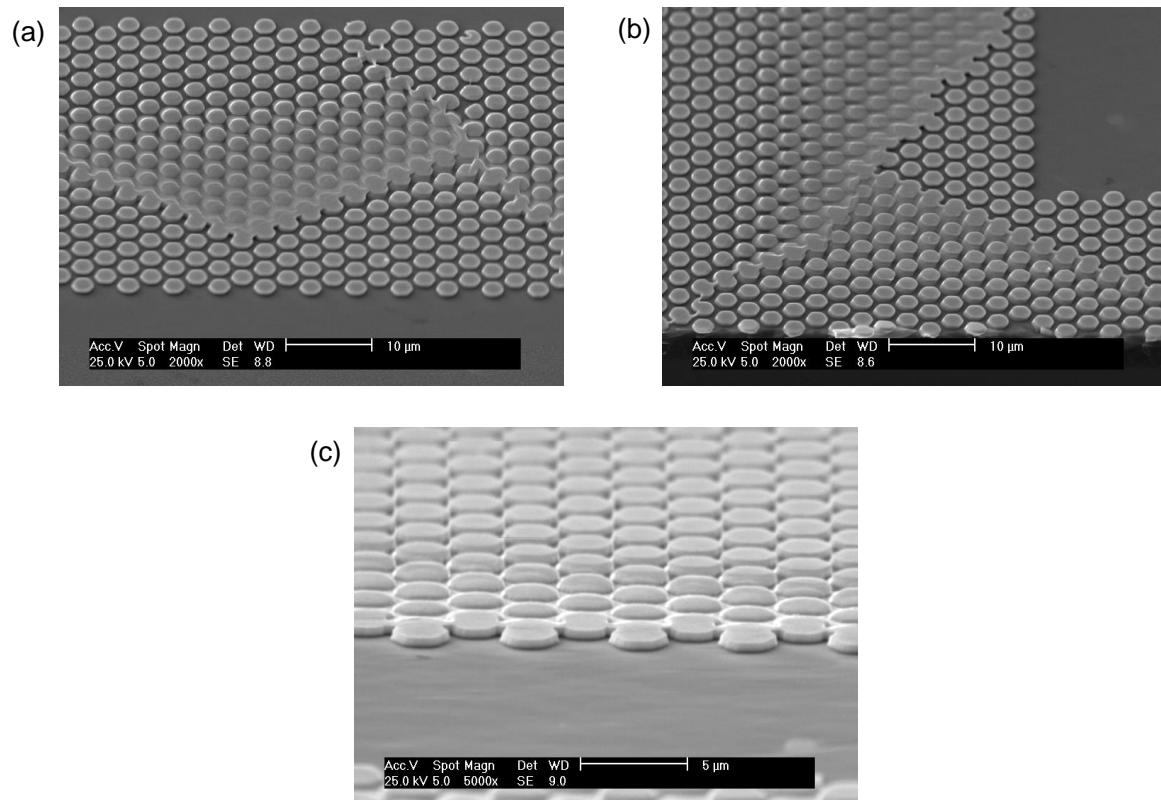
Figure 4.4.1: NTA 2 antenna lift-off using Au. (a) and (b) show areas of unsuccessful Au lift-off. (c) shows how the remaining Au has sunk into the cavities making this micro-antenna array unsalvageable.
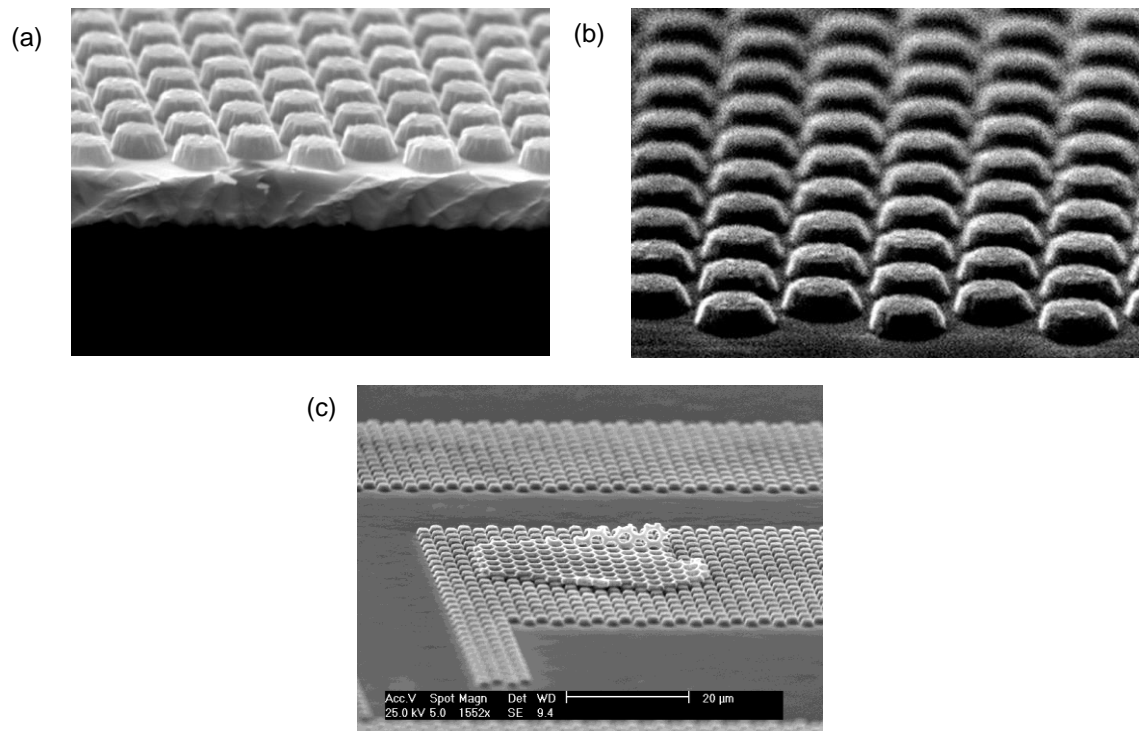
Figure 4.4.2: NTA 2 antenna lift-off using Al. (a) Al antenna array lift-off when t = 950 nm, w_H= 1.0 µm, w_A= 0.7 µm (b) Successful Al antenna array lift-off when t=750 nm, w_H= 1.0 µm, w_A= 0.7 µm (c) an example of unsuccessful lift-off when the aluminium is not sinking into the cavities.

4.5) Equipment and suppliers

Section: 4.2

Equipment: Hydrofluoric acid, Nitric acid, AZ 726 MIF developer, AZ 9260 resist, Primer H.M.D.S, AZ 5214E Image Reversal Resist

Supplier: MicroChemicals

Section: 4.2

Equipment: Microposit MF 319 developer, Microposit S1818 resist, PMGI SF11 resist

Supplier: A-Gas

Section: 4.1

Equipment: MBE growth chamber

Supplier: Veeco Gen II

Section: 4.2

Equipment: Resist spin coater

Supplier: Laurell Technologies
Corporation

Section: 4.2

Equipment: Profilometer

Supplier: Ambios Technology

Section: 4.2

Equipment: Evaporator

Supplier: Scientific Vacuum Systems Ltd

Section: 4.3.3

Equipment: Autoprober, Probe needles

Supplier: Wentworth Laboratories

Section: 4.3.5

Equipment: Agilent B1500A
Semiconductor device

Supplier: Agilent Technologies

Section: 4.3.5

Equipment: FTIR unit

Supplier: ARCoptix

Section: 4.2

Equipment: Lactic acid

Supplier: VWR

Section: 4.3.1 and 4.3.3

Equipment: Mask aligner

Supplier: SUSS Microtech

Section: 4.3.2 and 4.3.4

Equipment: Propanol and Acetone

Supplier: Fischer Scientific

Section: 4.3.4 and 4.3.4

Equipment: Au, Al, Ag, Cu, Ti, Cr source
metal
Supplier: Pi-Kem

Section: 4.3.5

Equipment: Transimpedance amplifier

Supplier: Zurich instruments

Section: 4.3.5

Equipment: Reflective microscope
objective

Supplier: Thor Labs

Section: 5.1

Equipment: FTIR spectrometer

Supplier: Bruker

4.6) Chapter 4 conclusion

The fabrication procedures concerning semiconductor epitaxial layer growth and micro-antenna fabrication are detailed in this chapter. The semiconductor growth technique that was chosen was molecular beam epitaxy (MBE) from layer thickness control and precision.

Photolithography is the method used to deposit micro-antennas on the surface with the intent of localised incoming radiation. Initial development involved reproducing the semiconductor photodetectors to assess minority carrier generation.

NTA 1 is the prototype that consists of one chromium mask. Its purpose is to assess the virtues of micro-antenna arrays by monitoring the reduction in surface reflectivity. The next design (NTA 2) is a more convoluted photolithography development procedure that verifies whether the incoming radiation is being redirected to the intrinsic layer. The development procedure involves a variety of different resists for different development steps, started with the micro-antenna growth, continuing with the mesa development and finishing with the metal contact pads that are used to assess the change in forward bias applied to the device.

The pitch of the antenna arrays is of the order of 2 microns and as such there has been considerable difficulty using soft or ductile materials like gold. Aluminium is suitably brittle at this pitch but there is still an antenna side wall gradient which will likely impact the results. Analysis for this is include in chapter 5 along with the other results quantifying how much the signal-to-noise ratio can be enhanced with the design discussed in chapter 4.

5) Chapter 5: Experimental results

In this chapter, the devices discussed in chapter 4 are fabricated, measured and compared to the theoretical simulations discussed in chapter 3. The experimental work has involved three mask set designs and thorough analysis of the 5%AlInSb control (no antennas). The standard semiconductor photodiode mask set (see section 4.2) has perimeter to area (P/A) structures designed to experimentally address the minority carrier generation problem for thin epitaxial layers. The NTA 1 antenna design prototype is composed of a single mask set that was to put down antenna arrays onto 5%AlInSb and to verify antenna resonance and antireflection at the considered pitch of the antenna arrays. NTA 2 is an improved mask set design which features different size mesas, contact pads to assess antenna influenced improvements in the signal-to-noise (S/N) ratio. In order to insure the CEM simulations are as accurate as possible, a hybrid simulation is introduced by integrating the dielectric properties of 5%AlInSb as well as taking into account any mechanical defects during experimental analysis. Although there are aspects of this work that are applicable to enhanced LED emission, these devices were fabricated to address the photodiode enhanced response.

5.1) The dielectric properties of $Al_{0.05}In_{0.95}Sb$

Introducing aluminium into the chemical composition of the semiconductor is necessary to insure that the response bandwidth of the semiconductor includes the 3.3 µm (90.8 THz) and 4.2 µm (71.3 THz) targets.

Altering the band gap of the semiconductor material will change the attenuation constant[94].

$$K = A\left(hv - E_G\right)^{\frac{1}{2}} \qquad\qquad\qquad (5.1.1)$$

Where K is the attenuation coefficient, v is the frequency, E_G is the energy gap and A is the absorption coefficient given as;

$$A \approx 3.38 \times 10^7 n^{-1} (m_e / m_0)^{\frac{1}{2}} (E_G / hv) \tag{5.1.2}$$

Where m_e is the conduction band electron mass, n is the refractive index and m_0 is the rest electron mass. The electron mass changes as a function of energy. When using $Al_{0.05}In_{0.95}Sb$, it gives a value of $m_e = 0.0116 \, m_0$. This in turn gives a value of A that has increased by a factor of 1.87 compared with InSb. The consequent 1D attenuation coefficient is shown in figure 5.1.1.
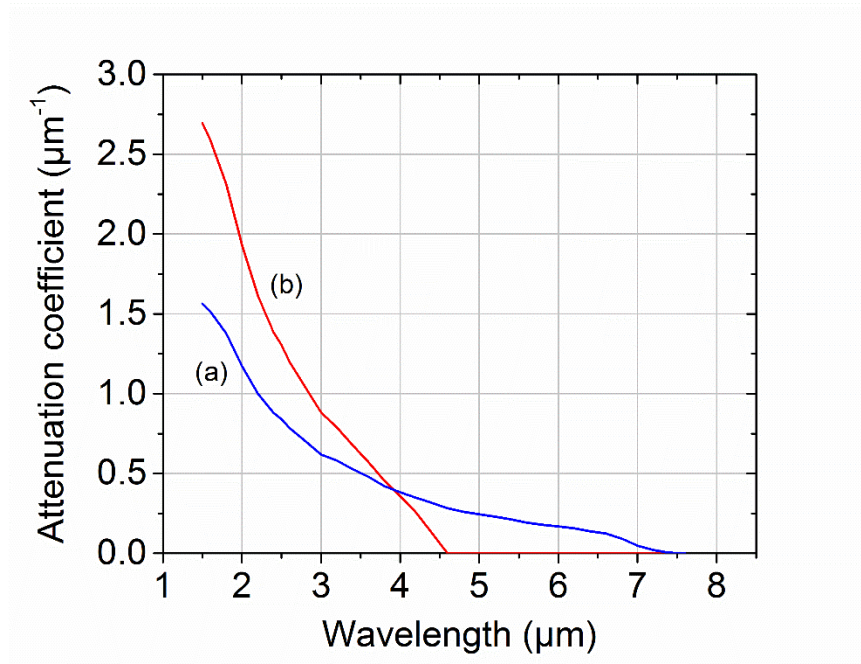
Figure: 5.1.1: The attenuation coefficient for different compositions of Al in InSb. (a) Documented attenuation coefficient data vs. wavelength for InSb (blue line) (b) Derived attenuation coefficient data vs. wavelength for $Al_{0.05}In_{0.95}Sb$ based on equation 5.1.1 (red line).

In this derivation, it was noted that the results are accurate to within a 50% accuracy. To ensure that these results are as accurate as possible for simulations, these attenuation readings are also determined experimentally by measuring the transmission through a 5.35 μm thick

semiconductor layer composition on a 600 µm thick GaAs substrate. This was done using a Brucker FTIR spectrometer[95].

The detector is a liquid nitrogen cooled Cadmium Mercury Telluride (CMT) photodetector. It operates between 420 cm^{-1} and 5000 cm^{-1} in wavenumbers or between 2 µm and 23.5µm in wavelength. The schematics for the instrument are shown in figure 5.1.2.
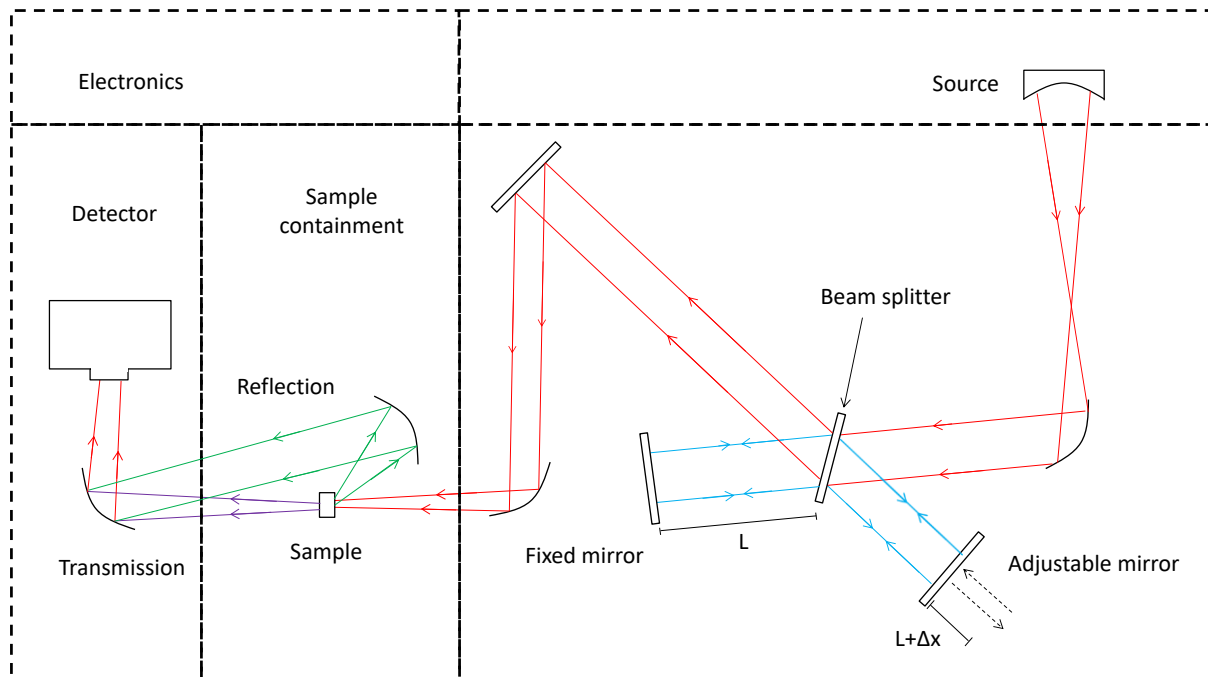
Figure 5.1.2: The different components in the FTIR spectrometer. The sample is held in the sample containment unit and the atmosphere is extracted so that the pressure inside the device is about 15 hPa (Hecto Pascals) during testing. The mirrors that redirect light to the detector can either be set up to measure the material transmissivity (purple arrows) or the reflectivity (green arrows).

The fixed mirror is distance L away from the beam splitter. The adjustable mirror is distance L+Δx away from the beam splitter. This means that the total path difference between these two mirrors, and consequently the two light waves is 2Δx. Therefore, the two light beams will interfere constructively and produce the maximum detectable interferogram signal when the path difference is a factor of the wavelength as shown in equation 5.1.3:

$$2 \cdot \Delta x = n \cdot \lambda \tag{5.1.3}$$

The relationship between the path difference and the signal intensity can be described in equation 5.1.4:

$$I(\Delta x) = S(v) \cdot \cos(2\pi \cdot v \cdot \Delta x) \qquad\qquad (5.1.4)$$

Where S is the intensity of the monochromatic source at frequency v and I is the intensity received at the detector. Upon reaching the detector, the beam of light will be focused in the centre so the signal will be maximised. This will produce concentric circles of decreasing intensity the further away the circles are from the centre i.e. when the optical path difference increases. In 2D, this creates an interferogram. An example of which is given in Figure 5.1.3:
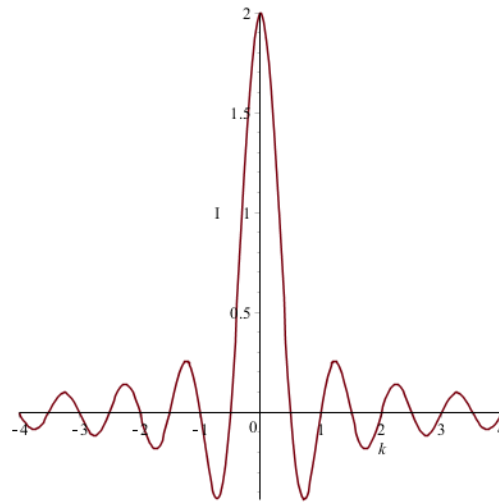
Figure 5.1.3: An example of an interferogram with large irregularities at its sides. $I(k)$ is the signal strength and k is the signal Optical path difference. This graph was produced in Maple 16.

The interferogram has a peak signal (the central burst) at the centre and the smaller oscillations at the sides are different harmonic oscillations that make the central burst less clear. Apodizations are a common practise in FTIR analysis[96]. They are used to minimise the effects of these leaky edges by applying an apodization function $A(x)$ so as to compute a revised signal $I(k)$ with dampened side lobes using the Fourier cosine transformation within the specified boundary conditions, a and $-a$.

$$I(k) = \int_{-a}^{a} \cos(2 \cdot \pi \cdot k \cdot x) \cdot A(x) dx \qquad\qquad (5.1.5)$$

An example of an apodization function is given below as Conne's function.

$$A(x) = \left(1 - \frac{x^2}{a^2}\right)^2 \qquad (5.1.6)$$

Substituting equation 5.1.6 into equation 5.1.5 gives:

$$I(k) = -\frac{6\pi ka \cdot \cos(\pi ka)^2 - 3\pi ka \cdot \cos(\pi ka) + 4\pi^2 k^2 a^2 \sin(\pi ka)\cos(\pi ka) - 3\sin(\pi ka)\cos(\pi ka)}{\pi^5 k^5 a^4}$$

(5.1.7)

The effect of the apodization function is that it will dampen the signal, but it will also dampen the side lobes to a more significant degree. This makes signal more clear and discrete.
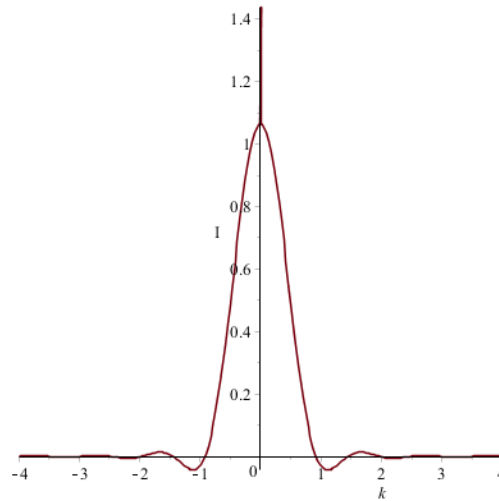
Figure 5.1.4: Figure 5.1.3 after Conne's apodization function is applied. *I(k)* is the signal strength and *k* is the signal Optical path difference. This graph was produced in Maple 16.

The results are given in terms of the reflectivity measurements and the transmissivity measurements. The transmissivity measurements are what are needed to derive experimental results shown in figure 5.1.5.
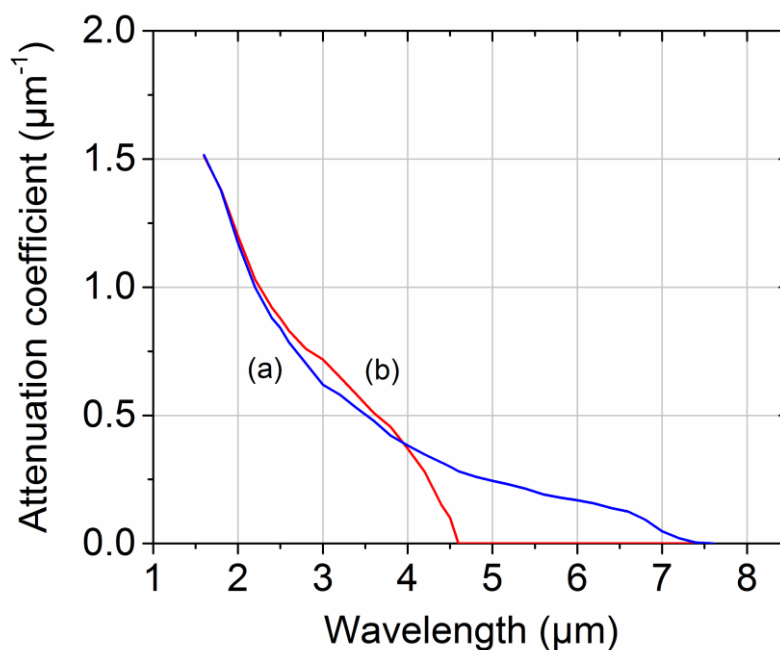
Figure 5.1.5: Measured modifications for figure 5.1.1. (a) Documented attenuation coefficient data vs. wavelength for InSb (blue line). (b) Measured attenuation coefficient for $Al_{0.05}In_{0.95}Sb$ (red line). This data was used to parameterise the simulator.

The practical results in figure 5.1.5 were used over the theoretical results in figure 5.1.1 on the grounds that the theoretical calculations are documented as approximations.

The electromagnetic simulator used to model this data (CST^{TM}) requires data of the real and imaginary dielectric constants if accuracy is to be extracted. The dielectric data can be derived from the relationship between the dielectric properties are the material refractive index and attenuation coefficient (see section 3.6)[75,76].

The method of 5%AlInSb dielectric parameterisation assumed the measured refractive index ($n = 4$) static and identical to InSb at wavelengths of interest between 1.5µm to 6 µm. This assumption is made on the grounds that there is a slow change in refractive index with energy band gap. The derivations are summarised in TABLE 5.1

TABLE 5.1: The derivations of the real and imaginary components of the Al$_{0.05}$In$_{0.95}$Sb dielectric constant from measured attenuation coefficient data.

Wavelength (μm)	Frequency (THz)	α (m⁻¹)	k	ε	n	ε'	ε''	tan δ
1.50	200	2.69E+06	0.32	16	4	15.90	2.571	0.16
1.80	166.55	2.31E+06	0.33	16	4	15.89	2.650	0.17
2.00	150	1.93E+06	0.31	16	4	15.91	2.460	0.15
2.50	120	1.22E+06	0.24	16	4	15.94	1.936	0.12
2.80	107	1.31E+06	0.29	16	4	15.92	2.330	0.15
3.00	100	8.81E+05	0.21	16	4	15.96	1.682	0.11
3.20	93.68	7.89E+05	0.20	16	4	15.96	1.607	0.10
3.80	78.89	4.55E+05	0.14	16	4	15.98	1.100	0.07
4.20	71.3	2.57E+05	0.09	16	4	15.99	0.687	0.04
4.40	68.13	1.27E+05	0.04	16	4	16.00	0.357	0.02

Figure 5.1.6 shows the results from a hybrid CST^{TM} generated model that uses the information in TABLE 5.1.6 to solve the power absorbed in the root volume of the i-type as a function of i-type thickness. The root volume is used here to relate this data back to the detectivity and its inverse proportionality to the root volume (see equation 3.1.5).
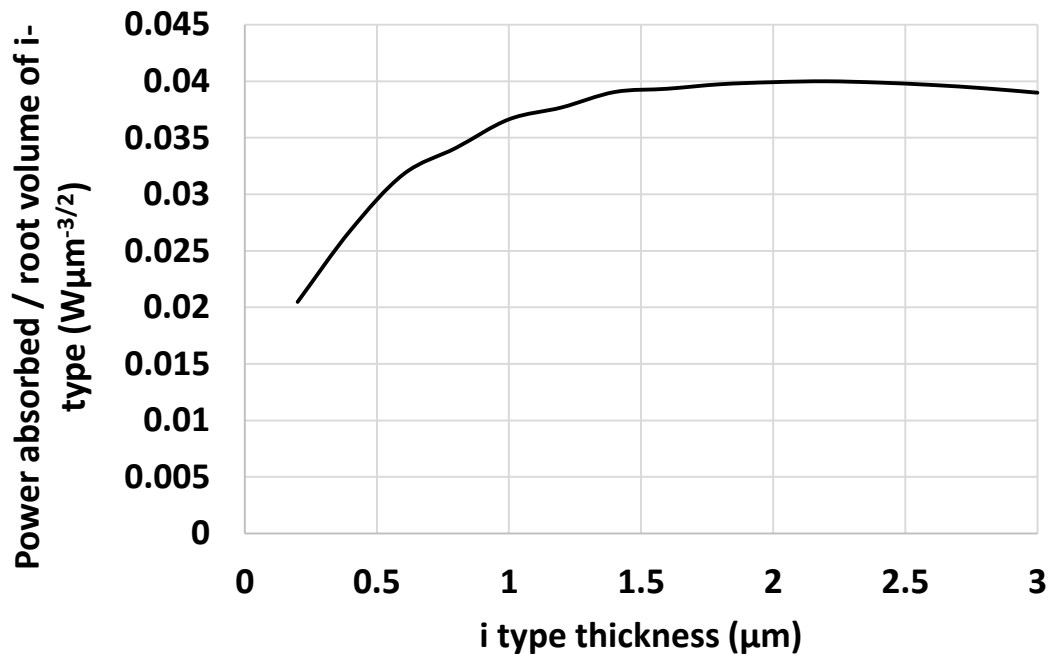
Figure 5.1.6: Simulated power absorbed in the i-type over the root volume of the i-type as a function of i-type thickness at 90.8 THz. The p-type thickness id 0.12 μ and the n-type thickness is 5 μm.

In the interest of pursuing an optimum signal the noise (S/N) ratio, semiconductor i-types are grown to a thickness of 2.5 μm - 3 μm. The data in figure 5.1.7 shows that the optimum

thickness is at 2.2 µm but that is a discrepancy based on the frequency being 90.8 THz. Lower frequencies will have a lower attenuation coefficient which will make the optimum thickness larger. It is noted that thinning down the i-type for waveguide manipulation will produce sub optimal i-type absorption. This is taken into account for chapters when the optimum possible design is addressed. However, for the purposes of chapter 5, the semiconductor p-type and i-type was requested to be as thin as possible (0.12 µm and 0.5 µm respectively) to better complement our efforts towards i-type focusing near the surface.

5.2) NTA 1 results analysis

As discussed in section 4.3.1, NTA 1 is a simple prototype design consisting of an array of micro-antennas of various sizes implemented of top of a layer of $Al_{0.05}In_{0.95}Sb$, 0.5 µm in thickness. It is used to provide a general indication that a reduction in reflectivity and a noticeable difference in transmissivity through the device at certain frequencies correlates to antenna resonance. These variations in transmissivity and reflectivity are recorded using the same Brucker FTIR spectrometer[95] described in section 5.1.

This section will make references back to figure 4.3.1.4 because that figure has information about where on the wafer the antennas were grown and what size and shape they are. Figure 4.3.1.4 has therefore been duplicated here for the reader's convenience. The numbers on the far left column of figure 5.2.1 (b) are referred to in this section as the feature sizes (FSs).

(a)

(b)

No.	Shape	l (μm)	w_H (μm)	w_A (μm)	x-axis pitch (μm)	y-axis pitch (μm)
1	Control (no antenna)	n/a	n/a	n/a	n/a	n/a
2	Hex	2.6	1.50	0.75	5.80	3.35
3	Hex	1.73	1.00	0.75	4.30	2.48
4	Hex	5.20	3.00	0.75	10.30	5.95
5	Hex	2.60	1.50	1.50	7.10	4.10
6	Hex	1.73	1.00	1.50	5.60	3.23
7	Hex	5.20	3.00	1.50	11.60	6.70
8	Hex	2.60	1.50	3.00	9.70	5.60
9	Hex	1.73	1.00	3.00	8.20	4.73
10	Hex	5.20	3.00	3.00	14.20	8.20
11	Squ	2.50	n/a	1.50	4.00	4.00

Figure 5.2.1: NTA 1 shape, size and positioning. (a) L-edit wafer map. (b) The conducting length (l), the hexagonal width (w) and aperture width (w_A) information for the individual antenna array. The numbers given in green co-respond to the antenna shapes, size and spacing given in Table 5.2.1 (b). The numbers given in red are the location indices located in the top left hand corner of each field. The location indices are arranged so that the y-axis number is first and the x-axis number is second.

Note: The reflectivity and transmissivity measurements are arbitrary and only have meaning when compared to one another.

(a)

Measured feature size 2

Legend:
- FS 2 F 46 refl
- FS 2 F 71 refl
- FS 2 F 97 refl
- FS 2 F 78 refl
- FS 2 F 46 refl
- FS 2 F 71 refl
- FS 2 F 97 refl
- FS 2 F 78 refl
- Control refl

(b)

Measured feature size 2

Legend:
- FS 2 F 46 trans
- FS 2 F 71 trans
- FS 2 F 97 trans
- FS 2 F 78 trans
- FS 2 F 46 trans
- FS 2 F 71 trans
- FS 2 F 97 trans
- FS 2 F 78 trans
- Control trans

Figure 5.2.2: The change in a) reflectivity and b) transmissivity of the antenna feature size 2 at different points of the wafer over a wavelength range of 2 µm - 6 µm (50 THz – 150 THz) compared to the control (no antennas). The FS (feature size) number refers to the feature parameters specified in figure 5.2.1 (b). The F (field) number refers to the place the antenna structures where grown on the mesa relative to the wafer centre. The thickness of these antennas (Au and Cr) is 0.75 µm.

The degree of reflectivity and transmissivity compared to the control (no antennas) for one of the smaller hexagonal structure (FS 2) are shown the figure 5.2.1 (a) and figure 5.2.2 (b) respectively. The antenna quality as a function of wafer position appears to be random, seeing as the two samples on the edge of the wafer produce the best reflectivity trough as well as the worse reflectivity trough. They have a consistent trough position at 3.7 microns. Based on the dipole rule this is 0.5 µm removed from the target wavelength that was intended for (4.2 µm). This is due to the side wall gradients that were discovered during SEM scans of these antenna arrays (see figure 4.3.1.2). These side walls retune the antennas to smaller wavelengths and lessen the antenna quality factor. For more details see section 5.3. If the side gradients are consistent, it is recommended that the hexagonal width is increased from 1.5 µm to 1.8 µm to re-align the reflectivity trough to the 4.2 µm target.

What could explain the variation in reflectivity quality for different samples is the fact that the lesser troughs have a wider bandwidth response. It might be evidence of an angle of incidence that is undesirably large, which can cause the array incorporate a broader frequency range (see figure 5.3.6). However, this was decided to be unlikely, after determining that a wavelength shift of 0.3 µm would mean that the angle of incident was about 20 degrees from the normal and even then it would shift the peak the a lesser wavelength, not a greater one.

It is therefore difficult to determine what causes these variations. It is none-the-less noted for future results to see if there is consistency.

The degree transmissivity shows a peak is at about 4.0 µm - 0.3 µm removed from the recorded reflectivity trough (Another out-of-the-ordinary feature). It is noted that the best reflectivity result also produces the least amount of transmissivity. An encouraging indication that the radiation is being redirected at an angle within the $Al_{0.05}In_{0.95}Sb$.
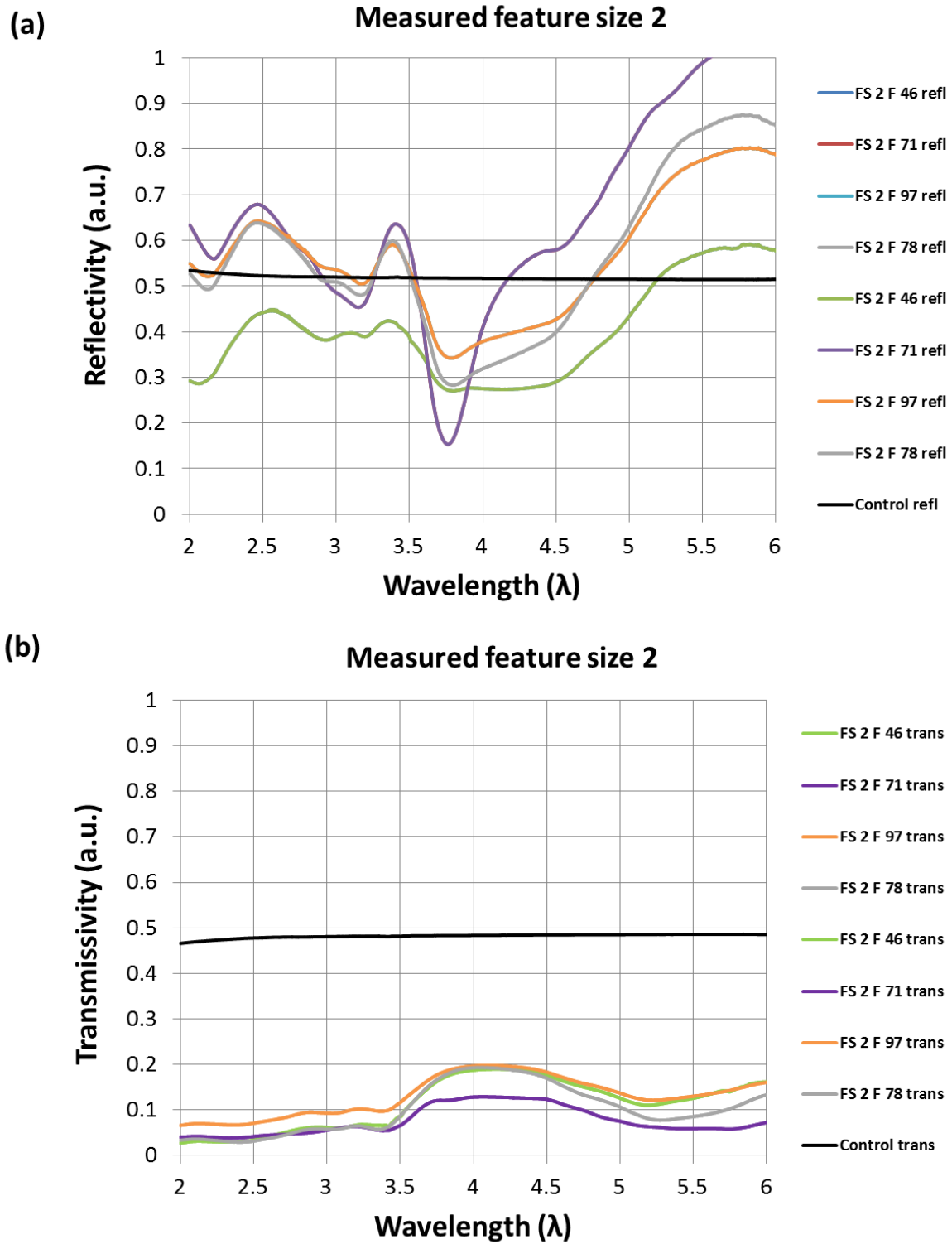
(a)

(b)
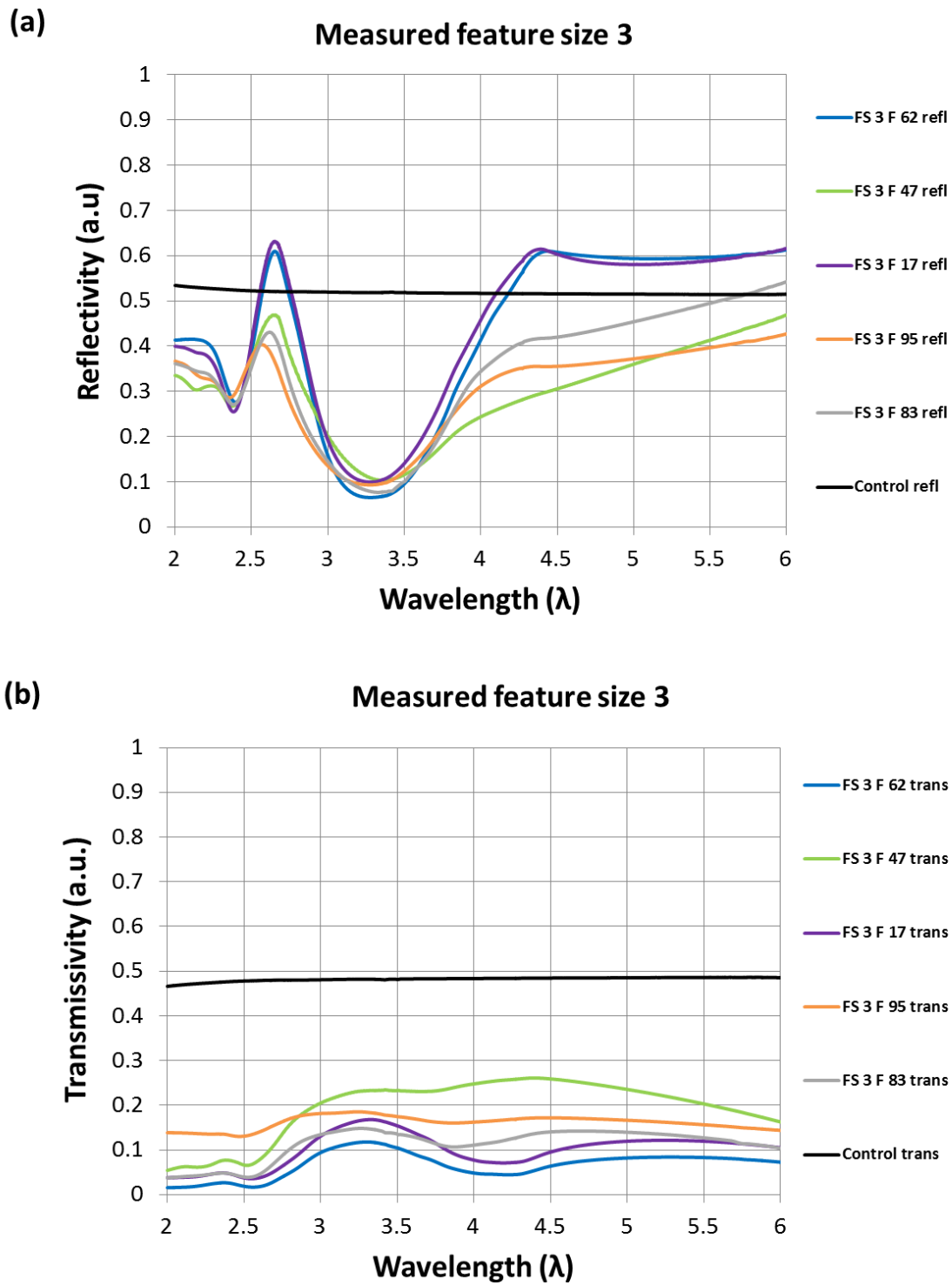
Figure 5.2.3: The change in a) reflectivity and b) transmissivity of the antenna feature size 3 at different points of the wafer over a wavelength range of 2 µm - 6 µm (50 THz – 150 THz) compared to the control (no antennas). The FS (feature size) number refers to the feature parameters specified in figure 5.2.1 (b). The F (field) number refers to the place the antenna structures where grown on the mesa relative to the wafer centre. The thickness of these antennas (Au and Cr) is 0.75 µm.

Feature size 3 shown in figure 5.2.3 show much more consistency in the reflectivity data with the best graphs being produced at the edge of the wafer, with the exception of the field 95. Field 95 is in a similar position to field 97 of FS 2. This could indicate something sub-par about that region of the wafer.

The bandwidth is wider than the best reflectivity graph of FS 2. Analysis has indicated that an improvement in antenna quality factor can lessen the bandwidth of the spectral response (see figure 5.3.4), but it should also shift the trough to a higher wavelength, thus suggesting that some arrays developed better than others.

The degree of reflectivity in FS 3 is generally much better than the reflectivity of FS 2. The aperture widths are kept the same for both of these different sizes which support equations 10 and 11 in figure 3.6.1 which state that there is a uniquely optimum aperture width for a certain wavelength response and FS 3 is closer to optimum resonance conditions.

The transmissivity peaks are much more aligned with the reflectivity troughs except for the graphs that are generally poorer quality. This indicates that the antenna arrays in all fields work but there is a degree of quality management that are related to wafer position if the antennas are to successfully filter out unwanted frequencies.

Within the prototype, the most successful graphs for each of feature sizes are summarised in figure 5.2.4. The red graphs are the measured reflectivity across the spectrum for the antenna array and the black graphs are the reflectivity measurements for the control (i.e. no antennas).
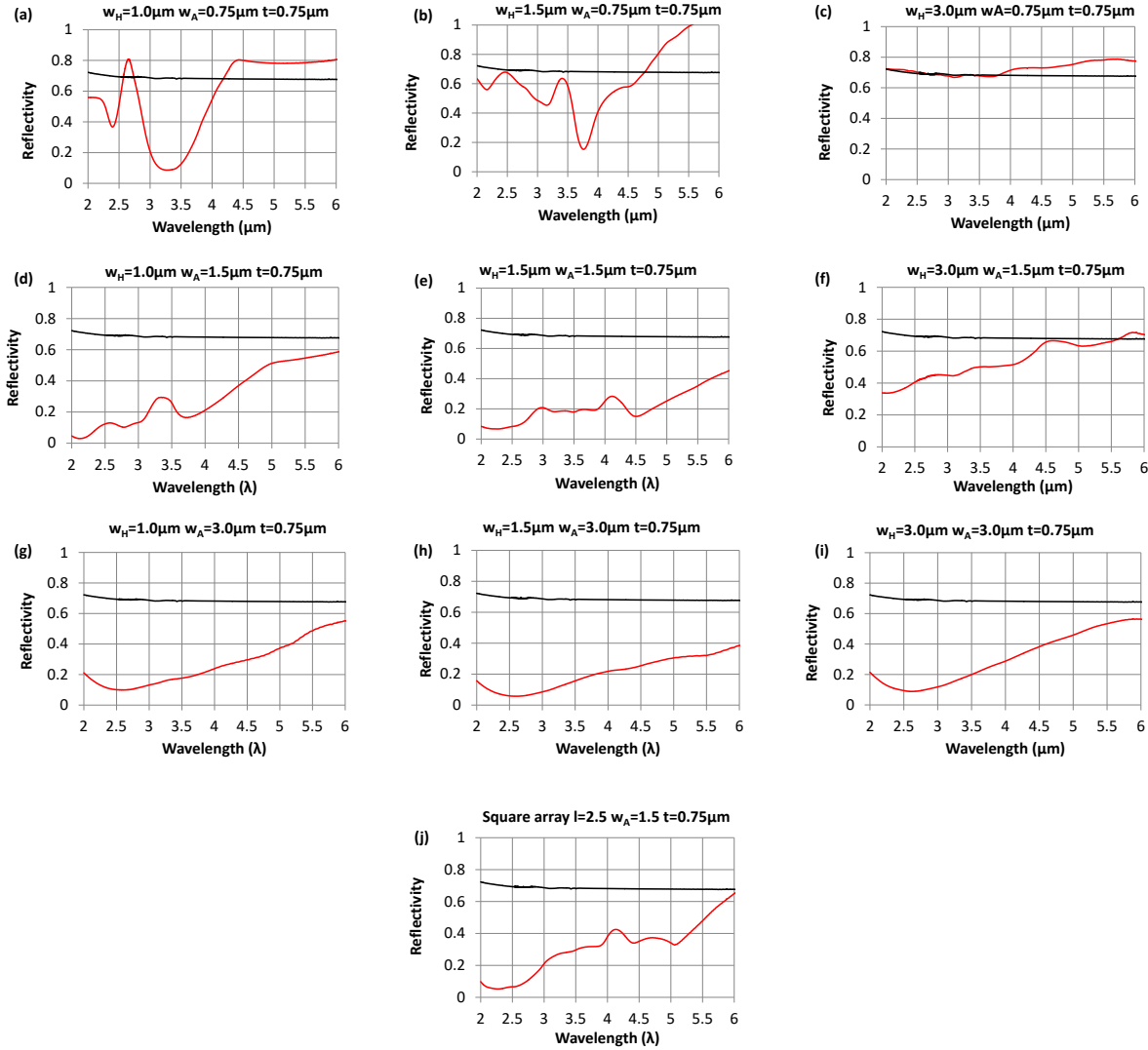
Figure 5.2.4: The average reflectivity measurements across a 2µm to 6µm wavelength range (50 THz – 150 THz) for the NTA 1 micro-antennas arrays (red graphs) and the control (black graphs). The antennas (Au and Cr) are grown 0.75 µm thick. The antenna width and thickness specifications are in the graph titles.

Figure 5.2.4 shows the progression from when an array acts like a resonating antenna to where the reflectivity is reduced based on aperture size. Graphs (a) and (b) are samples demonstrating a resonating response due to shaper peaks and a strong dependency on the antenna geometry. Graphs (g), (h) and (i) are samples demonstrating the trough positions reliance on an aperture width of 3.0 µm and not the antenna geometry. Graphs (d), (e), (f) and (j) also have a reliance on the aperture width with the reflectivity trough shifted to a lower wavelength than the larger aperture with. The square antenna (j) has a similar reflectivity

response to the hexagonal structure with a similar conducting length (e) showing that this experiment is not overly reliant on the shapes being hexagonal in particular. Graph (c) has an antenna array that resonates at higher wavelengths outside the measured spectrum and the aperture width will show a reflectivity trough at much smaller wavelengths.

Although the bandwidths for the aperture width dependant graphs are considerably much larger than the graphs based on antenna resonance, they still provide an indication that successful reduction in reflectivity is achievable if the surface is corrugated to the right pitch.
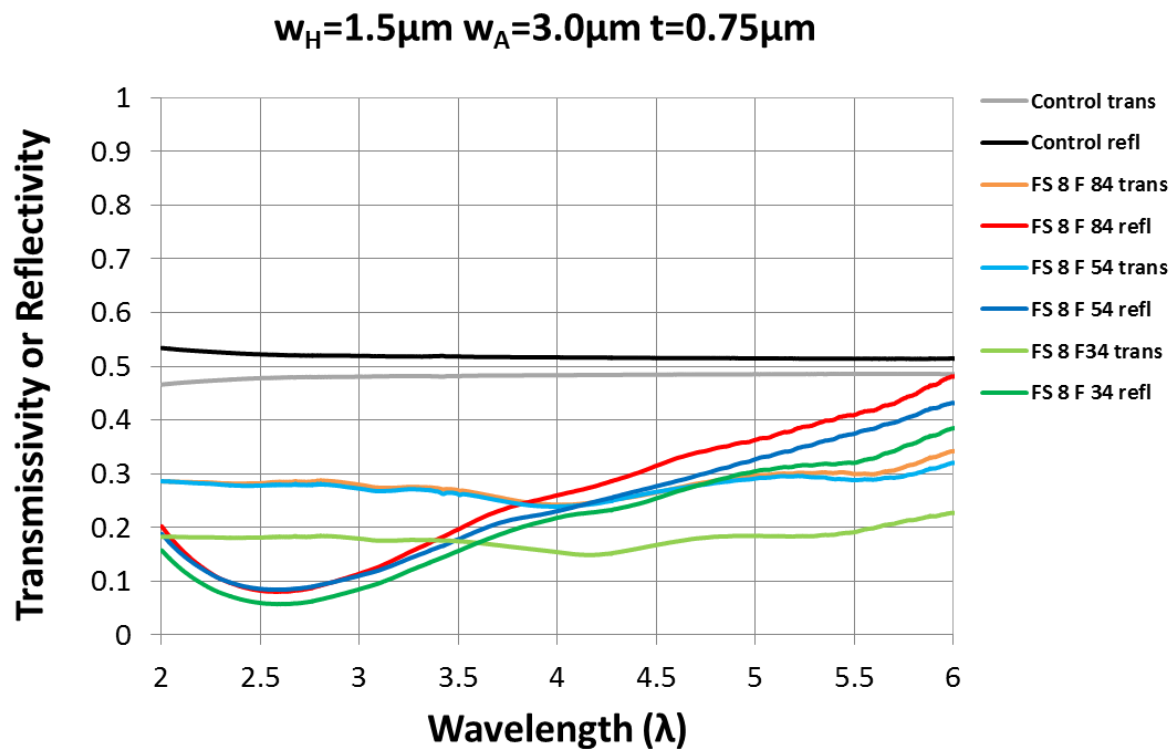
Figure 5.2.5: The change in a) reflectivity and b) transmissivity of the antenna feature size 8 at different points of the wafer over a wavelength range of 2 μm - 6 μm (50 THz – 150 THz) compared to the control (no antennas). The FS (feature size) number refers to the feature parameters specified in figure 5.2.1 (b). The F (field) number refers to the place the antenna structures where grown on the mesa relative to the wafer centre. The thickness of these antennas (Au and Cr) is 0.75 μm.

As shown in figure 5.2.5, the transmissivity peaks are not as well defined as the resonant dependant antennas and since the transmissivity graphs are of a similar shaper in FS 4 to FS

11, the wavelength filtering capabilities of these devices are questionable. Further investigation is warranted to quantify the difference.

The parameters in FS 2 were further analysed to investigate a reflectivity dependence on thickness to assess how easily the antennas can be tuned. The target for the changes in thickness was 4.2µm, i.e. the wavelength at which CH_4 and/or CO_2 will absorb. This target was met with antennas 1.5 µm in hexagonal width and 0.92 µm in thickness.
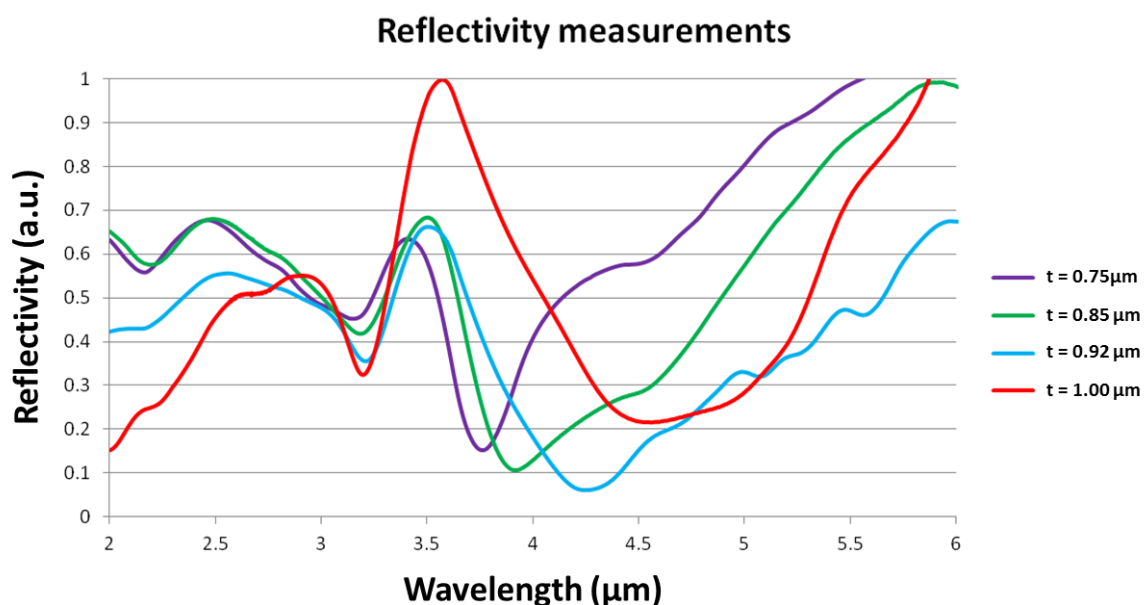
Figure 5.2.6: Reflectivity vs. wavelength as a function of the thickness of FS 2.

The thickness of the antennas depicted in figure 5.2.6 were programmed into a metal evaporator and verified with an SEM with a typical accuracy of ± 5 nm. The results support the antenna resonance theory and its linear dependence on antenna parameters (see figure 3.6.1, equation 1), but also demonstrate that antenna resonance lengths and aperture widths need to be optimised to achieve the minimum amount of reflectivity.

This section concludes that a micro-antenna array does reduce the reflectivity and cause a higher amount of incident energy to be absorbed in the substrate as a whole. However, this does not prove that the energy is necessarily being absorbed in the i-type region as it could

just be absorbed in the antenna array, which would mean that the antenna array is either blocking the incoming light or scattering the light in an undesirable direction. A second mask set was therefore designed to provide answers to this speculation (see section 5.5).

5.3) Side gradient analysis

After dissecting the samples and observing the development under a scanning electron microscope, it was discovered that the antennas had developed side gradients of approximately 70° - 75°. The images show that the spacing is also reduced. It is estimated that the enlarged bottom layer of the hexagon takes up approximately 30% of the total length changes introduced by the side gradient. A reduced top layer length accounts for the remaining 65% - 70% change in length. Thus indicating a pivot point about a third of the way up from the antenna base.
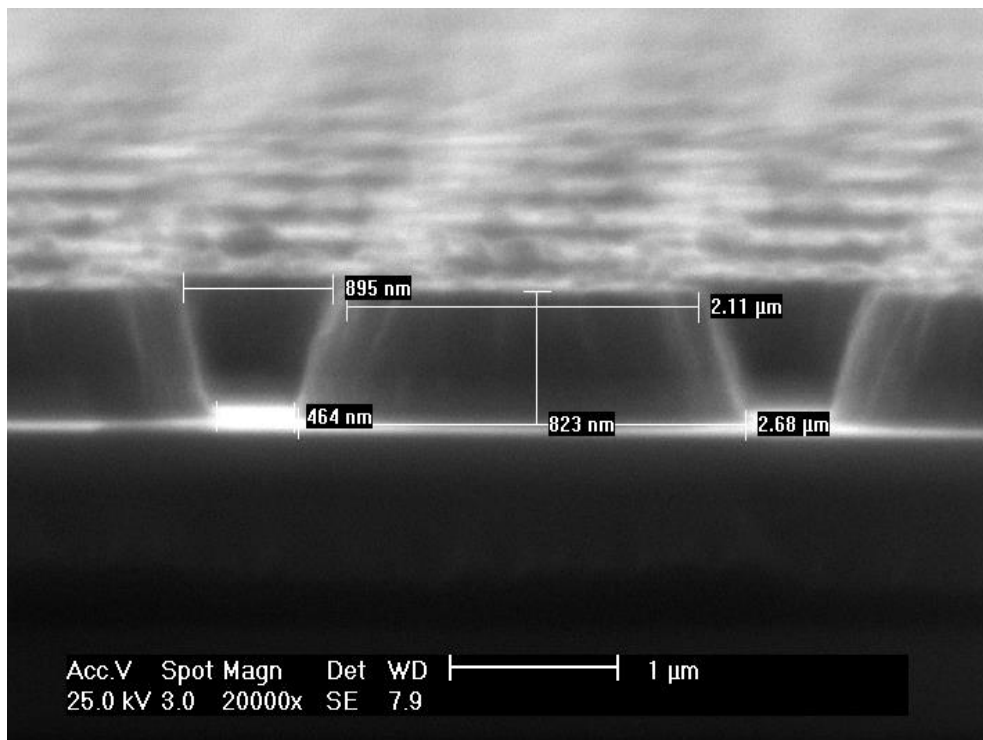
Figure 5.3.1: An SEM scan of the defects of NTA 1 FS 2 micro-antenna development. This is a replica of figure 4.3.1.2 (d).

The antenna arrays needed to be grown to compensate for shape imperfections by either enlarging the hexagonal width within a 1.5 µm hexagonal width minimum limit for 0.7 µm in aperture width, or enlarging the thickness up to 1.0µm. These revisions were incorporated into the figure 5.2.6 and yielded an agreement shown in figure 5.3.2.
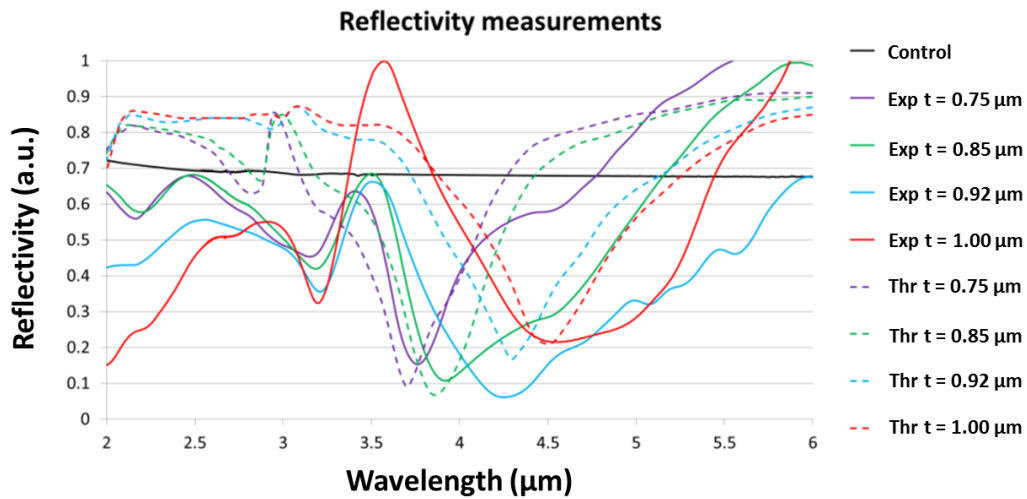
Figure 5.3.2: The comparison of the NTA 1 modelled results to experimental results (solid lines) after dielectric and side wall calibration in the model (dashed lines).

Further analysis of the detrimental effect of side-wall angle was conducted using CEM simulations. These results are intended for application to the final modified photodiode product that the NTA 2 mask set is designed to produce (see section 4.3.3).
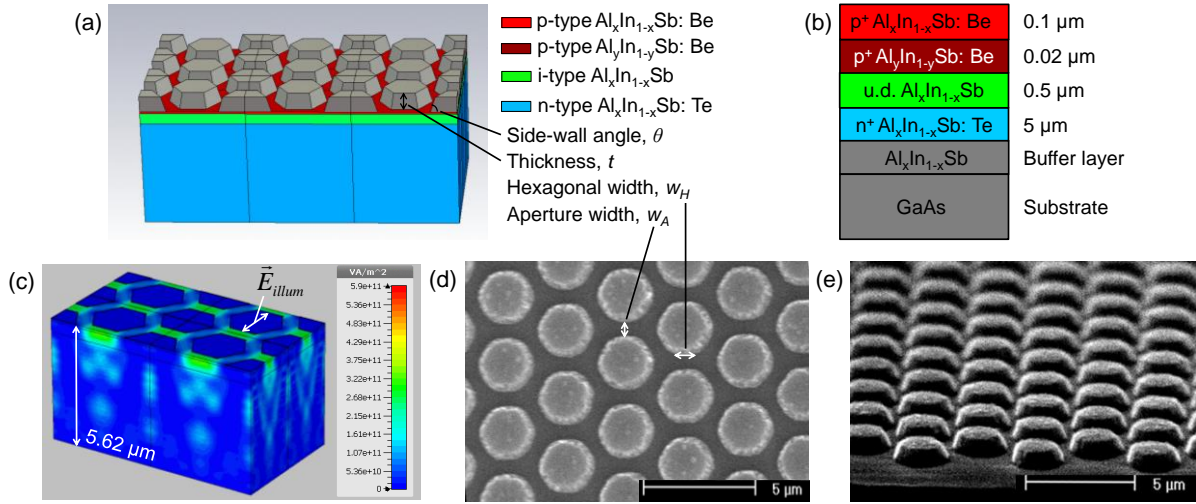
Figure 5.3.3: Side gradient experimental and modelling comparisons. a) Schematic diagram of modelled micro-antenna array with side gradient included. (b) Photodiode epitaxial layer structure for the NTA 2 design, where x = 0.05 and y = 0.20. (c) Schematic diagram illustrating energy flux density distribution within the semiconductor for an antenna array under uniform, polarised illumination. The amount of absorption in the 600µm thick GaAs wafer is less than 1% of the total incident power and was therefore excluded from the simulation to reduce computation time. (d) Plan view and (e) tilted SEM images of the experimental antenna array the model is based on, $t = 0.75$ µm, $w_H = 1.4$ µm and $w_A = 0.7$ µm.

Figure 5.3.3 (a) illustrates the necessary adjustments to the simulated antenna array if an accurate depiction of how the light is coupled into the semiconductor and how much is absorbed in the semiconductor i-type (highlighted in green in figure 5.3.3 (b)) is obtainable. These adjustments as well as the measured $Al_{0.05}In_{0.95}Sb$ attenuation coefficient derived in section 5.1, a hybrid model is created to not only enhance model accuracy, but also to provide context as to how much fabrication defects will alter the results.

With reference to benefits of heterostructures (see section 3.3) the simulation will incorporate a heterostructure barrier (given in dark red in figure in figure 5.3.3 (b)) within the standard epitaxial layers.

With reference to an enlarged base hexagonal width and a reduced aperture width as a consequence of these side wall defects, the term base hexagonal width and base aperture width are introduced where the remaining dimensions of the antennas can be derived if the side wall gradient is known.

Figure 5.3.4 shows two antenna designs are considered for this analysis. Design 1 (associated with a1 and b1) has an antenna thickness of 0.65 μm, a hexagonal width of 1.21 μm and an aperture width of 0.50 μm. It was chosen as a modelled antenna design to maximise the i-type power absorbed. The antennas will resonate at 3.3 μm with vertical (90°) side wall angles. Design 2 (associated with a2 and b2) has an antenna thickness of 0.75 μm and with a side wall angle of 73 degrees, has a base hexagonal width of 1.28 μm and a base aperture width of 0.56 μm. This is a design that more closely matches the numerous practical results taken.
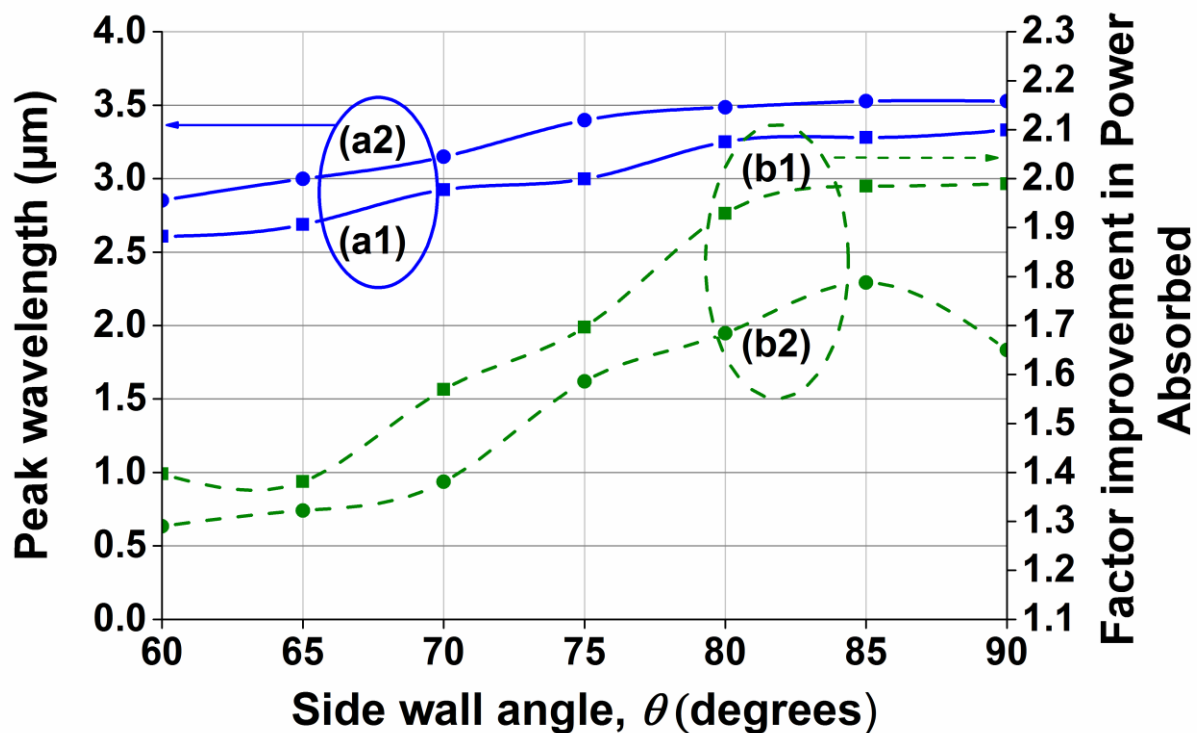
Figure 5.3.4: Simulated side-wall angle dependency of a) the peak wavelength (solid lines) and b) the factor improvement in the power absorbed at the peak wavelength relative to a device without micro-antennas (dashed lines). Micro-antenna design 1 (square markers) has a peak response at 3.3 μm with a vertical sidewall (w_H = 1.20 μm, w_A = 0.50 μm, t = 0.65 μm) whereas design 2 (circular markers) has a peak response at the same wavelength but with a 73° side-wall angle ($w_{H\ (base)}$ = 1.28 μm, $w_{A\ (base)}$ = 0.56 μm, t = 0.75 μm).

It can be seen that increasing the side-wall angle blue shifts the peak response and reduces the i-type absorption at the peak response wavelength. The comparison between design 1 and design 2 is meant to demonstrate how beneficial an antenna array can possibly be and how

much signal is lost when realistic development is considered. This data was taken from the modelling results and compared to practical results (wherever possible) to within an accuracy of 5%, similar to the data comparison in figure 5.5.

Under optimum conditions, the amount absorbed with the $Al_{0.05}In_{0.95}Sb$ is 92% where approximately 6% is absorbed in an aluminium antenna array (see TABLE 3.9). Just over a third of what gets absorbed in the $Al_{0.05}In_{0.95}Sb$ gets absorbed in the i-type layer (see figure 5.3.5). About three-quarters of the remainder is reflected or redirected away from the surface and the remaining quarter is absorbed by the 600μm GaAs wafer underneath.

Despite the fact that some of the incident light is dissipated in the antennas, the average power absorbed within the active region of a device (i.e. between a depth of 0.12 μm and 0.62 μm for the structure simulated here) with antenna design 1 has increased by a factor of 1.93 above that of the bare material and by a factor of 1.29 above that expected from the idealised AR coating (i.e. no surface reflections, no localised focusing). An amplification factor about 1.6 from design 2 is still an improvement to an AR coating, but until the development procedure can produce better side wall angle is the best these devices can do.

The absorption of each of the semiconductor layers and their dependence on incident trajectory angle for design 1 is shown in figure 5.3.5. Surface reflectivity starts to decrease after 20 degrees making this unable to compete with AR coating in terms of trajectory angle. Note: the system is the entire device.
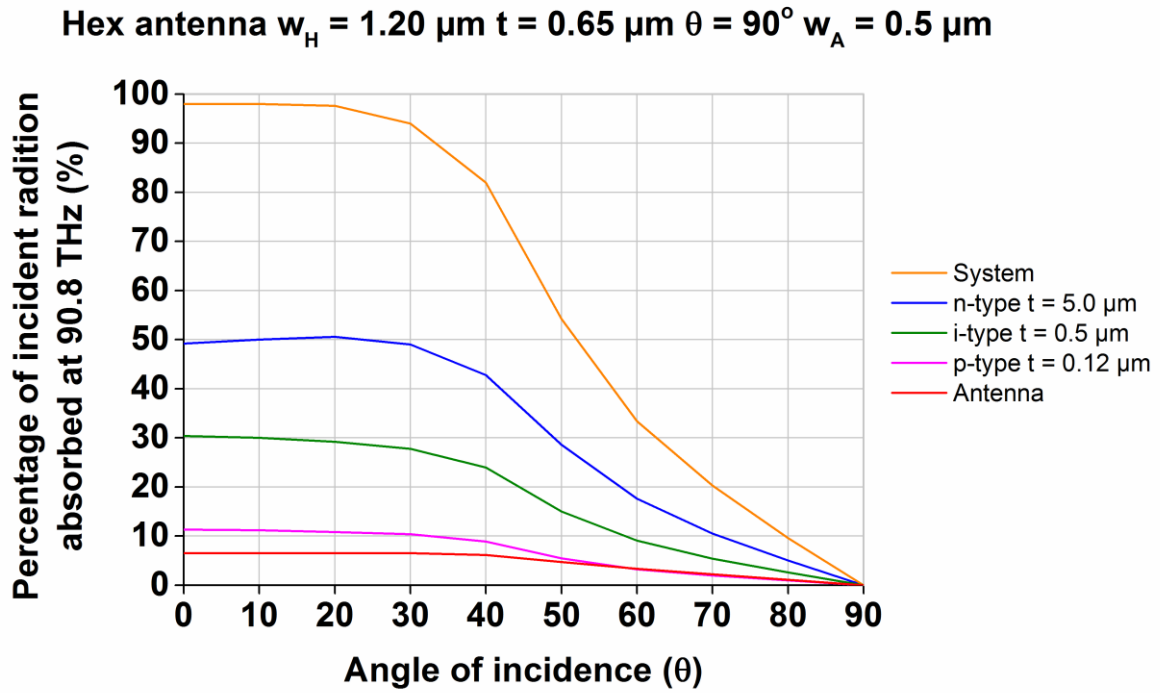
Figure 5.3.5: The change the power absorbed in the system, p-type, i-type, n-type and antenna as a function of trajectory angle for the micro-antenna design 1 with a side wall angle of 90°.

Figure 5.3.6 shows the change in peak absorption wavelength as a function of incident trajectory angle. It is observed that there is a slight difference in system absorption and i-type absorption at lower angles of incidence. Both graphs will blue shift as a consequence of wide trajectory angles. The change of accepted wavelength would infer that a varying incident angle has an influence on the plasmon propagation constant. More specifically it causes the localisation focusing length to increase so that more radiation of a higher frequency and therefore higher attenuation coefficient is absorbed in the i-type region.
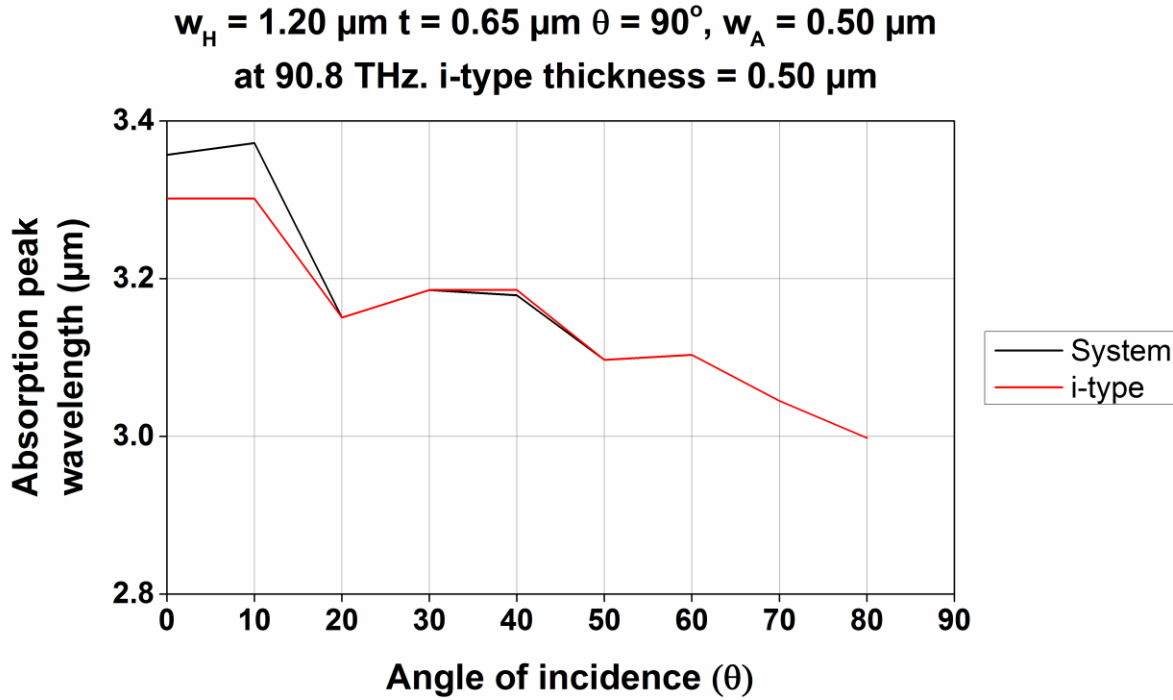
Figure 5.3.6: The change the peak position in the system and the i-type layer as a function of trajectory angle for the micro-antenna design 1 with a side wall angle of 90°.

A revised version of figure 5.3.5 is provided in figure 5.3.7 which takes into account the effects of the observed side wall angles. The i-type absorption has decreased but a design with a side wall angle is noticeably more tolerant of wide incident trajectory angles. It maintains an i-type absorption that is roughly consistent until 30 degrees.

Hex antenna w$_H$ = 1.20 µm t = 0.75 µm θ = 73° w$_A$ = 0.7 µm
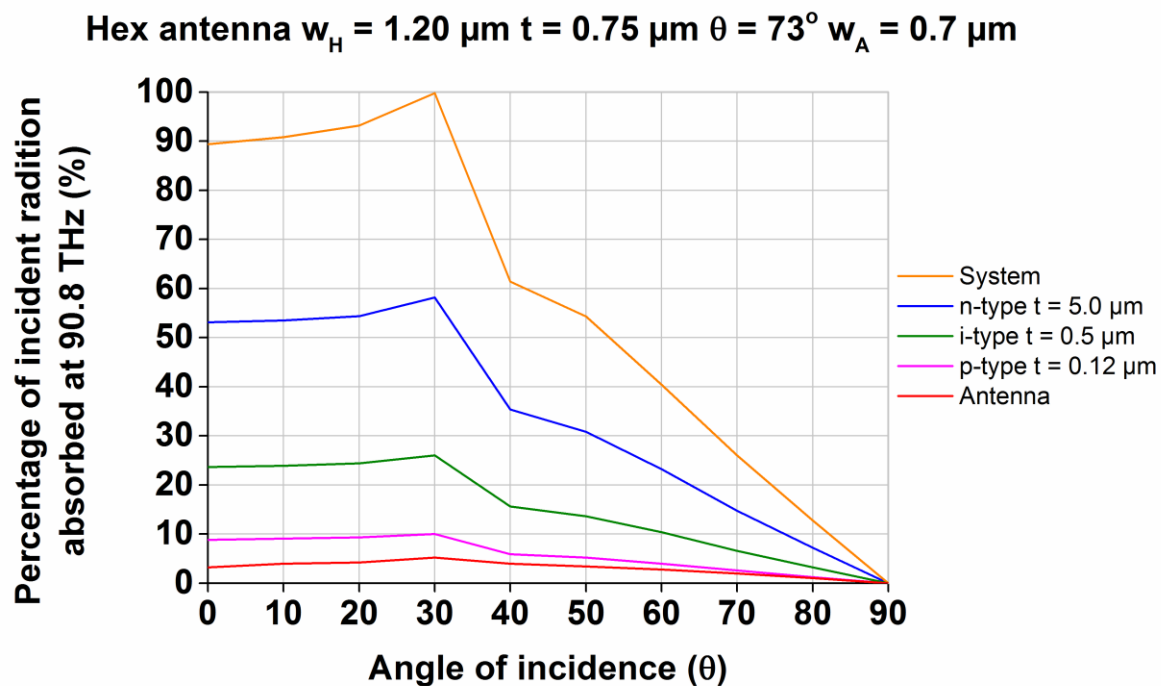
Figure 5.3.7: The change the power absorbed in the system and the i-type layer as a function of trajectory angle for the micro-antenna design 2 with a side wall angle of 73°.

Side wall angles are consistent with all fabricated arrays. They provide a small improvement to the antenna arrays tolerance to trajectory angles, but are generally detrimental to photodiode signal improvement. The manufacturing produce (section 4.3.4) does at least produce a consistent side wall gradient between 70° and 75°, which minimises complications when comparing antennas of different sizes. These manufacturing defects are expected in for NTA 2 analysis, but will be verified under the SEM none-the-less.

5.4) The minority carrier generation effect

The prospect of covering semiconducting mesas with conductive materials is expected to produce a leaky diode in the form of minority carrier generation when applied the semiconductor epitaxial layers. The features shown in figure 5.4.1 show an assortment of contact pads on different size squared mesas that was used to assess the degradation of

homostructure photodiode quality with the surface cover by Au plates with a thin Titanium

adhesion layer. These devices consist of four perimeter to area (P/A) test structures S1, S2 S3

and S4 of approximately 100 μm x 100 μm, 200 μm x 200 μm, 300 μm x 300 μm,400 μm x

400 μm respectively in size. In preparation for adding conducting antennas on the

semiconductor surface, it was necessary to test the effect of putting a conducting surface area

onto the surface of the semiconductor substrate and how the effect of the minority carrier

generation affects the quality of the diode.
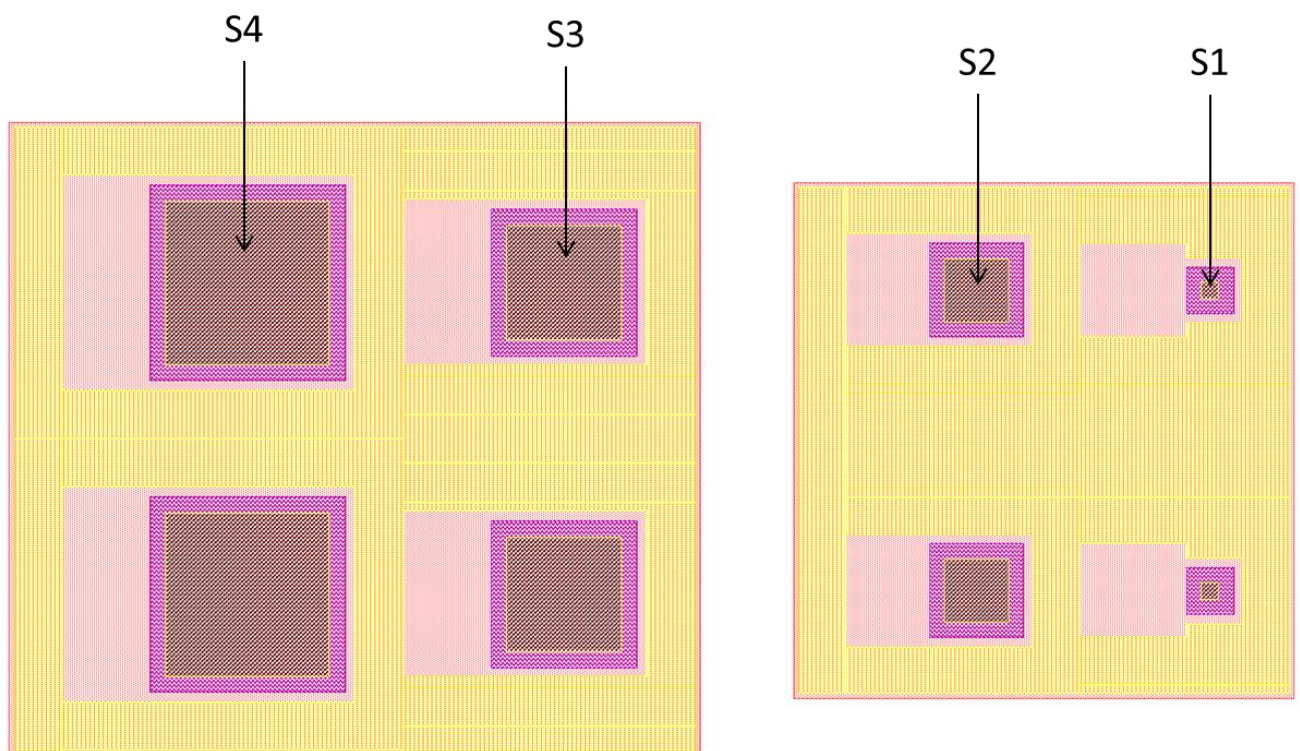
Figure 5.4.1: Test sample S1, S2, S3 and S4. The area in brown is the top metal contact where probe 1 is to
come into contact during testing. The purple area is the mesa frame. The yellow area is the bottom metal
contact where probe 2 comes into contact. The frame (the gap between the metal contact (brown) and the mesa
edge (pink)) has a consistent length of 31 μm. This diagram was produced in L-edit. Drawn to scale.

The P/A structures are tested by probing the p-type contact (figure 5.4.1 brown area) and the

n-type layer (figure 5.4.1 yellow area).

The resistance (and by extension, quality) of the semiconductor homostructure is dependent on three factors;

1) The proximity between the conducting surface materials and the i-type layer.

2) The volume of the semiconductor i-type (see equation 3.1.5).

3) The surface area covered by the conducting materials.

The use of thin epitaxial layers is necessary for maximum efficiency when using antenna influenced localised focusing. However, minority carrier generation underneath the gold metal contact causes the diode to become leaky. This effect is much more apparent in thin diodes as opposed to standard epitaxial thicknesses. It is also dependent on how much of the top mesa is covered in a conductive metal contact. This leakage can be minimised under the condition that the surface area covered by metal also minimised.

Figure 5.4.2 (a) and (b) show experimental results which demonstrate the effect of these factors. The samples given as Wood anemone, Wood Sorrel and Dog's Mercury are semiconductor homostructures with standard epitaxial thicknesses where the p-type has a thickness of 0.5 µm the i-type has a thickness of 3 µm and the n-type has a thickness of 5 µm. Q and Oleander are semiconductors with thinner epitaxial layers designed with antenna near field focusing in mind. They are semiconductor homostructures with a p-type thickness of 0.1 µm, an i-type thickness of 0.5 µm and an n-type thickness of 5 µm.

The test structures were measured on Q and results were compared to standard diodes (shown in figure 5.4.2 (a)). These readings were later confirmed by Oleander, which has similar results (shown in figure 5.4.2 (b)).
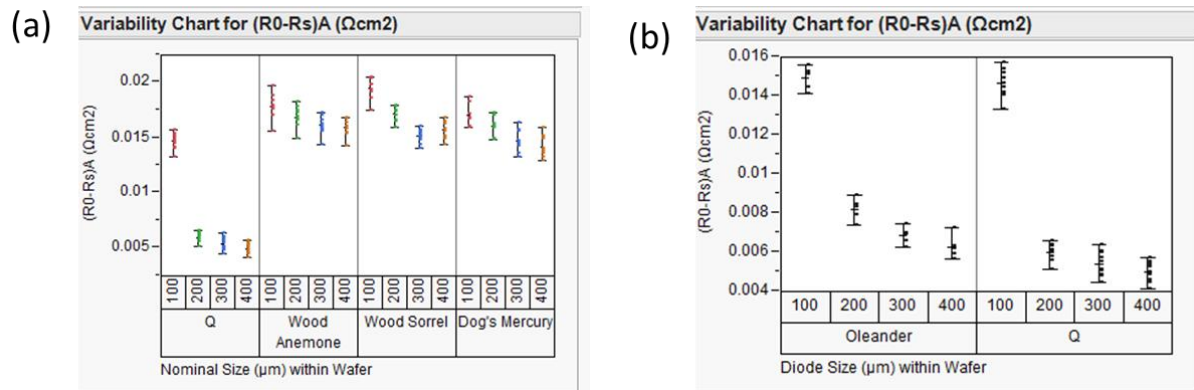
Figure 5.4.2: The resistance of the diode associated with the surface area of the metal contact where R0 is the zero bias resistance and Rs is the minimum reverse bias resistance. Each whisker plot shows the range and average of 9 mesa samples taken across the entire sample. (a) The resistance of small epitaxial thicknesses (from Q) compared to the resistances from (b) Q and Oleander zero bias dependency P/A structure size, meant to provide consistency in thin epitaxial layer results.

Rs is the minimum reverse bias resistance. It is usually very marginal and it is taken away from the zero biased resistance to account for the discrepancies in the resistance at high forward bias voltages. Figure 5.4.2 shows the zero bias resistances of the semiconductor photodiodes (see figure 4.3.5.1 (b) for example of zero bias resistance readings). The resistance data provides information on the diode quality and how leaky it is. It shows that for the thicker epitaxial layers, the dependency on the semiconductor surface area is largely linear with the minority carrier generation per unit surface area producing a relatively negligible effect, whereas the minority carrier generation per unit surface unit covered has a much more significant effect on the thinner epitaxial layers. The experiment has assumed that minority carrier generation originates from the metal in close proximity to the i-type layer and by extension the larger the area that is covered by the metal contact compared to the surface area of the semiconductor, the more leakage will occur. The 100 μm by 100 μm P/A structure (S1) has the largest mesa surface area to metal contact surface area ratio and demonstrates that the diode quality improves exponentially for thin epitaxial layers as the surface area covered by metal decreases. This means that it is not only beneficial to have the

mesa size as small as possible, but also to reduce the area covered by the metal to a minimum.

To provide mathematical context to the impact of the surface conducting material on thin epitaxial layers, the dependency of diode resistance with metal surface area was examined.

The components of the diode are in parallel. This means that the resistance of the diode (R_0) can be expressed in terms of the resistance of the surface metal (R_{Metal}) and the resistance of the frame (R_{Frame}) when considering the equivalent circuitry after surface induction where:

$$\frac{1}{R_0} = \frac{1}{R_{Metal}} + \frac{1}{R_{Frame}}$$
(5.4.1)

Equation 5.4.1 can be expressed in terms of the surface area the metal contact occupies when both the top and the bottom are multiplied by the surface area:

$$\frac{1}{R_0} = \frac{(x - 2 \cdot L)^2}{R_{Metal} A_{Metal}} + \frac{x^2 - (x - 2 \cdot L)^2}{R_{Frame} A_{Frame}}$$
(5.4.2)

Where x is the semiconductor mesa square length and L is the distance from the edge of the metal contact to the edge of the frame. L has a consistent value of 31 μm.
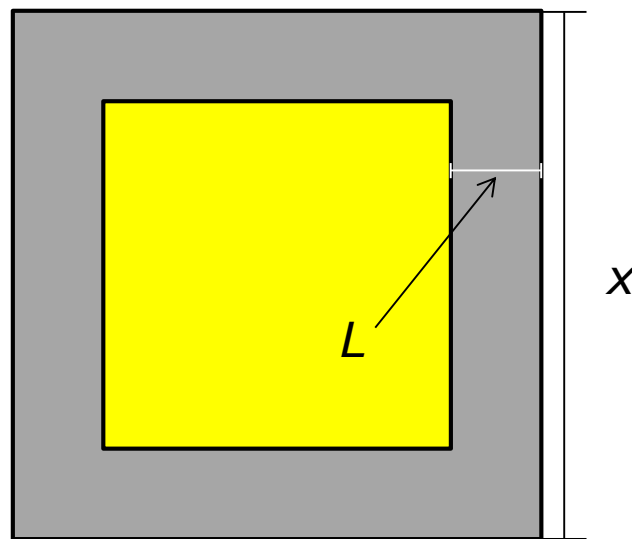
Figure 5.4.3: A diagram of a top-down view of the semiconductor mesa with a depiction of the lengths L and x used in equations 5.4.1 and 5.4.2.

This leaves two unknowns ($R_{Metal}A_{Metal}$ and $R_{Frame}A_{Frame}$) which can be approximated when

the R_0 values are substituted for the R_0 -R_s values in figure 5.4.2. For simplicity, $R_{Metal}A_{Metal}$

and $R_{Frame}A_{Frame}$ will be expressed as M and F respectively.

$$R_0 = \frac{1}{\dfrac{(x - 2 \cdot L)^2}{M} + \dfrac{x^2 - (x - 2 \cdot L)^2}{F}}$$ (5.4.3)

The result is an approximation of M and F of 0.00317 Ωcm^2 and 0.03715 Ωcm^2 respectively.

These values can provide an estimate of the diode resistance in accordance to square length

of the frame with the following graph shown in figure 5.4.4.
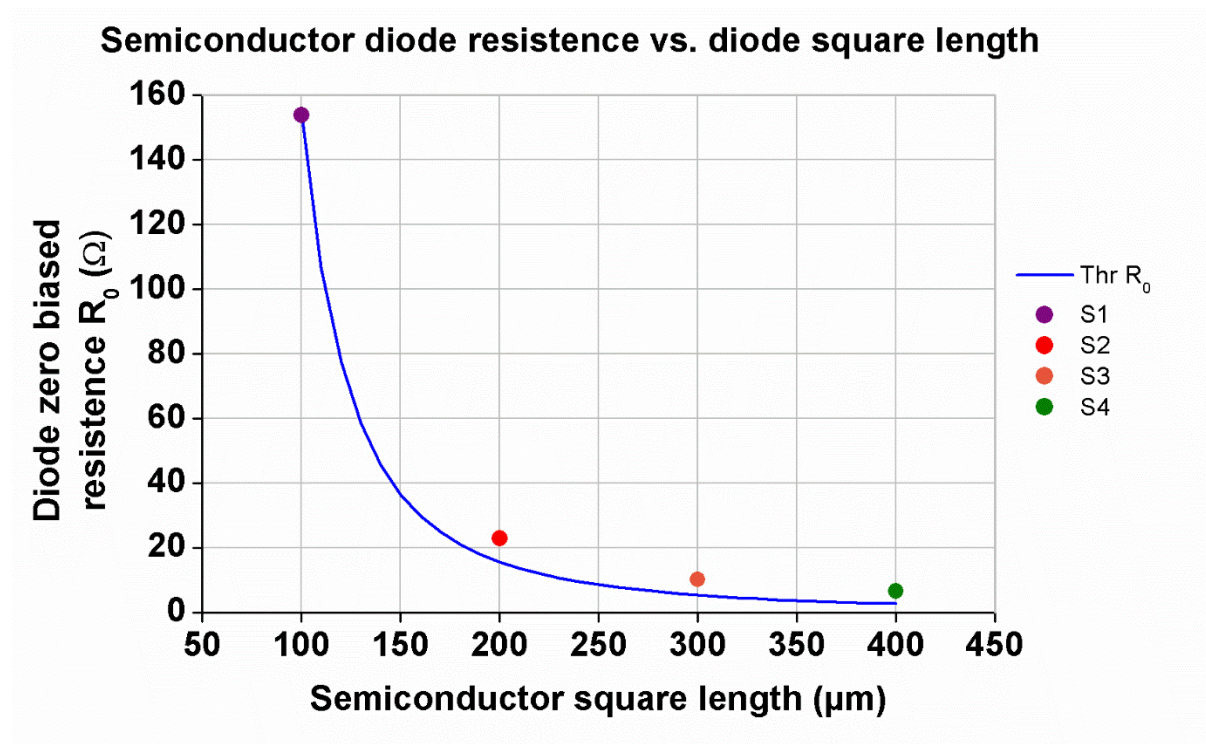
Figure 5.4.4: Diode zero biased resistance vs. the diode square length. This theoretical graph (Thr R_0) assumes that the metal surface is a square test structure. The points along the graph are average experimental values of the diode resistances based on the surface area of the metal and the surface area of the frame.

While this initial analysis provides good context to the surface metal impact, the P/A

structures are not representative of a design that micro-antennas will be implemented on. To

address that, further analysis is needed on mesas which support annuluses on the surface.

Within each field of the gas sensor mask design, there are 12 4 x 4 arrays of mesas (see figure

4.2.2 for example), each with 2 different annulus sizes on top as shown in figure 5.4.5:
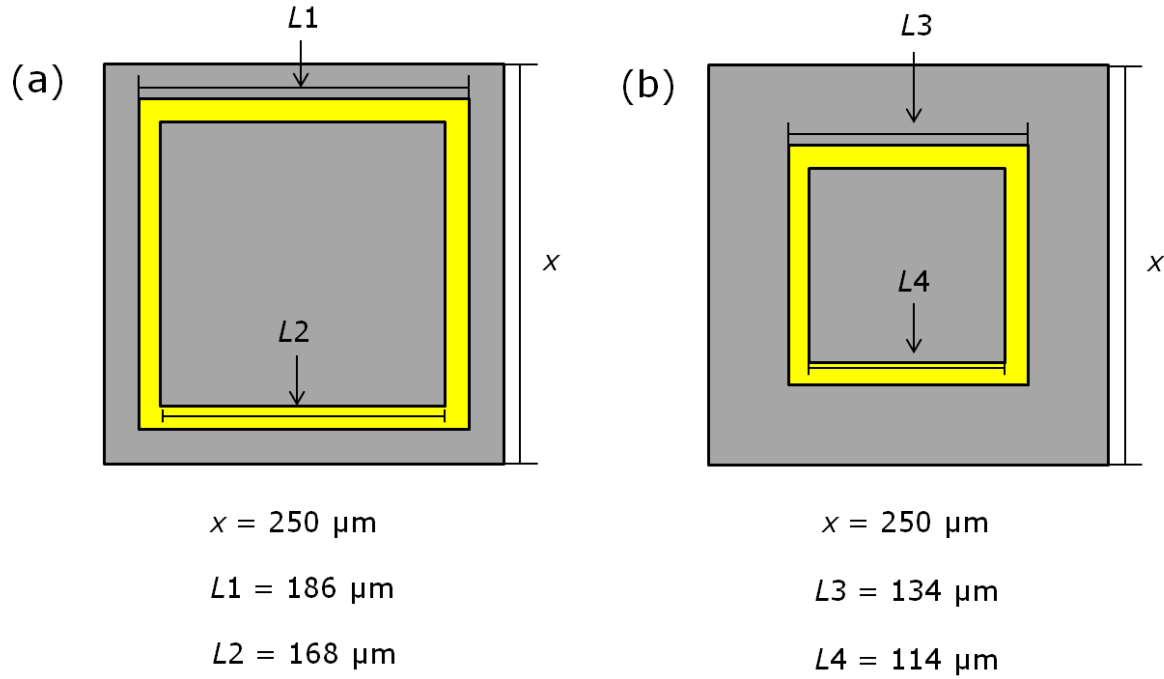
Figure 5.4.5: The two different array sizes. (a) The large annulus has a surface area of 6.37 x 10^{-5} cm^2. (b) The small annulus has a surface area of 4.90 x 10^{-5} cm^2.

By inputting the relative areas of the metal annulus and the mesa frame, the resistance for a

250 μm by 250 μm mesa can be estimated by substituting the values of L1, L2, L3 and L4

into equation (5.4.3). The surface areas of the metal annuluses are smaller than a square metal

surface would be, so a higher diode resistance is expected.

$$R_0 = \frac{1}{\dfrac{(L1)^2 - (L2)^2}{M} + \dfrac{x^2 + (L2)^2 - (L1)^2}{F}} \qquad\qquad (5.4.4)$$

$$R_0 = \cfrac{1}{\cfrac{(L3)^2 - (L4)^2}{M} + \cfrac{x^2 + (L4)^2 - (L3)^2}{F}}$$

<div align="right">(5.4.5)</div>

The approximate values of the diode resistance were calculated and included in figure 5.4.6
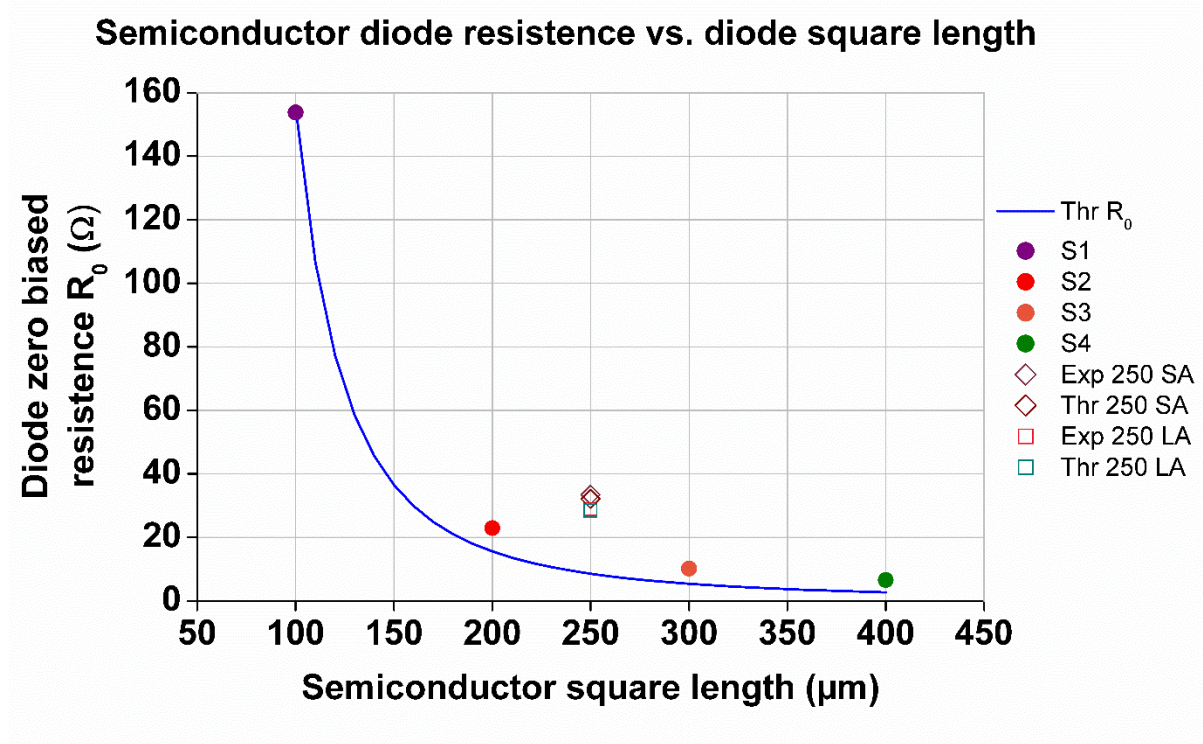
Figure 5.4.6: Figure 5.4.4 with the average resistances of the 250 µm x 250 µm mesa with a large and small annulus shown as plus sign and cross sign respectively. This graph demonstrates the difference in zero bias resistance when using thin epitaxial layer for a solid contact (figure 5.4.3) and an annulus contact (figure 5.4.5).

The resistance values were measured using the probe station by carefully putting the gold probes in contact with the top annuluses (on the p-type) and bottom annuluses (on the n-type). The measured values were taken in 8 different fields of the Oleander sample. The average measured diode resistances for the large and small annulus was 28.9 Ω and 33.4 Ω respectively. When using the derived values of M and F, the theoretical results for the large and small annulus was 28.4 Ω and 32.1 Ω respectively. It is reassuring to see that the margin of error between the experimental work and theory is less than 5% and the values approximately overlap.

The studies regarding minority carrier assessment is based on original readings, calculations and modelling. It is noted that the model is more accurate as the surface area of the contact pad decreases, which could warrant additional calibration, but the experimental results can conclude that conducting materials on the diode surface contribute significant minority carrier generation that needs to be addressed by incorporating heterostructures (see section 3.3) or another form of minority carrier buffer (see section 6.1) if the diode quality is going to be maintained.

5.5) NTA 2 results analysis

To demonstrate the improvement in near surface coupling, the percentage of incident power absorbed in an $Al_{0.05}In_{0.95}Sb$ detector at 90.8 THz has been calculated for uncoated material; material having an idealized anti-reflection (AR) coating; and material patterned with aluminum hexagonal micro-antennas (see figure. 5.5.1).

The modelled diode is made of the same thin layers as depicted in figure 5.3.3 (b) to capitalise on the localised focusing. The antennas are of the same parameters as depicted in figure 5.3.4 design 1.

The idealized AR coated sample is defined as having zero reflection over the frequency range of interest. To minimize computation time, the data in figure 3 was generated using uniform, polarised (normally incident) illumination. The inset of figure 5.5.1 justifies simulation using a polarised source as it demonstrates that the variation in the power absorbed with polarisation angle is only $\pm$ 0.09%. Fig. 5.5.1 illustrates that patterning with the micro-antennas increases the absorption in the near surface region of the $Al_{0.05}In_{0.95}Sb$ compared with that in uncoated material and even with that in the ideal AR coated material.
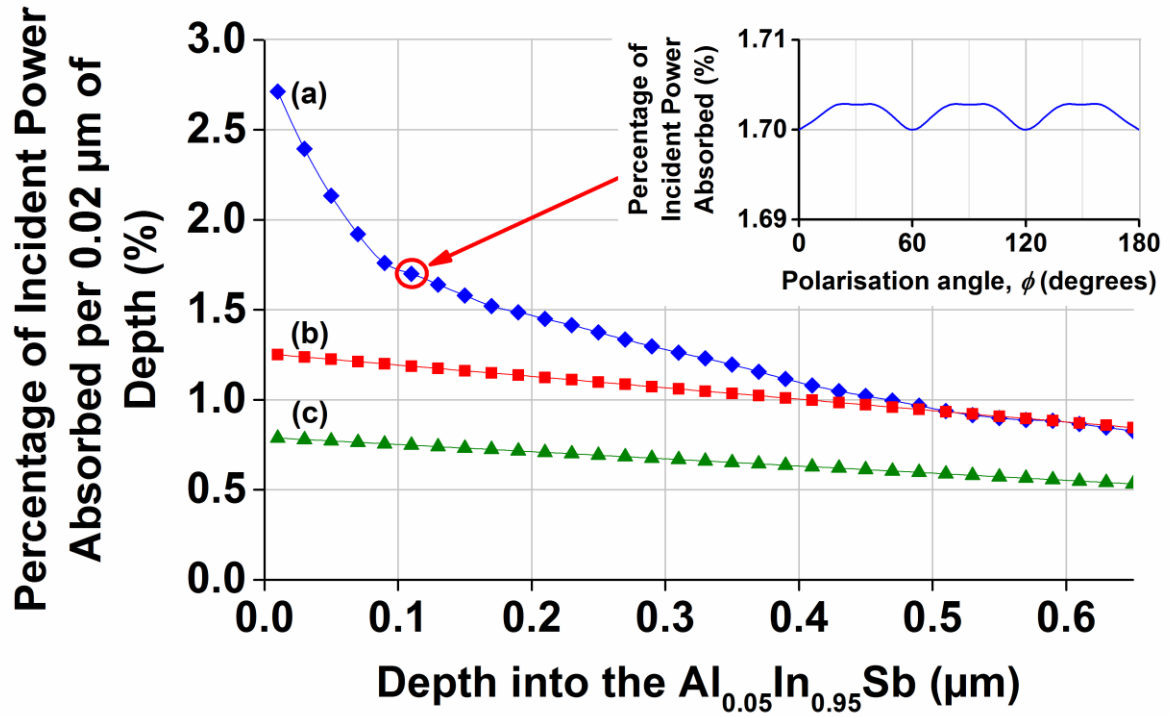
Figure 5.5.1: Simulation of the power at 90.8 THz (3.3 µm) absorbed in each 0.02 µm increment of depth in the semiconductor photodetector; (a) with an aluminium hexagonal array $w_H = 1.21$ µm, $w_A = 0.50$ µm, $t = 0.65$ (b) Perfect AR coating; (c) uncoated semiconductor material. Inset shows the variation with polarisation angle for a detector with antenna at a depth of 0.14 µm as indicated. The same epitaxial layers shown in figure 5.3.3 (b) were used.

Figure 5.5.1 demonstrates ideal localised focusing with a 90° side wall angle. Figure 5.5.2 shows the expected side wall gradient of between $70^o - 75^o$, which will degrade the i-type absorption in the same fashion depicted in figure 5.3.4. This effect is taken into account for data comparison of the spectral analysis.
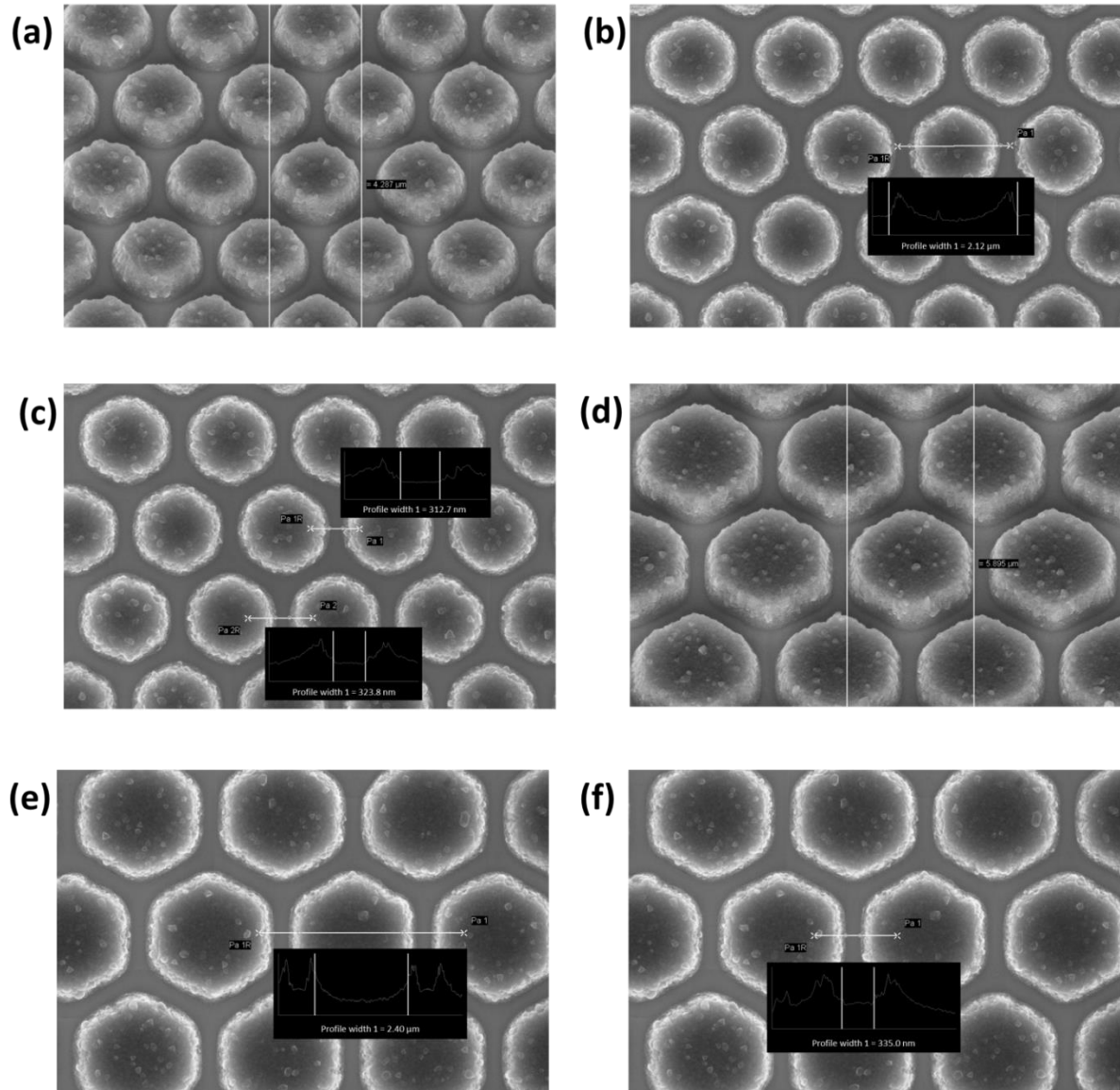
Figure 5.5.2: SEM scans of wafers with aluminium antennas from NTA 2 W4 Al t = 750 nm. (a), (b) and (c) are from mesa set label F X4 Y2 M X5 Y0 and corresponds to the smallest antenna array ($w_H = 1.0$ µm, $w_A = 0.7$ µm). (d), (e) and (f) are from the mesa set label F X4 Y2 M X6 Y3 and correspond to one of the larger antenna arrays ($w_H = 1.4$ µm, $w_A = 0.7$ µm)

The theoretical overlay had to be done by analysing the i-type absorption in the CST software at every 5 THz integers between 65 THz and 200 THz for different antenna array designs. As an example, the change in i-type absorption between the control (derived for the data in TABLE 5.1) and the antenna arrays was recorded as depicted in figure 5.5.3.
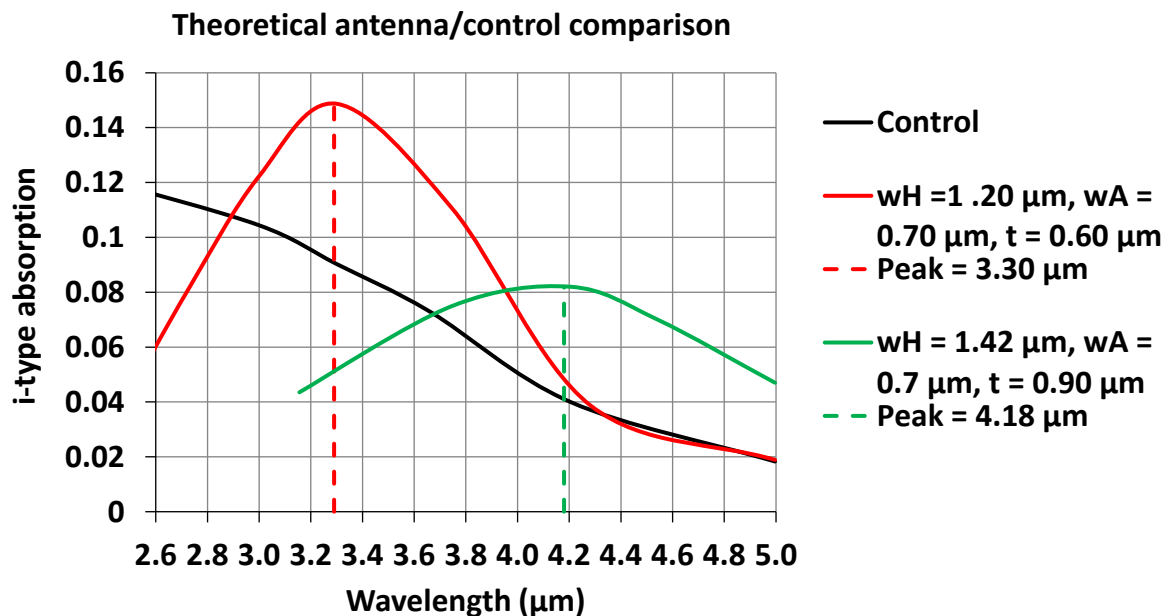
Figure 5.5.3: The simulated absorption enhancement in the i-type region for two hexagonal designs examples that are most responsive at 3.3 µm and 4.2 µm respectively. Both have a 90° side wall angle, but are not optimised.

Figure 5.5.3 is an example of CST^{TM} simulation data used to create a theoretical overlay to compare to theoretical results. In order to compare this to experimental data, the theoretical peaks are normalised to the theoretical control data to give a factor increase or decrease at certain wavelengths.

There are things to address during the analysis of NTA 2:

1) To investigate the improvements heterostructures can provide for the photodiode (see section 3.3).

2) To compare the spectral response to the CEM simulations.

3) To investigate the improvements of photodiode operation at low temperatures.

5.5.1) NTA 2: Homostructure and heterostructure comparison

W1 (Wafer 1) is a semiconductor homostructure patterned with varying antenna sizes and pitches (see figure 4.3.3.4). Figure 5.5.1.1 shows the spectral response obtained from W1 when the antennas are grown 950nm and 1000nm in thickness compared to a control device (no antennas on the mesa surface) given in black. The parameters of this device is representative of successful results obtained from NTA 1 (see figure 5.2.6) and is more suitable for a response at 4.2 μm, particularly f X2 Y2 M X0 Y4 ($t = 0.95$ μm, $w_H = 1.50$ μm, $w_A = 0.70$ μm).
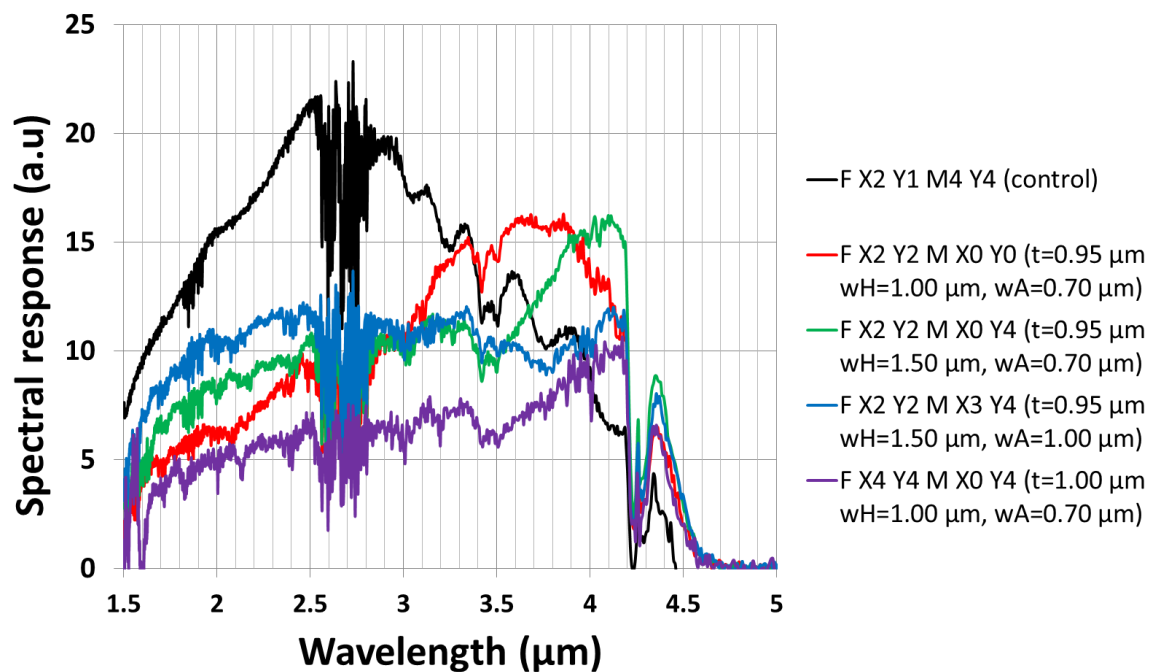
Figure 5.5.1.1: The spectral response of different size antennas compared to the control, after data normalisation, as a function of antenna hexagonal width, aperture width and antenna thickness and wavelength on W1. All mesas in the data shown are 200 μm by 200 μm. Gold probes when used to measure the response of these devices.

It demonstrates how the antennas amplified the signal within a certain bandwidth to the detriment of the signal strength elsewhere. F is the field number and M is the mesa set number. These results were obtained from the experimental set up shown in section 4.3.5.

Similar to the NTA 1 observations, the peak signal changes with hexagonal width in accordance to the conventional antenna physics specified in section 3.6, where the smaller antenna size deviates towards the secondary wavelength target (3.3 µm). The signal peak will also change position as a function of aperture width as this will cause the effective volume (V_{eff}) to vary. The peak signal strength will also diminish as the aperture width (w_A) deviates from the optimum, which for a wavelength of 4.2 µm is about 0.7µm.

Figure 5.5.1.2 shows the R_0 for two different semiconductor quarter wafers using semiconductor homostructure W1. These R_0 measurements only concern the diode quality. The antenna array performance is a separate issue. All mesa structures are fabricated using the NTA 2 mask set. The wafer was dissected into quarters where two of them were grown with a thickness of 950 nm and 1000 nm respectively. The figure shows that the R_0 varies for different positions on the wafer and also varies on wafers that are nominally fabricated to be the same. The control data seems to vary the most, so to insure that the diode resistances are not disproportionately large due to any variations across the wafer, it is good practice to measure the photodiodes and compare them to the control in the same or nearest field.

Figure 5.5.1.2: The zero bias resistance (R_0) of the antenna enhanced devices with 950nm or 1000nm thick antennas compared with the controls implemented on semiconductor homostructures (see figure 3.3) of W1. The figure has results from mesas 200μm, 250μm, 300μm and 400μm in square length respectively. There is a measurement of at least one antenna hexagonal width and spacing for each grown antenna thickness. The 24 antenna variations are specified in figure 4.3.3.4.

There is a noticeable difference between the antennas and the control. The control is larger than the mesas covered with antennas by a factor of 1.68 at the worst of recorded cases. This is because of the antenna influenced minority carrier generation, adding to the diode saturation leakage current (see section 5.1). For each antenna thickness, the R_0 does not appear to vary across different antenna parameters and pitches significantly. The problem to consider is the stimulated signal being forwarded to the transimpedance amplifier (TIA) for spectral analysis (see figure 4.3.5.2). The TIA is necessary as the stimulated current is only of the order of several hundred micro amps.
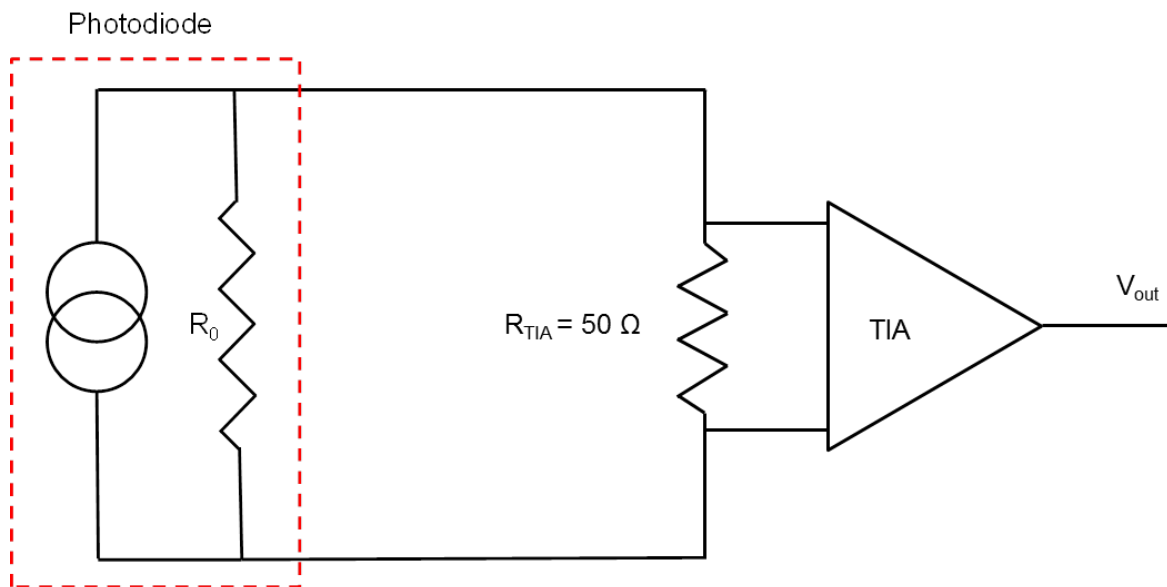
Figure 5.5.1.3: The photodiode equivalent circuit set up demonstrating a smaller current being forwarded to the TIA if the photodiode resistance is too low.

A diode resistance that is small than the TIA resistance (50 Ω) would mean that the signal being forwarded to the TIA would vary considerably in relation to Kirchhoff's law:

$$I_0 = I_{TIA}\left(1 + \frac{R_{TIA}}{R_0}\right) \tag{5.5.1}$$

$$R_0 = \frac{I_{TIA}R_{TIA}}{I_0 - I_{TIA}} \tag{5.5.2}$$

$$\frac{I_0}{I_{TIA}} = 1 + \frac{R_{TIA}}{R_0} = AF \tag{5.5.3}$$

Where I_0 is the photocurrent before signal amplification through the TIA and I_{TIA} is the current after amplification through the TIA. Equation 5.5.2 shows that as zero bias diode resistance increases I_{TIA}. The data needs to use the adjustment factor (given as AF) before a like-for-like comparison can be achieved. This is so as to be sure that any signal enhancements are due to localised light focusing and not a difference in diode quality. A large adjustment factor is undesirable as it means the diode is of poor quality and produces a lot of leakage, but the adjustment factor can be minimised if the photodetector resistance is as high as possible or at least larger than the trans-impedance amplifier resistance (R_{TIA}).

The temperature was kept at a constant 22^oC and the measurements were taken is a dark faraday cage to minimise external influences. For a homostructures this readjustment of data accounts for an antenna array signal adjustments by about 15% for 200 μm by 200 μm mesas and up to 40% for 400 μm by 400 μm mesas. The impact antennas have on leakage is evidently high and techniques to lower these readjustment factors will be used to minimise them.

In order to create devices that can work at the room temperature, quantum barriers can be incorporated. As discussed in section 3.3, the quantum barriers (products of heterostructures) can be introduced into the semiconductor system. This is done by growing the p-type layer as two different layers with the lower portion of the p-type being 20 nm thick and having a higher percentage of aluminium content as indicated in figure 5.5.1.4.

p$^+$ Al$_x$In$_{1-x}$Sb: Be	0.1 μm
p$^+$ Al$_y$In$_{1-y}$Sb: Be	0.02 μm
u.d. Al$_x$In$_{1-x}$Sb	0.5 μm
n$^+$ Al$_x$In$_{1-x}$Sb: Te	5 μm
Al$_x$In$_{1-x}$Sb	Buffer layer
GaAs	Substrate
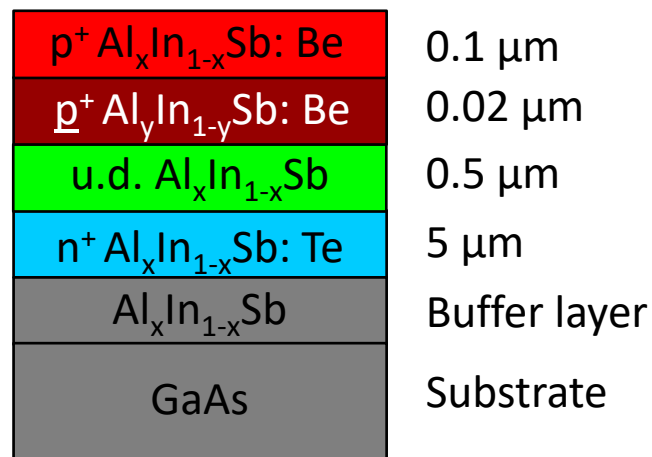
Figure 5.5.1.4: The improved heterostructure semiconductor epitaxial grown design made to restrict minority carrier generation flow from the p contact to the active region and maintain a consistent R_0 for both mesas with micro-antenna arrays as well as the control mesas. x = 0.05, y = 0.20.
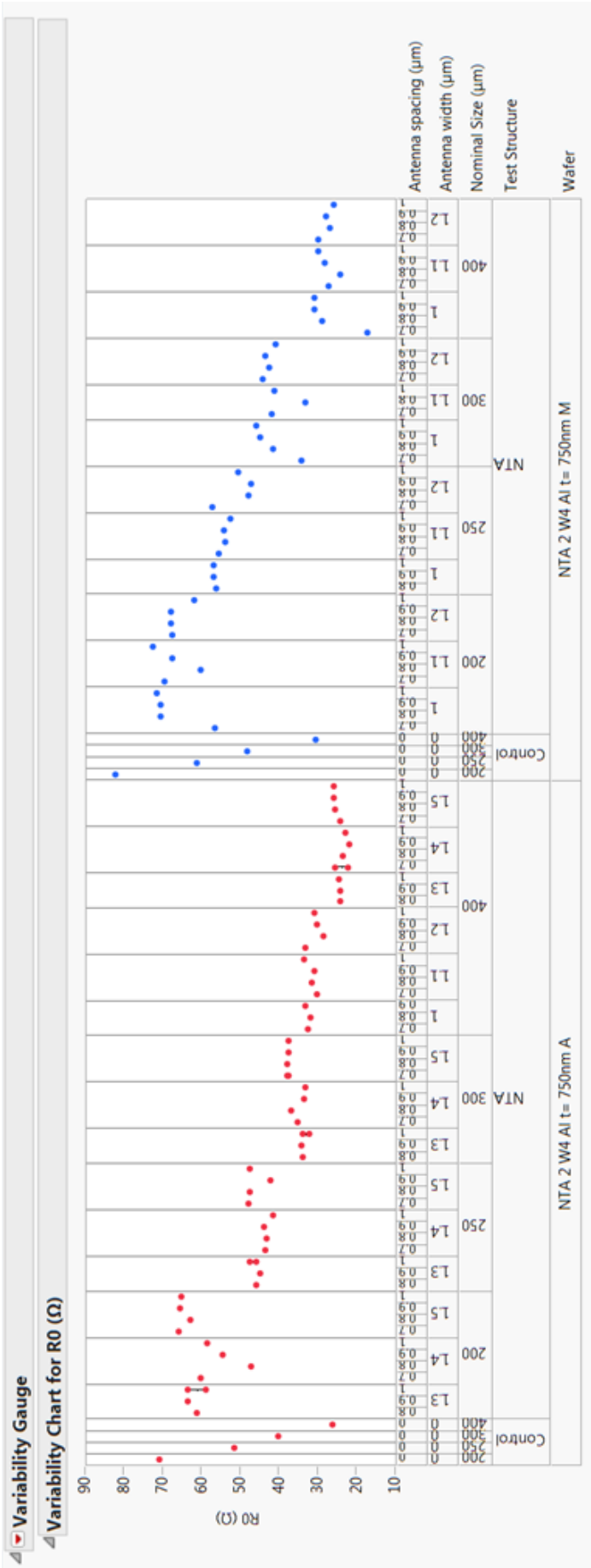
Figure 5.5.1.5: The heterostructure resistance measurements on the manual prober (M – right hand side. Blue points), which uses gold probes and the autoprober, (A – Left hand side. Red points) that uses P7 probes. The semiconductor was grown with thicknesses shown in figure 5.5.1.4.

Figure 5.1.1.5 shows the R0 measurements using the gold probes (blue) on the manual probe station and the P7 probes (red) on the autoprober for devices made on a quarter wafer with a quantum barrier, W4. Both sets of measurements were taken on the same day and both were taken on fresh devices (no scratches). This was done so that any damages that are detrimental to the resistance readings could be avoided. The autoprober with P7 probes appears to produce a slightly lower resistance than the manual prober with gold probes. Despite the slight signal variations, the heterostructure implementation was successful and the R_0 resistance value increased to an average of 70-75 ohms for mesas that are 200 μm in square length. This is above the 50 ohms resistance of the TIA, which will reduce the attenuation of the signal by the TIA and therefore also reduce the required correction factor. The normalisation with heterostructure accounts for a maximum 5% signal adjustments. This demonstrates the improvements implemented by heterostructure compared to the homostructure shown in figure 5.5.1.2.

Figure 5.5.1.6 shows the experimental spectral responses for detectors with an antenna thickness of $t = 0.75$ μm, a side-wall angle of 73°, an aperture width $w_{A(base)} = 0.56$ μm and a range of hexagonal widths, $w_{H(base)}$. Water vapor and CO_2 absorption troughs are visible at 2.6 μm and 4.2 μm respectively due to the absence of spectrometer purging. The spectral response of the control device is consistent with that published for $Al_{0.054}In_{0.946}Sb$[70] with a peak response at ~2.65 μm. The position of the peak response shifts systematically to longer wavelengths as the hexagonal width (w_H) is increased. Figure 5.5.1.6 also shows the experimental results compared to CEM simulation data, given as dashed lines overlaying the experimental solid lines. These overlays where done by comparing absorption results in the i-type layer for both the control and the antenna array of the six different conducting antenna lengths.
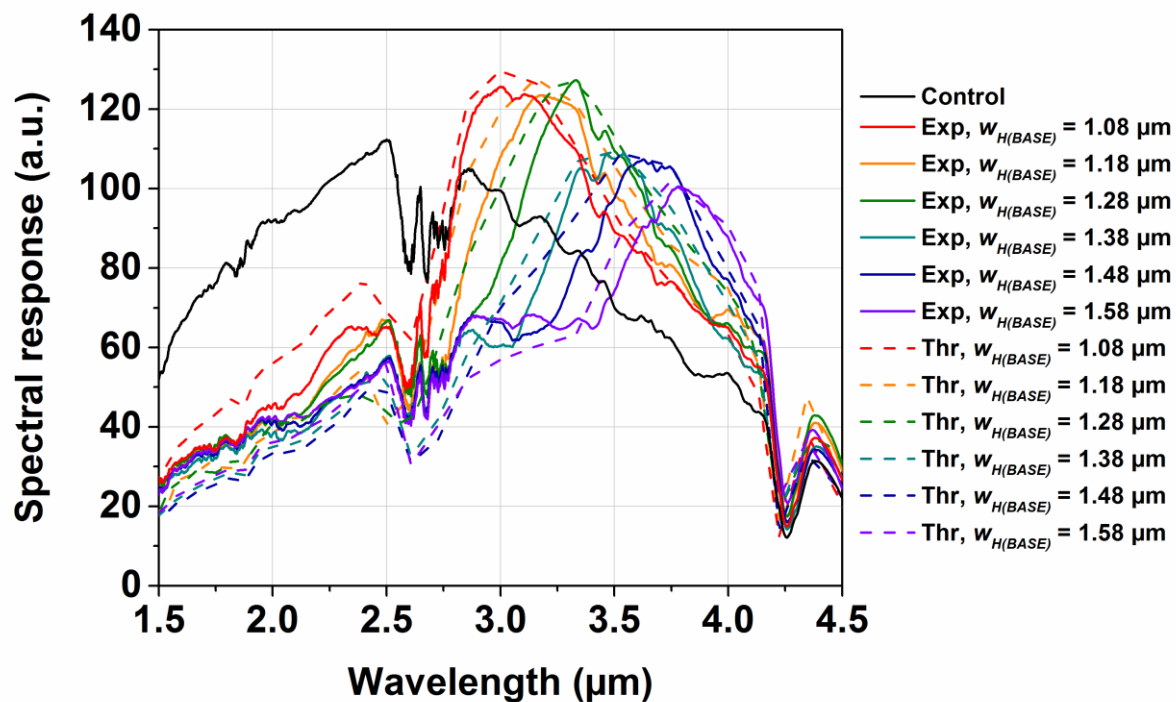
Figure 5.5.1.6: Semiconductor heterostructure W4 theoretical and experimental spectral results. Experimental (solid) and simulated (dashed) spectral responses with micro-antennas of thickness $t = 0.75$ µm, aperture width $w_A = 0.7$ µm, side-wall angle $\theta = 73°$. The semiconductor epitaxial layers are the same as depicted in figure 5.3.3 (b). The control (black line) has no antennas on the surface. The legend shows the whether the data is experimental (Exp) or theoretical (Thr) as well as the base hexagonal width after side gradient intricacies are taken into account.

The margin of error shows a difference between the theoretical and experimental results of below 5% for the majority of the spectral results. It can be seen that for all the micro-antennas designs considered there is very good qualitative and quantitative agreement between the experimental and simulated data. Despite the improved coupling efficiency of the micro-antennas into the semiconductor, the peak signal level decreases with increasing w_H because the bulk absorption coefficient (α) is reduced as the band edge is approached. The largest peak response, a factor improvement of 1.56 above the control, was obtained at 3.3 µm on device (d) where $w_{H(base)} = 1.28$ µm. This result is consistent with the modelled data plotted in figure 5.3.4. The enhancement factor has been noted to increase even higher towards the 3.8 µm wavelength where (g) demonstrates of factor improvement of up to 1.70. The point of providing simulated results is to assess model accuracy and used the calibrated model for

alterations to the device so that the diode quality can be improved even further (see chapter 6). The data in this chapter shows effective coupling when the antennas are tuned to higher order resonant harmonics (i.e. the conducting length is approximately ¾ λ and not ¼ λ). This supports the coupling theory described in equation 2.0.

5.5.2) NTA 2: Low operating temperatures

Cooling the semiconductor devices is an alternative method to improve device performance without needing to use heterostructures in the epitaxial layers. Under such conditions, the R_0 ratio of the control and antenna array is much smaller and both and much higher than R_{TIA}, thus the results are more comparable without normalisation procedures. Compared to the homostructures labelled as W1 (figure 5.5.1.2), the signal adjustments of the 400 µm by 400 µm mesas with antennas has dropped to 17% at -35°C and 12% at -50°C. The signal adjustments of the 200 µm by 200 µm had dropped to below 5% at -35°C and below 1% at -50°C. The 200 µm by 200µm data in figure 5.5.2.1 was compromised due to excessive use but this was confirmed in additional measurements as indicated in figure 5.5.2.2.
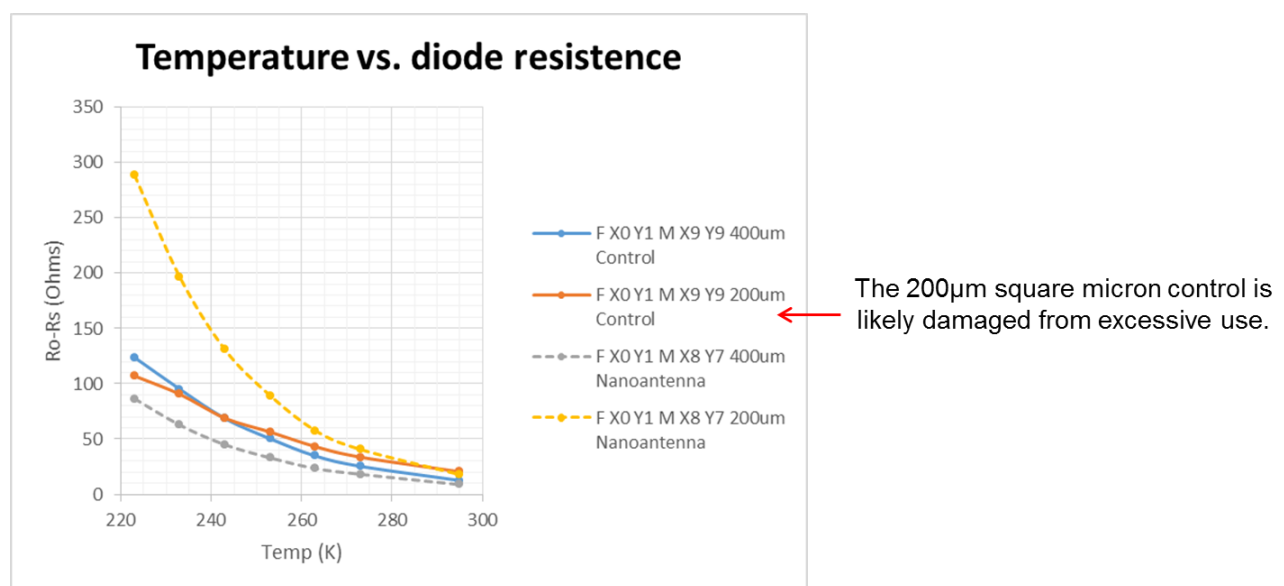
Figure 5.5.2.1: The change in R_0 with temperature for the developed semiconductor, W1. The resistance of the 200µm by 200µm control is not increasing at the same rate as the antenna array of the same size due to damage

of the contact pads from excessive use. There is no such deviation from the 400μm by 400μm mesa structures. Gold probes when used to measure the response of these devices.

Figure 5.5.2.1 not only demonstrates how the zero bias diode resistance changes with temperature, but also the potential for "wear and tear" effects of testing devices that have been probed multiple times and are therefore scratched and damaged. Because of this, the R_0 was recorded at the same time as the spectral analysis to ensure the validity of resistance values. At the point of recording this data is was clear that W1 had been overused. Thus, wafer 3 (W3) was fabricated in an identical way the W1 in order to ensure that the resistance is not influenced by device fatigue during low temperature experiments.

W3, Al antenna, t = 0.75 μm, w_A = 0.70 μm, θ = 73°, T = -35°C
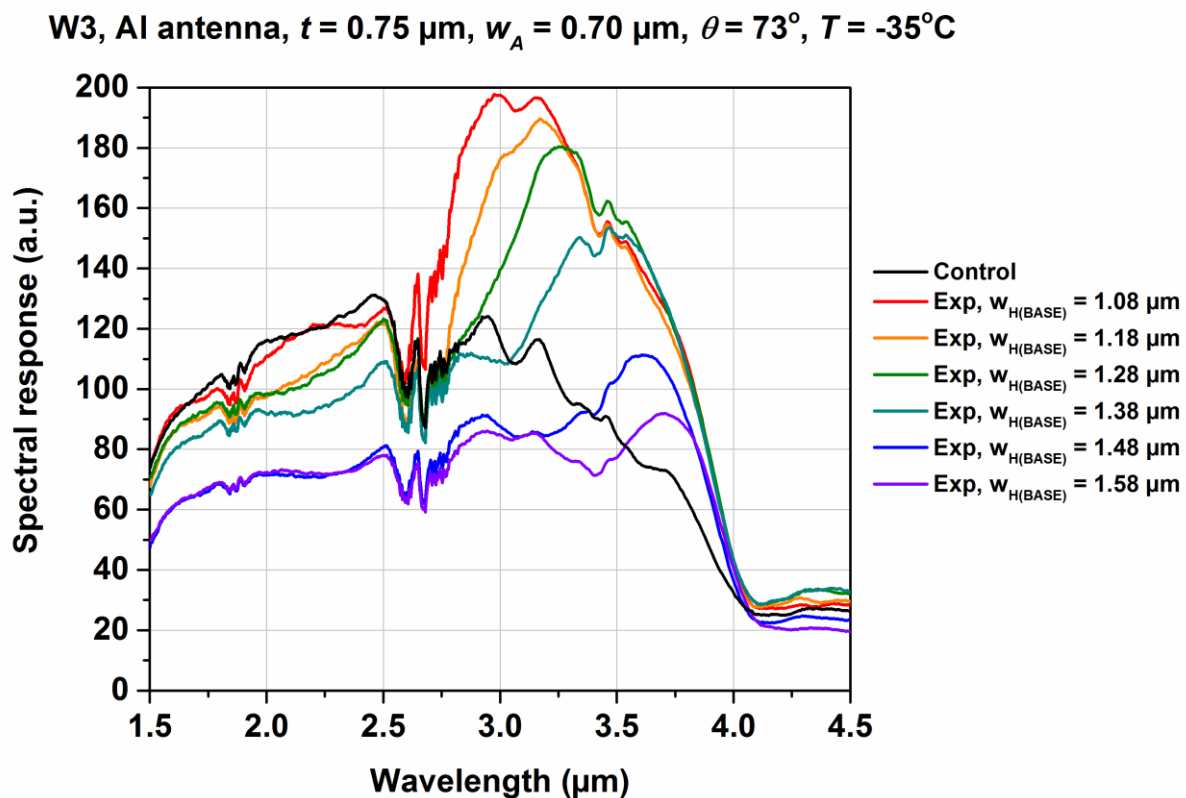
Figure 5.5.2.2: The antenna array signal enhancements obtained experimentally for an antenna thickness of 0.75 μm, and aperture width of 0.70, a side gradient of 73° and a temperature of -35°C. These antennas were grown of W3 with the same semiconductor epitaxial thicknesses as shown in figure 5.3.3 (b). The control (black line) has no antennas on the surface.

In the example shown in figure 5.5.2.2, the semiconductor zero bias resistance and spectral response was measured at -35 degrees C. At this temperature, the control R_0 for 200 μm square devices varies between 300 Ω and 420 Ω and the antenna substrate vary between 250

Ω and 350 Ω as indicated in figure 5.5.2.3. Whilst this range is significant all values are much greater than the TIA impedance, so variations in the attenuation of the signal between antenna devices and control devices is very little, thus eliminating the need for resistance normalisation during signal analysis. The difference is that the antennas on top have a thickness of 750 nm so as to focus the device to a 3.3 μm peak resonance target which is more in the centre of the $Al_{0.05}In_{0.95}Sb$ response bandwidth shown in black in figure 5.5.2.2.
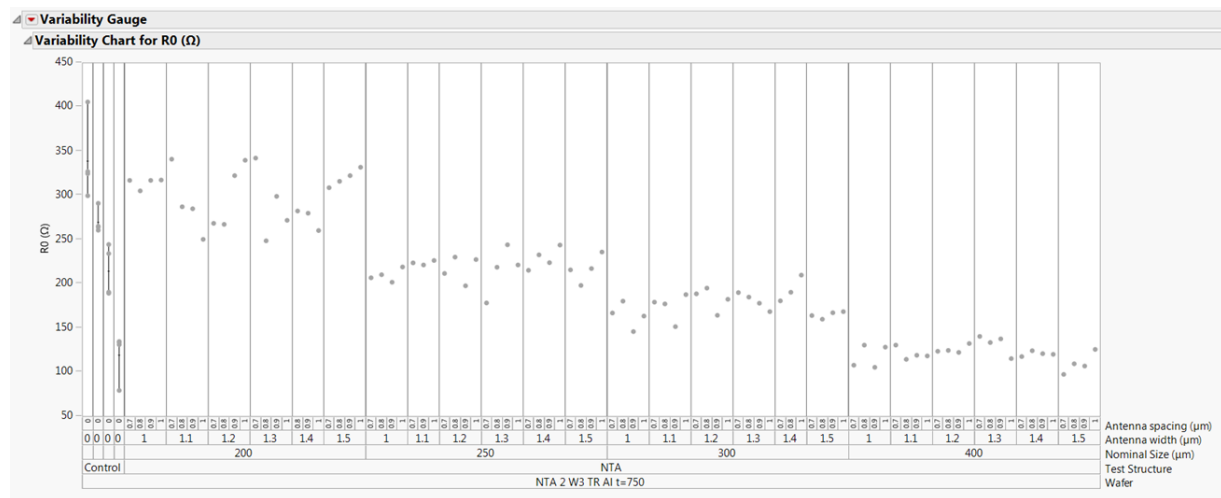
Figure 5.5.2.3: The zero bias resistance (R_0) of the antenna enhanced devices with 750nm thick antennas compared with the controls implemented on semiconductor homostructures of W3 at -35 degrees. The figure has results from mesas 200μm, 250μm, 300μm and 400μm in square length respectively. There is a measurement of at least one antenna hexagonal width and spacing for each grown antenna thickness. The 24 antenna variations are specified in figure 4.3.3.4.

It is encouraging to have a record of the devices' success that is almost entirely due to the merits of antenna resonance with significantly less signal normalisation required. However, if room temperature is a requirement for these gas sensing devices then heterostructures are the recommended method to minimise the effect of minority carrier generation.

5.5.3) NTA 2: Lossy antenna materials

To recap, the Q (quality) factor is dependent on the amount of energy the antennas can incorporate in their conducting material as well as the power loss in the system. When assessing the performance of different antenna materials in simulation it was noted that this also has an effect on the response bandwidth. It is therefore a worthy endeavour to assess whether different degrees of tangential loss (derived from the dielectric constant – see TABLE 3.9 and figure 3.6.1, equation 3) would produce significant advancements for the photodiode response. The results of which are displayed in figure 5.5.3.1.
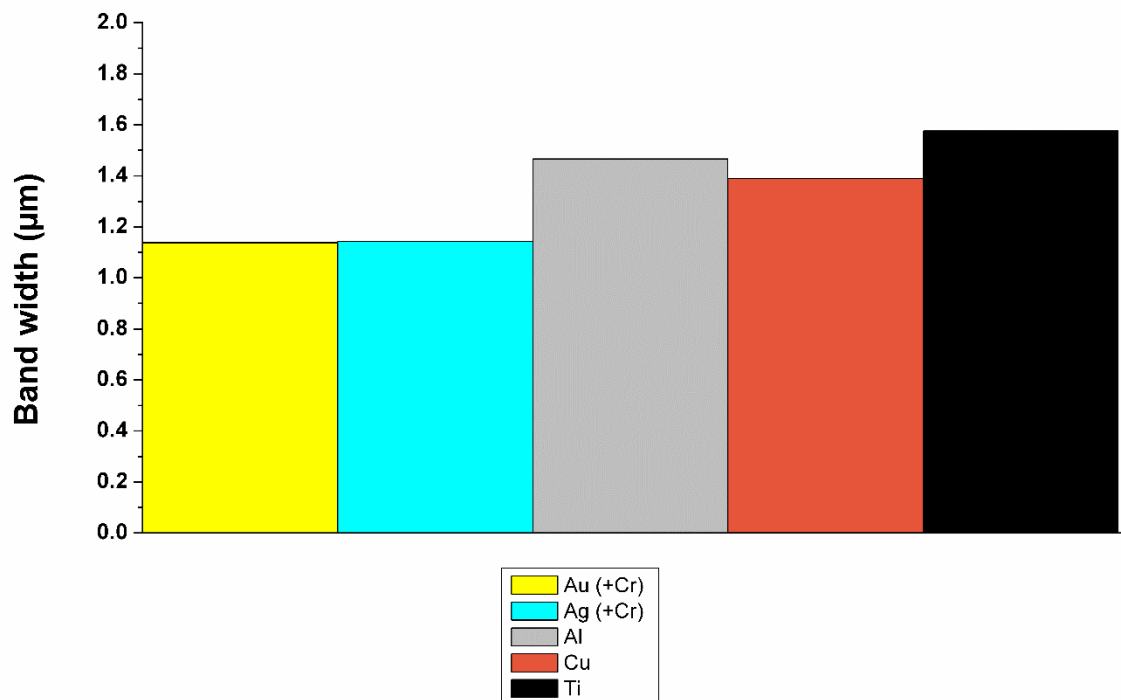
Figure 5.5.3.1: The size of the bandwidth and a function of different material. The materials that have been considered for this are Aluminium, Gold, Copper and Silver. This graph does not consider volume adjustments which need to be made if each material is to resonate at the same frequency. Instead these materials are kept at constant volumes.

The data in figure 5.6.1 shows that the bandwidth decreases when less energy is absorbed in the antennas. However, the change in bandwidth is decidedly not so significant that it can justify the added cost, manufacturing difficulty or loss of signal. This means that making

antennas out of aluminium or copper a reasonable manufacturing decision under the condition that they are not too lossy.

To provide better context how lossy the antennas can become before the losses are unjustifiably large, antennas made out of titanium were pursued both theoretically and practically. Ti is a material that was purposely picked for its lossy dielectric properties to verify that surface patterning alone is enough to get an i-type enhancement that can compete with other more conductive materials.

The shape of the antennas is the same as the Al antennas recorded in figure 5.5.1.6 (grown to a thickness of 750nm). The modelled results shown in figure 5.5.3.2 illustrate the differences in the normalised power absorbed in the semiconductor i-type when aluminium or titanium is used. The dielectric data for both are listed in the appendix.

It has been seen that the Ti antennas absorb more than the Al antennas by a factor of ten due to the metals poorer conductivity. The Al antennas have a peak wavelength at 83 THz because after coupling into the semiconductor, higher frequencies are absorbed first in the p-type and i-type. A higher proportion of the lower frequencies going straight through give the illusion of strict resonance peak at 90.8 THz. The Ti antennas are lossy as has been well established. It has an essence of the peak in aluminium antennas but the absorption as a function of attenuation coefficient supersedes absorption by a decreased reflectivity by a factor of 10.

The practical results are displayed in figure 5.5.3.3. The R_0 for each diode was measured and compared to previous device to ensure that any changes in signal are entirely to do with the antenna material.
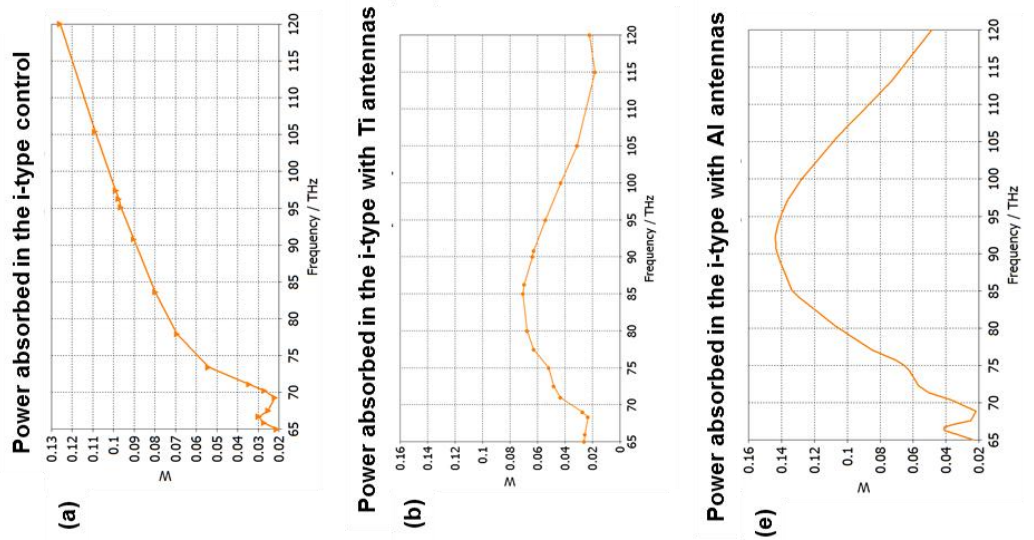
Figure 5.5.3.2: The simulated degree of power absorbed as a function of frequency in Ti antennas. The input power is 0.5 normalised Watts (a) the control $Al_{0.05}In_{0.95}Sb$ i-type layer (b) the $Al_{0.05}In_{0.95}Sb$ i-type layer with Ti antennas (c) the Ti antenna (e) the $Al_{0.05}In_{0.95}Sb$ i-type layer with Al antenna (f) the Al antenna. (d) and (g) are illustrations of the power density variation within the substrate with different antenna metals on top where (d) is pattern with Ti antenna and (g) is patterned with Al antenna. Note: 65 THz – 120 THz is equivalent to 2.50 μm – 4.61 μm.
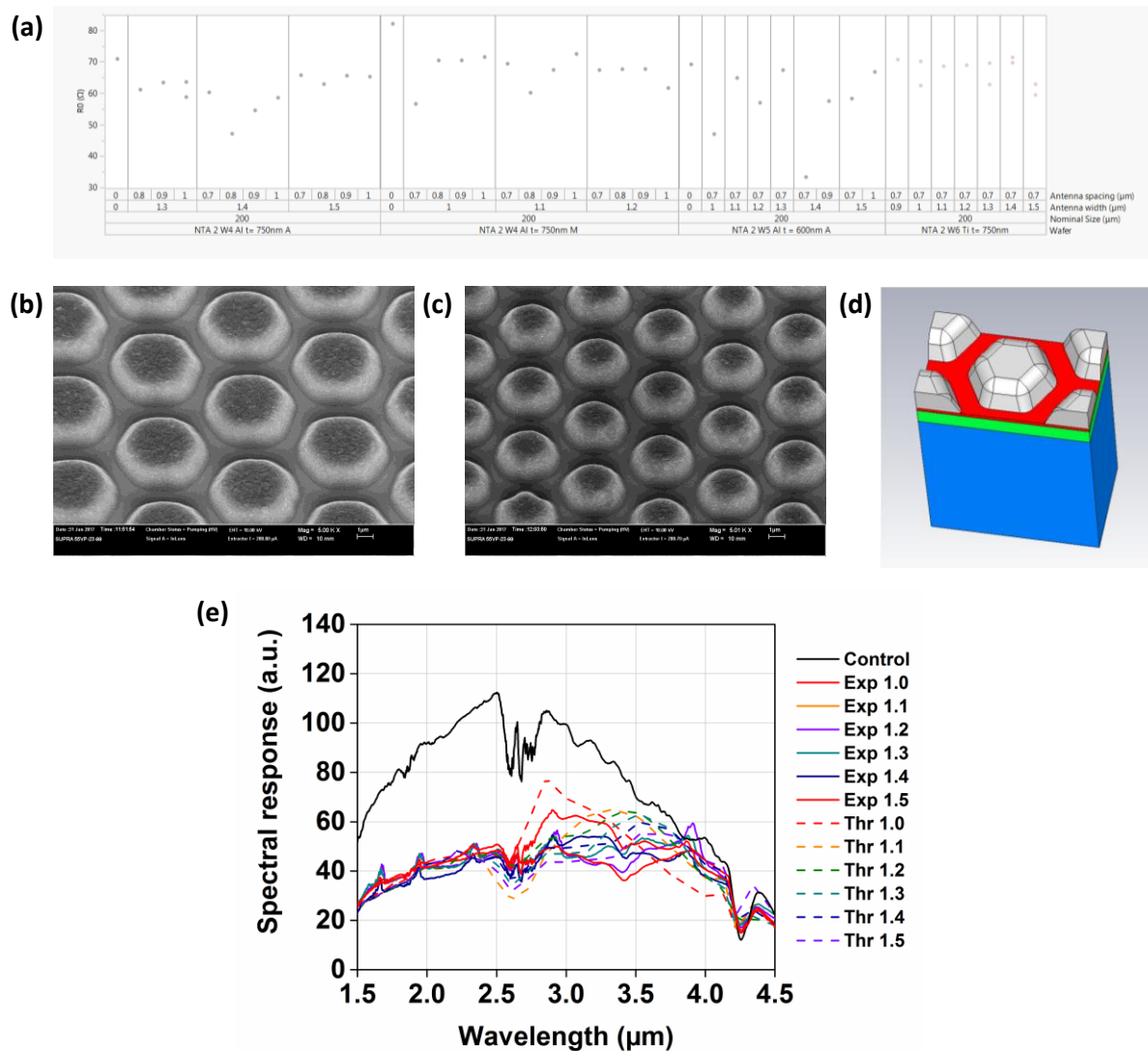
Figure 5.5.3.3: Experimental and theoretical results comparison of the Ti antennas (a) The R0 of the devices with the Ti antennas compared to previous results. (b) The developed Ti antennas when $w_H = 1.5$ µm and $w_A = 0.7$ µm. (c) The developed Ti antennas when $w_H = 1.0$ µm and $w_A = 0.7$ µm. (d) Model alteration done to replication a higher degree of rounding on Ti antennas. (e) The experimental (Exp) readings (solid) and the theoretical (Thr) spectral response readings (dashed) of the diode with the Ti antennas.

The experimental results demonstrate agreement with the model and that significantly less photon energy is being absorbed in the i-type region at the required wavelength. The simulation was done assuming that the Ti antennas would have the same development as the experimental Al ones. However, Ti appears to be much more susceptible to rounding (produces larger side wall angles). This is why the agreement between the theoretical and experimental results is not as close as to that of the results shown in figure 5.5.1.6, but the results are still in general agreement, demonstrating that antenna conductivity is an important

factor during antenna design and development and the surface cannot simply by corrugated to achieve signal enhancements.

5.6) Chapter 5 conclusion

All fabricated semiconductor photodiode enhancements have been analysed in this chapter to verify antenna based improvements to the photodiode quality. NTA 1 is the mask prototype which consists of a micro-antenna array fabricated on a plain 5% AlInSb layer. It has shown examples of an antenna length based dependency with the position of the lowest surface reflectivity trough. The data also features a reflectivity trough based on the size of the aperture width, but simulation analysis confirms that a corrugated surface will not achieve the intended S/N ratio improvement as the enhancements are too reliant on the antenna conductivity.

The NTA 1 devices were tested with a FTIR spectrometer. This is the same fundamental way the $Al_{0.05}In_{0.95}Sb$ attenuation coefficient was derived. The dielectric constant of the $Al_{0.05}In_{0.95}Sb$ material was derived by extension and integrated into the CEM simulations to produce a hybrid model with enhanced accuracy.

Side gradients are featured in all fabricated antenna arrays as a result of antenna rounding during development. This has undesirable consequences such as lowering the antenna quality Q factor and blue shifting the resonance peak. The antenna conducting length can be altered to retune the wavelength of peak response and (with a factor enhancement of between 1.56 and 1.70) the response is still an improvement to applying an antireflection coating on the photodiode surface, but a more refined side gradient is still desirable for future development.

The NTA 2 semiconductor devices were fabricated with the intent to capitalise on localised light focusing. Their thin semiconductor epitaxial layers were able to do so but not without

diode leakage that comes from enhanced minority carrier generation from surface conducting materials in close proximity to the i-type layer. The used of heterostructures and low temperature operating conditions have been investigated to minimise this effect. Both have been successful at reducing the signal loss to below a 5% difference. However, growing heterostructures in the semiconductor epitaxial layers was preferable because of the advantage of room temperature operation.

6) Chapter 6: Semiconductor photodiode alternative designs for further development

Alternative designs to the antenna enhanced semiconductor photodetectors are investigated in this chapter. The aim is to demonstrate more elaborate but fundamentally more beneficial designs that can enhance the signal-to-noise ratio even further than simply developing a better side gradient for the antenna arrays demonstrated in chapter 5. New considerations will include dielectric layers as an alternative means to reduce localised minority carrier generation, selective removal of the semiconductor to minimise the volume based noise, and designs which verify whether enhanced coupling is possible with considerably smaller antenna array then what has been used for higher order harmonic resonance. These design alterations are presented here as theoretical models on the grounds that most of them have a considerably more difficult manufacturing procedure. The aim of this chapter is to use the same hybrid CEM model that has been fully developed from previous chapters to provide context the how efficient the antenna designs in chapter 5 are compared to how beneficial they can possibly be.

6.1) Dielectric anti-reflection (AR) layers

Although cooling the devices or use of the quantum barriers has minimised the minority carrier generation influence, antireflection layers are considered here as a design advancement to reduce the minority carrier generation further while providing a transparent layer so that coupling into the semiconductor is unaffected.

It is common practice to use metal oxides as anti-reflection coatings when they are grown at the right thickness to be resonant with the incoming target wavelength[97-98]. Aluminium oxide (Al_2O_3) is the anti-reflection coating considered in this modelling experiment. The dielectric properties for this material are provided in the appendix.

For the examples given in this modelling scenario, the target wavelength is taken to be 3.3µm. What the thickness has to be depends on the dielectric constants, but for an alumina layer it is roughly 0.5 µm 0.6 µm, as shown figure 6.1.1 (b). To simplify the problem, perfect shapes are assumed.

(a)

AR coating
p-type
i-type
n-type

(b)

(c)
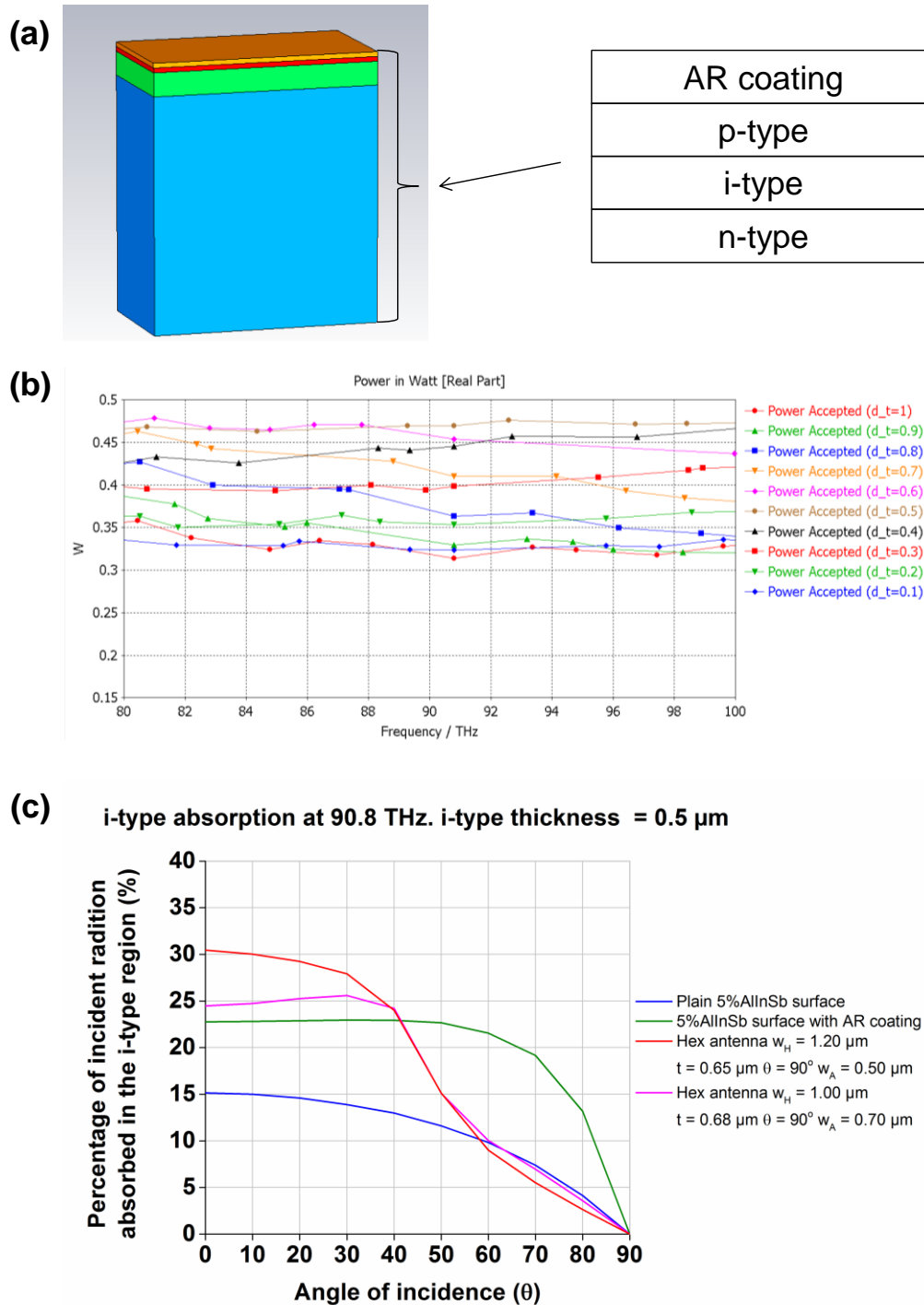
Figure 6.1.1: The antireflection dielectric layer theoretical experiment. (a) The Al_2O_3 anti-reflection coating 3D visual aid (b) A parameter sweep demonstrating the optimum dielectric layer thickness for the target wavelength of 3.3 μm or 90.8 THz .The least amount of reflectivity is shown when the anti-reflection coating is 0.5 μm in thickness. 22.90% of the incoming light is absorbed in the i-type region in this instance. (c) The percentage absorbed in the i-type region as a function of the angle of incidence for a plain 5%AlInSb semiconductor (blue) the plain $Al_{0.05}In_{0.95}Sb$ semiconductor with an anti-reflection coating 0.5 μm (green), the hexagonal antenna design in the NTA 2 mask set for a 1.00 μm hexagonal width and 0.68 μm in thickness (magenta) and the fully optimised hexagonal antenna design (red). Note; 80 THz - 100 THz = 3.00 μm – 3.75 μm

Figure 6.1.1 (c) provides additional information to figure 5.3.5, where the fully optimised hexagonal antenna design (red graph) graph is featured. The absorption in the same i-type thickness 0.12 μm to 0.62 μm in depth is shown for the control (blue graph) and the control with an antireflection coating on the surface (green graph). The magenta graph is a design with a justifiable antenna width to aperture width ratio for a realistic lift-off outcome during manufacturing. It is this antenna design that will be used for further development in this section where perfect side gradients are assumed so that any changes in the i-type absorption will be due to the new dielectric layer and not any discrepancies in the antenna side gradients.

Figure 6.1.2 (b) shows that the dielectric layer causes a more lateral distribution before transmission into the i-type layer. The minimum dielectric thickness to mitigate the minority carrier generation would be of interest because the thinner the dielectric layer underneath the antenna array is, the lower the surface reflectivity will be. Figure 6.1.2 (c) demonstrates an increase in the scattering parameter with AR coating thickness while figure 6.1.2 (d) shows that the i-type absorption has been reduced to 23% from the 26% it would have had with no AR coating at all, according to 6.1.1 (c). There is also no substantial improvement in the bandwidth.
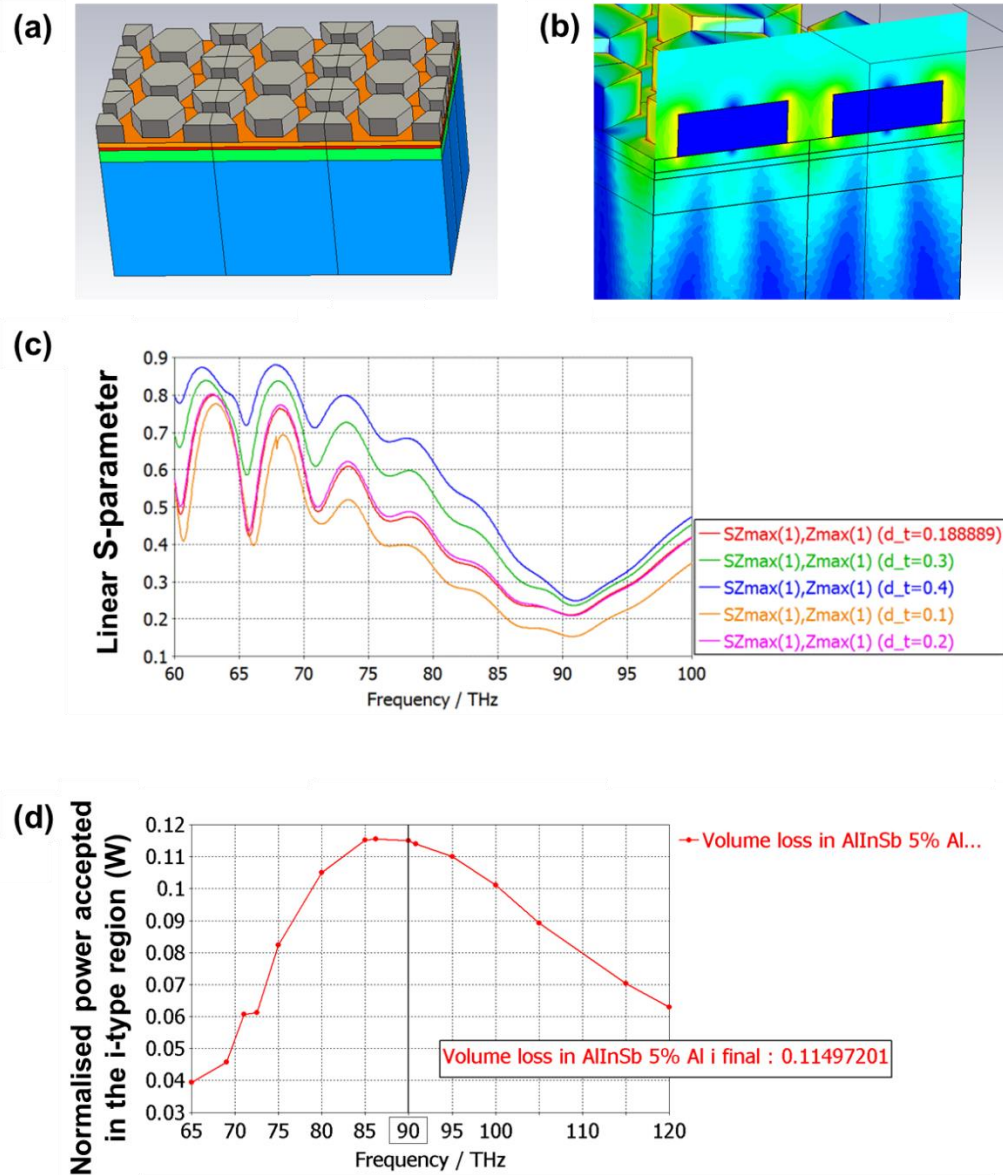
Figure 6.1.2: The transparent dielectric antenna buffer theoretical experiment featuring the hexagonal antenna design in the NTA 2 mask set. $w_H = 1.00$ µm, $t = 0.68$ µm $w_A = 0.7$ µm: (a) Schematic diagram showing the Al_2O_3 dielectric layer implemented underneath the antenna components visual aid. (b) The power density distribution as show in the power flow field monitor. (c) The thickness parameter sweep to determine the antenna thickness that will produce the optimum S-parameter. (d) The degree of i-type absorption with antennas on top of a 0.1µm thick dielectric layer showing a peak of about 0.115 W (or 23% of the total 0.5 W incident power). Note; 60 THz – 120 THz = 2.5 µm – 5.00 µm.

Overall, a dielectric coating underneath the antenna array only degrades the design, with the only redeeming factor being minority carrier mitigation. It is for this reason that this design is only recommended if further minority carrier reduction takes precedence over signal accumulation.

6.2) Selective removal of the semiconductor

Attempts thus far to amplify the S/N (signal-to-noise) ratio have been to amplify only the signal. In this section, the signal-to-noise ratio increase when considering a reduction in noise will be addressed. Equation 3.1.5 depicts the photodetectors detectivity and its relationship to the noise inducing semiconductor generation and recombination rate. The equation also addresses the benefits of increasing the optical path length by means of localised focusing. This section explores the concept of reducing the bulk volume of the semiconductor photodiode and using antenna influenced localised focusing to focus the signal on the remaining i-type volume.

6.2.1) Dielectric cavities

Figure 6.2.1.1 shows the initial design of how the semiconductor is removed in areas when there is no localised light focusing (i.e. directly underneath the antenna array). This region is considered an inefficient use of volume that generates a higher ratio of generated noise than absorbed signal and for the purposes of the modelling experiment will be changes to a transparent dielectric material (Al_2O_3). Figure 6.2.1.1 provides visual aid to this experiment.
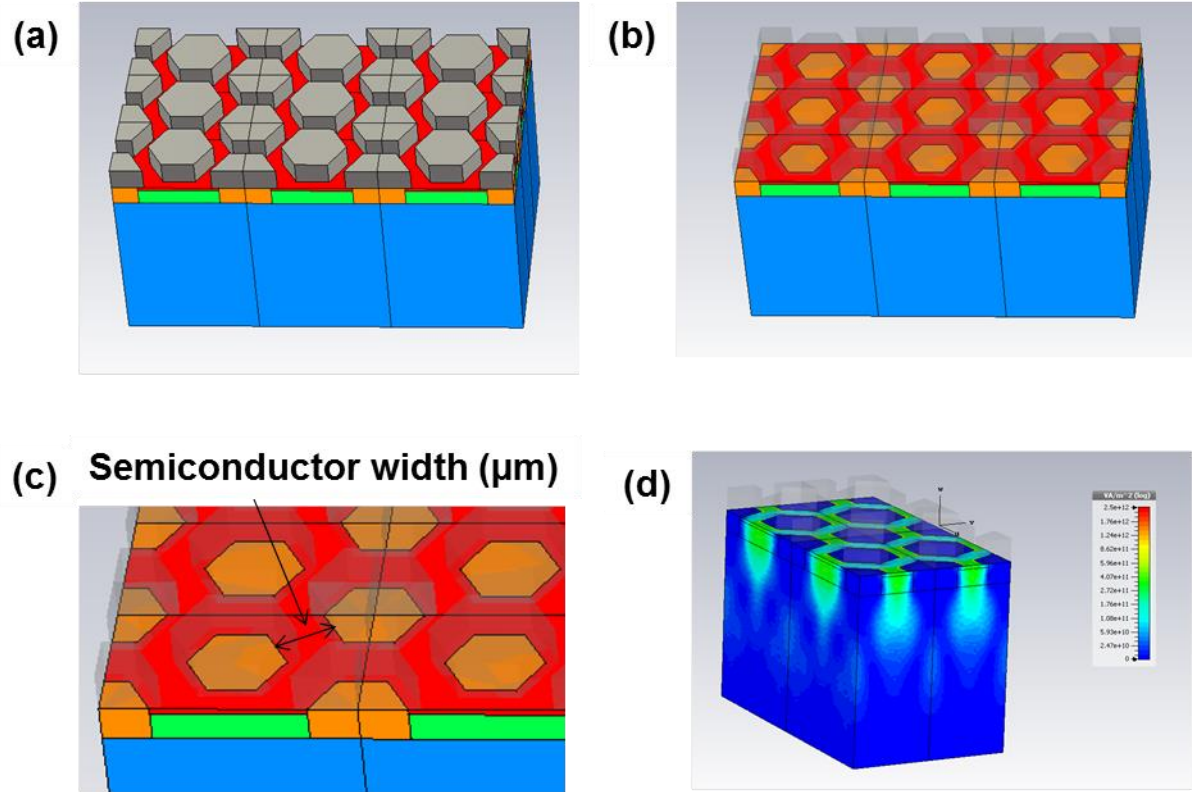
Figure 6.2.1.1: Simulations of semiconductor selective removal. A hexagonal antenna array with $w_H = 1.00$ µm, $t = 0.68$ µm $w_A = 0.7$ µm (a) The 3D modelling diagram demonstrating the trimmed out Al_2O_3 dielectric layer (b) The 3D modelling diagram demonstrating the cavities underneath the antenna array (c) The semiconductor width (d) The power flow diagram demonstrating that localised focusing can once again be obtained.

Figure 6.2.1.2 shows the (S/N) values and the overall S/N enhancement factor. When comparing the power accepted in the cut out semiconductor volume with antennas, P_A, to the i-type power accepted in the control (no antennas, no selective removal), given here as P_C where P_C is 0.07638 W at 90.8 THz. The normalised S/N factor, A is given in equation 6.2.1 under the assumption that there are negligible contributions to leakage current, and therefore noise, from the contact region or the periphery of the device.

$$A = \frac{\left(\dfrac{P_A}{P_C}\right)}{\sqrt{\left(\dfrac{V_I}{V_U}\right)}}$$
(6.2.1)

Where V_I is the volume of the minimised i-type region and V_U is the maximum volume of the

i-type region in the entire unit cell (i.e. the control i-type). The denominator is the root

volume because of the detectivity dependence on it (see equation 3.1.5). Figure 6.2.1.2

indicates that the optimum condition is to have the cavity underneath the antenna 0.1 μm

wider than the antenna aperture width on top. Note: all results in equation 6.2.1 are obtained

via simulation. The simulation set-up is based on integrated data and calibration during

analysis with practical data in chapter 5.
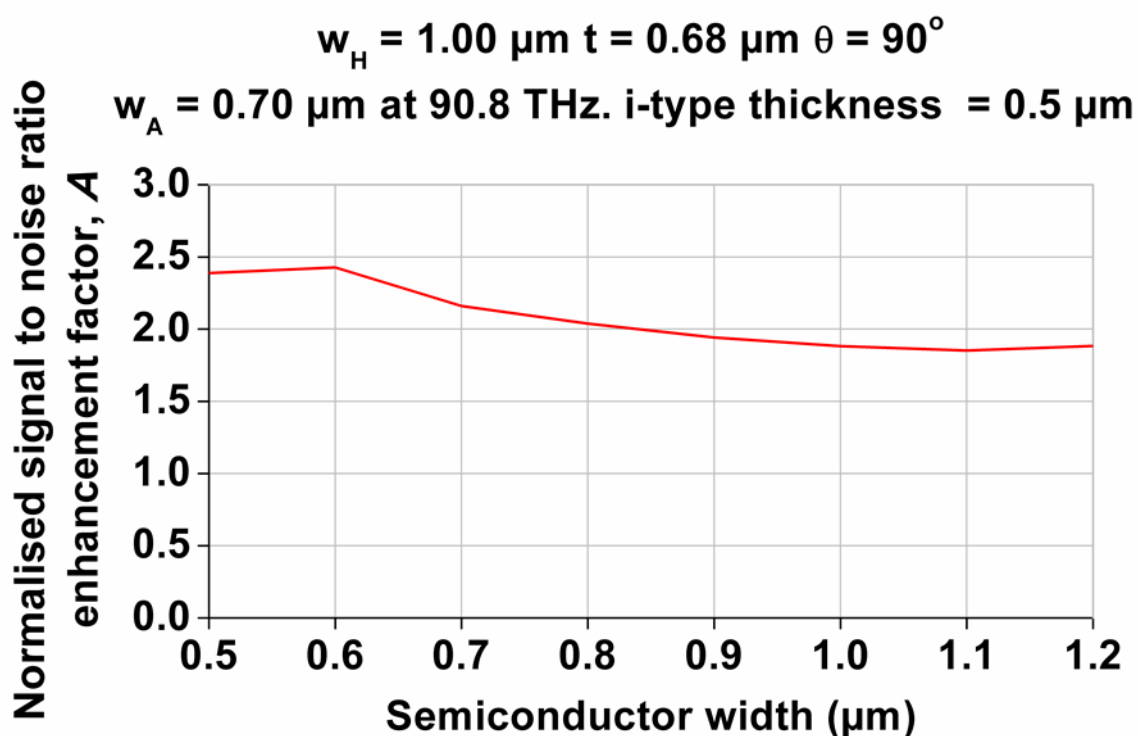
Figure 6.2.1.2: Enhancement factor of the normalised S/N ratio enhancements compared to bulk material as a function of semiconductor width.

The benefit of increasing the S/N ratio by eliminating unnecessary volume is just under a

factor of 2.5 increase compared to the control. This is considerable and makes the proposal to

developed cavities underneath the antenna arrays a justifiable proposal for future

development, despite the precision difficulty in manufacturing and aligning.

6.2.2) Lateral semiconductor optimisation

Taking this research a step further, the semiconductor size has been minimised to not only determine where the regions of greatest focusing is in the semiconductor, but also to determine the semiconductor size that must be used to get the maximum power density (Wμm^{-3}) per unit volume. Figure 6.2.2.1 (a) shows this model design. Figure 6.2.2.1 (b) is the same as (a) except with the antennas made to be transparent. The semiconductor length and width are adjusted as depicted in figure 6.2.2.1 (c). The semiconductor design with the optimum parameters for the best possible power density shown in figure 6.2.2.1 (d) and (e).
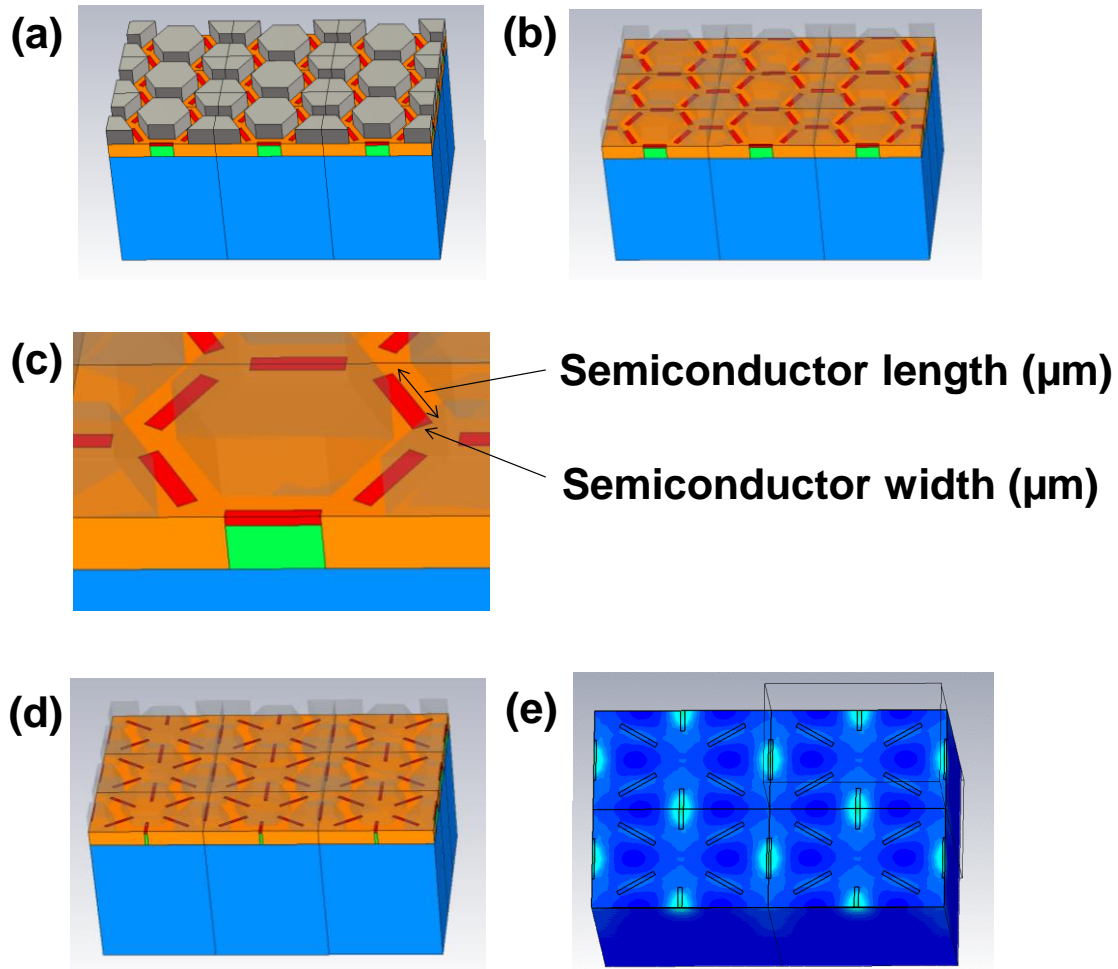
Figure 6.2.2.1: Simulated selective optimisation featuring an antenna array with w_H = 1.00 μm, t = 0.68 μm and w_A = 0.70 μm; (a) (b) and (c) show the 3D modelling diagram featuring a minimised semiconductor volume. (d) The optimum semiconductor length and width in regards to the i-type concentration within the apertures. (e) The power density field monitor with a z-axis cutting plane in the i-type centre.
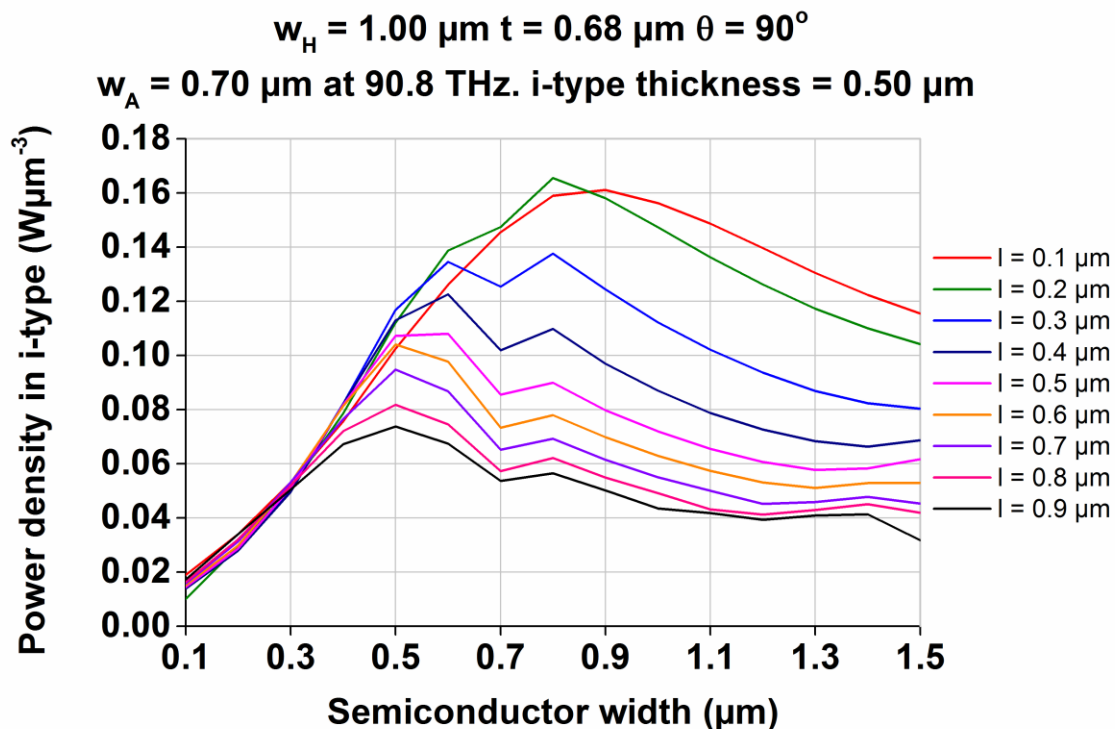
Figure 6.2.2.2: The power density readings as the semiconductor length (l) and semiconductor width varies for a minimised semiconductor size.

The power density in the i-type region is shown figure 6.2.2.2 versus semiconductor width with semiconductor length as a parameter. The results show that the maximum amount of light focusing occurs in the centre of the aperture that is perpendicular to the antenna width. For this reason a small semiconductor length provides a more favourable power density. As the length increases from the optimal the maximum amount of power density is obtained if the width is reduced. This indicates the power density AEI grid within the i-type is of the form of an ellipsoid shape. This is visually demonstrated in figure 6.2.2.1 (e).

Figure 6.2.2.3 shows the power density described in figure 6.2.2.2 applied to the normalised enhancement factor given in equation 6.2.1.
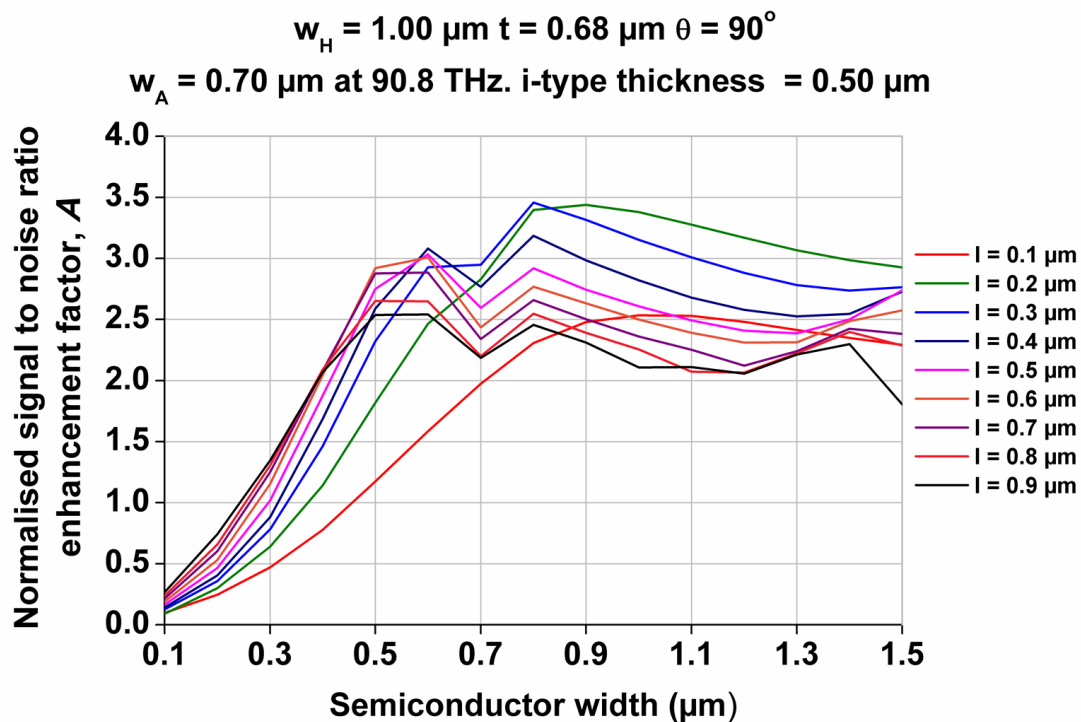
Figure 6.2.2.3: Simulated enhancement factor of the normalised S/N ratio compared to bulk material when considering semiconductor length (l) and semiconductor width adjustments shown in figure 6.2.2.1.

Although the optimum power is situated in the centre of the ellipsoid, there is a limit to how small the semiconductor can be designed before the loss is signal starts to supersede the reduction in noise. In this model, the optimum semiconductor size is 0.3 μm in length and about 0.8 μm in width. This means that selective removal of the semiconductor can provide a 3.46 factor increase in S/N ratio compared to the bulk substrate.

There are changes in the peak resonance wavelength position as the size of the semiconductor varies as indicated in figure 6.2.2.3. This is because the semiconductor impedance of the remaining material is a function of its volume. This is demonstrated in figure 6.2.2.4.
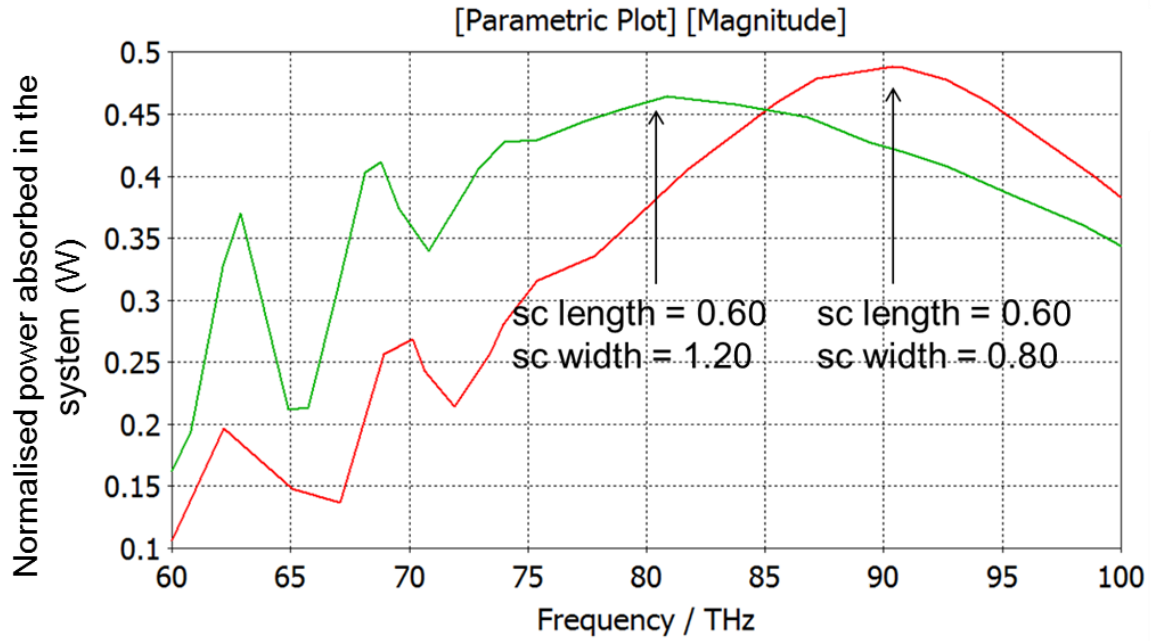
Figure 6.2.2.4: The change in peak response in the system as the size of the semiconductor varies, but the antenna parameters remain constant. $w_H = 1.00$ μm, $w_A = 0.70$ μm, t = 0.68 μm.

It is therefore noted that taking readings at one particular frequency (i.e. always at 90.8 THz) will not necessarily mean the response is at its peak i-type absorption value. To demonstrate this, the normalised power absorbed in the i-type is displayed in figure 6.2.2.5 when the responses were taken at their peak value and not a specific frequency.
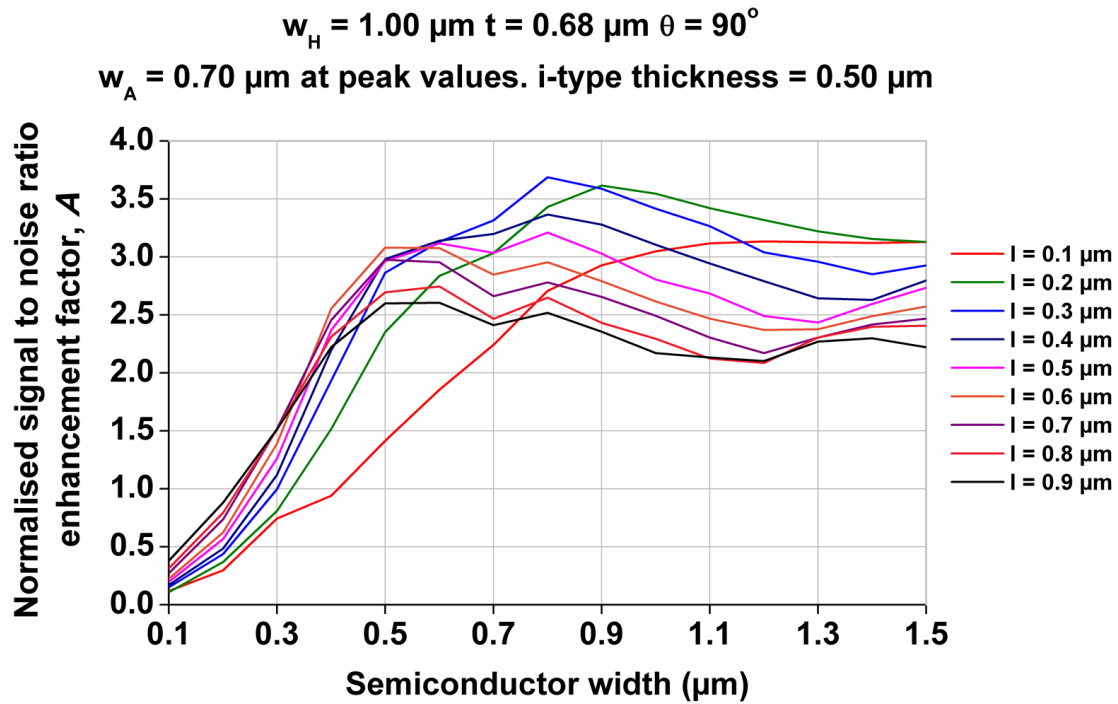
Figure 6.2.2.5: The S/N enhancement factor compared to the bulk material when taken at peak values.

Under these conditions a semiconductor cut outs will provide an optimum enhancement factor of 3.69 as shown in figure 6.2.2.5, but it will shift the peak frequency to 3.45 µm (86.885 THz), because of a more favourable frequency impedance matching based on semiconductor volume and by extension, the resistance of the volume. There are instances where the semiconductor size will produce a peak at 90.8 THz and although reducing the semiconductor size will blue shift this peak, the benefits of the reduction in noise will supersede the signal loss as a result of being a sub-optimum value. However, if there is a lack of signal alignment between the antenna peak response and the semiconductor volume response, the optimum signal will be compromised.

6.2.3) Semiconductor thickness optimisation

In chapter 5, an i-type thickness of 0.5 µm in thickness was examined so that the focusing effect featured in the antenna design could compete with anti-reflection coatings while also demonstrating potential benefits in semiconductor size reduction. It is known from external literature and our own investigations that with regards to the signal/noise generation in a standard semiconductor, this i-type thickness is too thin to produce optimum S/N ratio[99]. The i-type regions are typically grown to 3 µm in thickness, beyond which the increase in generated noise supersedes the increase in signal absorption. The data from figure 5.1.6 is reused here in figure 6.2.3.1 with additional information regarding the per root unit volume with a perfect antireflection coating on the surface (green graph), an antenna array when $w_H =$ 1.00 µm, t = 0.68 µm, w_A = 0.70 µm on the surface (magenta graph) and an optimised antenna array when w_H = 1.20 µm, t = 0.65 µm, w_A = 0.50 µm. Due to the antenna focusing effect, the antennas can have an optimum thickness of 1.0 µm, but varies depending on how far you are off optimum resonance conditions whereas the control with an anti-reflection coating will reach an optimum thickness at about 2.2 µm at a frequency of 90.8 THz. The parameter listed in the red graph may be difficult for an antenna lift-off process, but considering the benefits it is worth further investigation to verify whether it is possible.
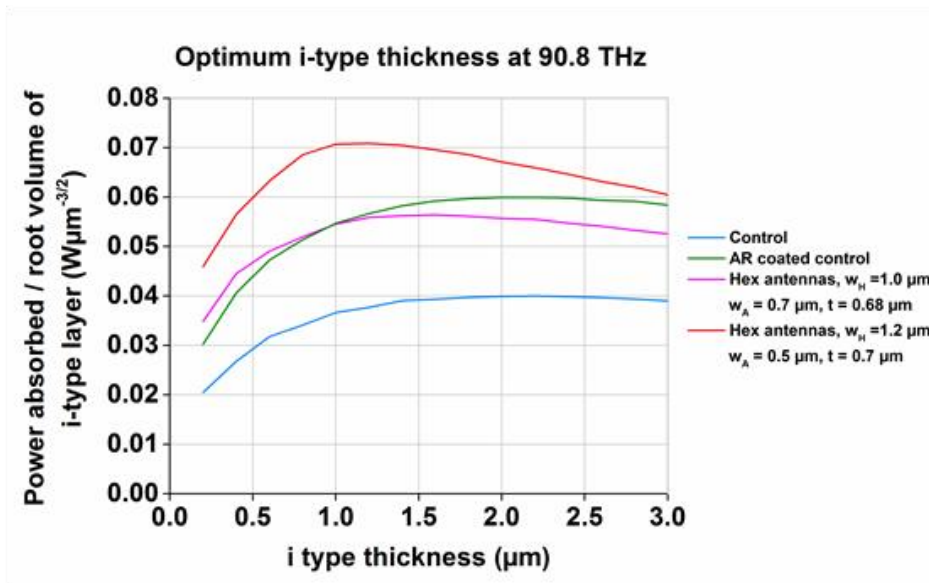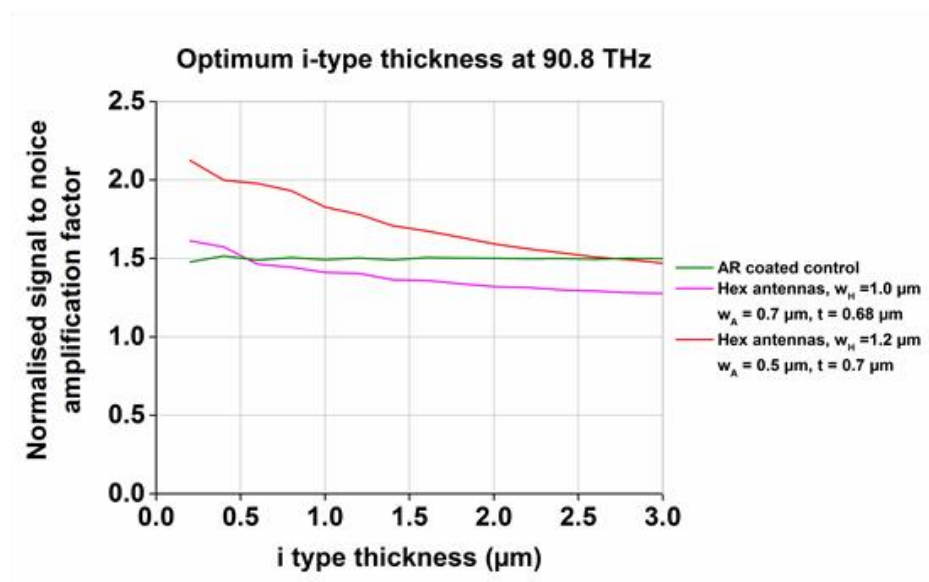
Figure 6.2.3.1: Enhancements as a function of i-type thickness. (a) The S/N ratio of the photodiode as a function of i-type thickness within the control (blue), the control with an anti-reflection coating (green), and when under the influence of an hexagonal antenna array when w_H = 1.00 µm, t = 0.68 µm, w_A = 0.70 µm (red) and when w_H = 1.00 µm, t = 0.68 µm, w_A = 0.70 µm (magenta). No selective removal is featured in this graph. (b) The S/N factor increase compared to the control for an anti-reflection coating (green) and a hexagonal antenna array when w_H = 1.00 µm, t = 0.68 µm, w_A = 0.70 µm (red) and when w_H = 1.00 µm, t = 0.68 µm, w_A = 0.70 µm (magenta). The p-type thickness and n-type thickness is 0.12 µm and 5.0 µm respectively for all cases.

Selective removal of the semiconductor antenna array gives a much better improvement in S/N ratio compared to an anti-reflection coating. The next part of this investigation is to optimise the i-type thickness after the lateral semiconductor parameters have been removed.

When increasing the i-type thickness from 0.5 μm to 1.6 μm the semiconductor length and width need to be re-optimised to absorb a much more centralised power density focusing (i.e. the semiconductor length and width is much more similar). The regions away from the central point of the aperture have been cut out due to high power densities in these regions near the surface, but a much higher dissipation rate deeper into the semiconductor.
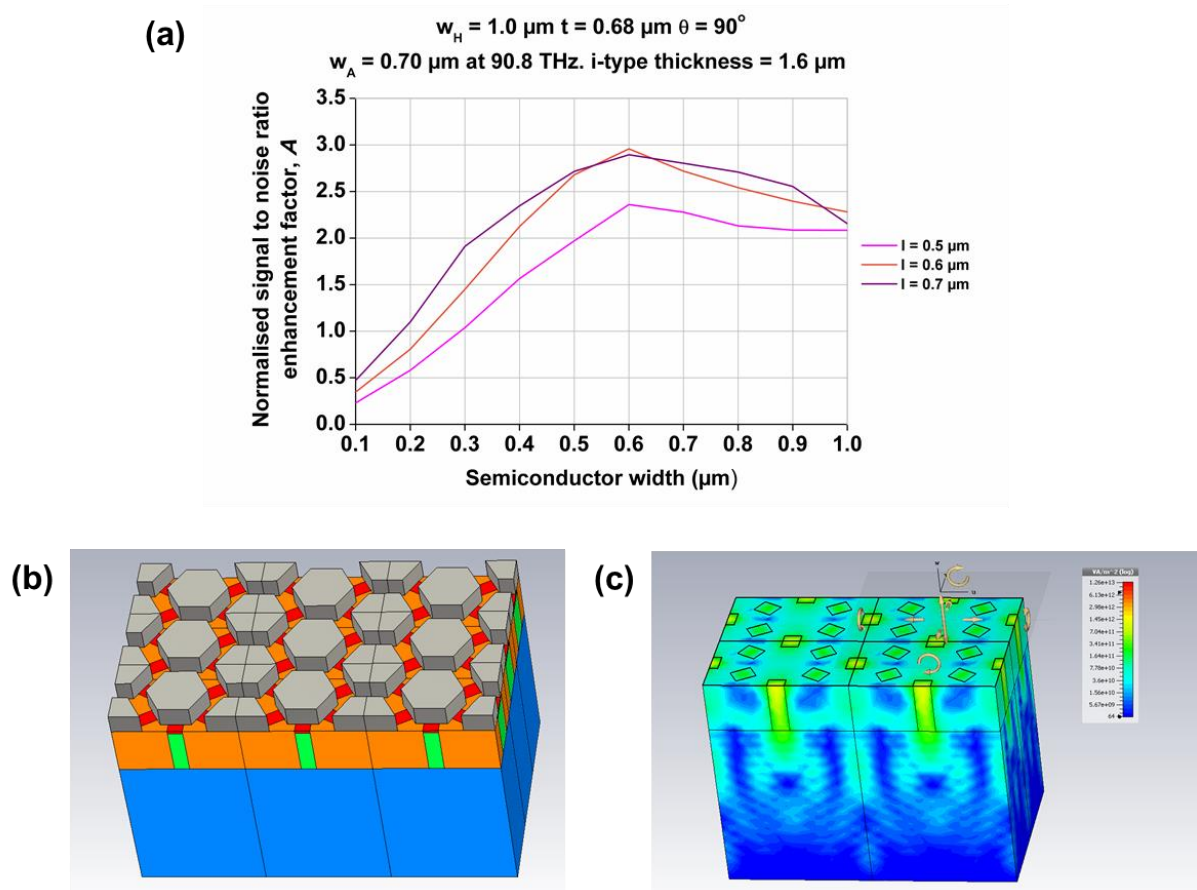
Figure 6.2.3.2: Optimum semiconductor size for a thicker semiconductor i-type. (a) Parameter optimisation of the semiconductor cut out for an i-type region thickness of 1.6 μm. (b) A 3D modelling diagram featuring a minimised semiconductor volume where the semiconductor width = 0.6 µm and the semiconductor length = 0.6 µm. (c) A power density field monitor of signal funnelling into the re-optimised semiconductor volumes.

Antennas benefit semiconductor photodiodes by virtue of enhanced coupling and localised focusing in close proximity to the semiconductor surface. As such, the thicker the i-type gets, the more this beneficial effect diminishes. From these observations, antennas and selective removal are most useful for very thin semiconductor layers.

6.2.4) Semiconductor interconnections

The problem remains that the semiconductor parts need to be interconnected in order to read out the stimulated photocurrent when probing the device. The design which takes this into account is shown in figure 6.2.4.1 (a) interconnecting parts will cause degradation in S/N ratio, but the enhancement is still substantial. With reference to figure 6.2.2.4, figure 6.2.4.1 (b) shows the S/N ratio enhancements at the peak response for a hex antennas ($w_H = 1.00$ μm, $t = 0.68$ μm and $w_A = 0.70$ μm) design as the peak signal varies between a frequency of 80 THz and 100 THz (3.00 μm - 3.74 μm) and figure 6.2.4.1 (c) shows the S/N ratio enhancements at the peak response for an optimised antenna design. Note: the data obtained for 6.2.4.1 (c) was obtained using the same method as 6.2.4.1 (b).

At a semiconductor width of 2.5 μm both semiconductor designs are interconnected. This causes degradation in the signal-to-noise ratio from 8.7 to 6.5 for the optimised antennas, and from 3.69 to 3 for the lesser design. There is however, another way to interconnect the cut out volumes. A metal network can be introduced to interlink the semiconductor. Figure 6.2.4.2 (c) shows the optimum semiconductor length and width that are interconnected with an aluminium contact 50 nm in thickness and 200 nm in width for the optimised antenna design. Silver and titanium are also considered where silver has a 5 nm adhesive layer featured.

(a)

Semiconductor
interconnections
underneath the
antennas

(b)

$w_H = 1.00$ µm $t = 0.68$ µm $\theta = 90°$
$w_A = 0.70$ µm at peak values. i-type thickness = 0.5 µm

(c)

$w_H = 1.20$ µm $t = 0.65$ µm $\theta = 90°$
$w_A = 0.50$ µm at peak values. i-type thickness = 0.5 µm
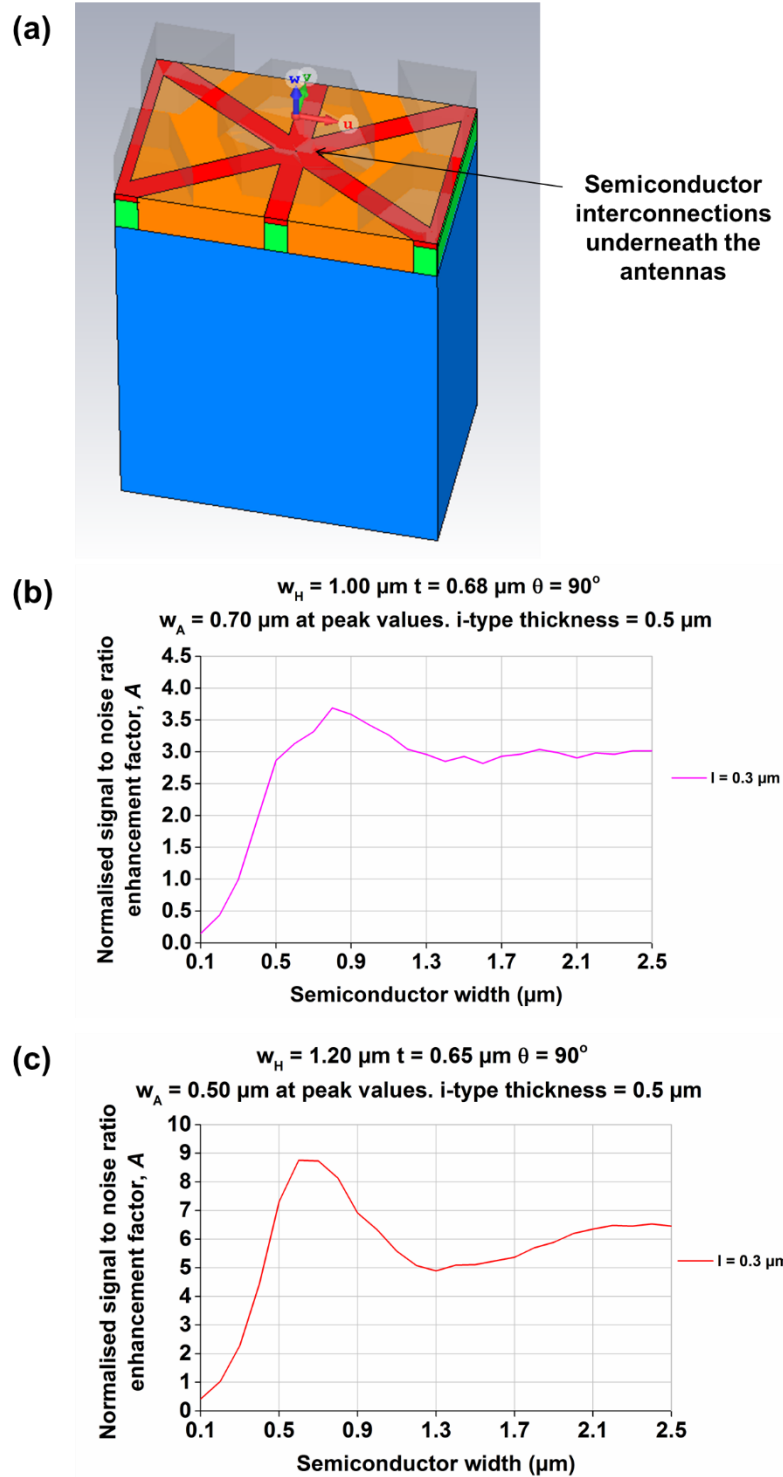
Figure 6.2.4.1: Interconnecting semiconductor sizes. (a) Schematic diagram of the interconnected semiconductor parts, when the i-type thickness is 0.5 µm. The semiconductor length is 0.3 µm and the semiconductor width is 2.5 µm. (b) The normalised S/N enhancement factor vs. semiconductor width when the semiconductor length, l = 0.3 µm for a hex array where w_H = 1.00 µm, t = 0.68 µm and w_A = 0.70 µm. (c) The normalised S/N enhancement factor vs. semiconductor width when the semiconductor length, l = 0.3 µm for a hex array where w_H = 1.20 µm, t = 0.65 µm and w_A = 0.50 µm.
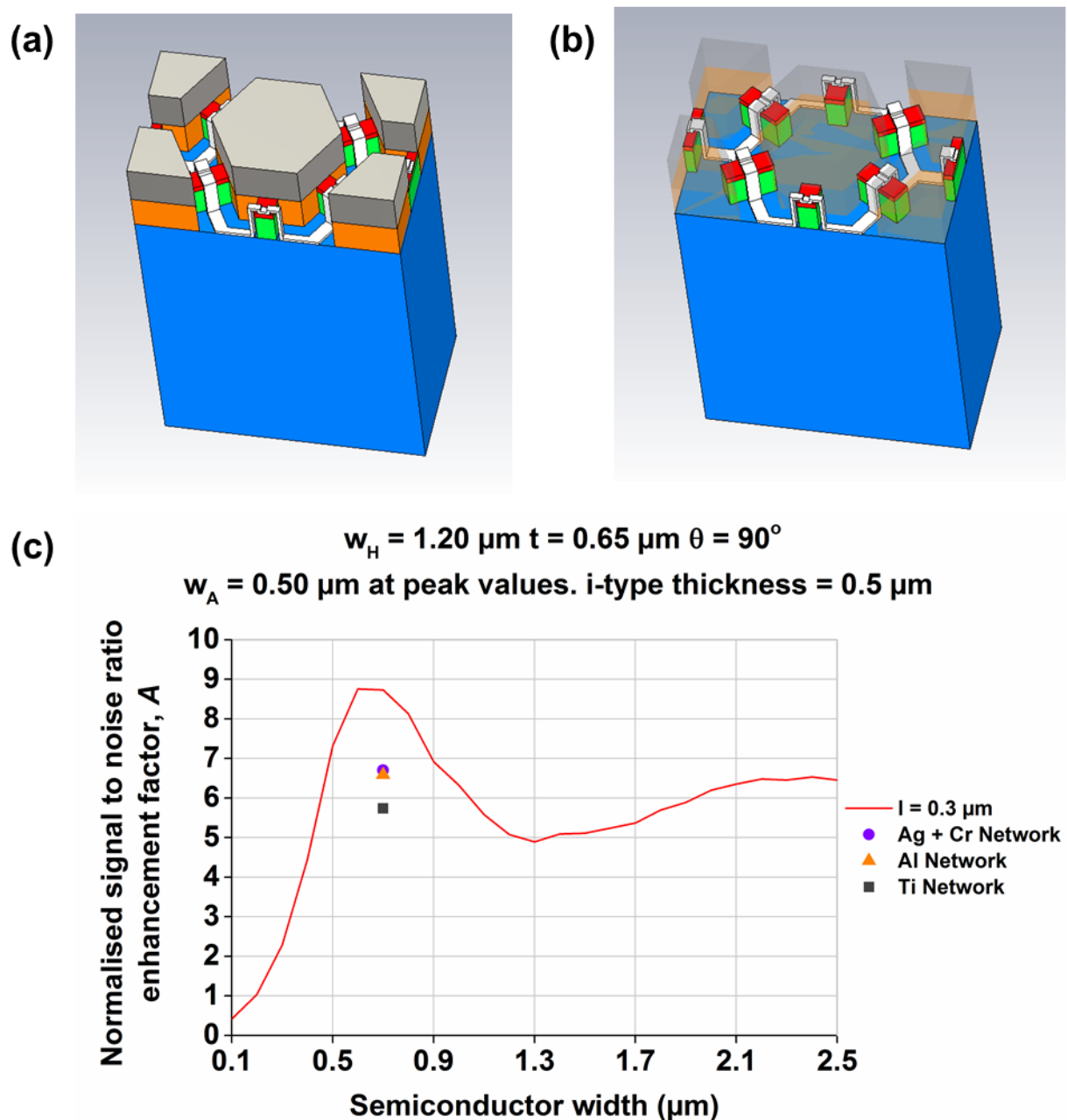
Figure 6.2.4.2: Interconnecting networks for an optimised antenna array. (a) CAD based diagram showing the optimum semiconductor parameters with a feed network included (white). (b) An image that provides a better view by making the antenna and dielectric support transparent. (c) A graph of the normalised S/N enhancement factor with a constant semiconductor length (l) at 0.3 µm and a varying semiconductor width where $w_H = 1.20$ µm, $t = 0.65$ µm and $w_A = 0.50$ µm. ●,▲ and ■ is the normalised enhancement factor taken at 90.8 THz with a respective silver + chromium, aluminium and titanium network (no adhesive layer required) included with consistent widths and thicknesses.

The results in figure 6.2.4.2 (c) show the interconnecting network has a detrimental effect on

the signal coupling. It should be noted that this model assumes an air bridge is used to avoid

placing the network in direct contact with the i-type layer (see figure 4.2.3). If an insulating

layer is used instead the effects are detrimental to the diode quality and the S/N ratio is

expected to decrease. There are different degrees of coupling into the semiconductor mesas that are dependent on the conductivity of the network although the influence of a silver network with a chromium adhesive layer is not significantly different to an aluminium network. The interconnecting network provides a very marginal improvement to interconnecting the semiconductors with their own volume (6.70 to 6.45 difference) and is likely not worth the effort the manufacture given the choice.

The final consideration to address is the fact that that the data in figures 6.2.4.1 and 6.2.4.2 are not taken at 3.30 μm exactly. Their peaks are fluctuating between 3.00 μm and 3.74 μm (80 THz - 100 THz) and difference values for the control absorptions need to be used to calculate this enhancement factors. Although the absorption data is not taken at the peak value, figure 6.2.4.3 shows the enhancements at 3.30 (90.8 THz) μm exactly.
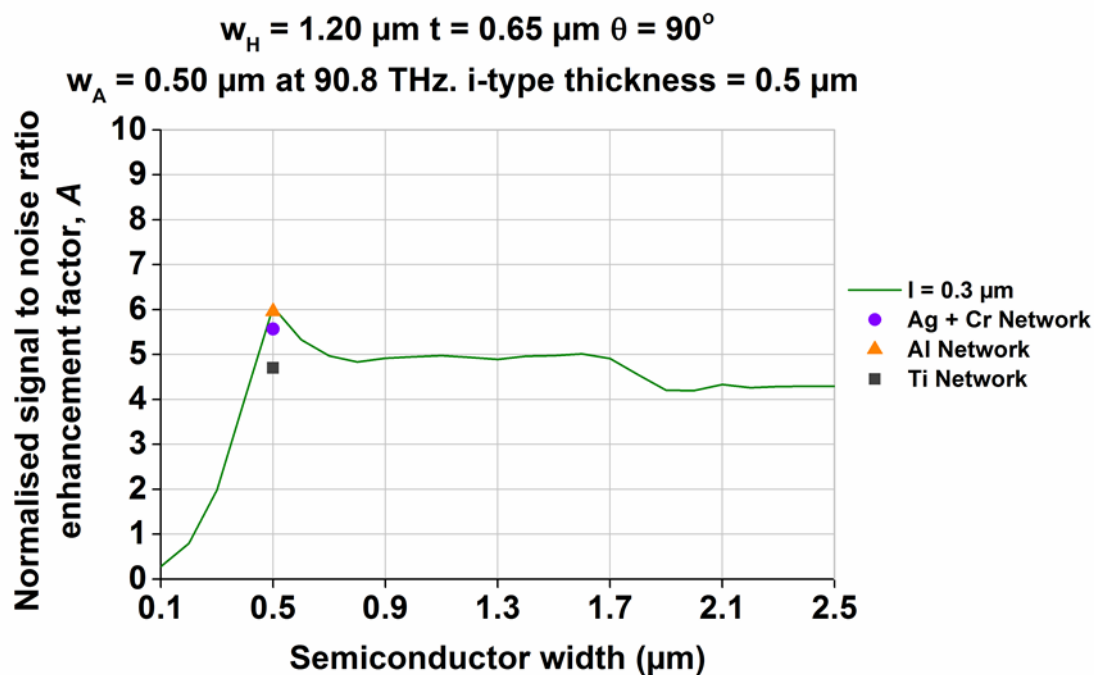
Figure 6.2.4.3: Interconnecting networks for a sub-optimum antenna array. A graph of the normalised S/N enhancement factor with a constant semiconductor length (l) at 0.3 μm and a varying semiconductor width where $w_H = 1.20$ μm, $t = 0.65$ μm and $w_A = 0.50$ μm. ●, ▲ and ■ is the normalised enhancement factor taken at 90.8 THz with a respective silver + chromium, aluminium and titanium network (no adhesive layer required) included with consistent widths and thicknesses.

The results at 3.30 µm show a further degradation to the results reducing the *A* factor to 6.05 with just the semiconductor volume. It is noted that the interconnecting network has a less deteriorating effect when the data is taken at non-peak values making the interconnecting network a more appealing option in this circumstance.

Despite the degradation in results when considering semiconductor interconnections, antenna aperture widths that produce a more difficult lift-off or the steps needed to probe the device; selective removal still produces significant enhancements to the diode quality and has shown a considerable dependency on antenna parameters and the semiconductor volume. Despite the manufacturing difficulties, it is this design that needs to be pursued if the photodiode quality is going to improve by several factors.

6.3) Radial feed point antennas

In an effort to enhance the S/N ratio by means of forwarding the incident light in a large unit cell pitch to a single point, designs which capitalise on the focusing effect of large, feed point antennas are introduced. In this design, the semiconductor size is very small compared to the antennas.

The design still needs to be suitable for incoherent light applications. The optimum design for single point focusing is the bow tie antennas or the feed point antennas. The bow tie antennas is the design that was chosen for this experiment, because it is more restrictive of the resonance bandwidth than a spiral or sinuous antennas, which are made up of interconnected and varying lengths. Figure 6.3.1 shows an example of the radial antennas shape in its early development stages.

In this modelling experiment, 6 bow tie parts are used to make the design more tolerant to wide polarisation angles. The more antennas that respond to incoming light (regardless of the polarisation angle) the higher the S/N ratio enhancement will be, on account of signal stacking.
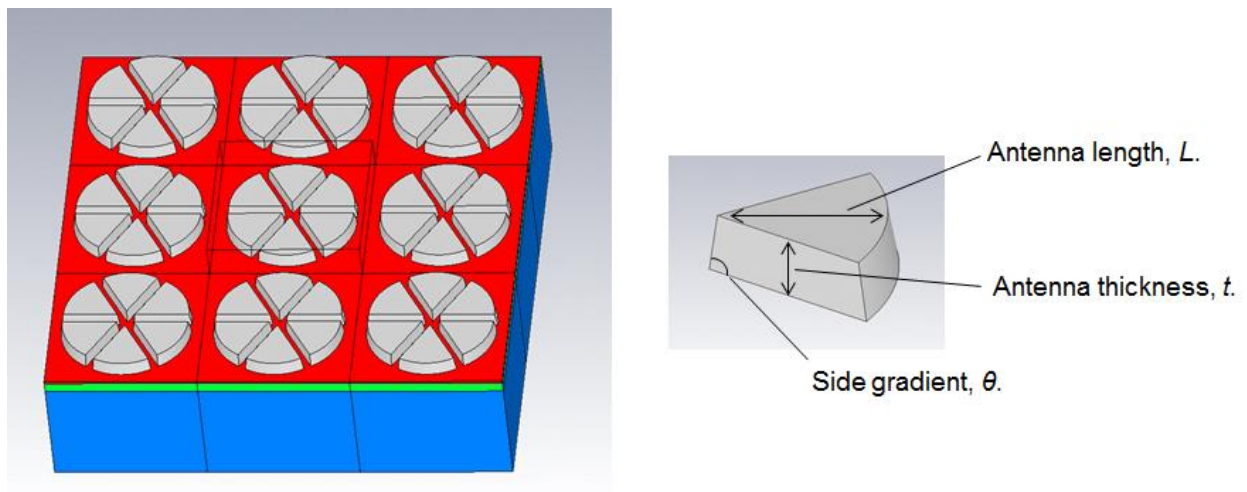
Figure 6.3.1: An example of a six-sided radial cone shape that is to be considered in this section. To simplify the model side gradient will be 90°.

The investigations began with an analysis of the response to polarisation angles. The array

response to different incoherent light is shown in figure 6.3.2:
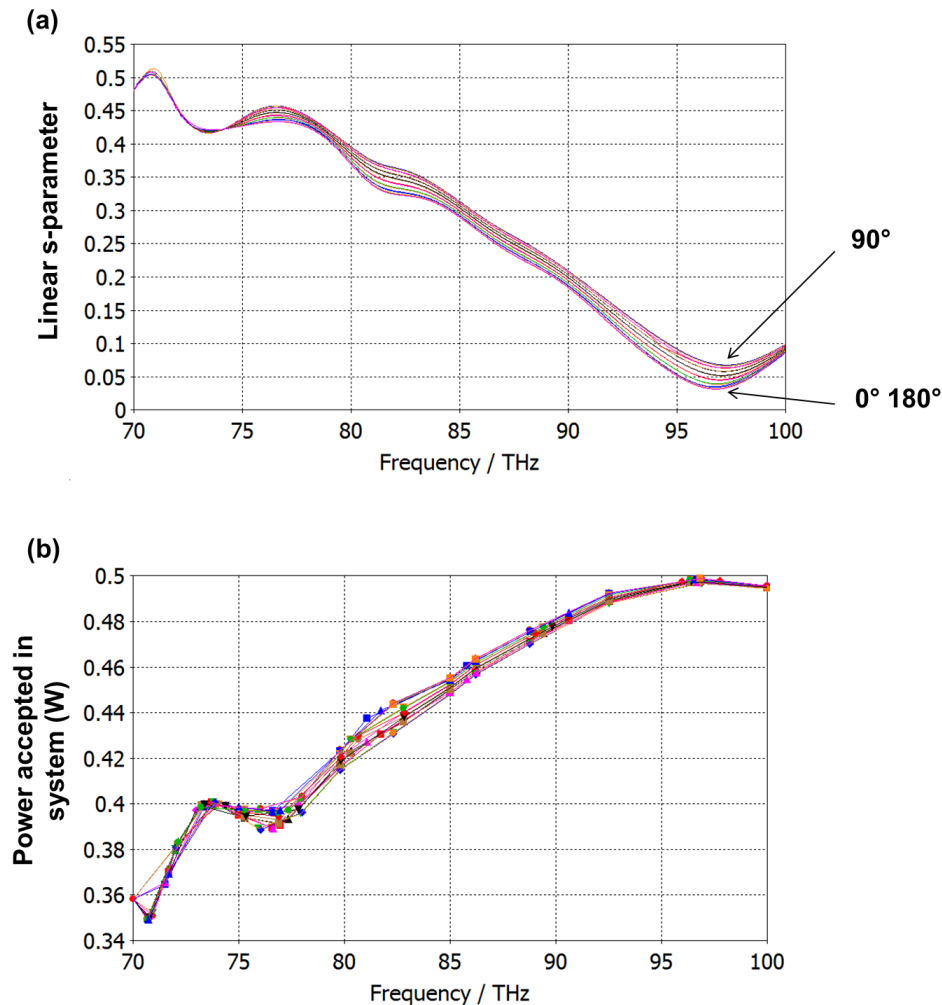
Figure 6.3.2: Assessment of the antenna's tolerance to polarisation angle. (a) The linear S-parameter for the radial cone array shown in figure 6.3.1 as a function of polarisation angle from 0° to 180° (b) The equivalent power accepted in the entire system as a function of angle from 0° to 180°. The biggest different in power accepted is 0.38%.

Similar to the hexagonal array, the radial bow tie array shows a considerable amount of

tolerance to different polarisation angles. The least amount of energy reflected off the system

occurs at a 90 degree side wall angle, which is measured as a 0.38% loss as the peak position.

It is shown that the design is very effective at light redirection for different polarisation

angles, but the design needs to be modified to address whether the light is redirected towards

the centre target and not towards the sides, which would be considered leakage.

An initial design for such the structure modification is shown in Figure 6.3.3 (a) which
illustrates the approximate ideal size of the semiconductor in relation to antenna size while
figure 6.3.3 (b) shows the metal contact networking for probing.
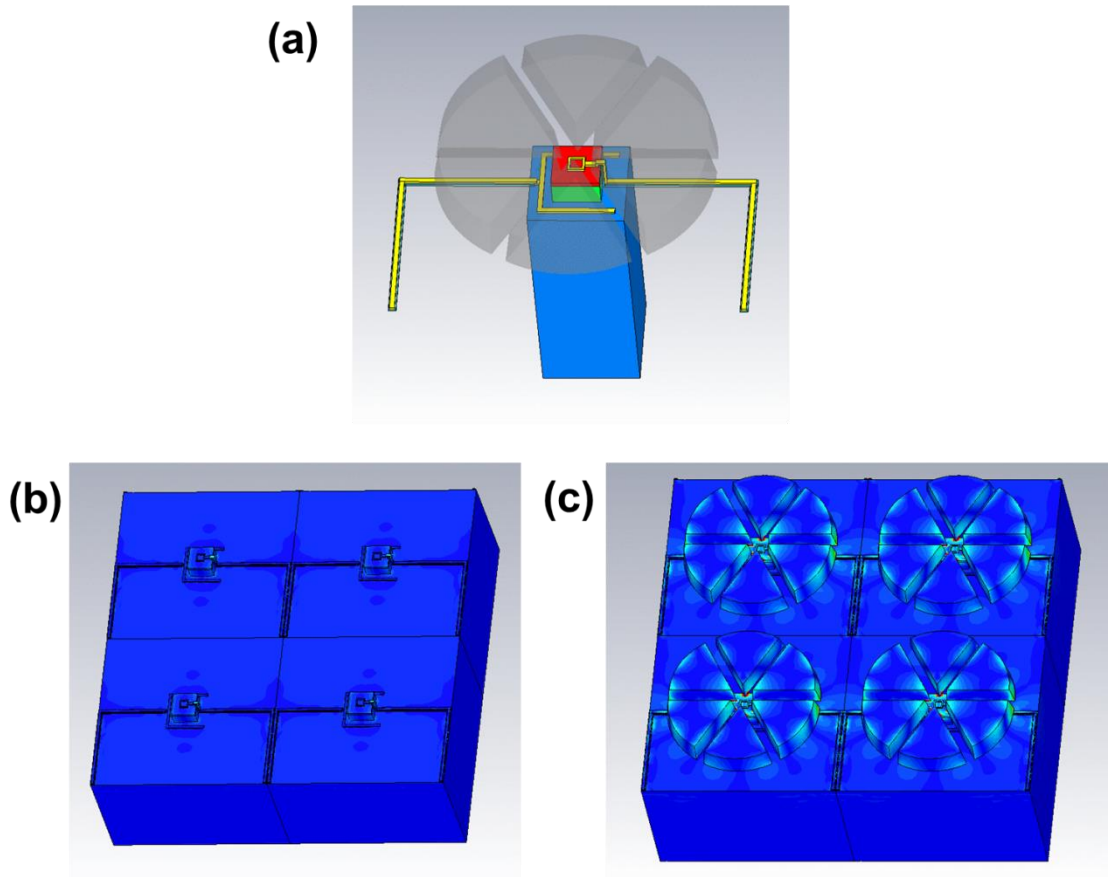
Figure 6.3.3: Hotspot analysis of the radial feed point antenna array. (a) The miniaturised semiconductor size
when maintaining the same thickness with the necessary contact networking for probing. (b) Colour code
diagram of the control. (c) Colour coded diagram of the antennas forwarding the signal to the semiconductor
"Bull's eye".

While the semiconductor volume can arguably be altered for convenience, the antenna size
and spacing is very restrictive if consistently good results are expected. At the wavelengths of
interest the distance between adjacent antennas must be between 0.5 μm and 0.7 μm. Any
larger will compromise i-type gain. As a result, the contact network shown in figure 6.3.3 (b)
needs to be as thin as 10 nm in order to be compatible with the antenna spacing. The radial
antennas will also need to rest on a support. A layer of transparent dielectric was considered
as a supporting structure, but in the interest of minimised impedance mismatch around the

radial antennas except the central semiconductor target, using the antennas themselves as air

bridges was selected. The antennas were to rest on a circular support annulus made of the

same semiconductor material as shown in figure 6.3.4. This support annulus required a

network gateway if the contact network featured in figure 6.3.3 was to be included. It was

later decided that the network was not a practical solution to the probing problem. It was too

thin and fragile. It also contributes the surface leakage when the mesa is of a comparable size.

It is for this reason that a different contact needed to be introduced.

Interconnecting the antennas were considered so that the antenna structures could support

each other over the air bridge, but was removed after it was realised that it will act as a feed

point to adjacent antennas which would increase the loss.

Central annulus is restrictive for small antenna spacing. Removed

No advantaged to having a square target. Changed

Contact network is too thin and fragile. Removed

Network gateways no longer needed. Removed

Interconnecting support will cause complications when one antenna is used as a contact. Removed
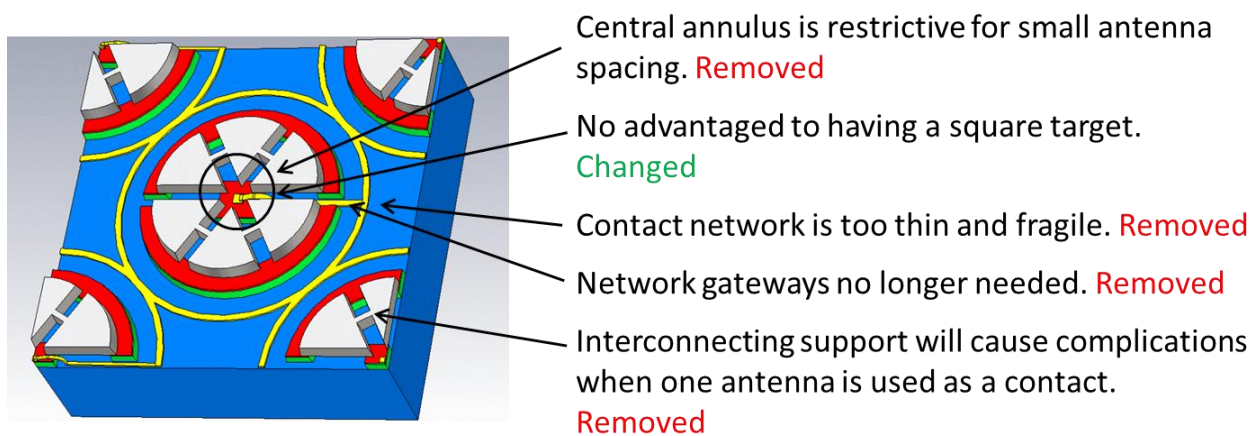
Figure 6.3.4: Changes to the initial radial feed point antenna array design after these features where deemed too fragile or detrimental to the signal gain.

In addition to the design changes illustrated in figure 6.3.4, considerations on what could be

done to minimise the coupling into the antenna support needed to be implemented. A new

dielectric layer was included to negate transmission into the radial antenna support.
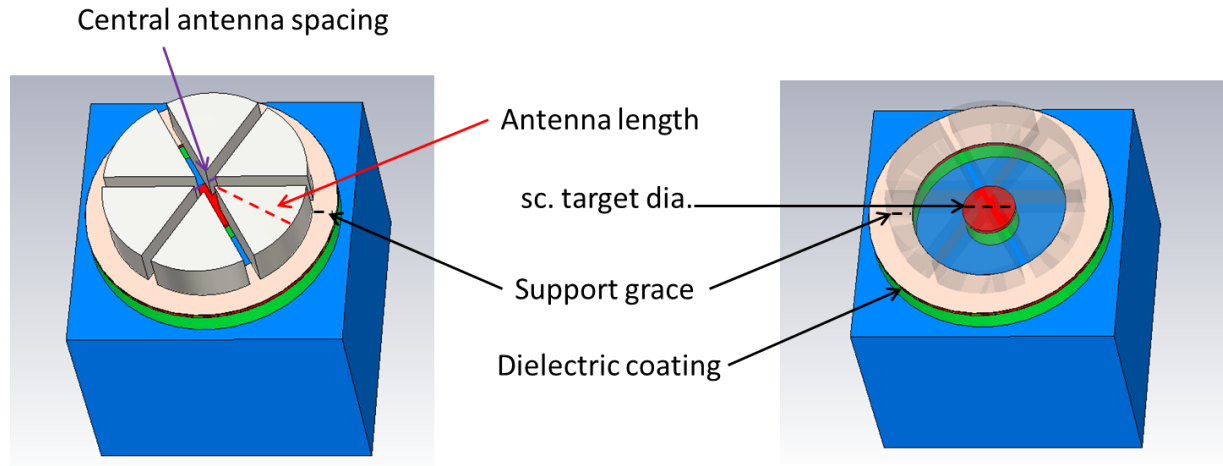
Figure 6.3.5: The radial feed point antenna with an air bridge underneath and an annular support for the antenna cone structures.

The support grace is a measurement of the mid-way point of the support annulus. In figure 5.3.5 the support grace is 0.4 μm as an indication of how much support the antennas will receive.

The network was replaced by the antennas themselves as contacts as opposed to using a thin network. By connecting one of the radial antennas to the lead out network the antennas can be in much closer proximity to one another. This alternative contact method is depicted in figure 6.3.6.

The disadvantage is that one of the contacts no longer functions as an antenna and thus the array is less tolerant of varying polarisation angles of the light. Alternatively, this may warrant additional radial cones so the contact takes up as small a space as possible. This is worth considering if the results show promise.
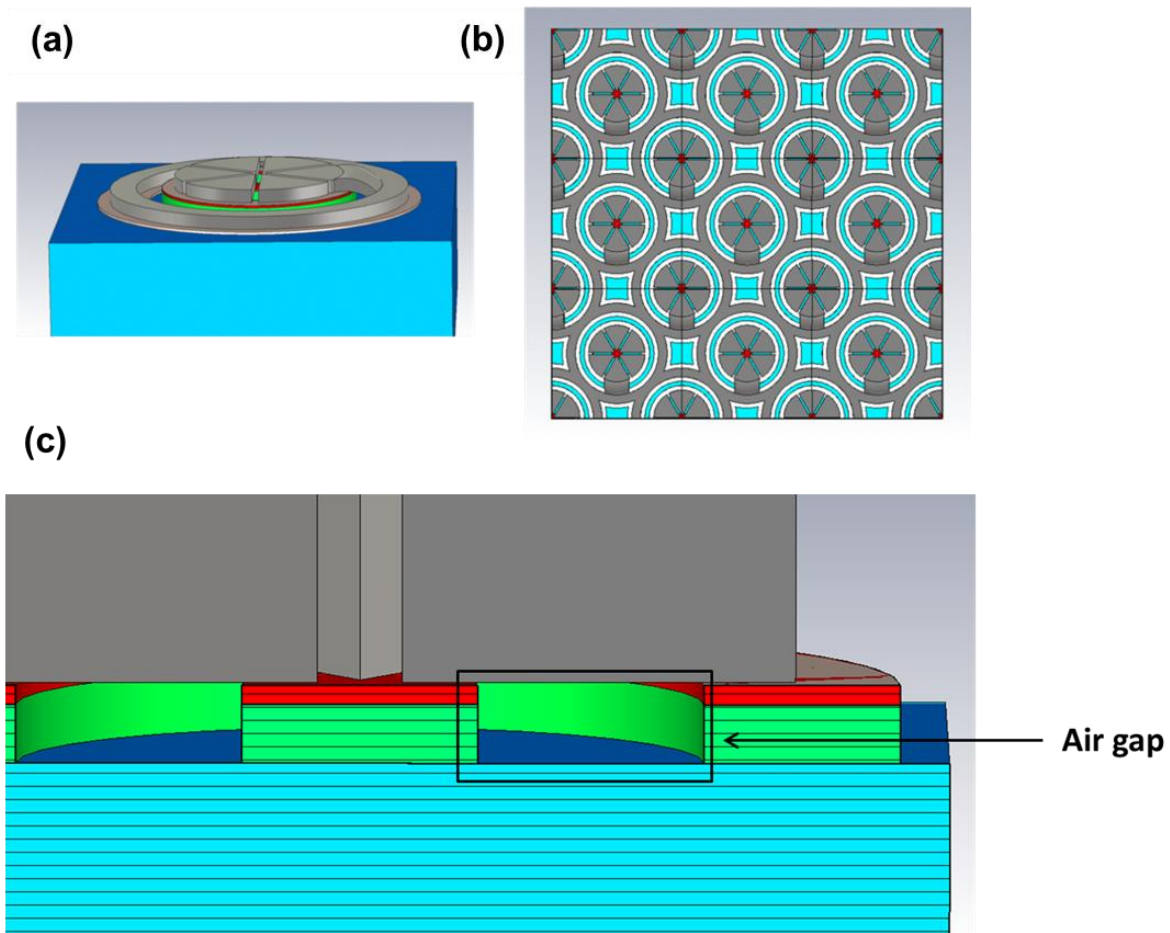
Figure 6.3.6: Interconnected radial feed point antenna design. (a) Schematic diagram of the radial antenna array with one cone serving as the contact network. (b) Plane view showing the contact network is interlinked with one another. (c) Schematic cross section cut out to show the air bridge etched in to the semiconductor wafer.

While a very large proportion of the antenna structure is suspended over an air gap, some amount of energy will remit from the bottom of the antennas and couple into the n-type across the air bridge, thereby adding another source of leakage to consider. This modelling of the behaviour of micro-antennas is strongly based on standing wave formation. It therefore follows that the air bridge can act as a resonant material despite its poor conductivity. This can lead to an uncharacteristically large antenna leakage unless the resonance air bridge height is identified and avoided.
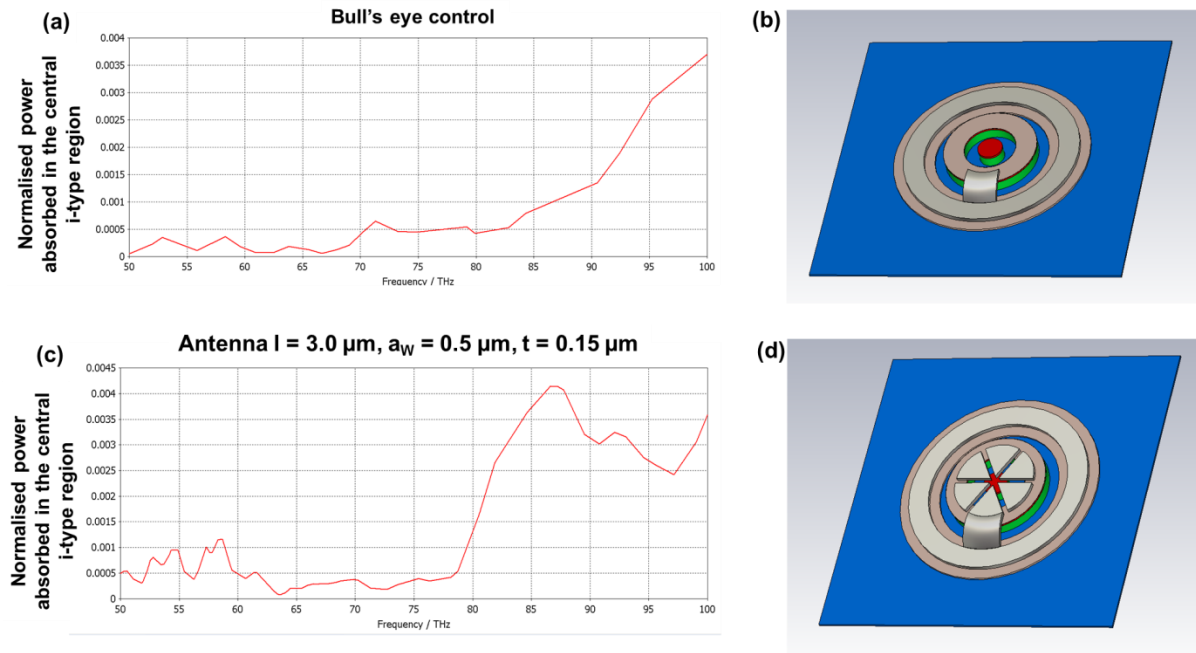
Figure 6.3.7: Simulated spectral analysis of the radial feed point antenna array. A conducting boundary was used at the bottom of the n-type layer. (a) The bull's-eye absorption response of the central i-type region. (b) 3D modelling view of the bull's eye structure. (c) The absorption response of the central i-type region with an antenna length of 1.5 µm and an antenna thickness of 0.15 µm. (d) 3D modelling view of the radial antenna structure. Unit cell pitch: 15 µm x 15 µm. p-type thickness = 0.1 µm, i-type thickness = 0.5 µm, n-type thickness = 0.1 µm. The bull's eye structure radius is 0.6 µm.

Figure 6.3.8 shows the change in central i-type absorption and bandwidth when antennas are added to a bull's eye target with an i-type region thickness of 0.5 µm. The shape of the enhancement has characteristics of the spectral response shown in figure 3.9.3. The slope increase near 100 THz is due an increase in material absorption at high frequencies. This is observed on another occasion in figure 6.3.8 (c). However, it has also been observed that the control devices have resonant peak customary of their size and that these absorption peaks change position as the thickness of the i-type changes. Figure 6.3.9 shows the same scenario but for an i-type region with a thickness matched to the optimum i-type thickness with localised focusing included (i.e. 1.6 µm) and a thickness that match the optimum thickness of the bulk material (i.e. 2.2 µm) (see figure 6.2.3.1).
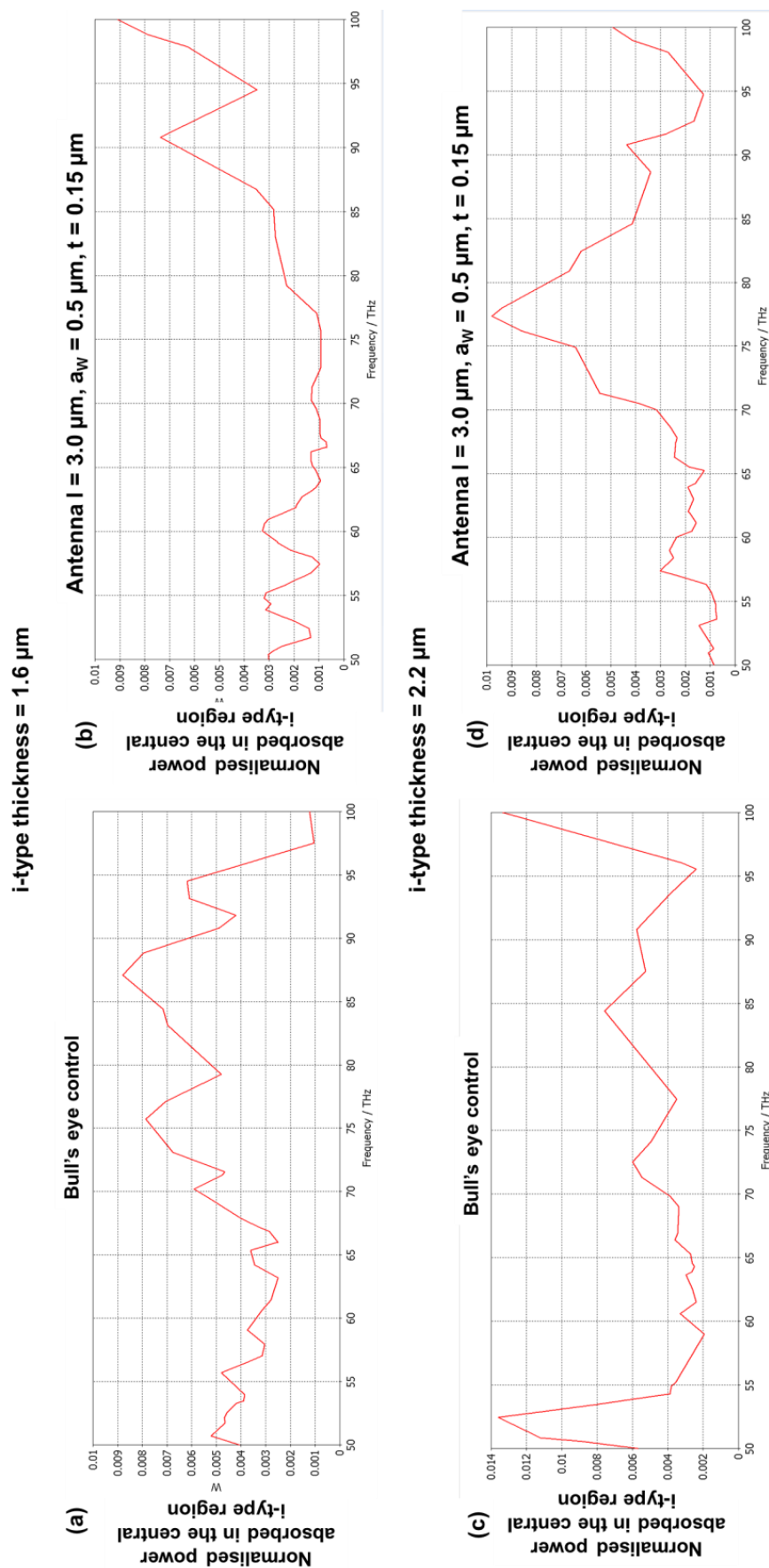
Figure 6.3.8: Antenna radial feed point analysis for different thicknesses. (a) The power absorbed in the bull's eye i-type region with an i-type thickness of 1.6 µm (b) The power absorbed in the central i-type region 1.6 µm thick with an antenna length of 3.0 µm and an antenna thickness of 0.15 µm. (c) The power absorbed in the bull's eye i-type region with an i-type thickness of 2.2 µm (d) The power absorbed in the central i-type region 2.2 µm thick with an antenna length of 3.0 µm and an antenna thickness of 0.15 µm. Unit cell pitch: 15 µm x 15 µm. p-type thickness = 0.1 µm, n-type thickness = 0.5 µm. A conducting boundary was used at the bottom of the n-type layer. The bull's eye structure radius is 0.6 µm. Note: 50 THz – 100 THz = 3 µm – 6 µm

There is a clear increase in i-type absorption by a factor of 1.82 near the 90.8 THz mark compared to the control. This seems like a promising result, but the majority of the signal has been lost due to much of the volume being cut away. Therefore, despite a response enhancement that is greater than that of the standard hex antenna array, the S/N ratio is substantially less than the S/N ratio of bulk $Al_{0.05}In_{0.95}Sb$.

To calculate this, the same calculation used in section 5.2.1 was used and the results are given in TABLE 6.3.

TABLE 6.3: The calculations of all the radial antenna enhancements compared to the bull's eye structure 1.2 µm in diameter compared to the standard control.

Data	Structure type	i-type thickness	Normalised i-type absorption	Peak frequency (THz)	Peak wavelength (µm)	Normalised enhancement factor at peak
Figure 5.3.7 (a)	Bull's eye	0.05	0.0009	86.0	3.49	0.15
Figure 5.3.7 (b)	Radial antenna	0.50	0.0042	86.0	3.49	0.71
Figure 5.3.8 (a)	Bull's eye	1.60	0.0060	90.8	3.30	0.46
Figure 5.3.8 (b)	Radial antenna	1.60	0.0072	90.8	3.30	0.55
Figure 5.3.8 (c)	Bull's eye	2.20	0.0045	77.0	3.89	0.39
Figure 5.3.8 (d)	Radial antenna	2.20	0.0100	77.0	3.89	0.86

According to the data in TABLE 6.3 as well as the figures graphs it is referencing, the bull's eye device has an inconsistent response in accordance on its own shift in resonance peak with size. The radial antennas can provide improvement in both S/N enhancements and bandwidth enhancement, where the bandwidths can be as low as 0.65 µm thanks to the collective forwarding of energy from all radial structures. Much of the signal has been removed and even though the radial antennas can enhance the S/N ratio of the reduced semiconductor volume by up to a factor of 4.7 (at the thinnest i-type layers) the device still struggles to compete with bulk control $Al_{0.05}In_{0.95}Sb$.

6.4) Localised surface plasmon resonance (LSPR)

A final alternative design to consider is an antenna array that utilises the plasmonic effect. At resonance, this array will concentrate the electric field in the cavities. The difference between this design and the higher order wavelength scale design used so far is that it can confine the electric field to a much smaller volume provided that the wave propagation constant, γ (which changes as a function of dielectric constant) is greater than the wave function, k_0[100].

$$\gamma = k_0 \sqrt{\frac{\varepsilon_1 \varepsilon_2}{\varepsilon_1 + \varepsilon_2}} \qquad (6.4.1)$$

Plasmonic structures work on the basis that if the material being used is of a sufficiently high dielectric constant than resonance will occur regardless of the antenna dependency on size. It is an interesting alternative in this field as it minimises the losses in the surface materials.

The examples given in this chapter are based on the plasmonic effect as documented in a research paper by S. Law et al[5]. They have analysed the resonate scattering of a doped InAs cylindrical antenna array on an undoped substrate. This experiment will replicate this work whilst providing additional information to whether this is applicable to photodiode enhancements.

InAs is a relatively poor conducting metal, but this is a requirement in order to achieve plasmonic scattering in Law's documented experiment. The requirement is that the magnitude of the antenna dielectric constant (ε_m) is twice that of the semiconductor underneath (ε_s)[101].

$$\mathrm{Re}\left|\varepsilon_m\right| = -2\varepsilon_s \qquad (6.4.2)$$
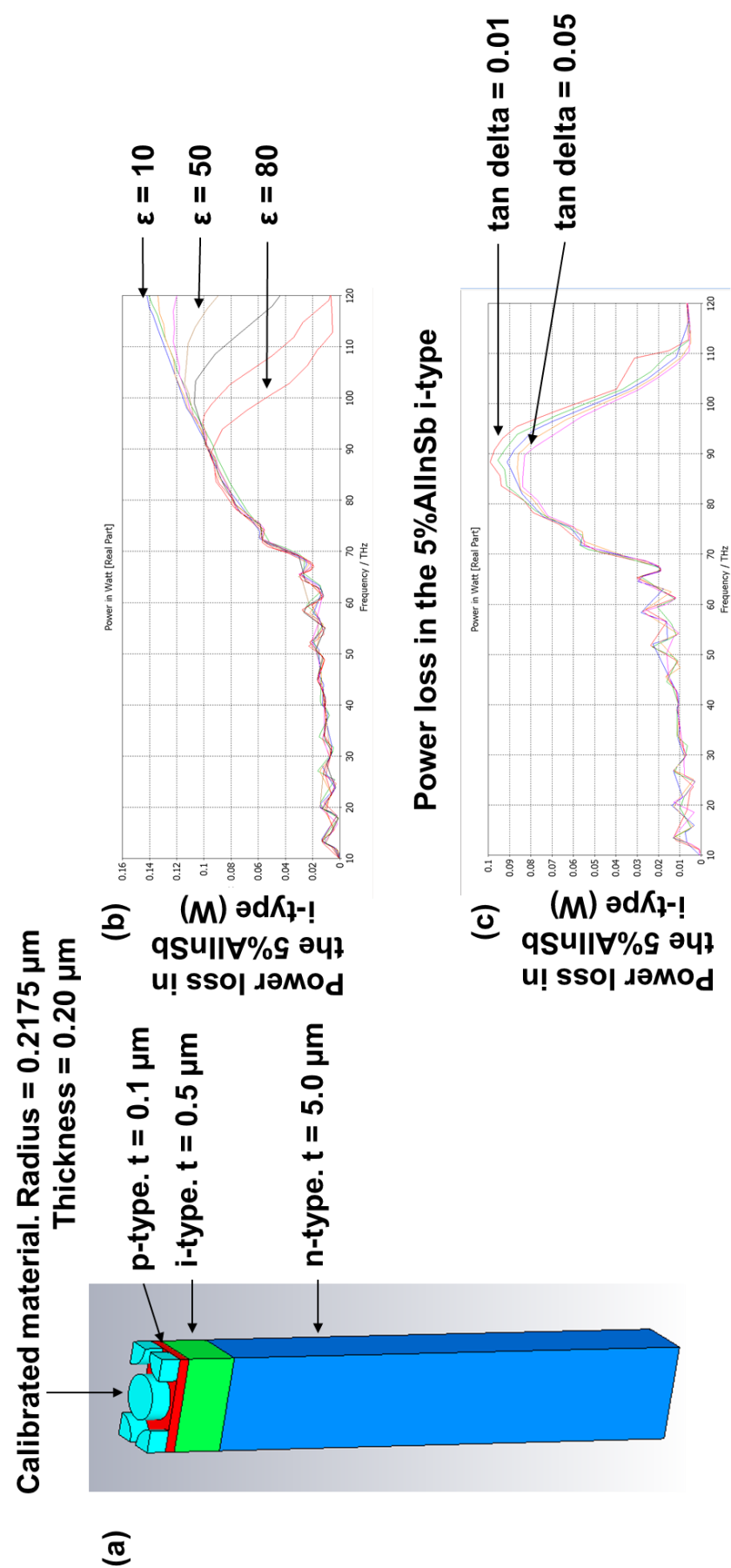
Figure 6.4.1: The change in the plasmonic resonance peak as the dielectric properties (ε) of the cylindrical antenna design on top. The thickness of the antenna is 200 nm. (b) Power absorbed in the i-type region as a function of the dielectric constant of the antenna material (ε). ε changes from 10 to 80 by integers of 10 as indicated in the diagram while the tangential loss (tan δ) remains at 0.01. (c) Power absorbed in the i-type region as a function of the antenna tangential loss (tan δ). Tan δ changes from 0.01 to 0.05 in integers of 0.01. The unit cell pitch is 1.04 μm and the vertical pitch is 0.6 μm.

This research has recorded peaks at 9.8 μm (or 30.6 THz). It is noted that InAs is transparent at these frequencies and isn't useful to the application when the figure of merit is the amount of absorb in the layers underneath the antenna – these layers need to absorb the signal as a necessity. As such, the same principle of dielectric dependant plasmonic antennas has been applied to $Al_{0.05}In_{0.95}Sb$ semiconductors where an antenna material with dielectric properties that are suitable for achieving resonance with $Al_{0.05}In_{0.95}Sb$ underneath are calibrated. Figure 6.4.1 demonstrates how a peak across the i-type region can be achieved for an antenna size much smaller than the dipole rule would dictate by altering the dielectric constant of the antenna material. The tangential loss is also altered and logically it would change the amount that gets absorbed in the antennas and reduce the amount that gets absorbed in the semiconductor by extension, but has little influence on the peak position.

The model calibration shows that the dielectric constant is considerably larger and the material is much lossier than the typical metals used in this thesis, thus far. As shown in figure 6.4.2, the antenna absorption increases with the dielectric constant. When the dielectric constant reaches 80 the antenna losses exceed 12% of the total incident power.
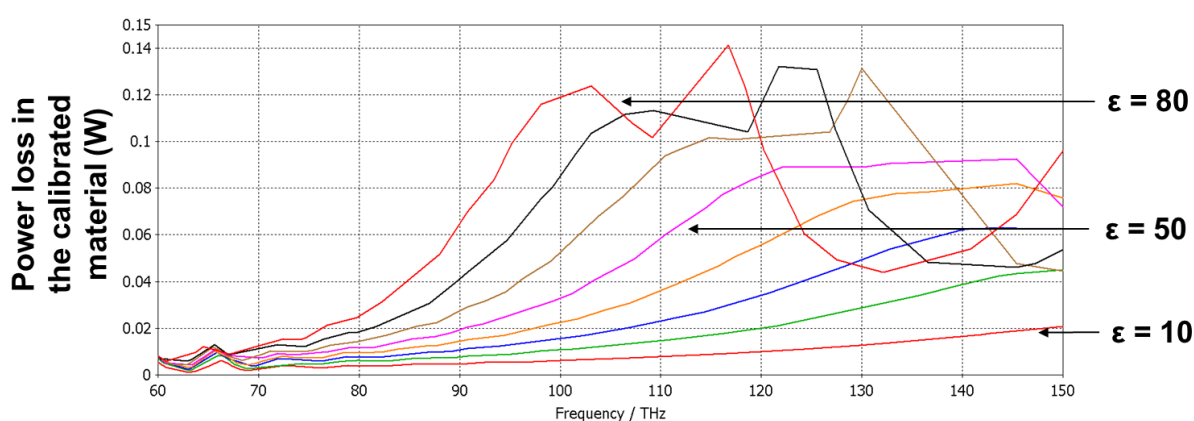
Figure 6.4.2: The absorption in the calibrated material when the tangential loss (tan δ) remains at 0.01 and the dielectric constant changes from 10 to 80 in integers of 10. The parameters of the antennas are the same as those listed in figure 6.4.1 (a).

In order to achieve the plasmonic resonance at 90.8 THz (3.3 µm) the material has to match the given values. Water is a close match and the dielectric constant and can be specifically tailored by altering the water temperature or salt content[102], but using a liquid poses considerable manufacturing difficulties at the NIR frequencies, but for the purposes of providing an answer to the theoretical benefits, it is noted that these difficulties will change the design to how it is represented in this section but will not be considered unless the design as it currently is shows promise and warrants further development.

Changing the dielectric constant to shift the peak response supports the fabrication proposition that if antenna enhancements based on LSPR in $Al_{0.05}In_{0.95}Sb$ is achievable. It is noted that antenna resonance is met when the dielectric constant of the antennas are roughly double that of the semiconductor (i.e. when $\varepsilon = 32$ the first order harmonic resonance should be at 121 THz). Increasing the dielectric constant further demonstrates how the dipole rule can be manipulated by making the plasmonic standing waves larger.

With reference to figure 6.4.3 the problem is that the enhanced absorption across the i-type region for plasmonic structures are much less than that featured in wavelength scale antennas that has been used thus far. This is due to different harmonics of resonances where plasmonic coupling has a projection pattern similar to the fundamental resonance harmonics and the wave length scale coupling has a coupling pattern similar to the higher order resonance harmonics[29]. As a result of a higher proportion of the signal going through the $Al_{0.05}In_{0.95}Sb$ i-type layer and the absorption in the antenna array almost doubling, the normalised S/N enhancements for the plasmonic coupling only amounts to a factor of 1.32 compared to the control.
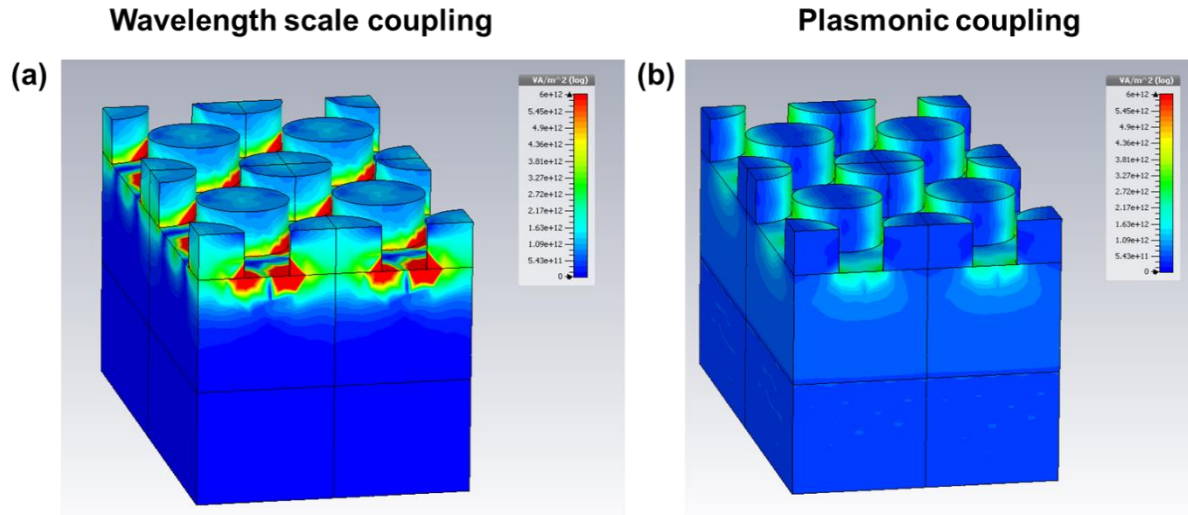
Figure 6.4.3: Different coupling patterns for different types of coupling. Higher order harmonic (wavelength scale) coupling is beneficial for localised focusing and fundamental harmonic (plasmonic) coupling is beneficial for signal projection into the substrate.

There may still be an advantage if the selective removal was applied to the plasmonic structures as well. Figure 6.4.4 shows the S/N enhancement factor following selective removal.

When the semiconductor length is 0.35 µm and the semiconductor width is 0.20 µm the normalised S/N enhancement factor is at a slightly improved value of 1.37. The enhancement factor is at its largest when the semiconductor volume : unit cell volume ratio is also large compared to ratio for the wavelength scale antennas.

With reference to figure 6.2.4.2 the enhancement is less than half that of the wavelength scale antennas after selective removal. Not because there is a large degree of reflection or loss in the antenna material, but because plasmonic resonance antennas tuned to first order resonance harmonics have a much more distributed coupling with low propagation angles to the normal than the wavelength scale antennas.
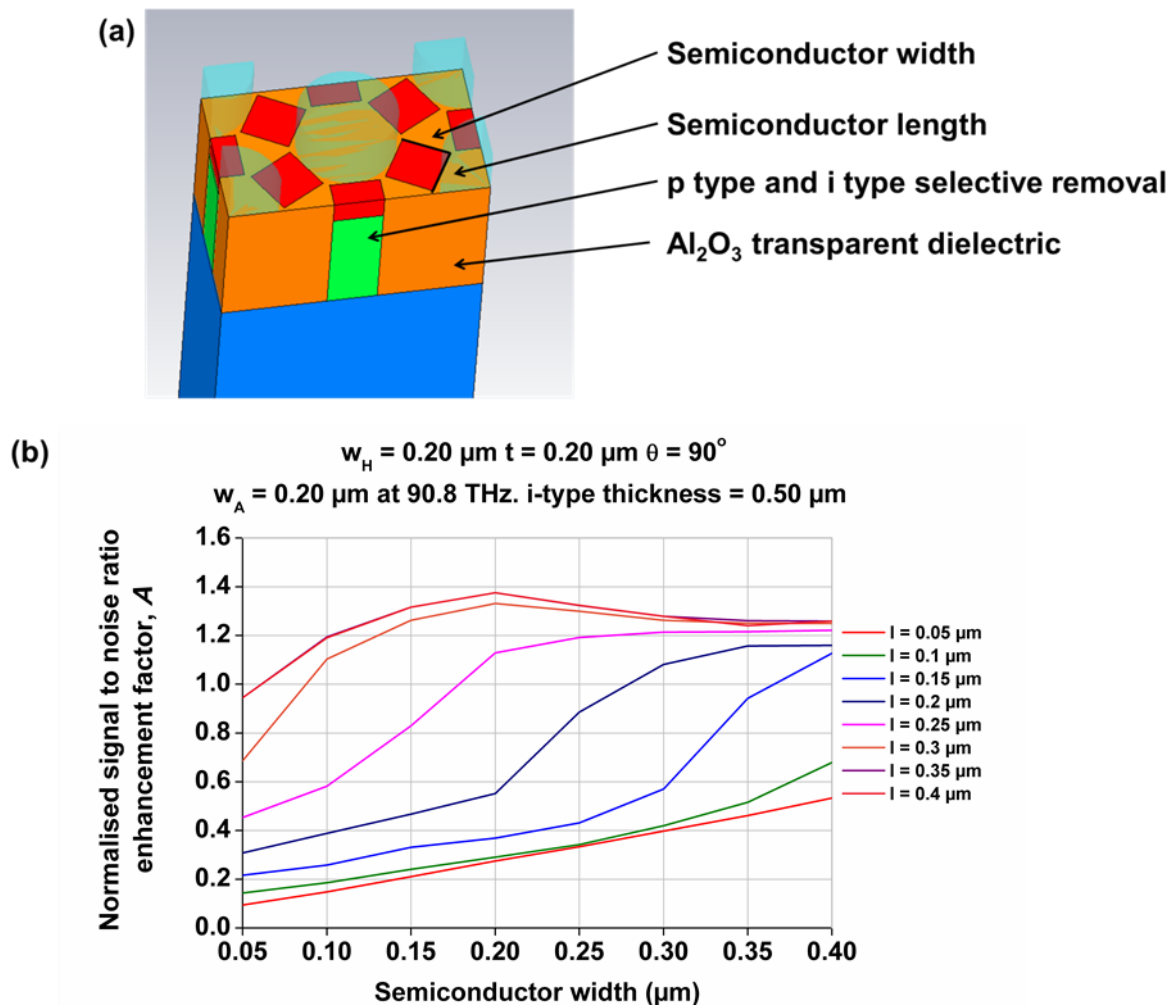
Figure 6.4.4: Selective removal of the semiconductor featuring fundamental harmonic coupling. (a) A diagram of the selective removal of a semiconductor utilising first order coupling. (b) The S/N enhancement following semiconductor selective removal for $Al_{0.05}In_{0.95}Sb$ 0.5 µm thick, versus semiconductor width and as a function of semiconductor length.

Figure 6.4.5 shows the normalised S/N enhancement factor for a 1.6 µm i-type region thickness. The results demonstrate a benefit to having a thicker i-type, thus giving further support that the plasmonic effect causes a more uniform coupling with low propagation angles to the normal than wavelength scale antennas. That is to say; figures 6.2.2.3 (b) and figure 6.2.3.2 (a) (i.e. wavelength scale antennas with i-type thickness of 0.50 µm and 1.60 µm respectively) demonstrate a reduction in signal to S/N ratio as the i-type thickness increases. Whereas comparing figures 6.4.4 (b) and 6.4.6 (i.e. plasmonic antennas with i-type thickness of 0.50 µm and 1.60 µm respectively) demonstrate the opposite effect.
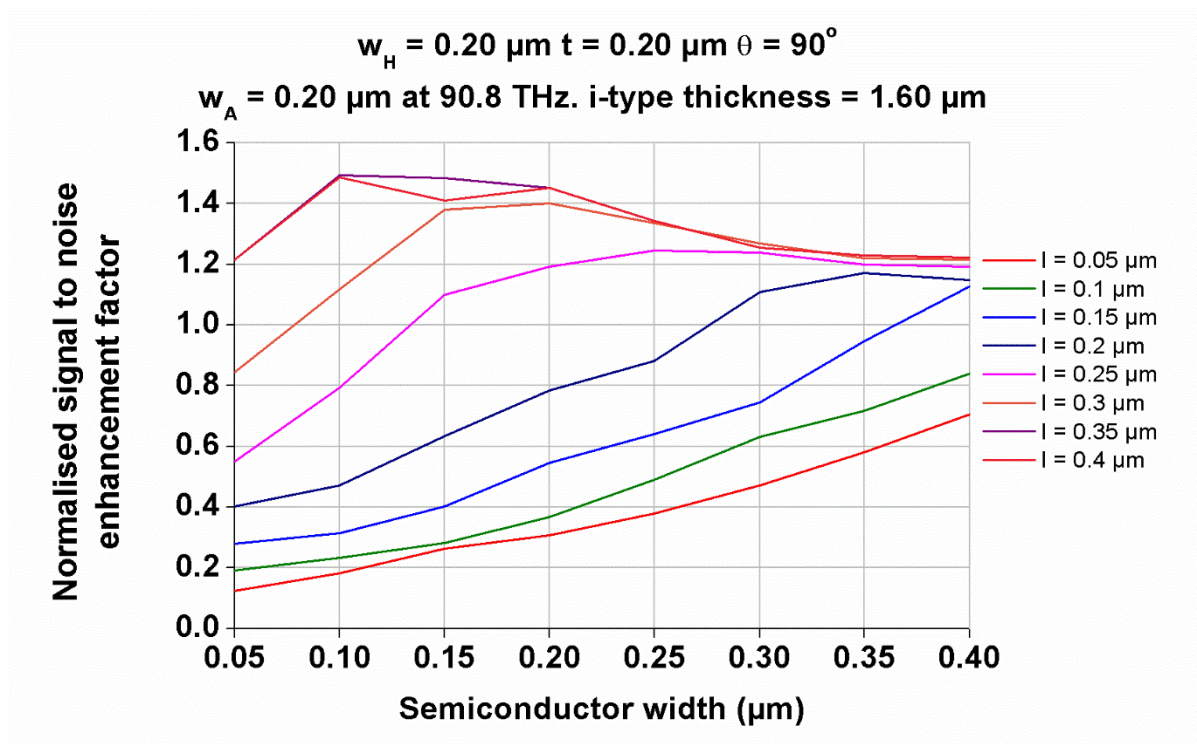
Figure 6.4.5: The S/N enhancement is a consequence of the semiconductor selective removal at 1.6 μm i-type thickness versus semiconductor width as a function of semiconductor length.

The final consideration is what S/N enhancement factors can be expected when these semiconductor volumes are interconnected. If a semiconductor length of 0.35 μm for the 0.5 μm thick i-type is considered, the semiconductor cut outs will already be connected to one another at every width so there is no need to take into account any losses when the semiconductor parts need to be interconnected as a necessity. The optimum parameters are shown in figure 6.4.6.
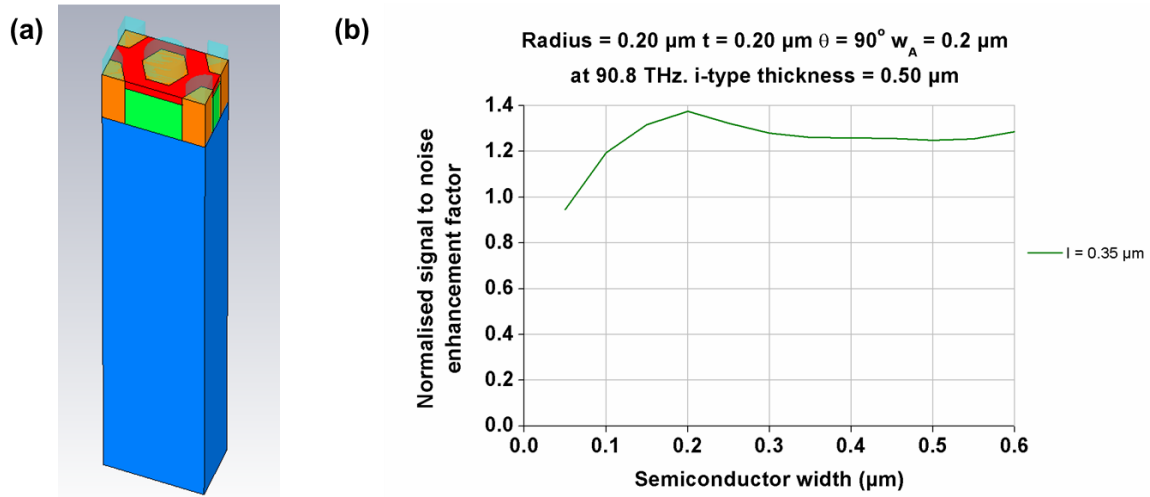
Figure 6.4.6: Semiconductor interconnections featuring coupling of the fundamental harmonic order. (a) Schematic diagram of the plasmonic selective removal when the semiconductor length is 0.35 µm, the semiconductor width is 0.20 µm and the i-type thickness is 0.5 µm. (b) The power accepted in the i-type region versus semiconductor width when the semiconductor length is kept at 0.35 µm.

In conclusion plasmonic coupling into the photodetector can work in theory and does feature efficient coupling of a different harmonic order. The problem is that the energy is coupled in such a way that is not useful to optimised i-type absorption. There is a benefit to selectively removing parts of the semiconductor, but the enhancements are much less substantial than the $(L = ¾ \lambda)$ wavelength scale antennas. The material that needs to be used is likely to be water which poses considerable manufacturing difficulties, but need not be taken further on account of underwhelming results for ideal parameters.

6.5) Chapter 6 conclusion

A number of alternative designs have been investigated as potential modifications to give S/N ratio enhancements compared to what has been achievable in chapter 5. These modifications are elaborate and most will pose a real difficulty when trying to fabricate them. As such, they are theoretical investigations based on as hybrid modelling data taken from practical measured and integrated into the simulation software. The margin of error is subject to the limitations of the software, but in margin of error of 5% was derived after model calibration of the last experimental comparison (see figure 5.5.1.6) for context of accuracy. The bar chart in figure 6.5 provides a summary of alternative designs that have been considered and the influence they have on the S/N ratio of the bulk $Al_{0.05}In_{0.95}Sb$ material. The thicknesses of the epitaxial layers are given (p-type = 0.12 µm, i-type = 0.5 µm, n-type = 5 µm) to make simple comparisons to previous data and to capitalised on the localised focusing.
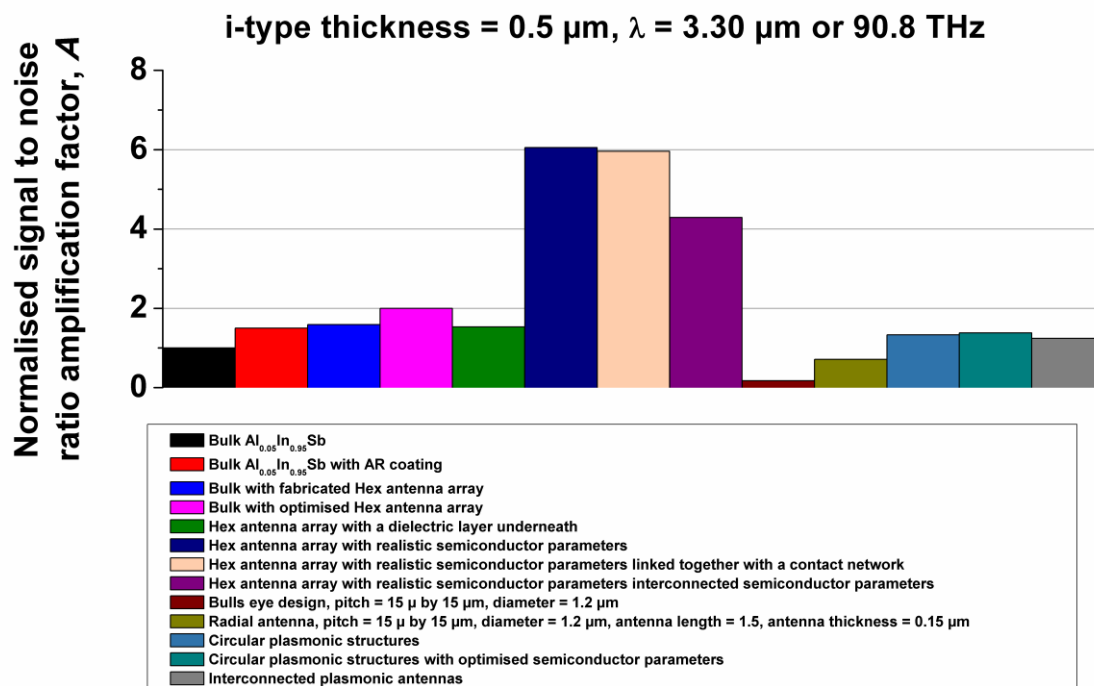
Figure 6.5: The change in normalised S/N enhancement factor when alternative antenna designs are used.

There have been considerations to the semiconductor i-type thickness where increasing the i-type from these designs does not have the same benefits as increases the i-type thickness of a standard photodiode with no enhancements at all. In fact it makes the S/N ratio worse except under the condition that the antenna resonates with 1st order harmonics. Plasmonic antennas have been recorded to oscillate at these harmonics. They are much smaller than conventional antenna designs and are dependent on the dielectric properties of lossy materials. Dielectric calibrations were done to investigate the application of plasmonic antennas on an $Al_{0.05}In_{0.95}Sb$ semiconductor and the fact that the closest materials to match the dielectric calibrations is water makes this design one of the more complex and difficult design to consider for manufacturing. It was determined that the coupling patterns of 1st order harmonics do not focus as well as the 2nd order harmonics making this design alternative not recommended.

The "Bulls eye" shape is the design name given to a structure where the semiconductor cylindrical active region is significantly smaller compared to the pitch. Although it is noted that the power absorbed in the minimised i-type increases by a factor of 3-4 under the influence of radial feed point antennas, this is also not a recommended design alternative because the amount absorbed in the i-type region is a fraction of what is absorbed in the bulk material, making it difficult the 3-4 S/N ratio factor increase to compete with the standard photodiode.

The design alternative that demonstrates the most potential is one based on the selective removal of the semiconductor. It works on the basis that the coupling into the semiconductor happens mainly at the hotspots in the aperture and that the remaining semiconductor volume generates unwanted noise with relatively little signal absorption. By only including the semiconductor hotspots this method can enhance the S/N ratio by a factor 6 compared to the

control (standard semiconductors). However, the semiconductor structures need to be interconnected which will degrade to S/N ratio. This effect can potentially be improved with an interconnecting network of conducting material (see figure 6.2.4.2 (a) and (b)).

7) Chapter 7: LED emission antennas

Chapter 6 depicts that the maximum possible S/N ratio enhancement is about a 6.0 factor increase. Chapter 7 discusses enhancements to the LED component. The purpose of this is to better understand what further benefit can be provided if the emission far field was focused or whether initial wavelength filtering could be introduced. These results will provide context to future work and justify whether these modifications are worth pursuing.

The normalised results were taken as the ratio difference between the antenna influenced radiative power and the control radiated power between the cut off frequencies of 2.5 µm and 4.25 µm in accordance to the measured emission data of $Al_{0.054}In_{0.946}Sb$[70]. For consistency with previous data, the aluminium hex antenna design was used for initial designs and testing. Further design alterations are featured to address the device limitations as they are identified and create a larger portfolio to draw conclusions from.

This chapter is a simulation based chapter which has a different port set-up compared to the photodiode detector. This will be addressed to provide context on how results are generated and how to replicate these results in the future.

7.1) Modelling isotropic emission

The bulk material before antenna enhancements are applied (control) needs to be representative of how LED radiation disperses. This means that the internal emission needs to be isotropic and the emission pattern needs to be Lambertain after taking into account total internal reflection of the semiconductor LED. Emission control (no antenna) samples will therefore be modelled after the Rayleigh Jean dispersion law[103] before being applied to design with antenna enhancements. This dispersion law provides a mathematical guide to how many modes the model needs to generate at the port. Port modes are different modes of

oscillation which produce different eigenvectors in the coupled spring problem that is featured in the waveguide port to simulate an oscillating wave input. An isotropic stimulation must meet the condition that the far field amplitude is 0 dBi (no projection in a particular direction) within the material. To achieve this, a large number of modes must be used and superimposed on top of one another to simulate an isotropic response. Using additional modes with increase the simulation time (i.e. 7 modes means the simulation needs to be done 7 times. 70 modes : 70 times, etc.). The results need to be combined in the CST^{TM} Template based post processing function.

The number of modes (N) required for isotropic internal emission ultimately depends on the size of the structure you are using and the wavelength, λ. The general expression for the amount of necessary modes is given in equation 7.1.

$$N = \frac{8\pi L^3}{3\lambda^3}$$
(7.1)

Where L is the cubic length of the LED.

Figure 7.1.1 shows the amount of modes required for different wavelength for cubic lengths.

Based on the information provided in figure 7.1 the simulation cannot be the actual size of the LED or simulation time will be unrealistically time consuming to account for realistic isotropic internal emission. A reduced size needs to be considered instead with the condition that the impact close proximity side wall effects are negated or minimised.

The proposed way to do this is to replicate the unit cell in a 5 by 5 array. It is likely that the cubic length will be approximately 10 μm since that accounts for a 2 μm pitch – which is a common requirement for the antenna designs that have been considered in this thesis thus far.

Under these conditions, the simulation will need to be run hundreds of times with different modes.
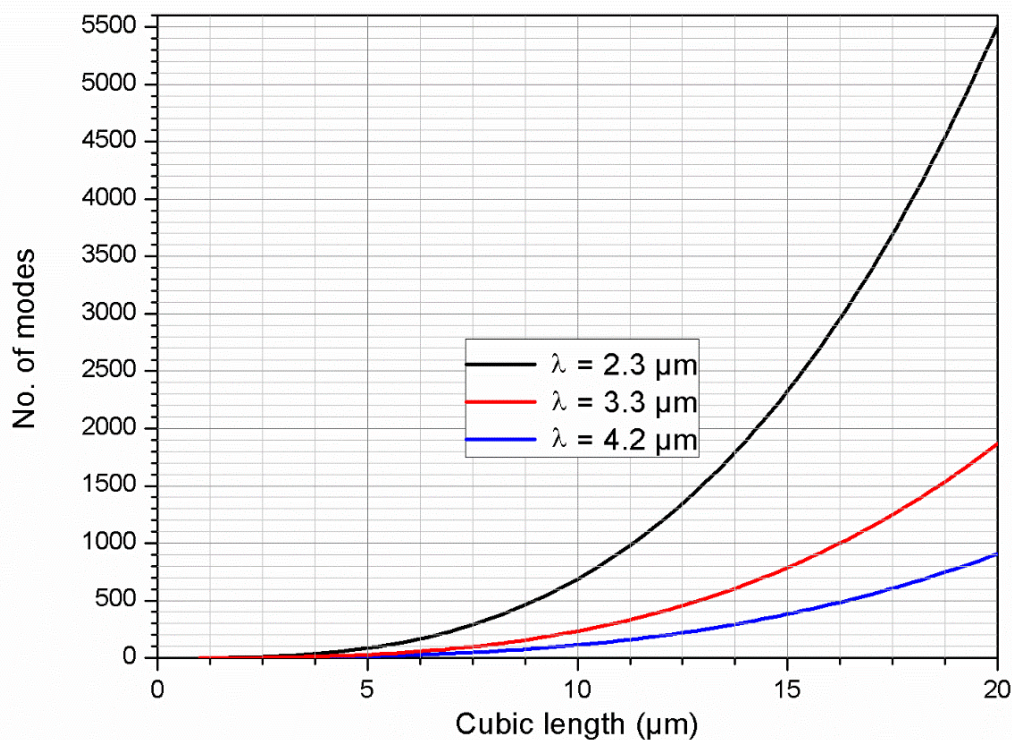
Figure 7.1.1: The necessary amount of port modes to achieve internal isotropic stimulation as a function of emitter volume. The wavelengths depicted here are 2.3 μm (black) 3.3 μm (red) and 4.2 μm (blue).

At the depicted size, the generated mesh comprises a few million hexahedral mesh units and the simulation time in CST^{TM} is 1.5 – 2 hours for a single mode. For this reason, only a few modes were considered to produce results in a realistic time frame. As a result, the Lambertian emission is not entirely Lambertian (circular). This is shown in figure 3.8.3 (replicated here as figure 7.1.2 for the convenience of the reader). This is recognised as a limitation of the software. If fewer than the ideal number of modes is used then the Lambertian far field pattern on the control device will be influenced.
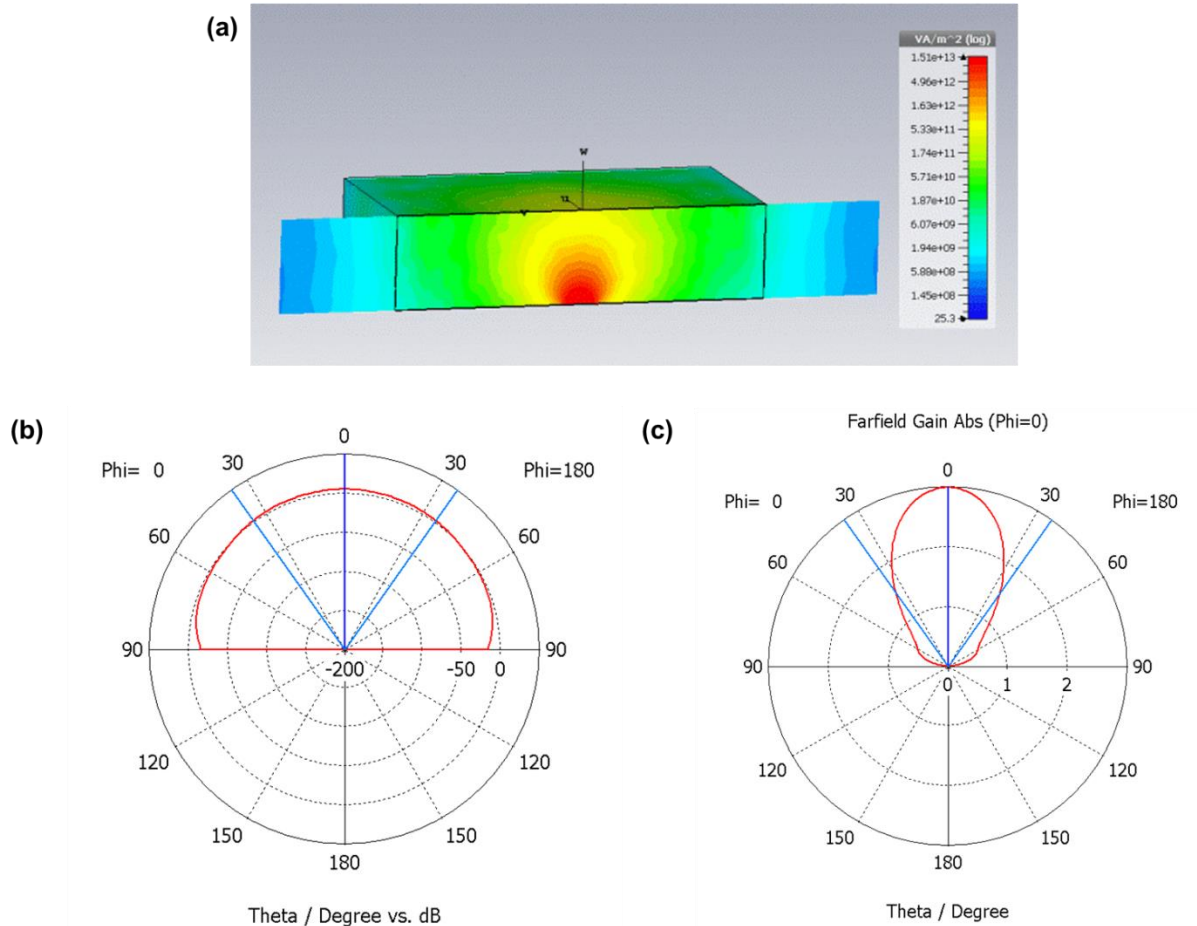
Figure 7.1.2: An illustration depicting the difference between linear and non-linear polar diagrams. The material is i-type AlInSb with a length and width of 2 µm and a thickness of 0.5 µm. (a) The propagation from a square waveguide port at the bottom of the substrate with a normal mode of oscillation after 20 port modes were combined. (b) The far field polar diagram shown in decibels after 20 port modes when combined. (c) The linear far field polar diagram.

However, the compromised Lambertian curve was observed to be inconsequential when the control was influenced by antenna waveguide material. Additionally, the surface impedance as a function of dielectric constant remains uncompromised.

7.2) Modelling total internal reflection

The general set-up is depicted in figure 7.2.1 where a waveguide port is applied to the emitter of arbitrary size that will re-radiate towards a photodiode approximately 1 cm away.
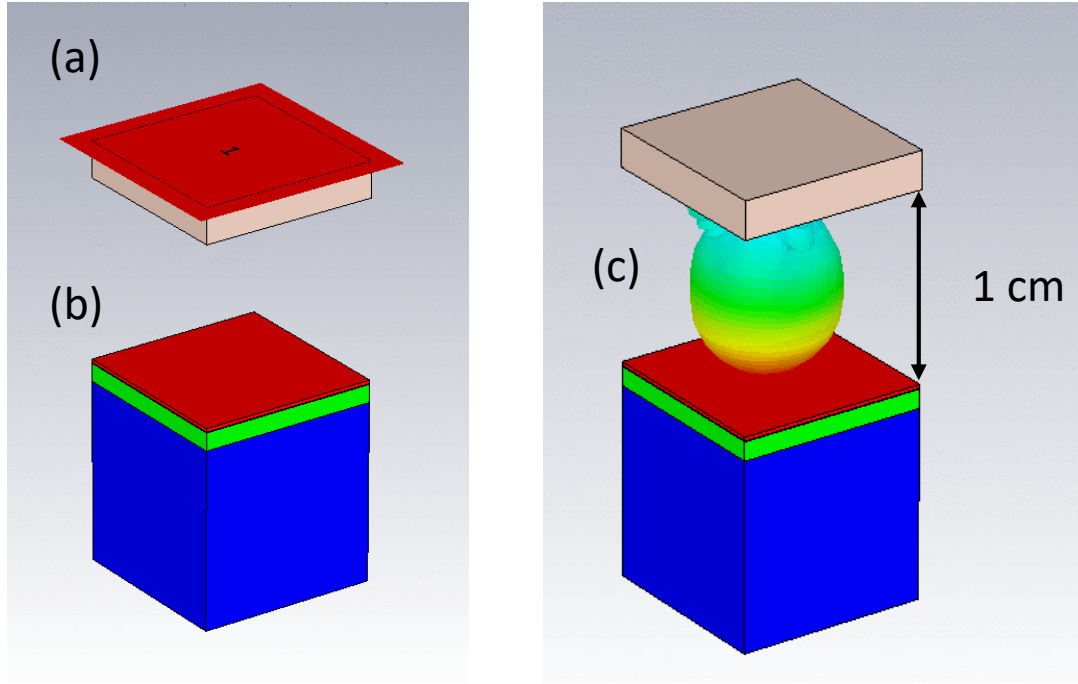
Figure 7.2.1: Diagram showing the emission antenna set up (not drawn to scale). (a) The port that will simulate a heated blackbody 5%AlInSb source. (b) The photodiode detector positioned 1 cm away. (c) The far field emission pattern.

The port suitable for this application is one that can stimulate the emission block with an emissivity of 1 (i.e. no reflection). To achieve this, a waveguide port needs to be used and the simulation is solved in a finite-difference time-domain (FDTD) simulation. The waveguide port differs from the floquet port used in the theoretical data for chapter 5 because it acts as a direct feed into the system with very low levels of reflection. These reflections can be set to zero when the port boundary conditions are set to a perfect electrical conductor (Et = 0).

The escape cone pattern is expected to be Lambertian and influenced by the materials critical angle, ϕ_c[104].

$$\phi_c = \sin^{-1} \frac{n_2}{n_1} \qquad\qquad\qquad (7.2.1)$$

Where n_1 is the refractive index of the material from which the projection is emanating and n_2 is the refractive index of the material surrounding it (usually air). The critical angle indicates the point away from the normal the internal light must be projected before total internal reflection is expected to happen. The higher the refractive index of the substrate, the more total internal reflection will occur. From this data, the fraction of light that will escape the blackbody is given by:

$$A = \int_0^{\phi_c} 2\pi r \sin\phi r d\phi = 2\pi r^2 \left(1 - \cos\phi_c\right)$$
(7.2.2)

Where r is the distance travelled by the propagating wave from the point of origin. By extension the proportion of escaping power can be determined by applying a ratio between the amount of light that will escape with the surface area of a sphere:

$$\frac{P_{escape}}{P_{source}} = \frac{2\pi r^2 \left(1 - \cos\phi_c\right)}{4\pi r^2} = \frac{1}{2}\left(1 - \cos\phi_c\right)$$
(7.2.3)

The ½ part of equation 7.2.3 accounts for half of the light going backwards. The shape of the emission pattern is dictated by Snell's law.

$$\frac{n_1}{n_2}\sin\phi = \sin\theta$$
(7.2.4)

Where ϕ is the trajectory angle within the material with refractive index n_1 and θ is the trajectory angle upon remission into a different material with a refractive index of n_2. This means that a higher refractive index would result in less radiation escaping and the Lambertian emission pattern would be thinner. Figure 7.2.2 illustrates the simulated power emitted at different values of refractive index.
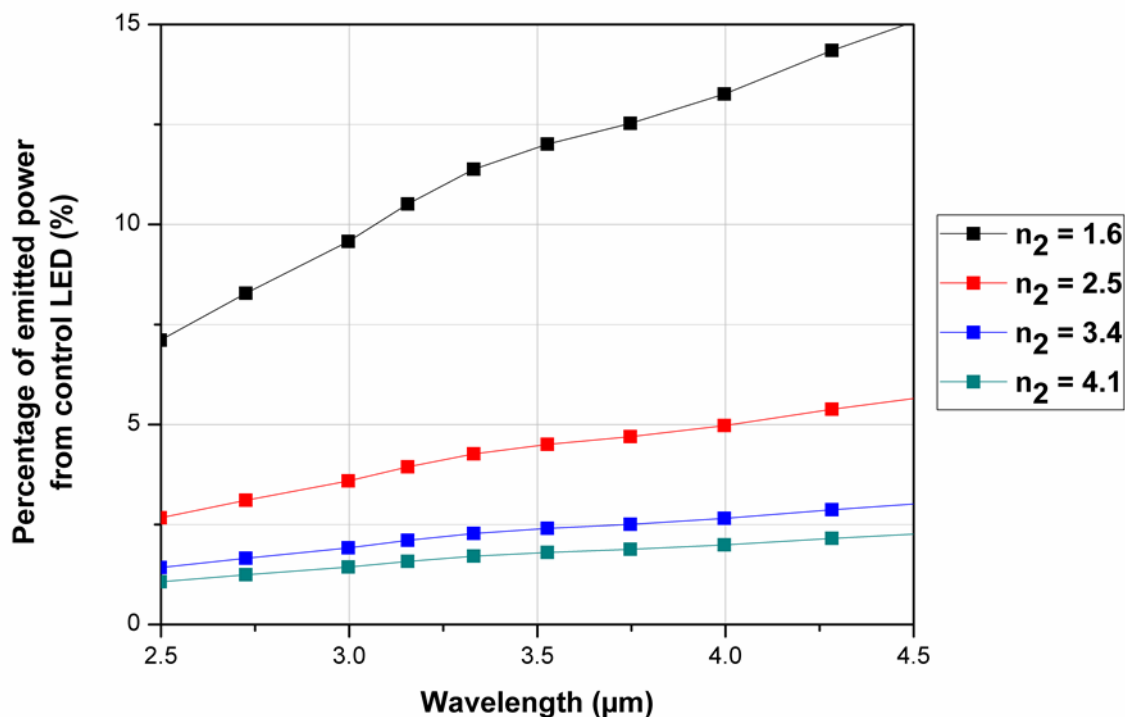
Figure 7.2.2: The simulated radiated power from the control substrate when combining 20 modes on a 1 μm cubed LED when the refractive index is 1.6, 2.5, 3.4 and 4.1.

The filtered emission will be detected by a photodiode about 1 cm away. There is therefore a further advantage if the antenna array can collimate the outgoing light. Collimated light is subject to fewer reflections when incident on the photodiode. Before the emitted light can be categorised as sufficiently collimated, however, it must have a far field angular width of < 5 degrees.

7.3) Antenna design for enhanced LED emission

Analysis will begin with the hexagonal antenna design shown in figure 7.3.1. This array has fluctuating radiative gains about 20 THz apart. It can produce a bandwidth but it is observed to be poor at filtering out the emitted power to a single frequency (i.e. multiple peaks observed).

Figure 7.3.1: The hexagonal antenna design applied to an LED. (a) The normalised emitted power vs. the simulation wavelength for a 5%AlInSb LED with a hexagonal array design. (b) The far field plot of the surface emission at 90 THz or 3.33 μm for the Al antenna array.

Out of all the materials used, the aluminium antennas produce the least amount of radiated power. The reason for this is because there is a significantly elevated surface reflection in the space the antennas occupy.

Using InAs materials demonstrates a much better far field enhancement, thus supporting the explanation that impedance mismatch below the antennas is a considerable factor that influences emitted power.

Using $Al_{0.05}In_{0.95}Sb$ antennas provide context to what would happen in the surface was corrugated with like material. What is observed is that there is a rise in transmissivity where bandwidths were featured in the InAs and Al materials, signifying that corrugated materials have increase reflectivity at resonating parameters on the surface. The parameters of the

corrugated shapes have been adjusted to produce a peak at 90 THz so as the comparison experiment as fair as possible.

Figure 7.3 (b) shows the far field pattern of the hexagonal array. Although the diagram features Al antennas at 3.33 μm, this pattern is consistent with the other two materials as well, the only difference is in the far field bulk magnitude (details are given in table 7.3). The far field has a beamwidth that is rounded but still wider than the control far field magnitude. According to the antenna dependency on trajectory angle, the absorption will not start to degrade until the trajectory angle goes beyond 20º, so a beamwidth of this size arguable has little impact.

The hexagonal antenna design has an inferior emission power density and although an emission bandwidth is possible to implement it contains questionable wavelength suppression at other frequencies. This design can therefore provide little benefit and other designs need to be considered.

The hexagonal grating antennas shown in figure 7.3.2 are the inverse of the hexagonal design that is considered as a design alternative. After the initial analysis of this design in section 3.9, it was established that this design had an advantage over other designs in terms of its single point focusing and might be able to reduce the beamwidth to provide an elevated power density the hexagonal antenna design lacked.

Figure 7.3.2: The hexagonal grating antenna design applied to an LED. (a) The normalised emitted power vs. the simulated wavelength for an Al, InAs and 5%AlInSb hexagonal grating design. (b) The far field plot of the surface emission at 90 THz or 3.33 μm for the Al antenna array.

Initial observations showed a clear advantage it regards to an established bandwidth. The amount of power radiated at the peak is similar to the hex design, but it is much better at suppressing other frequencies. The emitted power is less dependent on the antenna material compared to the hexagonal antenna. Similar to the previous example, using like materials still show an enhanced reflectivity at resonant wavelengths, although the reflectivity is dampened.

The far field pattern features several emission beams with the central one having the main bulk magnitude. It has been observed that the higher the degree of coupling there is in the

antennas, the more dispersive the far field is. It is for this reason that Al antennas will feature a larger central bulk magnitude.

The dipole design was investigated to verify if the far field pattern can be manipulated to be more suitable for a dipole design on the receiver. Similar to the example in section 7.3.1, the design has poor frequency suppression capabilities. The majority of the readings are similar to the control emission.

Far field focusing only occurs for a single orientation (0° degree cut off), but because the angular width is so large in the other orientation (90° degree cut off) the beamwidth is generally not a competitive size.
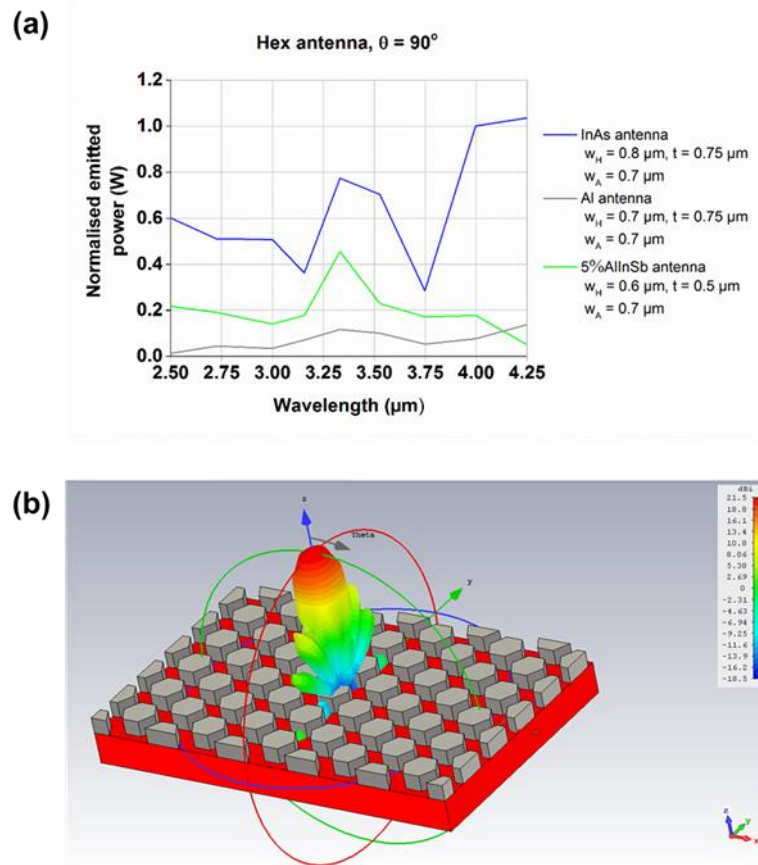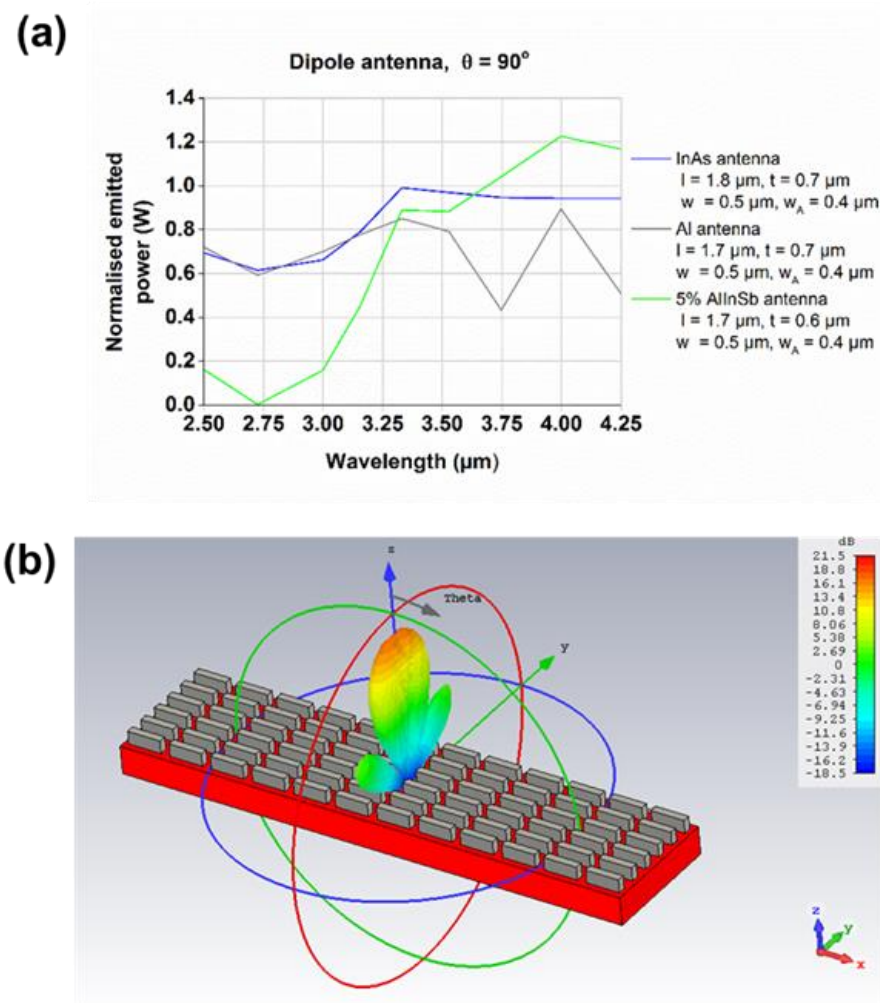

Figure 7.3.3: The dipole antenna design applied to an LED. (a) The normalised emitted power vs. the simulated wavelength for an Al, InAs and 5%AlInSb dipole design. (b) The far field plot of the surface emission at 90 THz or 3.33 μm for the Al antenna array.

The dipole grating has better bandwidth capabilities but is far more suppressive compared to the hexagonal grating example. This is because most of the emitted light is the wrong orientation for the dipole grating array to be responsive to it. The material used once again accounts for a significant difference in radiated power.

Both this design and the dipole antenna design have an advantage of a narrow beamwidth for one orientation (0° degree cut off) and if the photodetector had a dipole antenna array of a perpendicular orientation then this design could benefit from a small beam width.
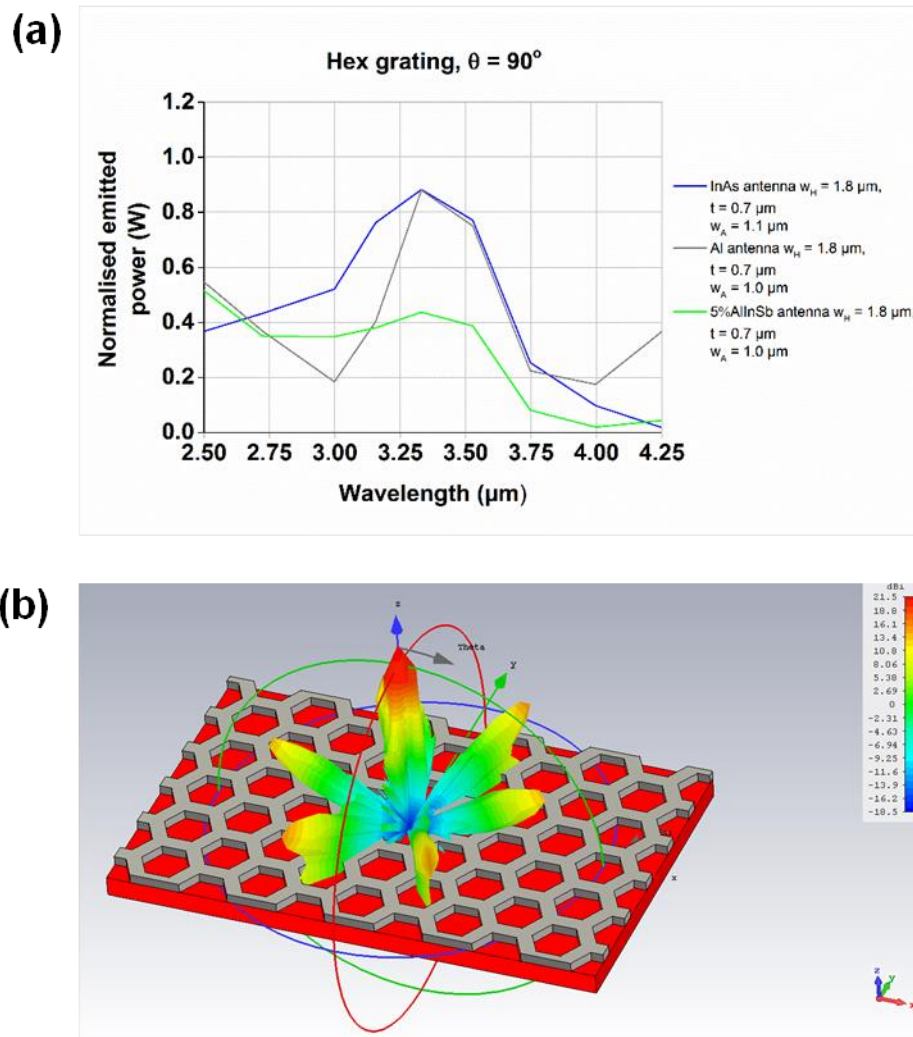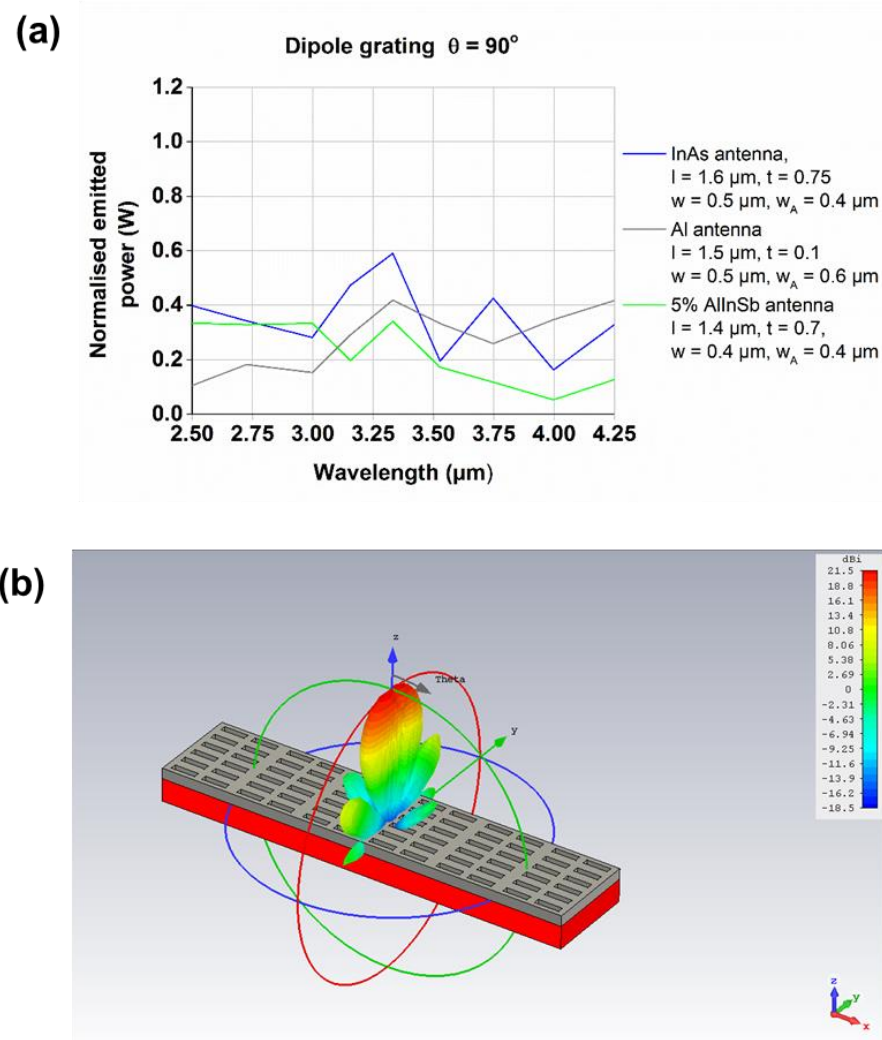

Figure 7.3.4: The dipole grating antenna design applied to an LED. (a) The normalised emitted power vs. the simulated wavelength for an Al, InAs and 5%AlInSb dipole grating design. (b) The far field plot of the surface emission at 90 THz or 3.33 μm for the InAs antenna array. (c) and (d) display the far field polar plot at a 0° and 90° cut angle respectively.

The results for all the tested designs are summarised in TABLE 7.3. Information regarding the antenna's use as a filtering mechanism is provided as the percentage of power radiated between 3.0 µm and 3.5 µm. The main lobe magnitude varies with antenna shape and conducting material. It is interesting to note that the InAs antennas produce better results when applied to a dipole design as a result of a more centralised emission after coupling. However, none of the designs produce an improved far field focusing. They are also only a fraction of the control main lobe magnitude. The hexagonal designs demonstrate that they can produce the narrowest beam where the hexagonal grating design can produce a beam that is also collimated. Such a thing would be ideal if most of the radiation was being emitted a wide trajectory angle.

TABLE 7.3: A summary of the far field results for the listed antenna designs.

Design	Percentage of radiated power between 3.0 µm and 3.5 µm (%)	Relative main lobe magnitude gain (linear)	Angular beam width (degrees)	
			At 0° cut off	At 90° cut off
Control	39	1.00	-	-
Hex antenna, Al	48	0.40	14.6	17.8
Hex antenna, InAs	47	0.28	12.5	14.8
Hex antenna, 5%AlInSb	47	0.12	12.5	14.6
Hex grating, Al	39	0.47	6.5	7.7
Hex grating, InAs	61	0.28	6.3	7.2
Hex grating, 5%AlInSb	43	0.17	7.2	6.3
Dipole antenna, Al	18	0.41	8.2	25.2
Dipole antenna, InAs	35	0.61	8.2	25.2
Dipole antenna, 5%AlInSb	35.1	0.45	8.2	25.2
Dipole grating, Al	41	0.18	8.3	27.5
Dipole grating, InAs	46	0.23	8.3	27.5
Dipole grating, 5%AlInSb	41	0.17	8.3	27.5

7.4) Chapter 7 conclusion

This chapter addresses the viability of applying micro-antenna designs to semiconductor LEDs. The far field control emission is sensitive to the number of port modes and the unit cell size making a consistent Lambertian emission difficult to obtain. The antenna designs, however, have a consistent beamwidth regardless of the unit cell pitch and can tolerate a reduction in port modes. The antenna influenced far fields can be compared with one another with suitable consistency.

The emission pattern bulk magnitude in all considered designs is not big enough to compete with standard LED emission. Despite efforts to optimised the radiated power, the conducting antenna material either block out or redirect a large proportion of the input power away from the centralised bulk magnitude. Impedance mismatch at the LED surface was recorded to be a relevant factor where the materials that coupling in the most light produce a more dispersed main lobe magnitude.

The smallest beamwidth is achievable if the antenna design is responsive to all polarisation angles. The hexagonal antennas and the hexagonal grating antennas demonstrate this. However, they also have a more suppressed and dispersed main lobe magnitude compared to dipole designs.

The antenna designs have been recorded to be frequency sensitive and can produce spectral emission bandwidths. Similar to the antennas used for the enhanced photodiode designs, the antennas are responsive to resonance conditions. This makes these enhancements beneficial as a bandwidth filter. The dipole antennas show small peaks on an emission curve that is generally similar to the control curve, but the grating antennas that show a clear bandwidth response, with the hexagonal grating antennas radiating 133% more than the dipole grating.

Using a corrugated surface to obtain a bandwidth is possible but produces inferior results to the other materials used. For the same parameter, antennas made out of the same material as the semiconductor produces a reduced overall emission and a reduced main bulk magnitude. The bandwidth it produces is roughly similar in size compared to the other antenna materials.

These investigations have concluded that the antenna arrays applied to LED are only useful as bandwidth filters to the detrimental of the emitted signal.

8) Conclusions and recommendations for future work

8.1) Main conclusions

The original contribution of knowledge in this thesis is an analysis both experimentally and in simulation for how micro-antenna enhancements can benefit non dispersive mid-infrared (NDMIR) semiconductor detectors. The intended application for this technology is hazardous gas detection in the mid infrared spectral range, where gases of interest include CO_2 which has high absorption at 4.2 µm and CH_4 which has high absorption at 3.3 µm. This research is needed to reduce path length in photodetectors, remove the need for wavelength filters and reduce the reflections at the semiconductor boundaries.

The semiconductor hazardous gas sensor functions by means of an LED that emits infrared light and a detector that records a reduction in intensity of the infrared light that hazardous gases will absorb. This PhD has focused on designing a series of antennas applied to photodetectors that have a peak spectral response between 3.0 µm and 4.5 µm. $Al_{0.05}In_{0.95}Sb$ LEDs and photodetectors were chosen as the vehicle for the designs and experimental verification material over numerous other emitters and detectors. The gas detection industry is vast, but $Al_{0.05}In_{0.95}Sb$ semiconductors can compete with most alternative gas sensing technologies (see section 1.2) due to their advantage of having fast response times, appropriate bandwidth sizes, small size, a long lifetime, little maintenance requirements, resistance to poisoning and competitive power consumption and component costs.

Documented literature in this field has demonstrated antenna influenced reductions in reflectivity and enhanced absorption capabilities but has not addressed the application to semiconductors used for gas detection and the dependency on the signal absorption at certain depths of the semiconductor after coupling. This thesis not only addresses this, but also has

examined the intricacies of enhanced absorption of infrared radiation in semiconductor photodiodes and emission of infrared radiation from the same semiconductor materials.

The work in this thesis has addressed the development and documentation of improvements to existing typical semiconductor devices by means of effective waveguide manipulation in the i-type region of semiconductor PIN diodes using wavelength-scale micro-antennas which feature effective localised coupling near the surface. The aim was to determine whether a factor of 8 increase in semiconductor gas sensor signal-to-noise ratio is achievable. Results have shown it is theoretically possible the achieve a factor of 6.0 increase when considering particularly elaborate designs that fully capitalise on the antenna influence localised focusing (see section 6.2). However, these designs pose considerable manufacturing difficulties such as precision alignment, fragile interconnections for probing requirements and densely packed antenna arrays that are different to successfully lift-off. It is a design that realistically cannot be made with conventional contact photolithography, but can achievable with other techniques such as nanoimprint lithography. The experimental work has therefore accumulated data from a more simple design with a theoretical factor increase of just under 2 under ideal circumstances. Micro-antenna designs were implemented experimentally onto semiconductor mesas after suitable consideration to the semiconductor processing method was given (see section 4.3 and 4.4). Compromises in the fabrication outcomes have degraded the signal-to-noise ratio to a factor of 1.5 to 1.7 increase, but these enhancements have still proven to be competitive with antireflection coating technology.

Aluminium is the most frequently used antenna material for these experiments because it is desirably brittle for pitches less than 2 μm in length; it requires no adhesive layer; and has only a very marginal difference in signal absorbed compared to other conductive materials. Aluminium antennas can enhance the spectral response further if they had a higher

conductivity, but those materials are soft and a high ultimate tensile strength has been recorded to be problematic during the lift-off phases for thicknesses between 0.5 μm and 1.0 μm (see section 4.4). A material's conductivity which stems from its dielectric properties and method of deposition is a key input when deriving the antenna quality (Q) factor, which is a measure of how much energy the antenna material can contain without losing that energy as heat. Non-adhesive materials such as gold have shown to be problematic when competing with more adhesive materials. The layers that one normally uses to promote adhesion of non-adhesive antenna materials to the semiconductor surface are titanium or chromium. Both of which will act as resistive barriers and will impede light coupling into the semiconductor.

Prior to experimental fabrication, the waveguide antenna enhancements were simulated using Finite-difference time-domain (FDTD) and Finite-difference frequency-domain (FDFD) simulations using EM simulation software (CST^{TM}) as a hybrid model. This means that the simulation software cannot produce results that are entirely accurate without data input from external sources. These being; the $Al_{0.05}In_{0.95}Sb$ attenuation coefficient, the influences on the zero biased resistance of the semiconductor devices and the circuitry impedances of the autoprober. A floquet port was used to replicate a single unit cell an infinite number of times. This was an approximation that was deemed appropriate since the number of antennas across different mesa sizes contained several hundreds of antennas both vertically and horizontally.

The mesas designs feature an annulus and a contact pad, which had little impact on the floquet port approximation, but was recorded to generate excess minority carriers and degrade the zero bias diode resistance if a barrier of $Al_{0.05}In_{0.95}Sb$ with higher Al content was not introduced in semiconductor devices with much thinner p-type thicknesses compared to conventional semiconductor thicknesses. Thin top epitaxial layers (i.e. a p-type thickness reduction from 1 μm to 0.1 μm) are necessary to capitalise on localised focusing. The

heterostructure design does not stop the photodiode leakage entirely, but limits the degradation in zero bias resistance to less than 5% when considering the equivalent circuit and Kirchhoff's law (see section 5.4 and section 5.5.1).

In order to ensure accurate simulation of the data, dielectric properties were either taken from reliable references or they were measured and derived experimentally if the information was not available. All of the materials that have been considered in this thesis have their real and imaginary dielectric constants specified for a spectral range of 50 THz to 200 THz (1.5 µm – 6 µm) documented in the appendix. $Al_{0.05}In_{0.95}Sb$ is one such material whose dielectric constants were not previously published. The values as a function of wavelength were measured and derived by assessing the absorption coefficient in an FTIR spectrometer.

There were defects in the micro-antenna fabrication that needed to be accounted for during analysis. There was a degree of rounding that caused a shift in the peak spectral response. This rounding reduces the top surface area and increases the bottom surface area of the antenna. SEM observations indicated that the pivot points of these side wall angles are about a third of the antenna thickness up from the base. For this reason, the bottom hexagonal width is given when a side gradient is featured. The other parameters can be logically derived. The side wall gradient of fabricated antenna arrays is recorded to be between 70° and 75° (where 90° is a vertical side wall). The impact of the antenna side wall of varying gradients is provided in section 5.3. Once these modifications to the antenna shapes were included in the simulation very good agreement between the simulation and experimental results was obtained, as shown in figure 5.5.1.6 (replicated here as figure 8.1 for the convenience of the reader).

W4, Al antenna, t = 0.75 µm, w_A = 0.70 µm, θ = 73°
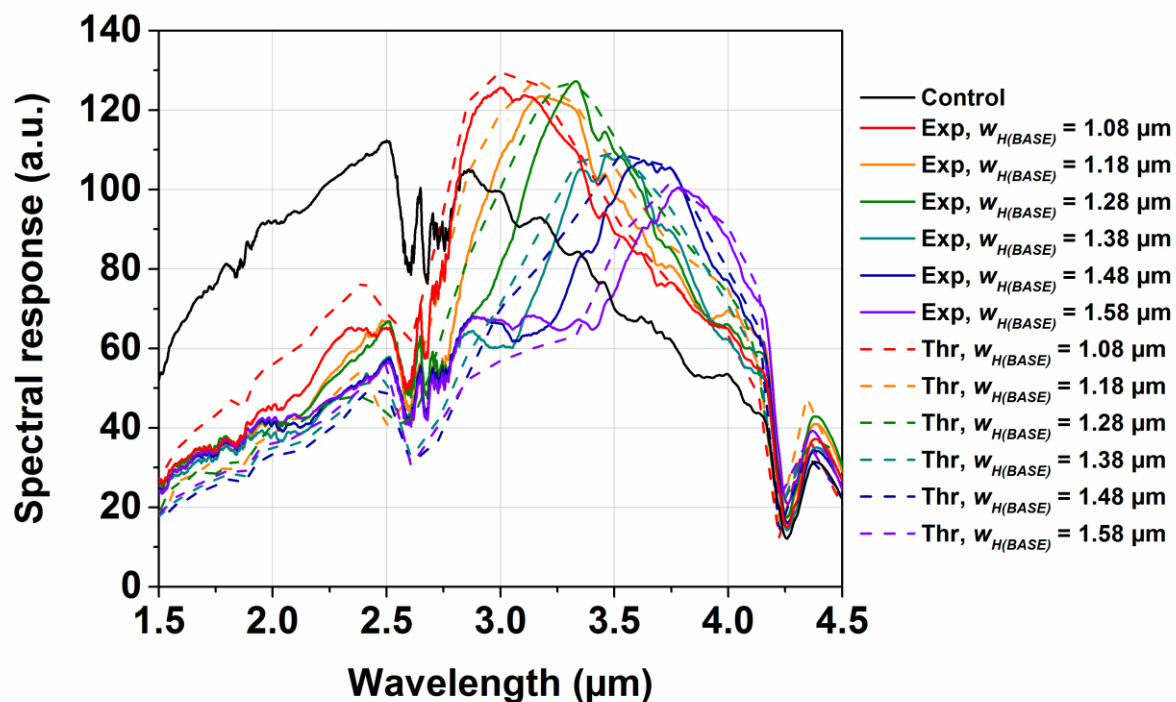
Figure 8.1: Experimental (solid) and simulated (dashed) spectral responses for (a) a detector without micro-antenna and (b) to (g) detectors with micro-antennas of thickness t = 0.75 µm, aperture width $w_{A(base)}$ = 0.56µm, side-wall angle θ = 73° and hexagonal widths $w_{H(base)}$ of (b) 1.08 µm, (c) 1.18 µm, (d) 1.28 µm, (e) 1.38 µm, (f) 1.48 µm and (g) 1.58 µm.

The results that have been experimentally achieved (solid lines) show a clear enhancement to the peak i-type absorption by a factor of 1.56 at 3.3 µm. The spectral bandwidth has been reduced to approximately 1.4 µm and although there is a side gradient defect in the fabricated antennas, analysis has shown that it has a greater tolerance to incoming light with a wider trajectory angle compared to antennas with vertical side walls.

There then followed a theoretical investigation of further improvements that may be feasible, building on the experimental results. They are summarised in figure 8.2 (which is replicated from figure 6.5 for the convenience of the reader) and serve as a summary for potential further work in this field and the S/N ratio one can expect from it.
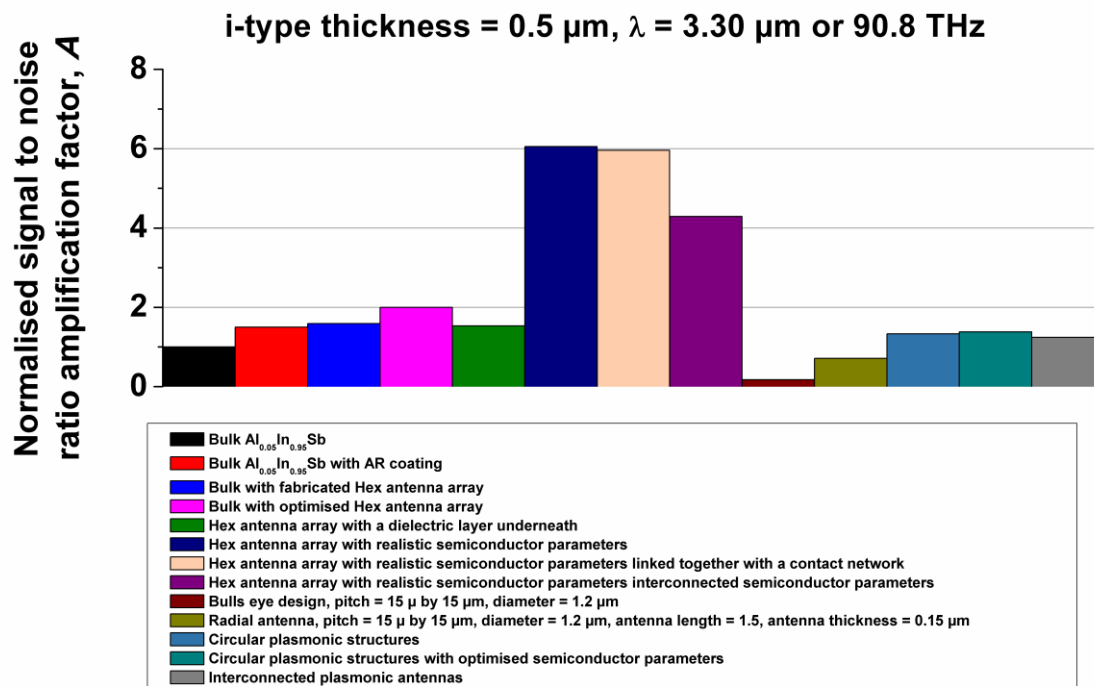
Figure 8.2: The change in normalised S/N enhancement factor when alternative antenna designs are used.

The hexagonal antenna array with optimised selectively removed semiconductor parameters (see section 6.2) has shown to produce the highest enhancement factor for this application. These semiconductors that were optimally selectively removed could not be probed and therefore require to either be interconnected or to have a conducting network that could connect each individual semiconductor part for which the conducting network yielded the better results.

Other methods that have been considered include anti-reflection layers, radial feed point antennas and plasmonic antennas. However, these alternatives show no improvements in the S/N ratio or the bandwidth compared with fabricated hexagonal antennas on bulk $Al_{0.05}In_{0.95}Sb$.

The radial feed point antennas (see section 6.3) can improve the S/N ratio on a bull's eye semiconductor 0.6 µm in radius and 0.5 µm in i-type thickness by a factor of 4.7. The radial

feed point antennas would have provided a competitive signal enhancement if a large proportion of the i-type wasn't removed over a 15 μm square pitch resulting in the bull's eye structure having only 15% of the controls S/N ratio. It could potentially compete with other enhancements if the semiconductor size was a fraction of the area as an original necessity of the design.

The plasmonic antennas (see section 6.4) have shown effective coupling at the frequency of interest when using much smaller antenna sizes. They work by using different lossier materials to alter the plasmonic wavelength so that the antennas resonate at wavelengths that are much larger than the dipole rule would allow. The coupling is more evenly distributed and the propagation into the substrate is at lower angles away from the normal. Therefore, plasmonic antennas cannot benefit from a reduced epitaxial layer thickness or selective removal as much as the higher order wavelength scale antennas.

Grating antennas were not the chosen design for semiconductor photodetectors on the grounds that they have a supressed peak and less energy is coupled into the semiconductor as a result. However, this design was reconsidered for enhanced emission of infrared radiation for an $Al_{0.05}In_{0.95}Sb$ LED. In these tests, it was verified that reducing impedance mismatching between the emitter and the antennas was beneficial, but reducing the impedance mismatches to zero by using like materials showed no benefit, as the surface no longer resonated. In both cases, grating antennas were the recommended design as it can produce a well-defined bandwidth for signal filtering. Using the antenna design as a signal filter was the only benefit the antenna enhancements could provide.

A square waveguide port was used instead of a floquet port to best simulate isotropic generation within the material. In order to achieve a completely isotropic source, many oscillation modes need to be included and combined. A compromise was necessary for the

number that was incorporated to provide sufficiently good agreement with theory data from internal reflections if the modes were specially selected. This was done to reduce simulation time and still maintain accuracy. A summary of the emission antenna results are given in TABLE 8.1 (replicated from TABLE 7.3 for the readers convenience).

TABLE 7.1: A summary of the far field results for emission antenna on LEDs displayed in section 7.3.

Design	Percentage of radiated power between 3.0 μm and 3.5 μm (%)	Relative main lobe magnitude gain (linear)	Beam angular width (degrees)	
			At 0° cut off	At 90° cut off
Control	39	1.00	-	-
Hex antenna, Al	48	0.40	14.6	17.8
Hex antenna, InAs	47	0.28	12.5	14.8
Hex antenna, 5%AlInSb	47	0.12	12.5	14.6
Hex grating, Al	39	0.47	6.5	7.7
Hex grating, InAs	61	0.28	6.3	7.2
Hex grating, 5%AlInSb	43	0.17	7.2	6.3
Dipole antenna, Al	18	0.41	8.2	25.2
Dipole antenna, InAs	35	0.61	8.2	25.2
Dipole antenna, 5%AlInSb	35.1	0.45	8.2	25.2
Dipole grating, Al	41	0.18	8.3	27.5
Dipole grating, InAs	46	0.23	8.3	27.5
Dipole grating, 5%AlInSb	41	0.17	8.3	27.5

In summary, this thesis has been an investigation into how waveguide manipulation can be used to advance semiconductor gas detection products beyond their capabilities and effectively compete with anti-reflection coatings utilising their focusing capabilities. Experimentally, wavelength scale antennas have been fabricated using photolithography in a

reliable and financially viable fashion. Further analysis has uncovered more elaborate designs to increase the S/N ratio by over 6 times compared to a plane substrate. The transmission antenna designs that can reduce the spectral bandwidth are grating antennas. The beamwidth is also minimised and even though there are some antenna materials that reduce emission losses to a minimum the antenna design will emit this radiation at wider angles and the main lobe magnitude will disperse as a result.

8.2) Recommendations for future work

As development of semiconductor photodetectors have shifted towards small devices with thinner epitaxial layers, these devices strongly benefit from localised focusing as many of the references in chapter 2 will mention. Micro-antenna influenced localised focusing has complemented the semiconductor development enormously by reemitting the light towards the thin top semiconductor layers, but in regards to future development it is worth emphasising that localised focusing can only effectively be achieved by using wavelength scale coupling. Plasmonic coupling (section 6.4) does have effective coupling capabilities but has shown that the signal propagation is directed deeper into the semiconductor which conflicts with semiconductor future development of making semiconductor active region thinner.

Thorough analysis of the experimental work and the computational electromagnetics (CEMs) has provided a number of further recommendations towards future development in both semiconductor LEDs and photodetectors. The majority of these improvements address the semiconductor photodetectors due to much more time in this thesis being dedicated to their improvement, but the most fundamental recommendation to make towards improved results for both devices is to minimise or avoid (if possible) creating side gradients during the manufacturing procedure of the antenna array (see section 5.3). Side gradients have been

recorded to degrade the quality of the antenna array, shift the peak response from the design's target wavelength and narrow the antenna array aperture width.

Effective waveguide coupling that is influenced by antenna arrays is very sensitive to the aperture width and it is recommended that the aperture width is suitably small for thin localised focusing applications. Note: The difficulty of doing this is that it will likely produce an aperture width to antenna width ratio that is difficult to successfully yield during photolithography lift-off procedures. The lift-off procedures can be made easier if brittle antenna materials with no required adhesive layers are used. Aluminium has been shown to have desirable properties to address precision based lift-off. While it has also demonstrated that it can compete with other conductive materials (such as gold, silver or copper) with marginal compromises to antenna quality, the manufacturer should be aware of using materials that are too lossy (such as titanium) or the signal will be absorbed before coupling into the semiconductor at the antenna terminals. The only exception to this is if the antenna material needs to be intentionally lossy to achieve resonance in small volumes of antenna.

Selective removal of the semiconductor has demonstrated the most promise for future development (see section 6.2). Investigations have shown that selective removal around the coupling hotspots is an effective way to increase the signal-to-noise ratio by virtue of removing volume based noise in regions that absorb a lower amount of signal. This requires elaborate precision based photolithography but is ultimately worth the effort due to significant improvements in the diode response. The interconnections are necessary but detrimental to the S/N ratio factor increase, but it has still been recorded to be as high as a 6.8 factor increase in ideal circumstances, but non-ideal manufacturing outcomes can still show a factor increase by up to a factor of 6.0.

There are some recommendations for future development that are only valid under certain circumstances. Radial feed point antennas are an example of this (see section 6.3). They are

effective at forwarding a signal to a relatively small target and are a valid engineering solution for signal accumulation in a nanowire or another application where most of the incident radiation misses the target in a large surface area. The problem when applying this to a semiconductor photodiode is that the incident radiation is not missing the target when the entire semiconductor surface area is a useful region to have a signal incident on it. By minimising the semiconductor surface area and forwarding the signal to the semiconductor target, it has been noted that the signal increases by several factors relative to the cut out semiconductor will no antennas at all, but a significant amount of signal has already been lost in the minimised semiconductor design. Results show that the design will struggle to match the efficiency of standard semiconductors. This development is only recommended if the surface area of the semiconductor is small compared to the antenna size as a necessity of the device design. Otherwise a great deal of signal is needlessly lost.

Another example of situational recommendations is antennas applied to LEDs (section 7.3). It has always been the case that antennas will absorb some degree of incident radiation but are advantageous on photodetectors because they capitalise on signal direction that would have gone straight through otherwise. LEDs do not have this benefit. The localised focusing occurs at the antenna terminals and not in the far field bulk magnitude. As a result, the total emitted power is reduced and so is the main bulk magnitude compared to no antennas on the surface. There is still a benefit to using these devices as wavelength filter if the aforementioned compromises to the emitted signal are acceptable. Further investigations using plasmonic antennas for LEDs may be warranted. They have been recorded to have a coupling pattern that projects the signal further away from the antenna terminals. This could minimise the impact on main lobe magnitude deviation or even increase it if the focal point is several centimetres away from the surface.

The supporting simulation data can only be directly compared to experimental results when the simulation has the manufacturing defects included and the optimum parameter results can only be assessed by extension of the hybrid model's current calibration but could use a more direct comparison if possible. Therefore, this thesis encourages repetition of data where improved side gradients or where experimental measurements for the more elaborate designs are possible. This is to assess the accuracy of the simulation data where results had to be logically derived but not verified.

Another proposal to future development is incorporating internal reflectors into the semiconductor detector so that further signal enhancement is achievable by virtue of continuous reflections in the i-type boundaries until the signal dissipates. This will likely interfere with the semiconductor physics in a way that the modelling used in this thesis cannot account for. However it is worth considering for a new design of efficient photodetectors.

Appendix

Material dielectric properties. This information was input into the EM simulation software used in this thesis.

Dielectric properties of Al_2O_3[105]:

Frequency (THz)	Wavelength (µm)	ε′	ε″
60	5.00	2.3232	0.011980
70	4.28	2.4184	0.0069013
80	3.75	2.4768	0.0044066
90	3.33	2.5167	0.0029825
100	3.00	2.5443	0.0021268
110	2.73	2.5645	0.0015694
120	2.50	2.5801	0.0011886
130	2.30	2.5924	0.00090302
140	2.14	2.6015	0.00074194
150	2.00	2.6089	0.00058147
180	1.67	2.6242	0.00035639
194.7	1.54	2.6295	0.00025945
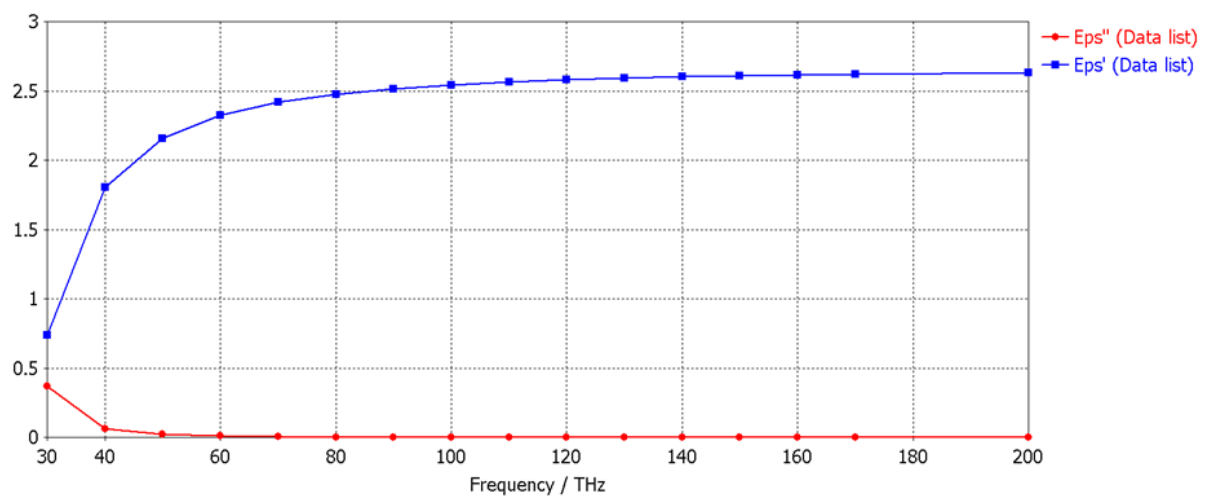
Dielectric properties of 5%AlInSb (n$^+$ type, i-type and p-type):

Frequency (THz)	Wavelength (μm)	ε′	ε″
66.6	4.501388258	15.97	0.29
69	4.344818232	15.96	0.53
71.3	4.204662805	15.96	0.75
73	4.106746	15.97	0.85
80	3.747405725	15.97	1.16
85	3.526970094	15.97	1.24
90.8	3.301679053	15.97	1.26
100	2.99792458	15.98	1.37
110	2.725385982	15.98	1.38
120	2.498270483	15.98	1.4
130	2.306095831	15.99	1.4
150	1.998616387	15.99	1.53
180	1.665513656	16.00	1.59
200	1.49896229	16.00	1.48
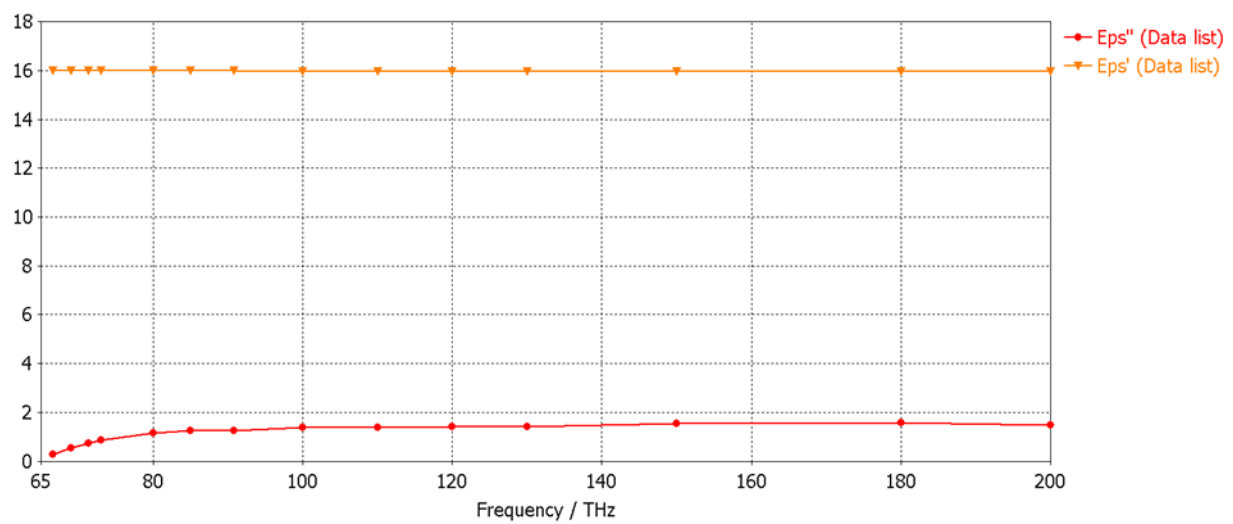
Dielectric properties of Al[106]:

Frequency (THz)	Wavelength (µm)	ε′	ε″
50	5.99584916	-2779.3	1295.9
60	4.996540967	-2062.6	867.01
70	4.2827494	-1588.7	602.62
80	3.747405725	-1264.0	435.89
90	3.331027311	-1023.4	322.9
100	2.99792458	-846.19	246.19
120	2.498270483	-623.29	170.38
150	1.998616387	-423.868	89.010
157.315	1.905682599	-331.757	78.804
169.396	1.769772946	-289.882	64.782
181.488	1.651858294	-235.256	54.378
193.548	1.548930798	-220.241	46.080
200	1.49896229	-235.256	42.504
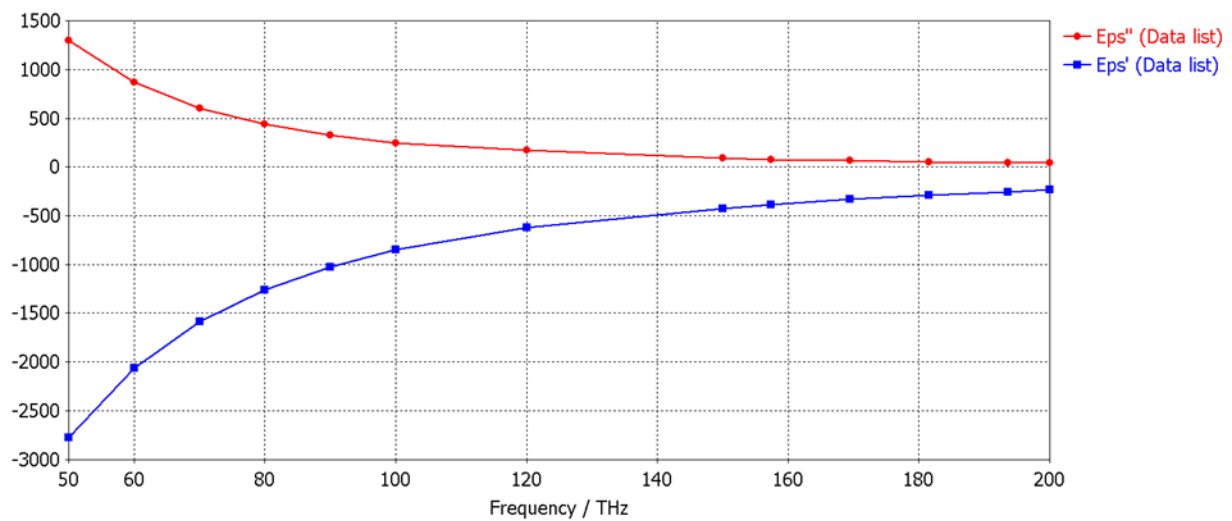
Dielectric properties of Cr[107]:

Frequency (THz)	Wavelength (µm)	ε′	ε′′
50	5.99584916	-354.01	170.44
60	4.996540967	-242.05	122.49
70	4.2827494	-172.57	95.227
80	3.747405725	-127.80	78.634
90	3.331027311	-96.395	67.433
100	2.99792458	-74.025	59.646
110	2.725385982	-57.488	53.998
120	2.498270483	-44.951	49.771
130	2.306095831	-35.253	46.546
150	1.998616387	-21.559	42.082
180	1.665513656	-9.4922	38.337
200	1.49896229	-4.7189	36.962
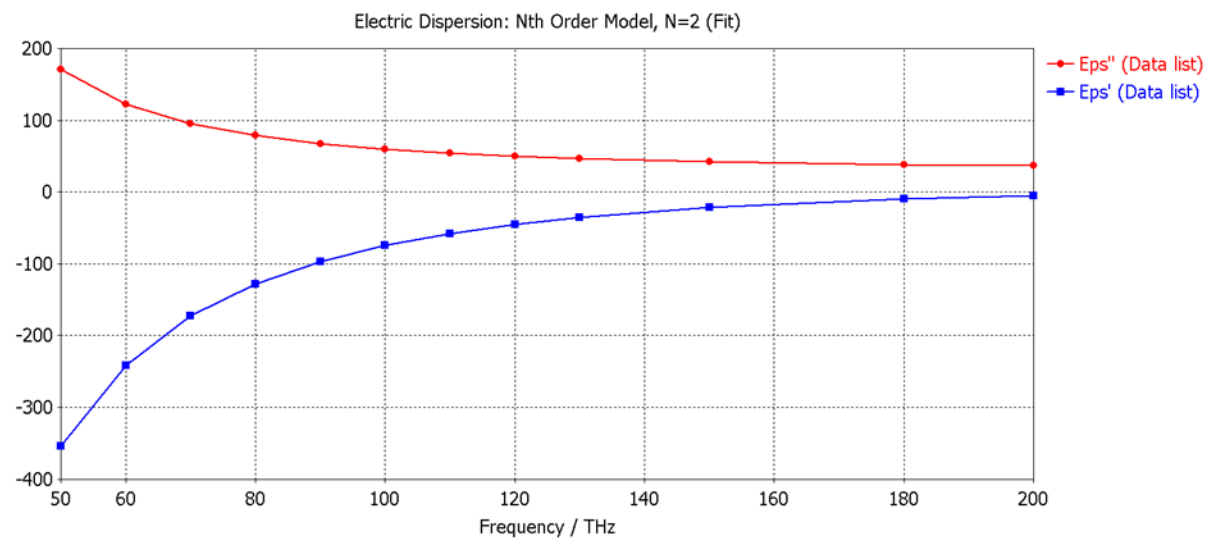
Dielectric properties of Ti[107]:

Frequency (THz)	Wavelength (µm)	ε′	ε″
50	5.99584916	-97.227	108.11
60	4.996540967	-62.89	85.266
70	4.2827494	-42.387	72.077
80	3.747405725	-29.515	63.581
90	3.331027311	-21.159	57.635
100	2.99792458	-15.601	53.185
120	2.498270483	-11.85	49.674
150	1.998616387	-9.2926	46.783
157.315	1.905682599	-7.5513	44.324
169.396	1.769772946	-6.3747	42.178
181.488	1.651858294	-5.6022	40.286
193.548	1.548930798	-4.6656	35.48
200	1.49896229	-4.6631	32.815
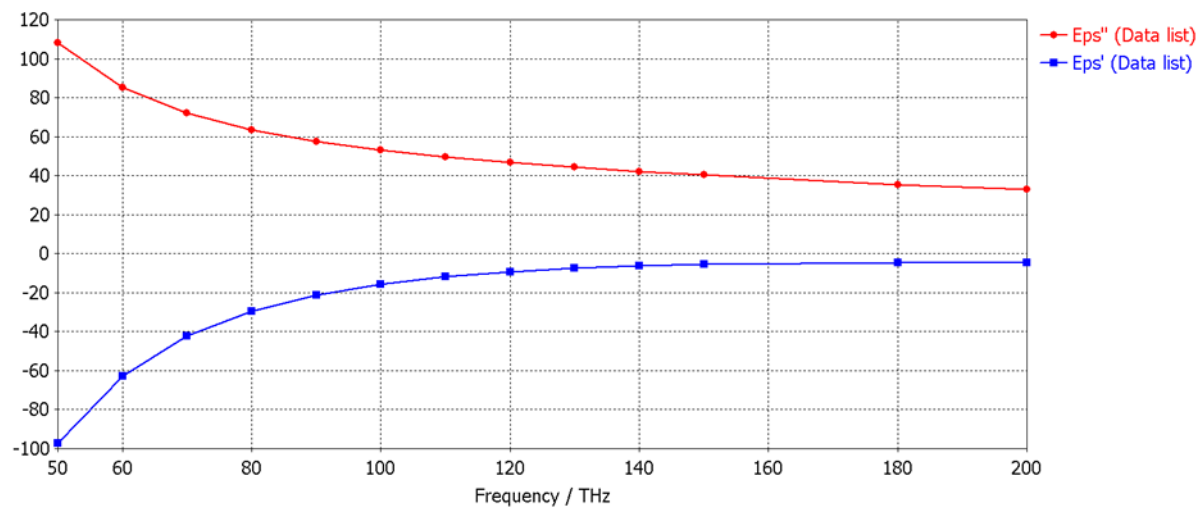
Dielectric properties of Pd[107]:

Frequency (THz)	Wavelength (μm)	ε′	ε″
50	5.99584916	-652.43	157.58
60	4.996540967	-439.23	136.48
70	4.2827494	-313.36	125.23
80	3.747405725	-234.94	118.69
90	3.331027311	-184.60	113.97
100	2.99792458	-151.74	109.31
110	2.725385982	-129.73	103.74
120	2.498270483	-114.23	97.115
130	2.306095831	-102.43	89.795
150	1.998616387	-84.442	75.254
180	1.665513656	-64.571	57.972
200	1.49896229	-54.647	49.750
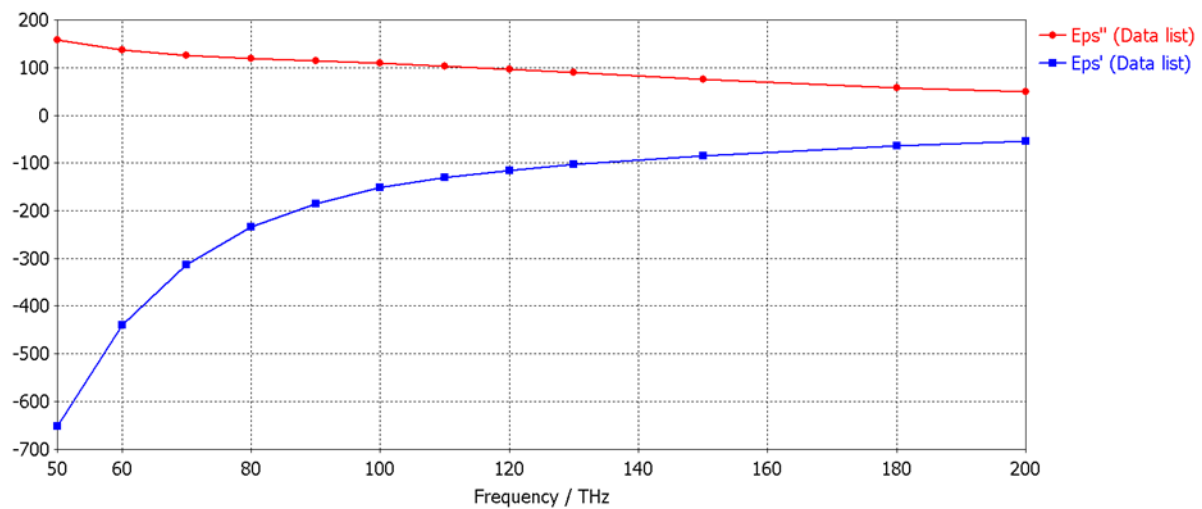
Dielectric properties of Au[108,109]:

Frequency (THz)	Wavelength (µm)	ε'	ε''
50	5.99584916	-1385	367.91
60	4.996540967	-977.43	223.9
70	4.2827494	-725.93	148.11
80	3.747405725	-559.83	104.11
90	3.331027311	-444.59	76.69
100	2.99792458	-361.45	58.599
110	2.725385982	-299.53	46.109
120	2.498270483	-252.19	37.143
130	2.306095831	-214.06	30.308
150	1.998616387	-162.05	21.544
180	1.665513656	-112.81	13.853
200	1.49896229	-90.678	10.59
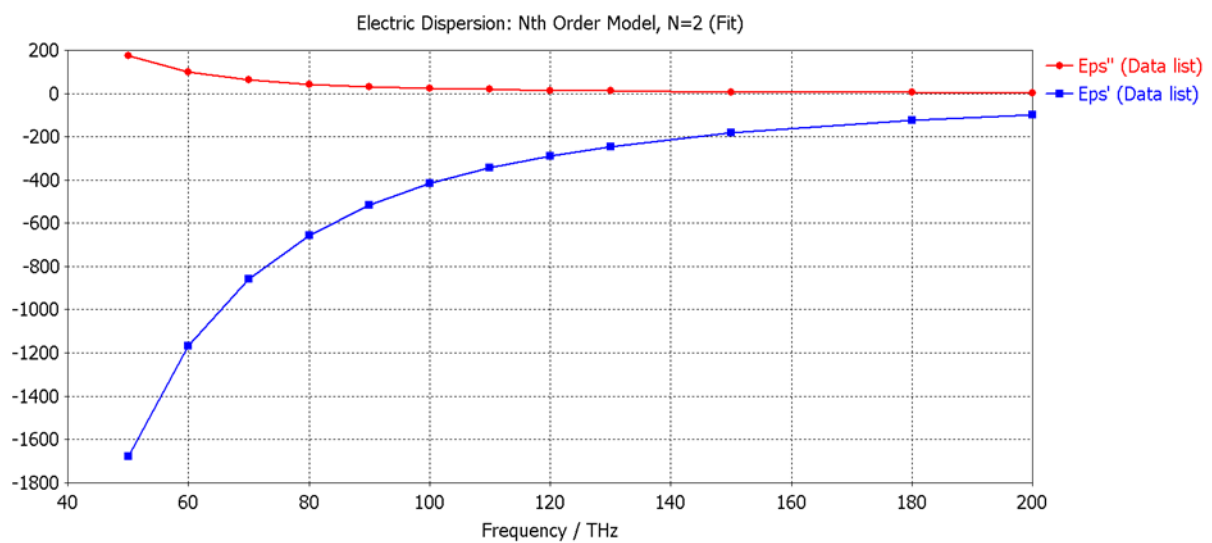
Dielectric properties of Ag[109]:

Frequency (THz)	Wavelength (μm)	ε'	ε''
50	5.99584916	-1915.7	153.22
60	4.996540967	-1340.9	91.368
70	4.2827494	-988.74	58.130
80	3.747405725	-758.57	39.367
90	3.331027311	-599.86	27.957
100	2.99792458	-485.92	20.580
110	2.725385982	-401.51	15.605
120	2.498270483	-337.16	12.133
130	2.306095831	-287.05	9.6472
150	1.998616387	-214.87	6.3812
180	1.665513656	-148.19	3.8066
200	1.49896229	-119.42	2.8720

Electric Dispersion: Nth Order Model, N=2 (Fit)
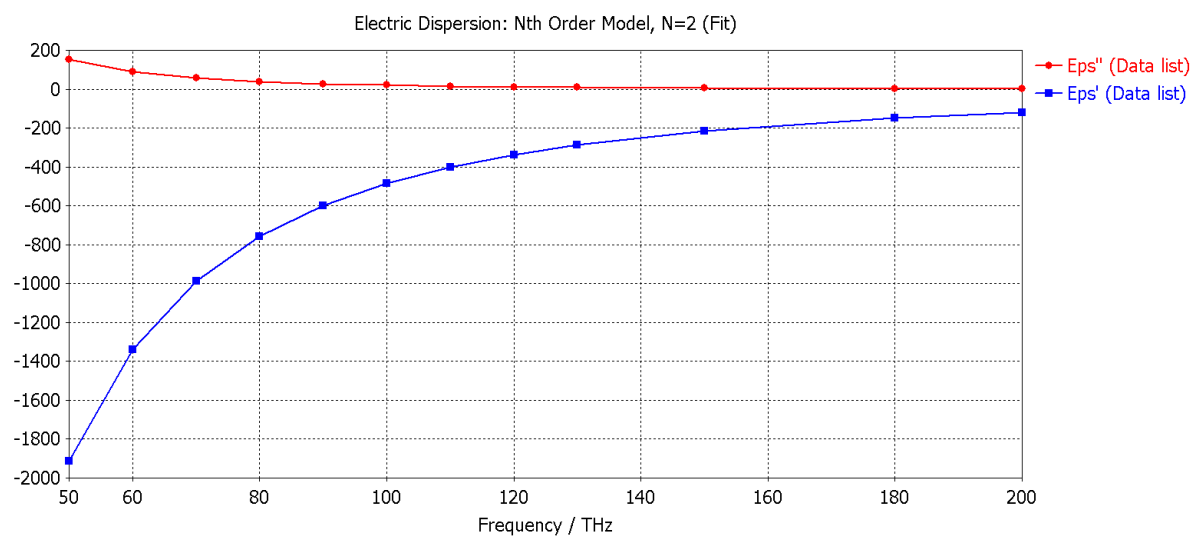
Dielectric properties of Pt[107]:

Frequency (THz)	Wavelength (µm)	ε'	ε''
50	5.99584916	-549.31	255.73
60	4.996540967	-376.69	162.92
70	4.2827494	-264.72	114.39
80	3.747405725	-190.38	88.336
90	3.331027311	-137.10	73.598
100	2.99792458	-99.144	65.931
110	2.725385982	-71.048	62.528
120	2.498270483	-49.647	62.087
130	2.306095831	-33.573	63.855
150	1.998616387	-16.655	70.724
180	1.665513656	-16.395	78.134
200	1.49896229	-23.097	73.623
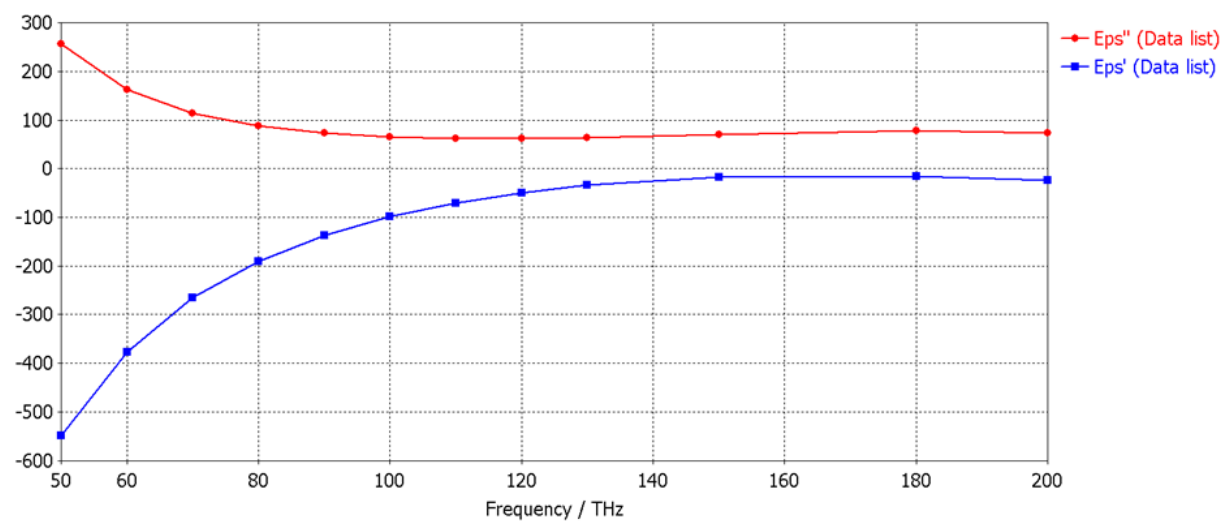
Dielectric properties of Cu[108,109]:

Frequency (THz)	Wavelength (μm)	ε'	ε''
50	5.99584916	-1500.6	295.32
60	4.996540967	-1055.8	202.55
70	4.2827494	-789.58	148.03
80	3.747405725	-615.94	110.63
90	3.331027311	-494.58	83.532
100	2.99792458	-405.56	63.744
110	2.725385982	-338.03	49.277
120	2.498270483	-285.62	38.657
130	2.306095831	-244.10	30.778
150	1.998616387	-183.54	20.366
180	1.665513656	-126.58	12.040
200	1.49896229	-101.66	8.9417
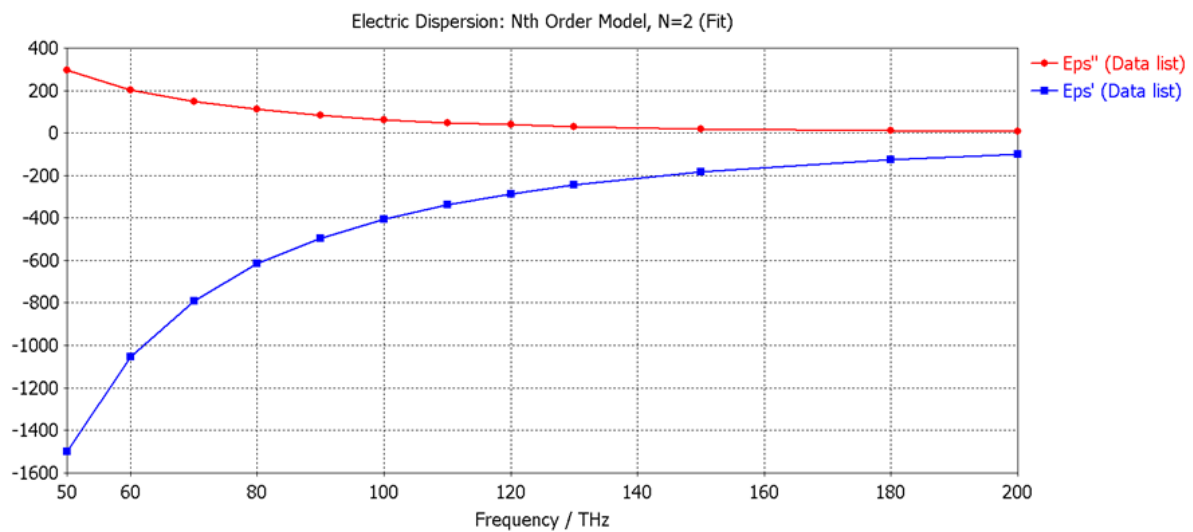
References

[1] H. W.Deckman, C. B. Roxlo and E. Yablonovitch. "Maximum statistical increase of optical absorption in textured semiconductor films". Opt. Lett. 8, pp 491–493 (1983)

[2] H. A. Atwater and A. Polman. "Plasmonics for improved photovoltaic devices" *Nat. Mater*, 9 pp 205–213 (2010)

[3] I. De Vlaminck, P. Van Dorpe, L. Lagae, and G.Borghs. "Local Electrical Detection of Single Nanoparticle Plasmon Resonance" Nano Lett. *7*(3), pp 703–706 (2007)

[4] F. T. Ulaby "Fundamentals of applied electromagnetics", ISBN 0130115541. *Prentice Hall,* pp.340-389 (1999)

[5] S. Law, L. Yu, A. Rosenberg, & D. Wasserman. "All-Semiconductor Plasmonic Nanoantenna for Infrared Sensing" *Nano Letters*, 13, pp 4569–4574. (2013)

[6] S. A. Maier. "Plasmonics : Fundamentals and Applications" *Springer Science + Business media*. ISBN: 0-387-33150-6, pp 66-72 (2007)

[7] R.L. Olmon, P.M. Krenz, A.C. Jones, G. D. Boreman and M. B. Raschke. "Near-field imaging of optical antenna modes in the mid-infrared", *Optics Express*, *16*(25)*,* pp 20295 (2008)

[8] L. Novotny. "Effective Wavelength Scaling for Optical Antenna". *Physical Review Letters*, *98*(26), pp 622802 1-4 (2007)

[9] P. Biagioni, J-S Huang and B. Hecht. "Nanoantenna for visible and infrared radiation" *Rep. Prog. Phy,* 75, pp 1-40 (2011)

[10] G. Harry, T. P. Bodiya and R. DeSalvo, *Optical Coatings and Thermal Noise in Precision Measurement* (Cambridge University Press, 2012), pp. 6-19 (2012).

[11] A. Nooke. "Gas Detection by Means of Surface Plasmon Resonance Enhanced Ellipsometry".*BAM Bundesanstaltfür Materialforschung und –prüfung*.ISBN 978-3-9815134-4-8, pp 5-10 (2012)

[12] G. F. Fine, L. M. Cavanagh, A. Afonja and R. Binions "Metal Oxide Semi-Conductor Gas Sensors in Environmental Monitoring". *Sensors*, 10, pp 5469-5502 (2010)

[13] C. Wang, L. Yin, L. Zhang, D. Xiang and R. Gao. "Metal oxide gas sensors: Sensitivity and influencing factors". *Sensors*, *10*(3), pp 2088–2106. (2010)

[14] Combustible Gas Safety Monitoring : Infrared vs. Catalytic Gas Detectors. *General Monitors White Papers*, 1. (2007)

[15] J. Chou. "Catalytic Combustible Gas Sensors". *Hazardous Gas Monitors: A Practical Guide to Selection, Operation and Applications*, pp 37–45. Retrieved from http://www.intlsensor.com/pdf/catalyticbead.pdf, (1999).

[16] M. J. Tierney and H. O. L. Kim. Electrochemical Gas Sensor with Extremely Fast Response Times. *Analytical Chemistry*, *65*(23), pp 3435–3440 (1993)

[17] E. Sánchez-Sinencio, B. Bhamidipati, and A. I. Colli-Menchi. "Low power complementary metal-oxide semiconductor class-G audio amplifier with gradual power supply switching." *IET Circuits, Devices & Systems*, *9*(4), pp 256–264. (2015)

[18] W.-B. Song and J.J. Talghader. "Design and characterization of adaptive microbolometers." *Journal of Micromechanics and Microengineering*, *16*(5), pp 1073–1079 (2006)

[19] D. Panda, and S. K. Pradhan. "Designing of Sensing Element for Bolometer Working at Room Temperature", (Mcsp), pp 47–52. (2016)

[20] R. A. Wood, C. J. Han and P.W. Kruse "Integrated uncooled infrared detector imaging arrays" *Solid-State Sensor and Actuator Workshop* (Hilton Head Island, SC, 2–6 June 1992) (Cleveland, OH: Transducer Research Foundation), pp 132–5 (1992)

[21] J. D. Vincent, S. E. Hodges, J. Vampola, M. Stegall, and G. Pierce. *"Fundamentals of Infrared and Visible Detector Operation and Testing"*, Second Edition. John Wiley & Sons, Inc. ISBN: 9781118094884, pp 92-102 (2016)

[22] D. Klocke, A. Schmitz, H. Soltner, H. Bousack and H. Schmitz, "Infrared receptors in pyrophilous ('fire loving') insects as model for new un-cooled infrared sensors," *Beilstein Journal of Nanotechnology,* 2, pp 186 (2011)

[23] D. Dooley. "Measuring THz radiation…choose a pyroelectric detector or Golay cell" *Application Note 1011, Spectrum Detector Inc.* (2009)

[24] N. Neumann and V. Banta. "P12-Comparison of Pyroelectric and Thermopile Detectors". *Proceedings IRS 2013*, pp 139–143. (2013)

[25] J. Tanaka, H. Imamoto, Y. Seki, and M. Oba. "Low power wireless human detector utilizing thermopile infrared array sensor". *Proceedings of IEEE Sensors*, 462–465 (2014)

[26] G.R. Nash. S. J. Smith, S. D. Coomber, S. Przeslak, A. Andreev, P. Carrington, M. Yin, A. KrierL. Buckle, M. T. Emeny, T. Ashley. "Mid infrared GaInSb/AlGaInSb quantum well laser diodes grown on GaAs." Appl. Phys. Lett 91, pp 311118. (2007)

[27] R. Adato, A. A. Yanik, J. J. Amsden, D. L. Kaplan, F. G. Omenetto, M. K. Hong, … H. Altug. "Ultra-sensitive vibrational spectroscopy of protein monolayers with plasmonic nanoantenna arrays". *Proc. Natl. Acad. Sci. U.S.A.*, 106(46), pp 19227–19232 (2009)

[28] W. S. M. Werner. "Optical Constants and Inelastic Electron-Scattering Data for 17 Elemental Metals", *Journal of Physical and Chemical Reference Data*, 38, pp 1013 (2009)

[29] F. T. Ulaby, Fundamentals of Applied Electromagnetics (Prentice Hall, 1999) pp.424-433.

[30] F. Neubrech., A. Pucci,, T. W. Cornelius, S. Karim, A. García-Etxarri, and J. Aizpurua. "Resonant plasmonic and vibrational coupling in a tailored nanoantenna for infrared detection" *Physical Review Letters*, 101(15), pp 2–5 (2008)

[31] F. Yi, H. Zhu, J. C. Reed and E. Cubukcu. "Plasmonically enhanced thermo mechanical detection of infrared radiation". *Nano Letters*, 4, 1638–1643 (2013)

[32] I. Malhotraa , K. R. Jhab and G. Singh. "Analysis of highly directive photoconductive dipole antenna at terahertz frequency for sensing and imaging applications". *Optics Communications*, *397* (January), pp 129–139. (2017)

[33] M. Ortolani, L. Baldassarre, A. Nucara, A. Samarelli, D. J. Paul, J. Frigerio, G. Isella, M. Finazzi and P. Biagioni. "Mid-infrared Plasmonic Antenna made of Electron-doped Epitaxial Germanium-on-Silicon." *38th International Conference on Infrared, Millimeter, and Terahertz Waves (IRMMW-THz)* (2013)

[34] P. Bharadwaj, B Deutsch, and L. Novotny, L. "Optical Antennas". *Advances in Optics and Photonics*, 1, pp 446-461 (2009)

[35] C. Langhammer, E. M. Larsson, B. Kasemo, and I. Zoric. AbstractTitle: Nanoplasmonic sensors. Chapter 8, "Nanoplasmonic Sensing for Nanomaterials Science, Catalysis, and Optical Gas Detection", *Springer Science+Business Media New York,* ISBN 978-1-4614-3932-5, pp 169-197 (2012)

[36] N. Ida. *Springer International Publishing Switzerland* ISBN 978-3-319-07805-2 pp 625 – 636 (2015)

[37] C. Loo, A. Lin, L. Hirsch, M-H Lee, J. Barton, N. Halas, J. West, R. Drezek. "Nanoshell-enabled photonics-based imaging and therapy of cancer." *Technology in Cancer Research & Treatment*, 3(1), 33–40. (2004)

[38] H. Atwater and A. Polman, "Plasmonics for improved photovoltaic devices." Nat. Materials, 9, pp 211 (2010)

[39] J. Henzie, J. Lee, M. H. Lee, W. Hasan, and T.W. Odom. "Nanofabrication of Plasmonic Structures." *Annual Review of Physical Chemistry*, *60*, pp 147–65 (2009).

[40] D. Gérard and S. K. Gray. "Aluminium plasmonics". *Journal of Physics D: Applied Physics*, *48*(18), pp 1-14 (2015)

[41] C.-C Chang, Y. D. Sharma, Y.–S. Kim, J. A. Bur, R. V. Shenoi, S. Krishna, … S. Y. Lin. "A Surface Plasmon Enhanced Infrared Photodetector Based on InAs Quantum Dots". *Nano Letters*, 5, pp 1704–1709 (2010)

[42] A. Gopalakrishnan, M. Malerba, S. Tuccio, S. Panaro, E. Miele, M. Chirumamilla, … E. Di Fabrizio. "Nanoplasmonic structures for biophotonic applications: SERS overview". *Annalen Der Physik*, *524*(11), pp 620–636 (2012)

[43] K. K. Choi, J. Sun, E. A. Decuir, K. A. Olver, and P. Wijewarnasuriya. "Electromagnetic modeling and resonant detectors and arrays". *Infrared Physics and Technology*, 70, pp 153–161 (2015)

[44] H. Guo, T. P. Meyrath, T. Zentgraf, N. Liu, L. Fu, H. Schweizer, & H. Giessen. "Optical resonances of bowtie slot antenna and their geometry and material dependence". *Optics Express*, 11, pp 7756–66 (2008)

[45] Z. Fang, L. Fan, C. Lin, D. Zhang, A. J. Meixner, and X. Zhu. "Plasmonic coupling of bow tie antenna with Ag nanowire". *Nano Letters*, 11(4), pp 1676–1680. (2011)

[46] R. Blanchard, S. V. Boriskina, P. Genevet, M. A. Kats, J-P Tetienne, N. Yu, M. O. Scully, L. Dal Negro, and F. Capasso."Multi-wavelength mid-infrared plasmonic antenna with single nanoscale focal point."*Harvard University,* 19 Issue: 22, pp 62-67 (2011)

[47] J. Yeo and J-I Lee "Planar log-periodic Bow-tie dipole array antenna with reduced size and enhanced front-back ratio". Microwave and optical technology letters, 54(6), (2012)

[48] F. J. González and G. D. Boreman, G. D. "Comparison of dipole, bowtie, spiral and log-periodic IR antenna". *Infrared Physics and Technology*, *46*(5), pp 418–428. (2005)

[49] D. K. Kotter, W. D. Slafer, S. D. Novack,P. Pinhero."Solar nantenna electromagnetic collectors". *Proceedings of the 2nd International Conference on Energy Sustainability*. pp 1–7. (2008).

[50] E. Donchev, J. S. Pang, P. M. Gammon, A. Centeno, F. Xie, P. K. Petrov, … N. M. Alford. "The rectenna device: From theory to practice (a review)". *MRS Energy & Sustainability*, *1*, E1 (2014)

[51] For more information see, http://www.antenna-theory.com/antenna/travelling/spiral.php

[52] Fibre optic cables stock image. https://www.istockphoto.com/gb/photos/fiber-optic?excludenudity=true&sort=mostpopular&mediatype=photography&phrase=fiber%20optic Downloaded on 15/4/17 for personal use only.

[53] Radio broadcast tower stock image. http://moziru.com/explore/Towers%20clipart%20radio%20wave/ . Downloaded on 15/4/17 for personal use only.

[54] The molecular absorption spectra for Carbon dioxide http://www.coe.ou.edu/sserg/web/Results/Spectrum/co2.pdf Downloaded on 8/1/2014 for personal use only.

[55] The molecular absorption spectra for Methane. http://www.coe.ou.edu/sserg/web/Results/Spectrum/ch4.pdf Downloaded on 10/1/2014 for personal use only.

[56] P. T. Moseley, J. O. W. Norris and D. E. Williams, "Techniques and Mechanisms in Gas Sensing", ISBN 0-7503-0074-4, pp 234. (1991)

[57] T. Ashley, N. T. Gordon. "Optimising Indium Aluminium Antimonide LEDs and Photodiodes for Gas Sensing Applications" *Proc. of SPIE*, 5359, pp 89-100 (2004)

[58] M. Asad, M. Ghorbanzadeh, G. Sareminia, and M. Fathipour. "Investigation of optimum junction depth of InSb infrared photodiode.".*ICEE 2012 - 20th Iranian Conference on Electrical Engineering*, pp 260–262 (2012)

[59] R. C. Jones, "Performance of detectors for visible and infrared radiaton," in Advances in Electronics, Vol. 5, L. Morton (Ed.), Academic Press, New York, pp 27–30 (1952).

[60] M. Obradov, Z. Jakšić, and D. Vasiljević-Radović, "Suppression of noise in semiconductor infrared detectors using plasmonics" *Journal of Optics*, *16*(12), pp 1-10 (2014)

[61] J. Hodgkinson, R. Smith, W. O. Ho,J. R. Saffell,R. P. Tatam. *Sensors and Actuators, B: Chemical*, 186, pp 580–588 (2013)

[62] H. R. Hardaway, T. Ashley, L. Buckle, M. T. Emeny, G. Masterton, G. Pryce. "Optimising Indium Aluminium Antimonide LEDs and Photodiodes for Gas Sensing Applications" *Proc. of SPIE*, 5564 pp 105–112 (2004)

[63] Ü, Tümkaya, "Performance assesment of indium antimonide photodetectors on silicon substrates" PhD Thesis. *Middle East technical university.* p 53 – 67 (2003)

[64] N.-T Yeh, P.-C Chiu, J.-I Chyi, F. Ren, and S. J. Pearton. "Sb-based semiconductors for low power electronics". *Journal of Materials Chemistry C*, 1, pp 4617 (2013)

[65] Company: Teledyne Judson Technologies. "Lead Sulfide Detectors and Lead Selenide Detectors." Product bulletin. October 2002. Downloaded on 23/1/2014 for personal use only.

[66] A. Krier, X.L. Huang and V.V. Sherstnev. e-ISBN 1846282098. *Springer-Verlag London Limited* pp 359-394 (2006)

[67] A.Rogalski "HgCdTe infrared detector material: history, status and outlook". *Institute of Physics Publishing 68*(10) pp 2267-2336 (2005)

[68] T. Ashley, and C.T Eliliot. "Operation and properties of narrow-gap semiconductor devices near room temperature using non-equilibrium techniques". *Semiconductor Science and Technology*, *6*, C99–C105 (1991)

[69] For example see; http://ir.microsensortech.com/pd.htm

[70] G. R. Nash, H. L. Forman, s. J. Smith, P. B. Robinson, L. Buckle, S. D. Coomber, M. T. Emeny, N. T. Gordon, and T. Ashley. "Mid-Infrared ALxIN1xSb Light-Emitting Diodes and Photodiodes for Hydrocarbon Sensing". *IEEE Sensors Journal*, *9*(10), 1240–1243. (2009)

[71] T. Ashley and C. T. Elliott "Operation and properties of narrow-gap semiconductor devices near room temperature using non-equilibrium techniques" *Applied Physics Letters*, 6, pp 99-105 (1991)

[72] G.R. Nash "Terahertz and Mid Infrared Radiation". ISBN: 978-94-007-0768-9. *Springer Science+Business Media B.V.* pp 113-121 (2011)

[73] B.K. Ridley. "Electrons and photons in semiconductor multilayers" Chapter 15.1 "Terahertz sources". *Cambridge university Press.* ISBN 978-0-521-51627-3, pp 369-392 (2009)

[74] U. Andersson, *Time-Domain Methods for the Maxwell Equations*. *Ph.D. Thesis*. ISBN 91-7283-043-3 (2001)

[75] For derivations see *Dielectric properties of materials* http://www.kayelaby.npl.co.uk/general_physics/2_6/2_6_5.html Online Version 1.0 (2005); accessed October 24, (2016).

[76] A. Note. "Agilent Basics of Measuring the Dielectric Properties of Materials. Measurement Techniques", pp 1-32 (2005)

[77] T. Søndergaard, & S. I. Bozhevolnyi. "Strip and gap plasmon polariton optical resonators." *Physica Status Solidi (B)*, *245*(1), pp 9–19 (2008)

[78] S. A. Maier, "Plasmonics: Fundamentals and Applications", Springer Science and Business Media, ISBN: 0-387-33150-6, pp 163-165 (2007).

[79] T. J. Seok, A. Jamshidi, M. Kim, S. Dhuey, A. Lakhani, H. Choo, … M. C.Wu. (2011). "Radiation engineering of optical antenna for maximum field enhancement". *Nano Letters*, *11*(7), pp 2606–10 (2007)

[80] N. Ida. *Springer International Publishing Switzerland* ISBN 978-3-319-07805-2 pp 723 – 929 (2015)

[81] N. Ida. "Engineering Electromagnetics", *Springer International Publishing Switzerland* ISBN 978-3-319-07805-2. pp 946 -954 (2015)

[82] R. L. Olmon, B. Slovick, T.W. Johnson, D. Shelton, S.-H. Oh, G. D. Boreman, M.B. Raschke. "Optical dielectric function of gold". *Physical Review B*, 86(23), pp 1-14 (2012)

[83] A. D. Rakic, A. B. Djurisic, J. M. Elazar, M. L. Majewski. "Optical properties of metallic films for vertical-cavity optoelectronic devices". *Appl Opt*, 37(22), pp 5271–5283 (1998)

[84] Information downloaded from http://www.infomine.com/investment/metal-prices on 26/03/2017 for personally use only.

[85] J. E. Ayers. ISBN 0-8493-7195-3. *Taylor and Francis group,* pp 88-92 (2007)

[86] M. T. Moneck, T. Okada, J. Fujimori, T. Kasuya, M. Katsumura, T. Iida, K. Kuriyama, W-C Lin, V. Sokalski, S. Powell, J. A. Bain, J-G Zhu. "Fabrication and Recording of Bit Pattern Media Prepared by Rotary Stage Electron Beam Lithography" *IEEE Transactions on Magnetics, 47*(10), pp 2656-2659 (2011).

[87] J.S. Greeneich.*Academic press*. ISBN 0-12-133550-X, pp 93-108 (1980)

[88] Product from Clariant-AZ Electronic materials. AZ *n*LOF^{TM} 2000 photoresist. pp 1–2

[89] G.R. Brewer. "Electron-Beam Technology in Microelectronic Fabrication". *Academic press.* ISBN 0-12-133550-2 pp 11-18 (1980)

[90] J. Turner and V.E.A.I. Derson. "Relativistic Ground-State Energy Eigenvalues of an Electron - Dipole System", *51*(1), pp 149-154 (1968)

[91] L. Novotny, "Strong coupling, energy splitting, and level crossings: A classical perspective" *American Association of Physics Teachers*, *78*(11), pp 1199 - 1202 (2010)

[92] MicroChemicals. "Lift-off Processes with Photoresists". *Web Brochure*. Retrieved from http://www.microchemicals.com/downloads/application_notes.html on 21/01/2016 for personal use only (2013)

[93] D. R. Frear, J. R. Michael, and P. F. Hlava. "Analysis of the Reaction Between 60Sn-40Pb Solder with a Pd-Pt-Ag-Cu-Au Alloy". *Journal of Electronic Materials*, *2*(22), pp 185–194 (1993)

[94] T. S. Moss, G. J. Burrell and B. Ellis, *Semiconductor Opto-Electronics* Butterworth & Co. Ltd, 1973, ISBN 0-408-70326-1 pp.60 and pp.332.

[95] For more information on the FTIR product used visit, https://www.bruker.com/products/infrared-near-infrared-and-raman-spectroscopy/ft-ir-research-spectrometers/vertex-series/vertex-8080v/overview.html

[96] Shimadsu, excellence in science, "Tips for FTIR analysis", Fourier Transform and apodization". http://www.shimadzu.com/an/ftir/support/tips/letter15/apodization.html, accessed for personal use on 28/2/17

[97] J. M. Khoshman, and M. E. Kordesch. "Optical properties of a-HfO2 thin films" *Surface and Coatings Technology. 201* (6), pp 3530–3535. (2006)

[98] T. Yang, X. Wang, W. Liu, Y. Shi and F. Yang. "Double-layer anti-reflection coating containing a nanoporous anodic aluminum oxide layer for GaAs solar cells" *Optics Express*, *2* (15), pp 18207–15. (2013)

[99] A. Rogalski, "Infrared Photon detectors", *Soc. Opt. Phys,* ISBN 0-8194-1798-X, pp 61-66 (1995)

[100] S. A. Maier, "Plasmonics: Fundamentals and Applications", *Springer Science and Business Media*, ISBN: 0-387-33150-6, pp 25 - 29 (2007).

[101] S. A. Maier, "Plasmonics: Fundamentals and Applications", *Springer Science and Business Media*, ISBN: 0-387-33150-6, pp 66 - 72 (2007).

[102] N. Gavish and K. Promislow. "Dependence of the dielectric constant of electrolyte solutions on ionic concentration: A microfield approach". *Physical Review E*, 94(1), pp 1–14 (2016)

[103] Hyperphysics. University of Georgia "Electromagnetic waves in a cubic cavity", http://hyperphysics.phy-astr.gsu.edu/hbase/quantum/rayj.html#c2. Used on 14/01/2017 for personal use only.

[104] E. Fred Schubert, "Light Emitting diodes" second edition, ISBN-10 0-521-86538-7 pp 93 (2003).

[105] J. Kischkat, S. Peters, B. Gruska, M. Semtsiv, M. Chashnikova, M. Klinkmüller, O. Fedosenko, S. Machulik, A. Aleksandrova, G. Monastyrskyi, Y. Flores, and W. T. Masselink. "Mid-infrared optical properties of thin films of aluminum oxide, titanium dioxide, silicon dioxide, aluminum nitride, and silicon nitride". *Appl. Opt. 51*(28), pp 6789-6798 (2012).

[106] A. D. Rakić. "Algorithm for the determination of intrinsic optical constants of metal films: application to aluminum". *Appl. Opt. 34*(22), 4755-4767 (1995)

[107] A. D. Rakić, A. B. Djurišic, J. M. Elazar, and M. L. Majewski. "Optical properties of metallic films for vertical-cavity optoelectronic devices" *Appl. Opt.* 37(22), pp 5271-5283 (1998)

[108] M. Theye. "Investigation of the optical properties of Au by means of thin semitransparent films", *Instit. Opt. 2*(8) pp 3060 - 3078 (1970)

[109] S. Babar and J. H. Weaver. "Optical constants of Cu, Ag, and Au revisited", *Appl. Opt.* 54, 477-481 (2015)